COMPOSITE ACTION OF FRP BRIDGE DECKS ADHESIVELY BONDED TO STEEL MAIN GIRDERS

THÈSE N^{O} 3135 (2004)

PRÉSENTÉE À LA FACULTÉ ENVIRONNEMENT NATUREL, ARCHITECTURAL ET CONSTRUIT

Institut de structures

SECTION D'ARCHITECTURE

ÉCOLE POLYTECHNIQUE FÉDÉRALE DE LAUSANNE

POUR L'OBTENTION DU GRADE DE DOCTEUR ÈS SCIENCES

PAR

Herbert W. GÜRTLER

Dipl.-Ing., Technische Universität Darmstadt, Allemagne
et de nationalité allemande

acceptée sur proposition du jury:

Prof. Dr T. Keller, directeur de thèse
Prof. Dr.-Ing. M. Hoeft, rapporteur
Dr J.-P. Lebet, rapporteur
Prof. U. Meier, rapporteur
Prof. Dr.-Ing. G. Sedlacek, rapporteur

Lausanne, EPFL
2004

CCLAB Composite Construction Laboratory

ÉCOLE POLYTECHNIQUE FÉDÉRALE DE LAUSANNE

Thèse présenté à la faculté environnement naturel, architecture et construit - Institut de structures - Section D'architecture pour l'obtension du grade de docteur ès sciences

Composite Action of FRP Bridge Decks Adhesively bonded to Steel Main Girders

Herbert W. Gürtler
Dipl.-Ing. Technische Universität Darmstadt

Composition du jury de thèse
Prof. Inès Lamunière - Présidente
Prof. Dr. Thomas Keller - Directeur de thèse
Prof. Dr.-Ing. Michael Hoeft - Rapporteur
Dr. Jean-Paul Lebet - Rapporteur
Prof. Urs Meier - Rapporteur
Prof. Dr.-Ing. Gerhard Sedlacek - Rapporteur

Lausanne, EPFL
December 2004

Für meinen Vater

Abstract

Up until today reinforced concrete has been used in most cases for the manufacturing of bridge decks. Depending on the quality of the work carried out, defects can already occur after only a few years. These defects mostly appear in the form of corrosion of the steel reinforcement due to concrete's sensitivity to de-icing salts and water. To reduce maintenance costs, which are mainly caused by corrosion of the steel reinforcement, attempts were made to eliminate the steel reinforcement in the bridge deck. This was achieved for example by replacing the whole concrete bridge deck with an FRP[1] bridge deck. FRP bridge decks, besides the advantage of the absence of steel reinforcement, exhibit the advantage of a low dead load (approx. 20% of a comparable concrete deck) combined with high strength. These properties resulted in the fact that today more than 200 bridges with FRP decks are in service worldwide. Most of them need steel or concrete main girders to bridge the required span. Despite the many bridges already in service, assessment of their load-bearing capacity or deflections still remains difficult. Some of the reasons for this this are as follows:

- Geometry and material properties vary considerably between different FRP bridge-deck types.
- The problem of the connection between main girders and bridge decks has only been partially solved.
- No design method exists which allows determination of the stresses and deflections of composite girders, and takes the degree of composite action of the bridge deck into account.

This thesis contributes to solve these problems.

Experiments with two different bridge decks were carried out in order to determine the necessary system properties (in-plane compression and shear resistance and in-plane compression and shear stiffness) for the calculation of the load-bearing behavior of steel/FRP composite girders. The method developed to determine the system properties can also be applied to other FRP bridge decks (e.g. sandwich decks).

In a second step, four composite girders (two with each bridge deck) were manufactured by bonding the bridge decks onto conventional steel girders. Local failure of the bridge deck, as occurs in girders with stud or bolt connections, is therefore prevented and a clear load transfer in the joint is assured. One of the two girders, with each bridge deck system, was tested statically and the other statically and under fatigue loads. The results of the girder experiments

[1] **F**iber **R**einforced **P**olymer

showed that adhesive bonding is a reliable connection technique, since failure always occurred first in the bridge deck and then in the adhesive layer. The stiffness and failure load of the composite girders could be increased considerably in comparison with the pure steel girder. The determined system properties concerning in-plane shear and compression stiffness were confirmed with the girder experiments.

The results of the experiments with the composite girders were compared with results of an analytical design method for concrete/wood girders adapted for steel/FRP composite girders. It was shown that the load-bearing behavior of composite girders consisting of steel main girders and adhesively- bonded FRP bridge decks can be determined with good accuracy in the linear-elastic region. Furthermore a design method was developed which allows the load-bearing capacity of the steel/FRP composite girders investigated in this thesis to be determined with very good accuracy.

Subsequently a parameter study was carried out in order to verify the assumption of full composite action in the adhesively- bonded joint. This is one of the requirements for application of the developed design methods. The study showed that the assumption is applicable for different adhesives and even for thicknesses up to 50 mm.

Zusammenfassung

Zur Herstellung von Fahrbahnplatten für den Brückenbau wurde bisher fast ausschliesslich der altbewährte Baustoff Beton eingesetzt. Je nach Qualität der ausgeführten Arbeiten können aber bereits nach wenigen Jahren Mängel auftreten. Meist äussern sich diese Mängel in Form von Bewehrungskorrosion welche durch die Empfindlichkeit des Betons gegenüber Wasser und Tausalz verursacht wird. Um die steigenden Unterhaltungskosten, welche hauptsächlich auf die Bewehrungskorrosion zurückzuführen sind, zu reduzieren wurde daran gearbeitet den Bewehrungsstahl zu ersetzen. Dies wurde zum Beispiel dadurch erreicht, daß die komplette Beton Fahrbahplatte durch eine aus GFK[2] ersetzt wurde. Fahrbahnplatten aus GFK haben ausser dem genannten Vorteil der nicht vorhandenen Stahlbewehrung noch den Vorteil des geringen Eigengewichtes (ca. 20% einer vergleichbaren Betonplatte) in Verbindung mit einer hohen Festigkeit. Diese Eigenschaften haben dazu geführt, daß weltweit bereits mehr als 200 Brücken mit GFK Fahrbahnplatten im Einsatz sind. Die meisten dieser Brücken benötigen Stahl- oder Betonhauptträger um die geforderten Spannweiten zu überbrücken. Trotz der sich bereits in Betrieb befindlichen großen Anzahl von GFK Brücken bereitet die Beurteilung der Tragkraft oder der Verformung erhebliche Schwierigkeiten. Dies, hat unter Anderen folgende Gründe:

- Die Geometrie und Materialeigenschaften unterscheiden sich beträchtlich zwischen den unterschiedlichen Brückenplatten (Hersteller).
- Das Problem der Verbindung zwischen den Hauptträgern und den Brückenplatten ist nur unzureichend gelöst (bisher mittels Schrauben und Kopfbolzendübeln).
- Es gibt keine Berechnungsmethode die es erlaubt, Spannungen und Verformungen unter Berücksichtigung des Traganteiles der Fahrbahnplatten zu ermitteln.

Die vorliegende Arbeit soll ein Ansatz sein diese Probleme Schritt für Schritt zu lösen.

Durch Versuche an zwei verschiedenen Brückenplatten werden die Systemeigenschaften (Druck- und Schubfestigkeit sowie Druck-und Schubmodul) ermittelt welche zur Berechnung von Stahl/GFK Verbundträgern notwendig sind. Die entwickelte Methode zur Bestimmung der Systemparameter kann auch auf andere Brückenplatten (z.B. Sandwichelemente) angewandt werden.

In einem weiteren Schritt werden insgesamt vier Verbundträger (zwei mit jeder Brückenplatte) durch Aufkleben der GFK-Fahrbahnplatte auf Stahlträger hergestellt. Durch das Kleben der Fahrbahnplatte auf die Hauptträger

[2] **G**las**F**aser-verstärkte-**K**unststoffe

wird lokales Versagen verhindert, da es weder Schrauben noch Kopfbolzendübel gibt, und ein eindeutiger Kraftfluss wird gewährleistet. Jeweils einer der beiden Träger wurde statisch getestet, der Andere statisch und auf Ermüdung. Die Ergebnisse der Trägerversuche haben gezeigt, daß Kleben eine verläßliche Verbindungstechnik zum Herstellen von Stahl/GFK Verbundträgern ist, denn Versagen trat zuerst immer im Brückendeck ein, nie in der Klebefuge. Außerdem konnte festgestellt werden, daß die Steifigkeit und die Bruchlast, im Vergleich zu einem einfachen Stahlträger, erheblich durch das Aufkleben einer GFK-Fahrbahplatte erhöht werden können. Die ermittelten Systemparameter bezüglich der Druck- und Schubsteifigkeit konnten durch die Versuche an den Verbundträgern bestätigt werden

Die Ergebnisse aus den Versuchen mit den Verbundträgern wurden mit Ergebnissen aus einer analytischen Berechnungsmethode für Beton/Holz Verbundträger, welche an die speziellen Anforderungen der Stahl/GFK Verbundträger angepasst wurde, verglichen. Hierbei hat sich gezeigt, dass das Tragverhalten (Spannungen und Durchbiegung) von Stahl/GFK Verbundträgern im linear elastischen Bereich mit guter Genauigkeit bestimmt werden kann. Weiterhin wurde eine Methode entwickelt, welche es erlaubt die Bruchlast von Stahl/GFK Verbundträgern mit sehr guter Genauigkeit zu bestimmen.

Im Folgenden wird mittels einer Parameterstudie gezeigt, dass die Annahme voller Verbundwirkung in der geklebten Fuge, welche in der vorliegenden Arbeit getroffen wird, auch für unterschiedliche Kleber sowie für Klebdicken bis zu 50 mm gerechtfertigt ist.

Resumé

Pour la construction de tablier de ponts, on utilise, jusqu'à aujourd'hui, presque exclusivement le béton. Toutefois, suivant la qualité du travail, des défauts peuvent apparaître déjà après quelques années. Ces défauts sont dans la majorité des cas des défauts de corrosion de l'armature dus à la sensibilité du béton à l'eau et aux sel. Pour réduire les coûts de maintenance de plus en plus grands, coûts surtout dus à la corrosion de l'armature, on a travaillé sur des solutions consistant à remplacer l'armature en acier. On a même remplacé tout le tablier en béton par un tablier en fibre de verre. Un tablier de pont en fibre de verre a, au-delà des avantages liés à la corrosion, l'avantage du poids propre très réduit (d'environ un cinquième du poids propre d'un tablier en béton armé) avec une résistance mécanique comparable. Ces caractéristiques on fait que l'on a construit jusqu'à présent environ deux cents ponts avec des tabliers en fibre de verre de part le monde. La plupart de ces ponts nécessitent des porteurs primaires en acier ou en béton pour enjamber les portées requises. Malgré le grand nombre de projets réalisés, il demeure encore très difficile de prédire la charge ultime et la déformation de ces constructions. Ceci est en partie imputable aux raisons suivantes :

- La géométrie et les propriétés mécaniques des tabliers diffèrent beaucoup d'un tablier à l'autre, d'un fabricant à l'autre.
- Le problème de la jonction entre le tablier et le porteur primaire en acier ou béton n'est que partiellement résolu (jusqu'à présent avec des goujons et/ou des boulons).
- Il n'existe pas encore de méthode qui permette de calculer et de prendre en compte les contraintes et déformations du tablier.

Le travail suivant se veut une ébauche pour résoudre ce problème pas à pas.

Des essais menés sur deux types différents de tabliers ont permis de déterminer des caractéristiques de système (rigidité à la compression et au cisaillement) nécessaires à la description et au calcul de poutres mixtes acier-fibre de verre. La méthode développée pour déterminer les caractéristiques de système est aussi valable pour d'autres tabliers en fibre de verre comme par exemple des tabliers sandwich.

Dans une deuxième étape, des essais sur quatre poutres mixtes acier-fibre de verre (deux fois deux essais avec des systèmes différents) obtenues en collant des tabliers en fibre de verre sur des poutres en acier on été effectués. Le collage permet de réduire la ruine locale, car il n'existe ni goujon ni boulon ; le flux des forces est optimisé. A chaque fois, un essai statique et un essai dynamique (de fatigue) ont été effectués. Les résultats on montré que coller est un moyen de connexion sûr, car la ruine s'est toujours produite en premier lieu dans le tablier. La rigidité est la charge maximale ont pu augmentées considérablement.

Les résultats de ces essais ont été comparés à des calculs menés avec une méthode analytiques pour des poutres composite béton/bois spécialement adaptée à la poutre mixte acier-fibre de verre. Il a été démontré que cette méthode prédit les contraintes et la déformation des poutres mixte acier-fibre de verre avec une bonne précision dans le domaine linéaire. D'autre part une méthode pour déterminer avec une grande précision la charge ultime du système a aussi été développée.

Par la suite, une étude paramétrique a démontré que l'hypothèse formulée dans ce travail, à savoir l'action composite dans la couche de colle entre le tablier et la poutre primaire en acier, est valable pour différentes colles jusqu'à des épaisseurs de colle de 50 mm.

Acknowledgments

Even if only my name appears on the first page as author, this thesis would not have been possible without the essential contributions from my colleges and friends, which I would like to thank. Among many others these were:

Prof. Thomas Keller who gave me the confidence and possibility to write this thesis. He has always supported me during the last three years.

Special thanks also go to the people who have accepted to act as experts for this thesis: Prof. Dr.-Ing. Michael Hoeft, Prof. Urs Meier, Dr. Jean-Paul Lebet and Prof. Dr.-Ing. Gerhard Sedlacek. Being expert in a jury is very time-consuming and assumes that the jury members consider the thesis worth reading. Thank you for your confidence.

My colleges at the CCLab, above all Martin Schollmayer and Till Vallée, who were very helpful with technical advice and encouragement at difficult times.

Dr. Jean-Paul Lebet, who showed me how to deal with composite bridges and was always all ears when I came to him with technical questions.

My colleges at the IBOIS, in particular Claudio Pirazzi, Klaus Kreher and Bernhard Stamm, who spent several hours with me discussing "composite problems" with "flexible shear connectors".

The whole team of technicians, especially Hansjakob Reist, who worked patiently with me many hours in the laboratory. Without their support, it would not have been possible to accomplish the extensive experiments.

Sylvain Demierre, who was able to solve all problems related to testing machines and measuring devices, no matter how difficult. I will never forget his "on trouvera une solution".

I also do not want to forget the help of the companies who supported this thesis with financial and material means. These were: Fiberline Composites Denmark, Martin Marietta Composites USA and Sika Switzerland. The Federal Roads Authority or Office Fédérale des Routes Switzerland of course I have to thank for financing my thesis.

The woman who spent a lot of time with me in finding the right words and discussing English grammar was Margaret Howett. Technical thesis are always difficult to correct, but we made it!

Last but not least, I want to thank my wife Caroline, who had to agonize when I came home late at night in a bad mood when something had gone wrong again at work, and all my family and friends who always believed in my success.

Thank you all!

Contents

Nomenclatures

Abbreviations

ACCS	–	Advanced Composite Construction System
CCLab	–	Composite Construction Laboratory
CFRP	–	Carbon Fiber Reinforced Polymers
CSS	–	Carbon Shell System
EMPA	–	Eidgenössische Materialprüfungs und Forschungsanstallt
EPFL	–	École Polytechnique Fédérale de Lausanne
FEM	–	Finite Element Method
FLS	–	Failure Limit State
FRP	–	Fiber Reinforced Polymers
GFRP	–	Glass Fiber Reinforced Polymers
PU	–	Polyurethane
SLS	–	Serviceability Limit State
ULS	–	Ultimate Limit State
VARTM	–	Vacuum Assisted Resin Transfer Moulding

Latin upper case

$A_{a,i}$	–	partial area of the steel girder
$A_{fl,FRP}$	–	cross-sectional surface of one face panel
A_i	–	cross-sectional surface of section i
B	–	bending stiffness of composite girders assuming full composite action between the cross-sectional parts
C_i	–	compression forces
E_a	–	modulus of elasticity of steel
$E_{c,330}$	–	compressive E-modulus of adhesive SikaDur 330
$\widehat{E}_{FRP}$	–	compression modulus of bridge deck perpendicular to the pultrusion direction
E_i	–	modulus of elasticity of section i
EI_m	–	calculated bending stiffness
$(EI)_{ef}$	–	effective bending stiffness
F	–	force; load per jack
$F_{Rs,FRP}$	–	maximum transmittable shear force between the face panels for the considered girder
$F_{c,FRP}$	–	appropriate force for compression failure in the face panel

$\widehat{G}$	–	in-plane shear modulus of bridge deck perpendicular to the pultrusion direction
H	–	height of complete cross-section
I_i	–	moment of inertia of section i
K_i	–	instantaneous slip modulus after EC5
$\widehat{K}$	–	in-plane shear stiffness of bridge deck
M_d	–	bending moment at the load level where the stresses in the composite girders were verified
M_i	–	bending moment in section i
$M_{II,i,(\zeta)}$	–	bending moment in section i for region II at location ζ in girders' longitudinal direction
N	–	normal forces
$N_{II(\zeta)}$	–	normal force for region II at location ζ in girders' longitudinal direction
P	–	single load
Q_i	–	shear forces in section i
R_s	–	in-plane shear resistance of bridge deck
T_i	–	tensile forces
$W_{i,j}$	–	moment of resistance in single cross-section i at location j

Latin lower case

a^2	–	proportion of the second addend in the parallel-axis theorem of the moment of inertia of the composite girder $(z^2 \cdot A)$
a_i	–	proportion of the bending stiffness of the single cross-section E_iI_i compared to the sum of bending stiffnesses $\sum E_iI_i$; distance between the neutral axis of the single cross-section i and the neutral axis of the composite girder in section 2
$\frac{a^2}{1-a^2}$	–	material and geometrical constant
b	–	width of specimen
b_{ef}	–	effective width
b^2	–	abbreviation for geometry, material and stiffness parameters
d_{max}	–	maximum distance from neutral axis of single cross-section 1
d_{FRP}	–	distance from neutral axis of single cross-section 2 to the lower face panel
$d_{a,o}$	–	distance of neutral axis of single cross-section 2 $\Leftrightarrow$ top steel flange
f_m	–	measured deflection at mid-span
$_{max}f$	–	calculated deflection at mid-span

e	–	difference between the neutral axes of the single cross-sections
Δe	–	distance between the two single cross-sections
h	–	height of specimen
k	–	shear stiffness of the joint
l	–	span
l_{ef}	–	length from support to point of change of sign in the shear force (Introduction length)
n_0	–	modular ration for short-term loading
q	–	distributed load
s_i	–	distance of the discrete connections (nails, screws...)
t	–	bridge deck depth; adhesive thickness
t_{fl}	–	thickness of face panel
u	–	relative displacement between deck face panels at girders' ends
$w_{II(\zeta)}$	–	deflection for region II at location ζ in girders' longitudinal direction
$z_{s,2}$	–	distance of neutral axis of single cross-section 2 $\Leftrightarrow$ lower steel flange
$*$	–	the star in all formulas is a sign for an adapted formula for steel/FRP composite girders. The origin can be in the EC 5 or in the verifications after Hoeft.

Greek upper case

Φ	–	distance support $\Leftrightarrow$ load

Greek lower case

α	–	angle
$\epsilon_{a,ex,i}$	–	measured steel strain in the corresponding partial area
$\epsilon_{c,fail,FRP}$	–	compressive failure strain of bridge deck
$\epsilon_{s,fail,FRP}$	–	axial strain at shear failure in the core of the deck
ϵ_y	–	yielding strain steel
γ	–	shear strain; stiffness factor for the part of composite action
λ	–	shear influence constant
ν	–	poissons' ratio
$\sigma_{II,1,j}$	–	stress in single cross-section 1 for region II at location j
$\sigma_{II,N}$	–	normal stresses for region II; single cross section 1 negative; single cross section 2 positive

$\sigma_{II,1,j,M}$	–	bending stresses in single cross-section i for region II at location j
$\sigma_{II,2,j,FRP}$	–	stress in the FRP part of single cross-section 2
$\sigma_{II,2,FRP,N}$	–	normal stress in the FRP part of single cross-section 2
$\sigma_{II,2,j,FRP,M}$	–	bending stress in the FRP part of single cross-section 2 at location j
$\sigma_{II,2,j,a}$	–	stress in the steel part of single cross-section 2
$\sigma_{II,a,N}$	–	normal stress in the steel part of single cross-section 2
$\sigma_{II,2,j,a,M}$	–	bending stress in the steel part of single cross-section 2 at location j
$\sigma_{II,2,max,a,u}$	–	maximum stress in single cross-section 2 for region 2 in the lower steel flange
$\sigma_{II,2,max,a,o}$	–	maximum stress in single cross-section 2 for region 2 in the upper steel flange
$\sigma_{i,m,d}$	–	design value of maximum stresses in the single cross-sections
$\sigma_{i,d}$	–	design value of the normal stresses in cross-section i resulting from the pair of normal forces in the full cross-section
$\sigma_{m,i,d}$	–	design value of the normal stresses in cross-section i resulting from the bending moments in the single cross-sections
τ	–	shear stress
τ_{fail}	–	shear shear system failure stress
ω^2	–	abbreviation for geometry, material and stiffness parameters
ζ	–	describes a location in girders longitudinal direction

1 Introduction

Although new materials such as FRPs[1] are now available for bridge construction [33], most bridge contractors throughout the world continue to use more traditional materials such as steel and concrete, thereby taking advantage of well-proven materials with appropriate design codes. These materials present inherent problems such as corrosion of concrete reinforcement (if the work was carried out not carefully) and a considerably longer construction period when compared to FRP materials. Those authorities who have decided to employ FRP materials in their bridge construction projects have used them as a first step for the strengthening of existing concrete bridges (CFRP[2] lamellas) [79]. A few years later FRP reinforcing bars were also applied in concrete structures.

The next step was the development of bridge decks composed entirely of FRP materials. The mechanical properties of FRP materials explain why they appear to be very convenient for use in bridge decks [60]. The most obvious characteristics are the low dead load combined with high strength and resistance to de-icing salts and water [89]. As a result of these advantages, different FRP bridge deck systems have already been developed (see Fig. 2.3, page 12) and a multitude of demonstration projects with smaller spans have been built [68].

While several pedestrian bridges have already been constructed entirely of composite material [66], most road bridges still need main steel girders to be cost-effective. The deck elements are usually bonded together and then fastened to primary steel girders with shear studs or bolts (see Fig.2.16, page 21), [68]. The connection to the main steel girder is one of the problems which has not yet been sufficiently investigated. Therefore the composite action between the two structural components, steel main girder and FRP bridge deck, which certainly exists cannot be considered in the design. A more material- adapted connection technique like adhesive bonding could help to solve this problem.

From the author's point of view, future steel/FRP composite bridges could look like the example shown in Fig. 1.1 on the next page. Figure 1.1 shows a single-span three-lane bridge with an FRP deck spanning transversely to the bridge axis. Spans longer than 50 m do not seem economic since the influence of the bridge deck in terms of composite action decreases with increasing span. The distance between the main girders is determined by the stiffness of the bridge deck transverse to the bridge axis. Investigations carried out at the CCLab [72] showed that this distance will be approximately 2.70 m for the bridge decks used in this thesis.

[1] **F**iber- **R**einforced **P**olymers
[2] **C**arbon **F**iber **R**einforced **P**olymers

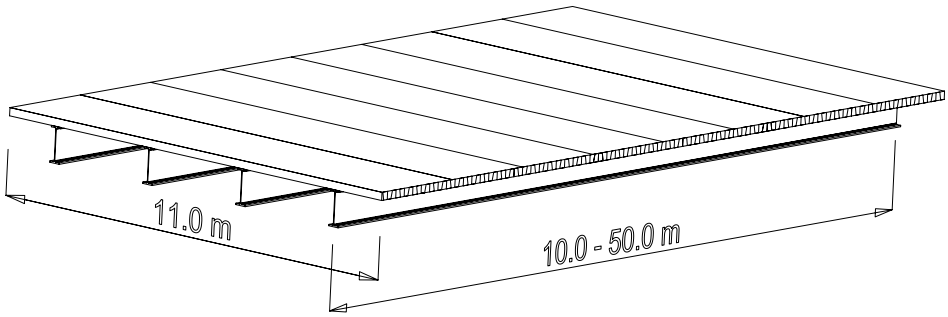

Figure 1.1: Layout of three-lane road bridges: steel girders with adhesively-bonded FRP bridge deck, girder spacing 3.0 m

1.1 Project motivation

Thanks to the various advantages offered by FRP bridge decks, they have rightly found their way onto the market. The most significant advantages of FRP bridge decks which led to their practical implementation are summarized below:

- Relatively small dead load (roughly 20% of a comparable concrete bridge deck)
- Rapid construction with minimum traffic interruption
- Low maintenance costs
- Reduction of lifecycle costs by roughly 20% over 75 years
- Possibility of installing a (remote) monitoring system
- Reliable quality assurance due to industrial fabrication
- Bridge restoration: swift replacement of corroded concrete decks, particularly for traditional steel-concrete composite bridges (concrete decks on steel girders)
- Bridge widening: Possibility of broadening a bridge from two to three lanes without significant additional loads for piers and abutments.

Nevertheless many things still remain to be improved, such as the load transfer between FRP decks and main girders or the development of an adequate design method which takes the composite action between materials into account. A standardized design method is very important for the future of FRPs in bridge construction not only to simplify calculations but also to provide engineers with a tool to effect the necessary verifications. A global overview of the interrelationships between FRP bridge deck and the targeted design method is shown in Fig. 1.3, page 4.

In the case of bridges with steel girders and concrete decks, the deck participates fully with the top chord of the steel girder. The connection of steel girder and concrete deck by means of shear studs enables full cooperation between the cross-sectional parts. This behavior is known as composite action. Full composite action is characterized by a plane strain distribution in the composite section, fulfilling the hypothesis of Bernouilli (see Fig. 1.2).

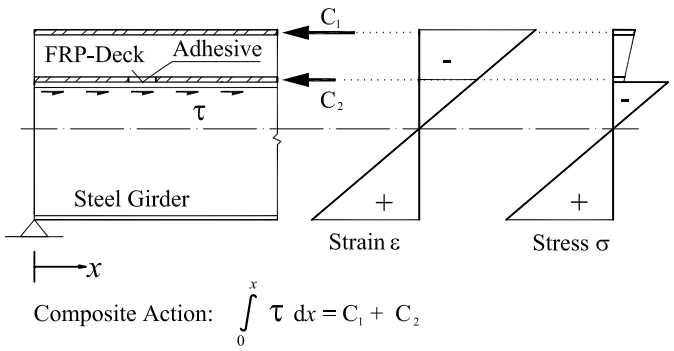

Figure 1.2: Principle of the composite action between steel girders and FRP bridge decks.

For composite girders with FRP bridge decks it is not apparent whether the section can comply with Bernouilli's law or not, because it is often unclear to what degree the bolted (or studs) girder-to-deck connections will transfer forces in the longitudinal direction of the bridge, thus allowing the deck to act as part of the top chord of the girder. Even if the connection allows full composite action, it is still unclear whether the in-plane shear forces can be fully transmitted to the upper face panel of the bridge deck in order to achieve a plane strain distribution. A competitive FRP-steel bridge must have a bridge deck which acts as part of the compression chord (level 2 in Fig. 1.3 on the next page). Taking composite action into account in the design decreases not only deflection but also the weight of steel section required for strength, and thus costs. For FRP decks to be used economically in the future, the contribution made by the composite action must be exploited.

To benefit from the same characteristics in construction with FRP-steel girders as in construction with traditional steel-concrete girders, a joining technique which allows the deck to participate as part of the top chord is needed. The primary requirement for such a connection is a clear load transfer making it possible to predict the joint's behavior. Current connection techniques, as described in Section 2.3.2, have a very complicated load-transfer mechanism and are thus not calculable, which is why composite action is currently not considered in the design (level 3 and 4 in Fig. 1.3 on the following page).

Due to the above-mentioned conditions of load transfer between bolted (studs) FRP decks and girders which are not precisely understood, girders and FRP decks are often designed very conservatively with two limiting conditions: girders are designed without considering any composite action of the

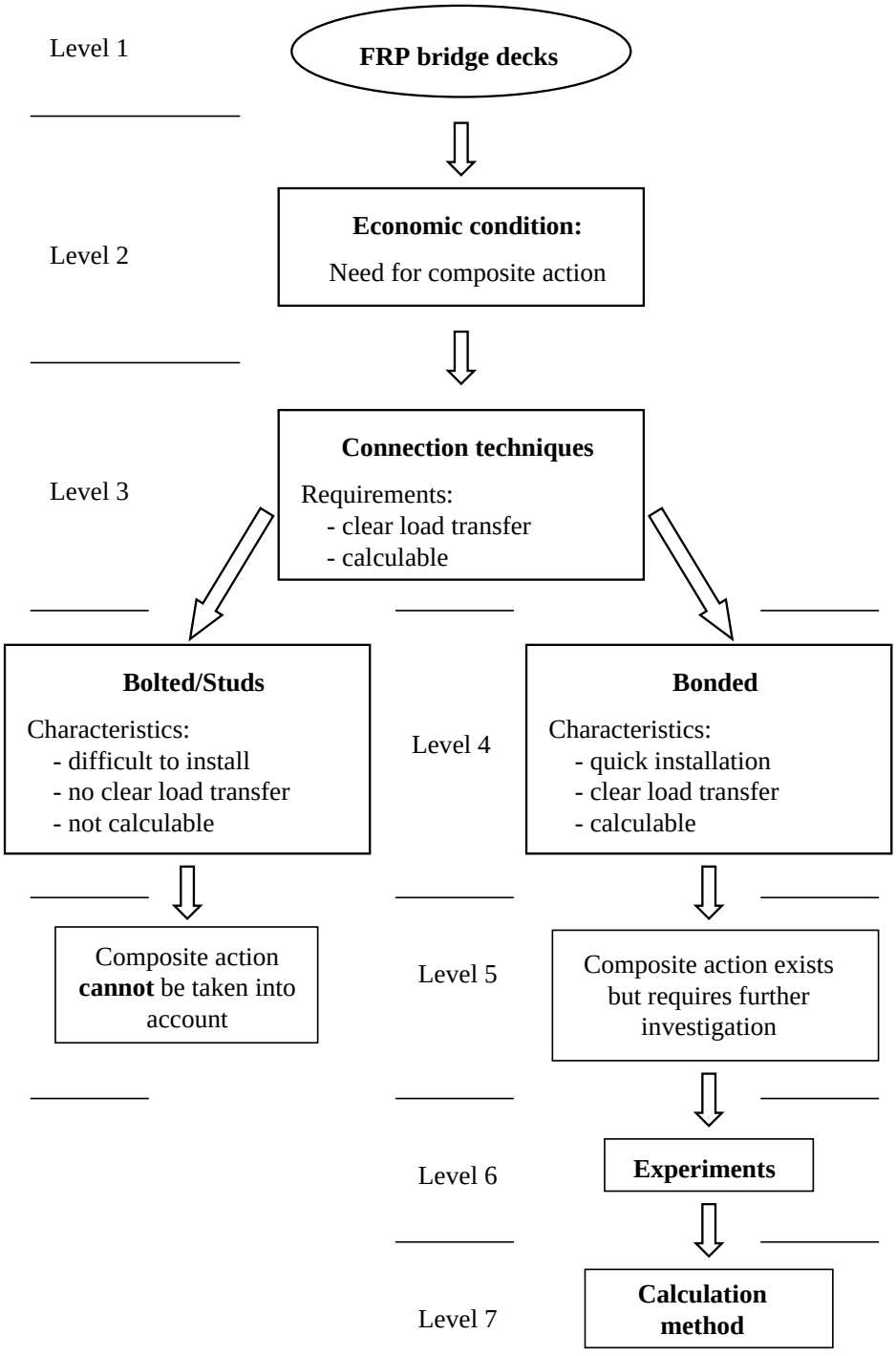

Figure 1.3: Overview of the interrelationships

FRP deck, and calculations for the deck are made assuming full composite action. In order to obtain accurate conditions, composite action is often deliberately prevented by construction details [2]. This situation is unsatisfactory since it places FRP decks at a disadvantage in comparison with concrete decks.

Adhesive bonding is by far a more material-adapted connection method [112] than bolting. It permits forces to be introduced uniformly in the flexible matrix, before they are transferred to the brittle fibers. The two major advantages of a bonded deck-to-girder connection are the ease of installation and the clearly defined load transfer, which enables a better understanding of the joint behavior (level 4 Fig. 1.3 on the preceding page). The prediction of the joint behavior is a very important issue when dimensioning composite girders with composite action, because without accurate information concerning the joint's behavior, the global deformation and failure behavior of the composite girder cannot be estimated either. At present, the load-carrying capacity of the girders with bolted (or stud) connections currently in use can only be determined by experimentation [2] (level 5 in Fig. 1.3 on the facing page). Therefore, the use of adhesives for the connections seems more favorable. A possible solution to that problem could look as shown in Fig. 1.4. With the results from experiments with adhesively bonded FRP-steel composite girders a design method for these girders can be developed (level 6 and 7 in Fig. 1.3 on the facing page). A straightforward design method which allows engineers

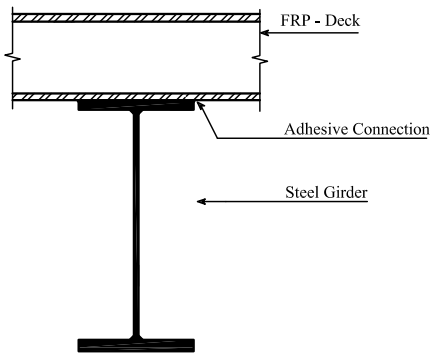

Figure 1.4: Adhesively-bonded connection between steel main girder and FRP bridge deck

to consider cost-effective solutions in bridge construction with FRP materials will certainly also lead to increased use in practice. The development of an adequate joining technique and an engineer- adapted design method facilitating calculation of the degree of composite action between FRP deck and steel main girder thus constitutes an essential element in the design of bridges with FRP decks.

1.2 Objectives

As described in Section 1.1, the most urgent developments needed for FRP-steel composite bridges are a viable design method taking composite action into account and a reliable adhesive-bonding technique which enables full composite action. To link theses two topics and provide engineers with a basis for the application of FRP-steel composite girders, the objectives of this thesis are:

- Demonstration of the feasibility and development of adhesively bonded deck-to-girder connection to provide full composite action (study of the static, fatigue and creep behavior behavior).
- Development of a design method for adhesively-bonded composite girders with composite action (consisting of steel girders and FRP bridge decks). This includes the prediction of the cross-sectional stress/strain distribution for all three load levels (SLS[3], ULS[4], FLS [5]), the calculation of the deflections at SLS load level and the prediction of the failure loads.

1.3 Scope and limits

Composite FRP/steel girders adhesively- bonded together under positive bending moment are the subject of this study. The main aim of the thesis is to develop a design method which allows the cross-sectional stress/strain distribution and deflection at mid-span to be determined. Particular attention is paid to the load transfer in the adhesively-bonded joint and between the two face panels of the bridge deck in order to take into account a possible partial "shear connection" either in the joint or between the face panels. The experimental girders were investigated under static and fatigue loads and only in longitudinal direction. The creep behavior is not a special task of this thesis, nevertheless one girder was also subjected for 4 hours to a constant load in order to find out wether there are deformations in the joint during this period of time or not.

This thesis is limited to the above-mentioned tasks. The following aspects and problems need further investigations:

- Single loads close to the abutments
- The load-bearing behavior in a transverse direction to the girder axis
- The creep behavior of the adhesively-bonded connections
- The different failure criteria for FRP composites
- Local punching failure of the treated bridge decks
- Environmental effects

[3]Serviceability Limit State
[4]Ultimate Limit State
[5]Failure Limit State

1.4 Methodology and organization of thesis

The general organization of the thesis is shown in Fig. 1.5.

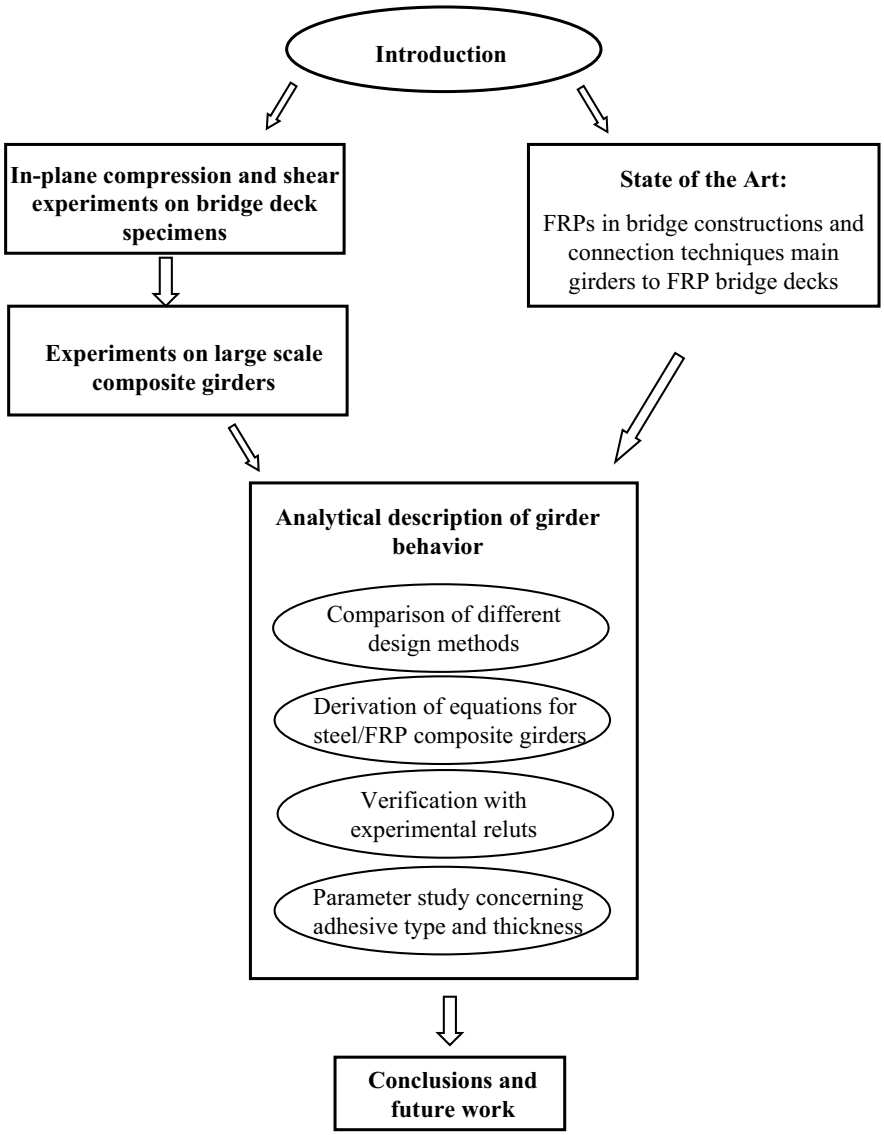

Figure 1.5: Methodology and organization of thesis

With the help of analytical verifications and experiments a design method for an adhesively-bonded FRP-steel composite girder will be developed. Two different kinds of experiments will be necessary: one series to investigate the system properties of the different bridge decks (Chapter 3, page 29) and one series on a large scale on composite girders (Chapter 4, page 61) to investigate the behavior of the whole girder. With the help of these experiments, the results of the proposed calculation method can be examined. Both the experiments and the calculations will serve as basis for a design method for an adhesively-bonded FRP-steel composite girder.

After the introduction (**Chapter 1, page 1**), the main part of this study starts with a detailed literature review concerning FRPs in bridge construction **(Chapter 2 on the next page)**. **Chapter 3, page 29** and **Chapter 4, page 61** present the experimental part of the thesis. In Chapter 3, the system properties (for explanation see page 29) of the two investigated bridge decks are determined by means of compression and shear experiments. In Chapter 4, four adhesively-bonded composite steel/FRP girders with two different bridge decks are manufactured. Thus there were two girders for each bridge deck system. One girder of each system was subjected to static loads and one to fatigue loads before the final failure experiment. In **Chapter 5, page 105** an analytical design method in a general form is developed and its validity is checked by means of numerical examples (recalculation of the tested girders and comparison with measured values). In **Chapter 6, page 141**, the problem of different adhesives and different adhesive thicknesses is addressed. The last chapter, **Chapter 7, page 147**, summarizes the conclusions of the thesis and gives proposals for future research in the domain of steel/FRP composite girders.

2 FRPs in bridge construction

2.1 Strengthening, reinforcement, cables

In the late 80s, Prof. Urs Meier was the first to propose using CFRP[1] laminates for strengthening bridges [81]. Hans Peter Kaiser [63], [83] from the EMPA[2], developed the basis for this. In [63] the author shows for the first time a design method for strengthening structures with additional externally-bonded CFRP laminates. A few years later, in the early 90s, a similar evolution took place in the United States [16], [87], but did not provide a design method as did H.P Kaiser in [63]. The first application of this new method of strengthening road bridges was in 1991, [80]. The Ibachbrücke, in the canton of Lucerne, Switzerland, was damaged by the drilling of holes for traffic lights. 2 x 20 wires of the prestressed reinforcement were cut through, preventing further use and a rapid repair was necessary. The bridge was then strengthened with three CFRP flat profiles. The operations were carried out during the night to minimize traffic interruption and only three nights were necessary for the work to be completed. Although most projects involving the strengthening of structures with CFRPs are carried out in combination with concrete, this technique can also be applied for steel [56], wood [82] and masonry structures [103]. Although research concerning CFRP laminates in bridge construction was extended to prestressed CFRP systems [36], [17], [4] the application and development of structures with "normal"CFRP laminates [95], [29] is still ongoing.

Another application is the strengthening of bridge piers to enhance resistance to earthquake damage [37] or increased live or (dead) load [52]. The piers are wrapped with FRP sheets to improve energy absorption capacity.

Externally-bonded reinforcements are not the only application for FRPs in bridge construction. The development of GFRP[3] reinforcing bars and tendons already started in 1978. The aim was to replace the corrodible steel reinforcement with GFRP bars in order to reduce life cycle costs. The prestressing system, called Polystal [118], consisted of pultruded FRP rods. Several projects, mainly in Germany but also in Austria [5],[21] were conducted but for economic reasons production has been discontinued. In the following years, more detailed investigations were carried out to better understand and predict the behavior of FRP-reinforced concrete beams [43]. The "steel free deck"philosophy was born and in the following years several institutes began to work on this topic [88], [30].

[1] Carbon-Fiber Reinforced Polymer
[2] Swiss Federal Laboratories for Materials Testing and Research
[3] Glass Fiber Reinforced Polymer

Corrosion is also one of the main reasons why FRPs are used for cables and tendons. The somewhat inaccessible tendons in suspension and cable- stayed bridges were very suitable for the use of FRP [98]. The non-corrosive material was expected to reduce the life cycle costs and number of inspections considerably [119]. FRP cables are used in footbridges [73] and road bridges [79]. The first bridge in the world to use CFRP cables was the Storchenbridge in Winterthur, Switzerland [78], which was installed in 1996. It is a cable-stayed bridge with 124-m span and two lanes, where two CFRP stay cables were installed. Another application of CFRP cables is the external post-strengthening of concrete structures, as for example the bridge in Verdasio, Switzerland [68].

2.2 Footbridges

The first use of FRPs in the construction of pedestrian bridges occurred in the early 1980s in the USA and Canada. Pultruded profiles (for pultrusion see fig. 2.3.1, page 12) from Strongwell and Creative Pultrusions were used to build pedestrian bridges. These "Techtonics"bridges (named after the company which designed them) have a maximum span of 25 m [68]. To date approximately 100 "Techtonics"bridges have been built [11]. The first all-composite footbridge in Europe was built in 1992 in Aberfeldy, Scotland, and was a cable-stayed bridge using the Maunsell system (see Fig 2.3, page 12), [22]. The term "all- composite"applied to this bridge is literally true, since all components (pylons, cables, beams, bridge deck, railing) are made of FRPs. Apart from the cables (Parafil[4] ropes) all components were produced by pultrusion. Most of the connections were effected using adhesive bonding. Only for the connection cables $\Leftrightarrow$ transverse beams were mechanical fasteners used.

Figure 2.1: All-composite footbridge in Kolding, Denmark. Erected in 1997

In contrast to the Aberfeldy bridge, the footbridge in Kolding, Denmark was erected exclusively using mechanical fasteners [18]. Again all components, beside the cables, were produced by pultrusion. At the end of the same year, 1997, the Pontresina bridge in the canton Grisons, Switzerland [109] was built. It consists of two simple beams each with a 12.5m span. To investigate the influence of different connection techniques on structural behavior, the con-

[4]Parafil is a trade name of Linear Composites Ltd

nections of one girder were effected using mechanical fasteners only and the connections of the other girder were in addition adhesively-bonded. Experiments at the Swiss Federal Institute of Technology Zurich showed that the girder with bonded connections was stiffer - even after removing the bolts. The youngest member in the GFRP footbridge family is a cable-stayed bridge in Germany near Schwerin, [10] opened in November 2003. It has a span of 45m and a width of 3m. The connections were adhesively- bonded as well as mechanical fasteners. For the superstructure, pultruded standard profiles (Angle, Chanel, Flat Sheet, I-Beam, Square Tube, Toe Plate and Wide Flange Beams) from Creative Pultrusions Inc. were used.

2.3 Vehicular bridges

2.3.1 Bridge decks

After the relatively small sections for pedestrian bridges, bigger profiles and sandwich panels, which could serve as bridge deck, were developed. One of the first researchers who published documents on FRP bridge decks was Plecnik and his co-workers (Ahmad and Azar) in 1991 [92]). He investigated the behavior of different FRP bridge deck cross-sections analytically (see Fig. 2.2). Due to its lowest deflection when compared to other deck configurations, it was later decided to manufacture Type II seen in Fig. 2.2 using a combination of filament winding and hand lay-up . Although this bridge deck is of only minor importance today, it is mentioned here because of its influence on subsequent research in FRP bridge decks.

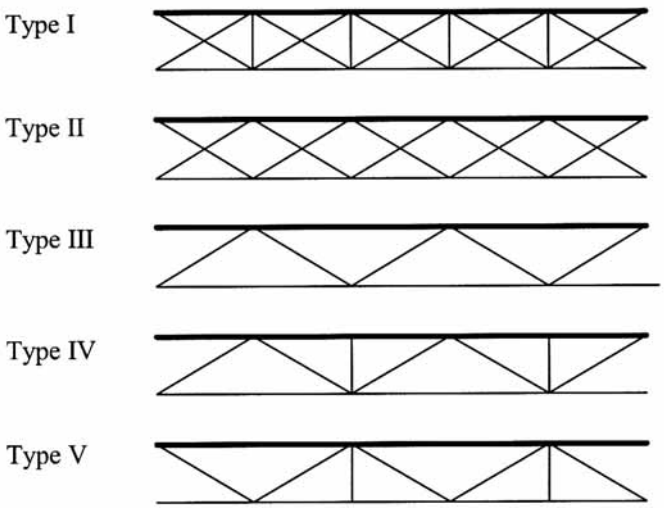

Figure 2.2: FRP cross-sections investigated by Plecnik

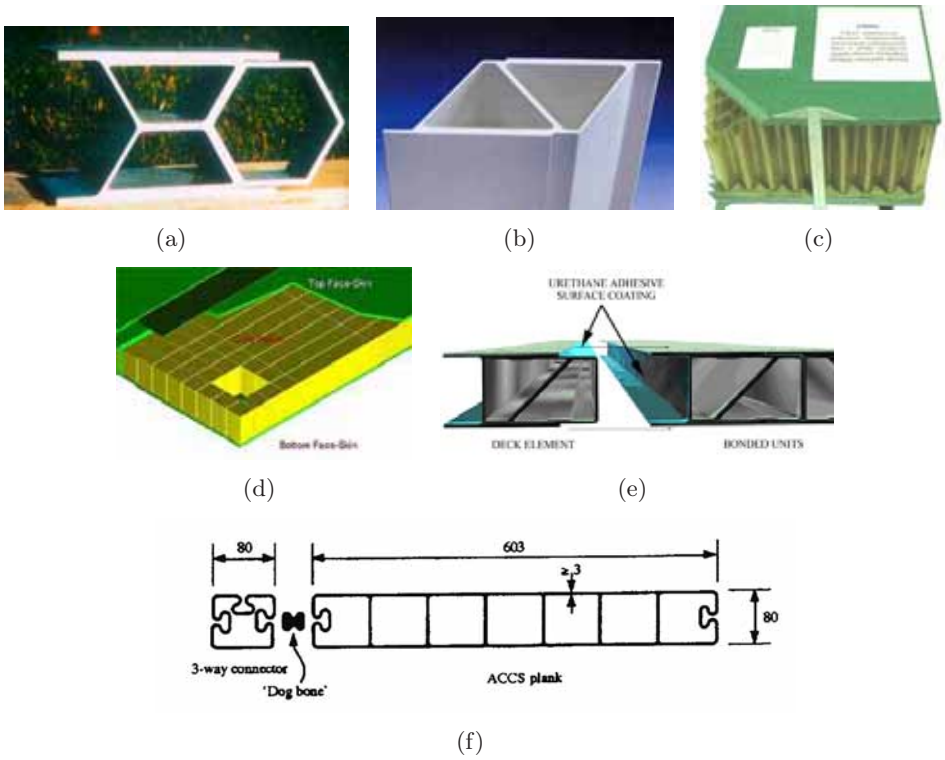

Figure 2.3: FRP bridge decks: (a) Superdeck, (b) ASSET, (c) Kansas, (d) Hardcore, (e) DuraSpan ®, (f) ACCS

The most common deck systems in use are shown in Fig. 2.3. These bridge decks can be subdivided into two groups: pultruded profiles and sandwich panels.

Pultruded bridge decks

All pultruded bridge decks (a,b,e,f in Fig. 2.3) consist exclusively of glass fibers with polyester or vinylester matrices (thermoset matrices) [68]. All of the systems are based on several profiles adhesively bonded together. Apart from sandwich bridge decks, they always need main girders as support (steel, concrete or wood). Pultrusion is a manufacturing process for producing continuous lengths of FRP structural shapes [90]. Raw materials include a liquid resin mixture (containing resin, fillers and specialized additives) and reinforcing fibers. The process involves pulling these raw materials (rather than pushing as is the case in extrusion) through a heated steel-forming die using a continuous pulling device. The reinforcement materials are in continuous forms such as rolls of fiberglass mat or doffs of fiberglass roving. As the reinforcement is saturated with the resin mixture ("wet-out") in the resin impregnator and pulled through the die, the gelation (or hardening) of the resin is initiated by heat from the die and a rigid, cured profile is formed corresponding to the shape of the die. Pultrusion is probably the best way to produce composite bridge decks, since it combines low processing costs and ensures a high performance level due to repeatability [64]. Another significant point is that the profiles are normally preassembled in a shop under controlled conditions which leads

to quick installation on site and thus short traffic interruption, as shown for example in [50].

The evolution of pultruded bridge decks started in the early 1990s in England. The Bonds Mill bridge, opened in May 1994, used the ACCS[5] elements developed by Maunsell Structural plastics (see Fig. 2.3 (f) on the opposite page). It was the first bridge built using the all-composite method and had an 8.5-m span and a 4.24-m width [62], [61]. The ACCS consists of a plank, three-way connector and toggle bar for connection. With this system, not only bridge decks, but even girders can be formed as was the case for Bonds Mill bridge. In 1995 the properties of girders consisting of the ACCS were investigated in detail in [76] (experiments and non-linear numerical analysis) and again in 2003 in [99] (experiments). The composed girders were stiff enough to provide small deflections but the local bending behavior had to be improved. This was accomplished by filling the hollow sections with a structural grade foam [21]. The ACCS system was recently improved with regard to the poor resistance against wheel loads [34]. The section was slightly modified in relation to the flange and web thicknesses.

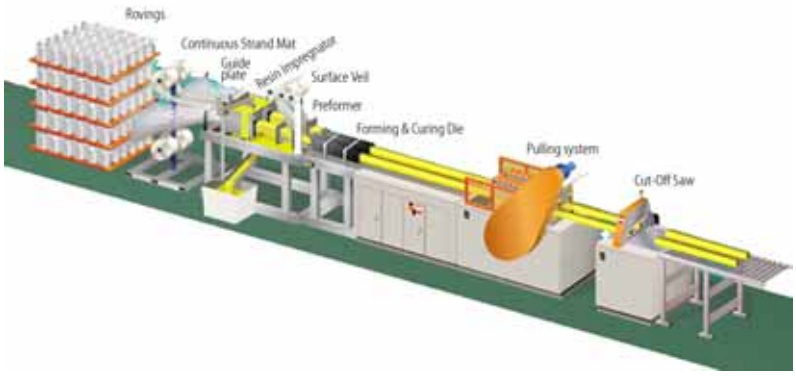

Figure 2.4: Diagram of the pultrusion process

Pultruded profiles with large cross-sections are often only produced to order in minimum-run quantities, which leads to a high price. Some researchers therefore continue to pursue the approach of Lee and Hollaway in [76] and investigate the behavior of bigger cross-sections built of systems of pultruded profiles [116], [75]. In [116] G. Turvey compares different stocked GFRP profiles in the context of beam bending and shows their limitations. Professor Kumar in [75] focuses on one profile which is arranged in different directions to act as beam and bridge deck (see Fig. 2.5 on the next page). Since the local bending behavior (e.g. wheel loads) cannot be improved by composing bigger cross-sections out of small profiles, bridge decks offering better resistance against local forces had to be developed. The result was the development of the bridge deck systems shown in Fig. 2.3 (a)-(e) on the opposite page.

A. H. Zureick in [121] in 1995 and four years later H. GangaRao in [49] abstracted the analytical and experimental work carried out up to that time in the United States. One of the conclusions was that experimental behavior must be predictable using analytical tools, a very important issue which has

[5] **A**dvanced **C**omposite **C**onctruction **S**ystem

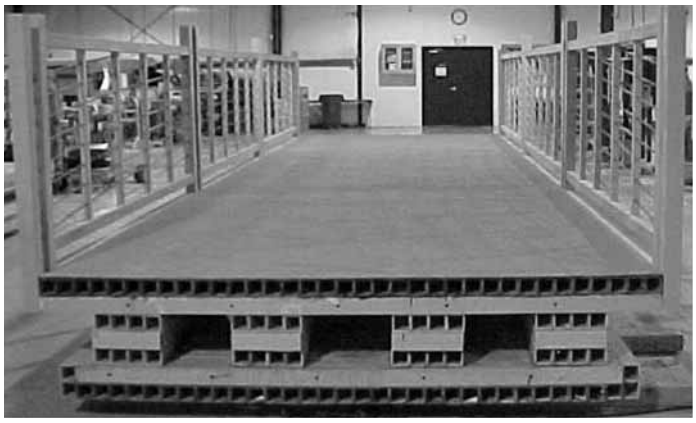

Figure 2.5: Longitudinal cross-section of the bridge deck investigated by Prof. Kumar in [75].

still not been resolved . Since experimental investigations often involve the "funding" problem much of the research was carried out using FEM[6] analysis. This vast field has been investigated by many Researchers, such as[100], [13], [48], [94], [14], [120], to mention only a few. All of them had to struggle against the same difficulties. Most modern FE programs offer the possibility of taking into account the anisotropy of the material by means of "composite"elements, but these elements require up to fifteen different material parameters, which in most cases are not available. Despite these difficulties, however, the use of FEM can result in progress regarding the geometry of bridge decks, for example, as was the case in [86]. The calculations helped a good compromise to be found between bending stiffness, lateral stiffness and local bending stiffness against wheel loads.

Figure 2.6: Cross-section of prototype carbon shell bridge with concrete and FRP deck

[6]Finite Element Method

A very innovative project which was also extensively reported in literature [24], [65], [23], [105] is the Kings Stormwater bridge, USA. The CSS[7] concept, developed by F. Seible in 1995, utilizes prefabricated thin carbon shells (produced by filament winding) which are filled with concrete on-site. The lightweight concrete provides compression force transfer and prevents the thin-walled CFRP tubes from buckling. The FRP/concrete girders can be connected either to a conventional concrete or an FRP bridge deck. The connection of main girders and bridge deck is effected either by steel reinforcement or with special FRP dowel connectors (see also Section 2.3.2, page 21). The bridge consists of a two-span superstructure with 10.0-m span and 13.0-m width. To complete the lightweight structure the DuraSpan® system was chosen as bridge deck. Fig. 2.6 on the preceding page shows the two cross-sections which were built - one with an FRP deck and one with a traditional concrete deck.

The most common pultruded bridge deck in the USA is the DuraSpan® system from Martin Marietta Composites. It was tested for static and fatigue behavior in [47]. More than 25 bridges are already in service [12]. Not all of them are completely new, since the bridge deck can also be used to restore old truss bridges as for example shown in [107]. All completed projects have steel or concrete main girders. In the bridge shown in Fig. 2.7, studs are used for the connection between the two construction elements. The maximum girder spacing for this type of bridge is ∼2.70-m, [72] resulting from the deflection limit of the deck. The example shown in Fig. 2.7 was installed in 1999 and has steel main girders for load transfer in a longitudinal direction.

Figure 2.7: Bridge over Woodington Run (1999), Darke County

An example where the webs and face panels are composed of pultruded quadratic profiles and pultruded panels is the Virginia Tech Deck [110], [111]. The deck is made up of quadratic tubes of 152-mm depth and two 9.53-mm-thick face panels. The tubes and plates are bonded with an epoxy adhesive before being mechanically fastened to the steel girders (see Section 2.3.2, page 21. A vinyl ester resin of 6.4-mm thickness and various sizes of angular quartz formed the wearing surface. Before installing the bridge deck at Troutville weight station (Virginia, USA) several tests on the section were conducted at

[7] **C**arbon **S**hell **S**ystem

the Virginia Polytechnic Institute and State University. The tests validated the safety of the composite deck and the Virginia Department of Transportation thus allowed it to be placed in service. In 2004 the influence of different loading patches as well as different connections between bridge deck and steel main girders were investigated in the same project (see also Section 2.3.2, page 21) [31]. Fig. 2.8 shows a section of the bridge deck[8].

Figure 2.8: End view of Virginia Tech Deck

A similar system to that shown in Fig. 2.9 is described by Rizkalla in [97]. This bridge deck is composed of a series of triangular tubes produced by filament winding and pultruded glass fiber bars and plates which form the upper and lower face sheet. After manufacturing, the triangular tubes, the upper and lower face sheets and the bars were bonded with the same epoxy resin . After the adhesive was applied, the deck was cured at 82°C for 8-10 hours. In [97] bridge decks with different lay-ups were tested. Three-point bending tests with 3.0-m span were carried out to investigate the load-deflection behavior. Fig. 2.9 shows one of the tested sections.

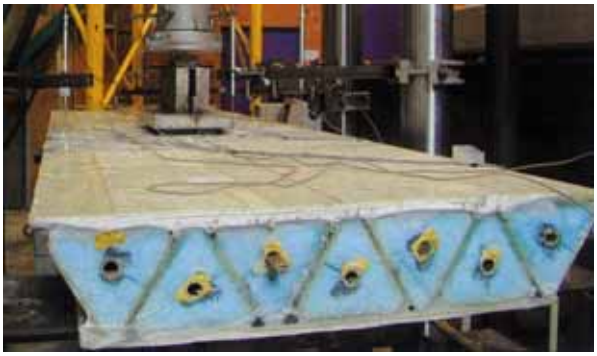

Figure 2.9: Cross-section of Manitoba deck

In Europe the development of large FRP bridge decks, comparable to the size of the DuraSpan deck for example, was much more conservative than in the USA and therefore began a few years later. Only one composites manufacturer (Fiberline Composites) ventured to assume this difficult task. In 1998 development of the so-called ASSET[9] deck of the Danish pultruder Fiberline began.

[8] Used by kind permission of J.J.Lesko

[9] adv**A**nced **S**tructural **S**yst**E**ms for **T**omorrows infrastructure

Only four years later, in October 2002, the first public highway bridge (West Mill) incorporating this bridge deck was opened in the county of Oxfordshire, UK [77]. It is a two-lane 10-m single-span bridge and was designed for load in accordance with the British Standard BS 5400 (40-t). Figure 2.10[10] shows an elevation of the bridge. A cross-section is shown in Fig. 2.24, page 26. All connections between stringer and bridge deck were adhesively bonded using a two- component epoxy adhesive [25].

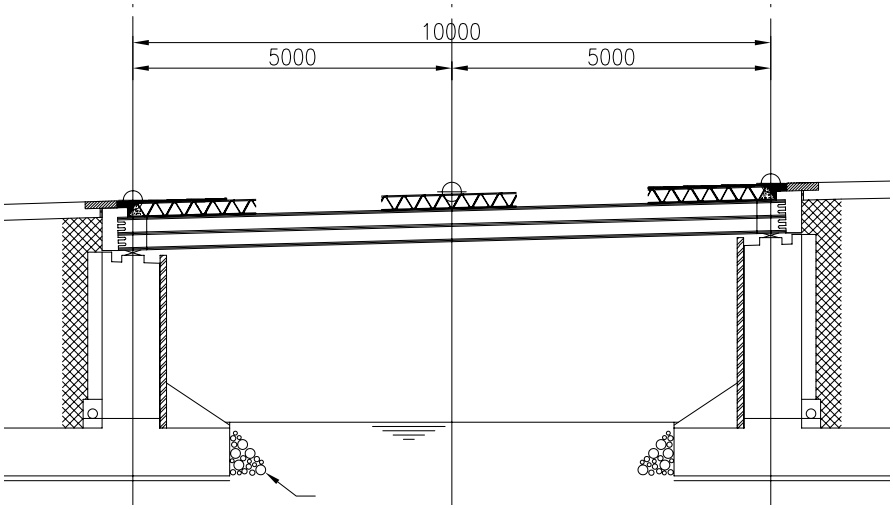

Figure 2.10: Elevation of West Mill bridge

In 2002 a design study was undertaken for a road bridge at Den Dungen, Holland [114]. In this project a steel upper lifting structure should have been combined with a full composite bridge deck - unfortunately, due to financing restrictions, the bridge was not built. It was planned to build a one-lane bridge with 9.8-m span and a superstructure of 16 adhesively bonded box beams of ∼400-mm depth and top and bottom plates of 14- to 24-mm thickness (see Fig, 2.11). Both the box beams and bottom plates were supposed to be produced by a resin infusion process. It is interesting that the evolution of this cross-section resulted in a similar form to that of pultruded bridge decks.

The exceptional thing about this bridge is that it was designed in accordance with the design rules presented in [108]. Unfortunately these design rules are published only in Dutch, which complicates the application considerably.

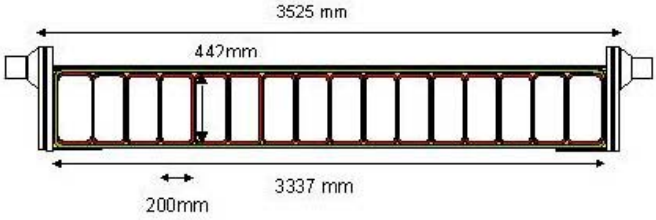

Figure 2.11: Bridge cross-section at rotation point

[10]Used by kind permission of Mouchel Parkman UK

Sandwich panels

Since the Kansas deck and the Hardcore deck (see Fig. 2.3, page 12) are by far the most frequently used sandwich panels in bridge construction [15], [12], this section will only deal with these two systems.

Sandwich structures are composed of strong, stiff face panels that carry flexural loads and a low-density, bonded core material that (more or less) ensures the deck's composite action. The manufacturing process allows the face panels and core material to be easily changed, thus enabling the thickness of the face panels and properties of the core to be optimized for each project. This flexibility is very appropriate and necessary since the requirements change frequently. The raw materials are glass fiber plus a polyester resin (Kansas deck), and vinyl ester resin (Hardcore deck). The main difference between the two products lies in the core. The Hardcore system has an orthotropic honeycomb core comprising hard foam blocks wound around with fibers, while the Kansas system has a thin-walled FRP honeycomb core [15]. The Hardcore system is fabricated using a mainly automated technology known as the VARTM[11] process, whereas the Kansas system still involves hand-lamination. As the name suggests, the VARTM process belongs to the Resin Transfer Molding (RTM) family. During manufacture of the bridge deck, the resin enters a previously assembled dry preform consisting of the reinforcement and the core. Using vacuum, the resin is infused with a distribution medium in order to disperse it quickly and evenly through the structure [64]. VARTM is a medium-rate production process, convenient for fabricating from 10 to 2000 parts, whereas for large quantities pultrusion is far superior [32].

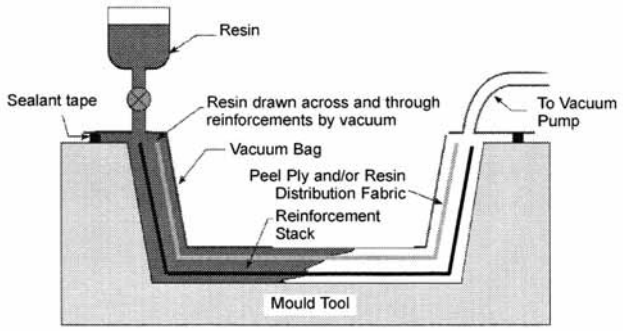

Figure 2.12: Diagram of the VARTM process

New bridge projects comprising sandwich FRP decks are often only considered for small spans, as for example described by S. Alampalli in [3]. One reason for this is the relatively low E-modulus of FRP materials which leads to large cross-sections of up to $\frac{l}{13}$, in order to avoid too large deflections. This is why the Kansas deck was developed for even small spans where no main girders are necessary [93]. Another reason is the difficulty of joining the bridge decks and main girders in projects with bigger spans. Connections between the structural components by the different techniques (studs, bolts) in use today, are very time-consuming and thus expensive. Adhesive bonding is certainly

[11] **V**acuum **A**ssisted **R**esin **T**ransfer **M**olding

a good alternative to traditional connection techniques which are not suitable for FRP materials.

The first all-composite public highway bridge in the United States was the bridge over No-Name Creek near Russel, Kansas [6] and was opened on November 8th 1996. It is a single-span (7.6-m), two-lane bridge and was built using the Kansas Deck [93]. The bridge deck was installed without any supporting steel or concrete stringers. The wearing surface is a 19-mm thick polymer concrete. Guard rails and posts are pultruded profiles. The bridge is still being monitored so that the long-term behavior can be analyzed. Further research concerning the Kansas deck was carried out by J. Davalos in [35]. He deals with the determination of the properties of face and core materials by means of FEM[12] analysis and compares the results with conducted experiments. He also gives an overview of completed bridge projects in which the Kansas deck was used. Fig. 2.13 shows the installation of the bridge deck over No-Name Creek.

Figure 2.13: Installation of bridge deck over No-Name Creek

In June 1997 the first vehicle bridge ("Magazine Ditch") with a Hardcore deck was installed in Delaware, USA. The bridge deck was supported by prestressed concrete girders and had a total span of 23.0 m and a width of 8.2 m [9]. Since then over 20 bridges have been built using this deck system in the USA [12], including the bridge over Mill Creek [45] in 1999. Like all other bridges constructed with this system, it is a simple beam and the span is ∼11.0 m. In this project the deck is supported by six steel beams and several tests were carried out by Structural Testing Incorporated to determine the bridge's structural behavior.

Both bridges (No-Name Creek and Mill Creek) are projects where the whole superstructure of a deteriorated concrete bridge was replaced, but this is not always necessary. In [1] and [2] for example, S. Alampalli describes the restoration of a steel truss bridge with a concrete deck located in Wellsburg, New York and in this case only the concrete deck had to be replaced. Another reason for the deck's replacement was improvement of the load rate of the 60-year-old

[12]Finite Element Method

bridge. An FRP bridge deck with its low dead load seemed the best solution to the problem. After repairing the steel truss the (Hardcore) bridge deck was installed. Different load tests were subsequently carried out and confirmed what had been assumed in the design. No composite action existed between the deck and superstructure and the joints between the different panels were only partially effective in transferring loads. Fig. 2.14[13] shows the installation of the deck.

Figure 2.14: Installation of Hardcore bridge deck at Bentley's Creek

Extensive research on sandwich structures was also carried out by Douglas A. Eckel in [38]. Experimental and theoretical studies were made to gain fundamental understanding of the structural behavior of sandwich bridge decks subjected to transversal loads. This study formed the basis for the replacement of Bridge 1-351 ("Bridge over Muddy Run") in Glasgow, Delaware, USA. In [51] J. Gillespie describes this project and in [39] Douglas A. Eckel confirms the predicted and experimentally measured behavior of the bridge by means of FEM calculations.

Figure 2.15: Completed bridge over Muddy Run

[13] Taken from [1]

One of many important theoretical works is the article written by He and Aref in 2003 [54]. They developed a good and easy-to-handle tool to allow engineers designing FRP bridge decks to estimate geometry and properties without performing detailed finite element analysis. This is especially important for projects involving sandwich constructions (frequently changing requirements).

Since 1996 about 100 bridges with FRP deck systems have been realized [117], encouraging engineers to continue their research and proving the need for such bridge systems.

2.3.2 Deck-to-girder connections

FRPs and their connections have been under investigation since the early 70s [53], [96] and research still continues [86], [115], [104], but most publications are restricted to applications unsuitable for bridges. Therefore "deck-to-girder connections"is a subject very little reported on in literature and only a few examples can be found.

Two types of connections exist: mechanical fasteners, such as shear studs or dowels, and adhesive bonding.

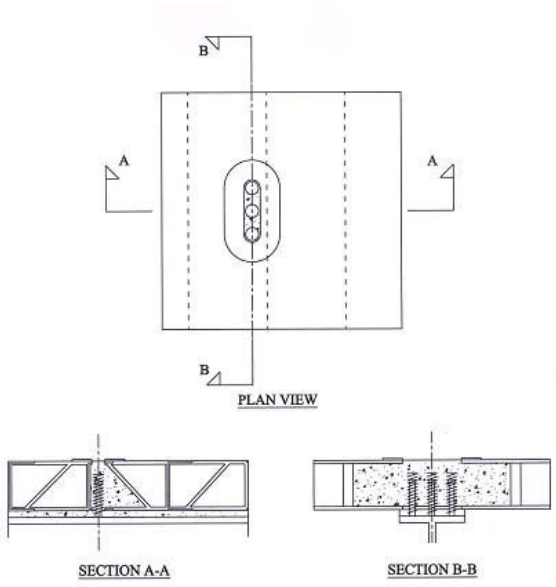

Figure 2.16: Typical joining technology using studs

Mechanical fasteners are adequate for traditional materials, but not well-suited to FRP materials for various reasons. Bolted connections, for example, cause high stress concentrations in the composite matrix at the edges of the holes. Stud connections do not present this characteristic to the same degree as bolts but installation is much more complicated. The studs are welded to the steel girders and non-shrink grout is poured into prepared openings in the FRP decks to develop the shear action (see Fig. 2.16) [26]. In [27] and [85] the authors deal with the same project and focus on the composite action between the bridge deck and steel main girders but do not explain to what extent the deck participates in the bearing capacity. The whole installation process is

very time-consuming and thus expensive. Figure 2.16 on the preceding page shows a connection using groups of headed studs (bridge deck: DuraSpan®). It also shows that for each group of headed studs, the hollow sections have to be closed to prevent the non-shrink grout from spilling out - one more step complicating the installation.

An example where dowels are used is the already-mentioned Carbon Shell bridge (see Fig. 2.17), [106]. From the author's point of view, this system is even more time-consuming than the stud solution, since holes must be drilled in the carbon tubes which have to be filled with concrete (partly offsetting the advantage of the light bridge deck and tubes) in order to fix the dowels.

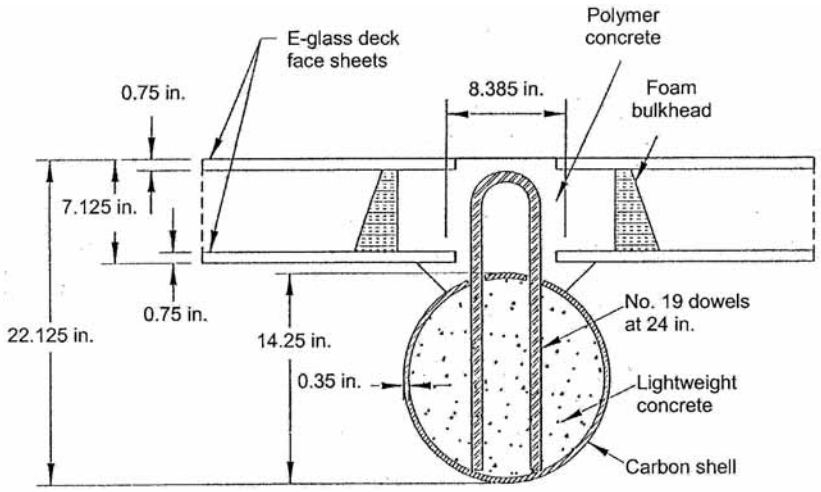

Figure 2.17: Deck-to-girder connection using dowels, Carbon Shell System

A connection with bolts is shown in Fig. 2.18[14] and Fig. 2.19 on the facing page. The FRP deck is fabricated from standard pultruded square profiles and bonded-top-and-bottom skin plates. The profiles are bonded together using steel rods to apply a clamping force. The transverse rods in the tubes serve not only to squeeze them together, but also as anchorage for the hook bolts [120]. The deck-to-girder connection using (hook) bolts illustrates the problem of high stress peaks around the holes. This occurs for example when there is a relative displacement between the main girder and deck. Fig. 2.19 also shows the Virginia Tech Deck but with simple bolts - once with a steel sleeve enclosing the top face panel and once with only a bolt fixing the lower face panel.

[14] Taken from [120]

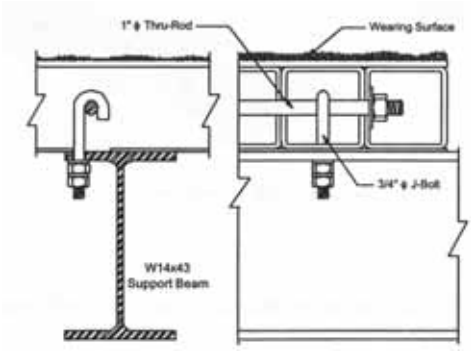

Figure 2.18: Hook bolt connection between deck and steel main girder

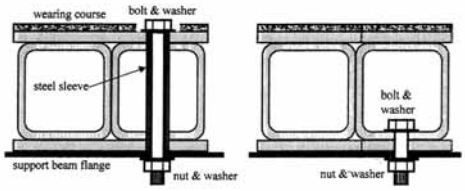

Figure 2.19: Connection of bridge deck using mechanical fasteners

The connection of sandwich decks to main girders is not as simple as that of pultruded decks. The varying section height (often greater than 50cm) prevents through rods or bolts. For this reason only the lower face panel can be attached to the steel girder as shown in Figs. 2.20[15] and 2.21 on the following page. Fig. 2.20 shows a solution whereby the bridge deck is clamped to the steel girder [19], [45]. Fig. 2.21 on the following page[16] is a construction detail of the rehabilitation of Bentley Creek (see also Fig. 2.14, page 20). To attach the deck to the steel girder, holes had to be drilled through the upper face panel and core.

Figure 2.20: Hardcore deck clamped to the steel girder ; bridge over Mill Creek

To the author's knowledge, there are only two projects conducted using an FRP deck on concrete girders. One is the already- mentioned (see Subsection 2.3.1, page 18) Magazine Ditch bridge near Delaware (USA), but no details concerning the deck-to-girder connection are known. The second is the bridge over Crow Creek in Iowa, also USA. It was installed in 2001 and is a three-span concrete-girder bridge with two 18.90-m spans and one 14.33-m

[15] Taken from [19]
[16] Taken from [1]

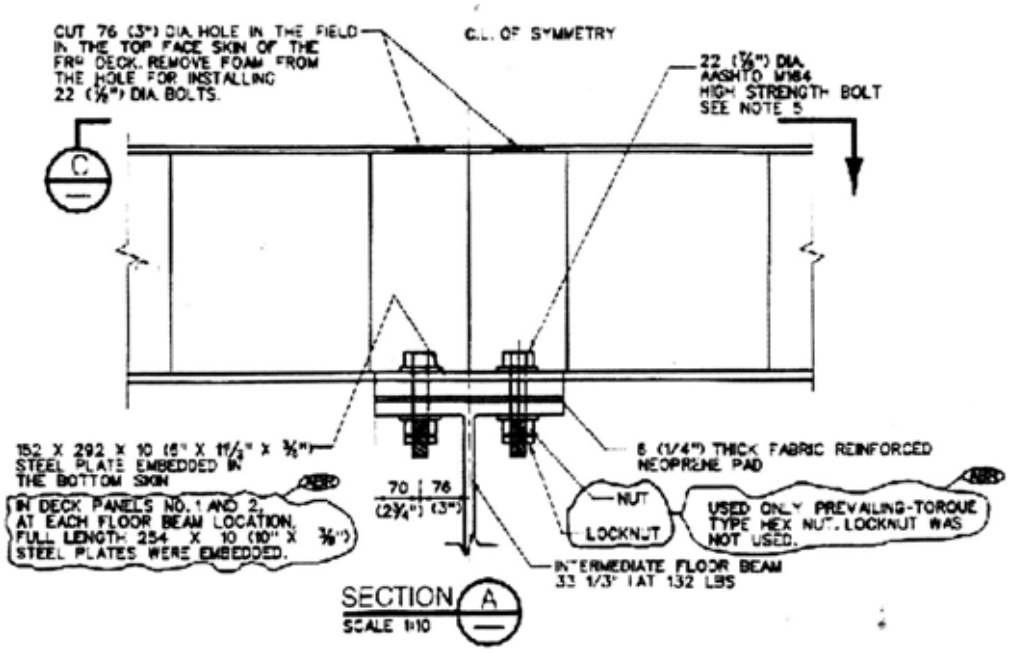

Figure 2.21: Lower face panel of Hardcore deck bolted directly to the steel girder, bridge over Bentley's Creek

span [107]. The two 18.90-m spans have a conventional concrete deck, whereas the short span was conducted with the DuraSpan system. The spacing of the prestressed concrete main girders is 2.32m. For connection between the girders and bridge deck, traditional steel reinforcement was used. A diagram of the cross-section is shown in Fig. 2.22.

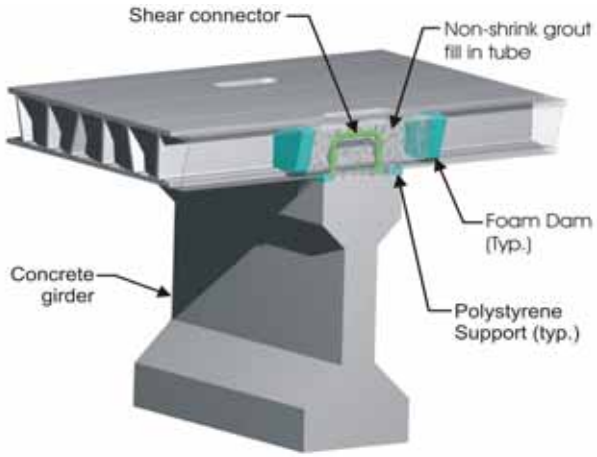

Figure 2.22: Concrete girder connection detail of Crow Creek bridge

The second type of deck-to-girder connection is adhesively- bonded joints. Adhesive bonding in bridge structures has been used since the early 60s [113]. The high shear-force-transferring capacity of the adhesive was used in steel

constructions to avoid slippage between the joined components. In the late 60s H. Hänsch and W. Krämer in the former German Democratic Republic developed bonded connections between steel main girders and prefabricated concrete bridge decks [58], [74]. Even at that time, the main reason for the application of bonded connections was the time-saving aspect [57]. It was the first time that adhesive bonding was used for such connections. The aim was to benefit from the high shear capacity of the adhesive connection to ensure composite action in the structure. These bridges are characterized by the fact that the adhesively-bonded joints were considered in the design and no supplementary bolts for security or assembly reasons were used. For the joints between the steel main girders and concrete deck and between the different deck elements, a two-component epoxy adhesive was used. At the beginning of this evolution, the prefabricated concrete decks were applied to a steel grid (multi-girder system, see Fig. 2.23), creating joint thicknesses of between 5 and 15 mm. These relatively thick joints were completely filled with epoxy adhesive [44]. Subsequently, propped systems were also introduced, enabling the dead load to act on the composite structure and even increasing the loading of the joint. Between 1968 and 1992 seven bridges with spans from 15 to 32 m were built using epoxy adhesive for the bonded connections and they are still in use [44]. After more than 30 years of experience with adhesively-bonded traditional steel- concrete composite bridges, it can be said that this is a reliable and economic way of building bridges.

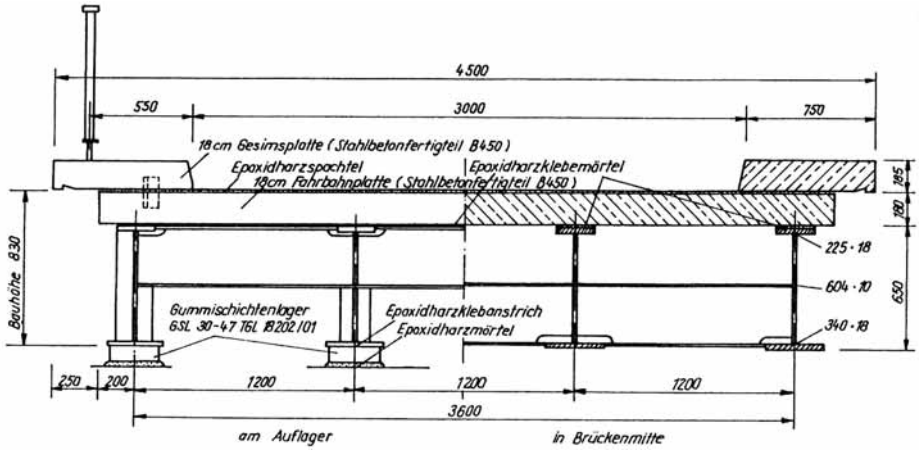

Figure 2.23: Cross-section of

Adhesive bonding did not only become popular in Germany however; in Switzerland too engineers tried to take advantage of this new technology. In [55] P. Hertig describes the use of epoxy resins in steel-concrete composite structures. A state-of-the-art technique for bonding metal with non-metallic materials in the early 70s is also reported in [102].

To date the use of adhesive bonding is not very common in FRP composite bridges. The transversal joints between pultruded bridge decks and the "shear keys"of sandwich decks are often bonded, but not the deck ⇔ main girder joint. A rare example is the West Mill bridge in Oxfordshire, UK. Main girders and bridge deck are standard pultruded profiles from Fiberline Composites,

Denmark. For all joints (transversal joints between deck profiles, deck ⇔ main girder joints and joints between the quadratic sections of the main girders) a two-component epoxy adhesive was used [77]. Fig. 2.24 shows a cross-section of the bridge.

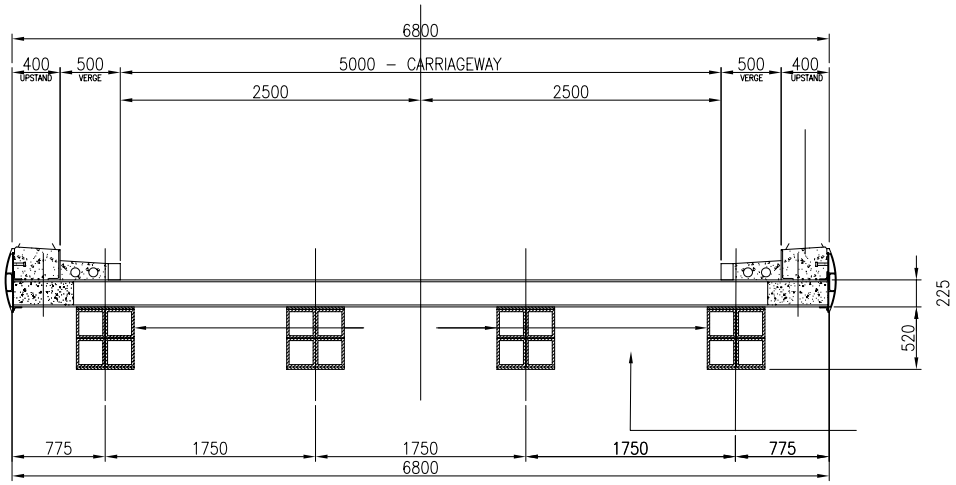

Figure 2.24: Cross-section of West Mill bridge

Another adhesively-bonded bridge is that over Laurel Creek in West Virginia, USA (installed 1997). This all-composite bridge has a span of 6.08 m and is composed of the Superdeck bridge deck and FRP wide-flange beams [68]. Although the bridge was designed for heavy truck loading, the small dimensions of the bridge demonstrate that this connection technique did not inspire much confidence. The span was also limited by the FRP main girders, which could only be produced within a specific height range.

Composite action and girder-to-deck connections

To date very little is reported in literature concerning the behavior of deck-to-girder connections with respect to composite action. The problem is that the load transfer is very complex and therefore difficult to describe analytically. Modern finite element analysis could help to better understand what happens in the joint and bridge deck, but programs demand up to fifteen different material parameters, often not available in practice. Due to the above-mentioned conditions of load transfer between bolted (studs) FRP decks and girders which are not precisely understood, the design of girders and FRP decks is often done very conservatively with two limiting conditions: girders are designed without considering the FRP deck's composite action , and deck calculations are made assuming full composite action.

These problems, complex load-bearing behavior and lack of easy-to-use calculation methods are the main reasons why composite action was not taken into account in design by engineers in the past.

Two researchers who address this difficulty are Patrick Cassity in [27] and Greg Solomon in [107], but their knowledge is based on load-testing on bridges. Thus they cannot predict girder behavior by means of calculations. Determi-

nation of the degree of composite action without testing the structure is not possible. Although the fact that the deck participates in the load-bearing capacity of a composite girder is certainly an important conclusion, it does not help engineers since they still cannot calculate load-bearing behavior without testing.

The experience with traditional steel-concrete composite bridges in the former German Democratic Republic is very significant regarding the use of adhesive bonding for the conjunction of main girders and bridge decks. Not only due to the fact that, with adhesive bonding, full composite action can be achieved, but also that , bridges already in use for over thirty years show that this connection technique is more than just an alternative to studs or bolts.

3 In-plane compression and shear experiments

3.1 Objectives

The bridge decks investigated in this thesis have already proved their suitability in projects in the USA and Europe. For several reasons, it was not possible to take into account the composite action of the main girders and GFRP bridge deck for dimensioning. One reason is that the bridge deck properties (pultruded and sandwich) for calculating behavior of a girder with composite action were not known. Usually, relatively small pieces are cut from the element to investigate the properties of the material (coupon tests), but for calculation of a composite girder with composite action, the properties of the bridge deck as a whole are needed. These system properties (E-modulus $\widehat{E}$ and shear modulus $\widehat{G}$), which take into account the geometry and influence of the adhesively-bonded joints, have not yet been investigated and thus a series of experiments was necessary in order to specify them. Therefore, these experiments treat the in-plane deformation and failure behavior perpendicular to the pultrusion direction of two different GFRP bridge decks (DuraSpan and ASSET). The term "in-plane"is used in this context on the deck system level and means in the deck plane. It must not be confused with the same term in laminate or failure theory of FRP materials. This definition also applies for Chapters 4 and 5. The results will serve as basis for the analytical description of the composite girders tested in Chapter 4, page 61.

3.2 Experimental program

The series of experiments consists of twelve DuraSpan, and for availability reasons, eight ASSET specimens. For each system, half of them were always loaded concentrically (see Figs. 3.6 and 3.7, page 35) and the other half eccentrically (see Fig. 3.15, page 40). The concentric experiments should provide information regarding maximum compression force and E-modulus and the shear experiments information regarding transmittable shear force and shear modulus. To assess the influence of the number of webs, the DuraSpan specimens were tested in two different sizes: six specimens consisting of three elements and six consisting of four elements. Thus, for each type of experiment (concentric and eccentric) there were three DuraSpan specimens of each size (see Table 3.1 on the next page). The designation of the ASSET specimens is shown in Table 3.2 on the following page. Detailed information is given in Chapter 3.4, page 34.

The bridge decks are normally positioned with the pultrusion direction perpendicular to the bridge axis and thus perpendicular to the steel main girders. Therefore the specimens are loaded perpendicular to the pultrusion direction.

Specimen	In-plane compression	In-plane shear
3 shapes	3as | 3bs | 3cs	3aa | 3ba | 3ca
4 shapes	4as | 4bs | 4cs	4aa | 4ba | 4ca

Table 3.1: Overview of DuraSpan specimens

	In-plane compression	In-plane shear
Specimen	AC1 | AC2 | AC3 | AC4	AS1 | AS2 | AS3 | AS4

Table 3.2: Overview of ASSET specimens

3.3 Experiment specimen

3.3.1 Dimensions

The DuraSpan specimens consist of three or four profiles respectively adhesively bonded together (see Figs. 3.3 and 3.4). The pultruded profile which build the basis of the DuraSpan specimens is shown in Fig. 3.1. The ASSET specimens all consist of four profiles, also adhesively bonded together, see Fig. 3.5.

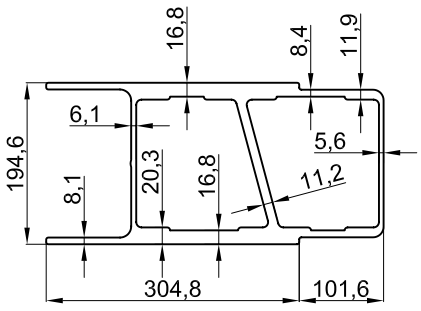

Figure 3.1: DuraSpan 766 element (Generation 5)

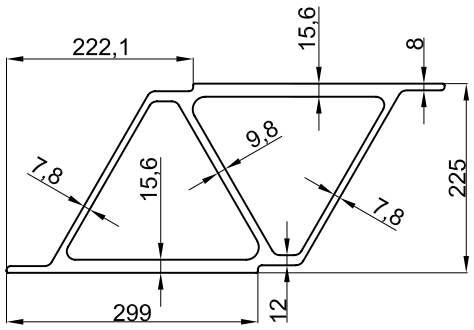

Figure 3.2: ASSET element

As to the possible failure mode, buckling around the weak axis was expected. To avoid stability failure, the specimens would have to have been much shorter but in that case assessment of the influence of the adhesively-bonded joints between the pultruded profiles would not have been possible. For this reason the specimens are relatively large in order to provide at least two bonded joints. The definitive dimensions of the specimens are shown in Fig. 3.3 on the facing page and Fig. 3.4 on the next page for the DuraSpan specimens and in Fig. 3.5 on the facing page for the ASSET specimens.

With regard to application of the experimental methods to other deck types, an adequate specimen height is required. For pultruded deck systems, the minimum specimen length should contain at least two adhesively-bonded joints in order that the influence of the bonded joints will not be underestimated. Furthermore global buckling should be prevented in the shear experiments.

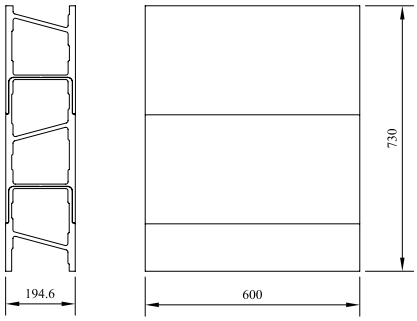

Figure 3.3: Three-element DuraSpan specimen

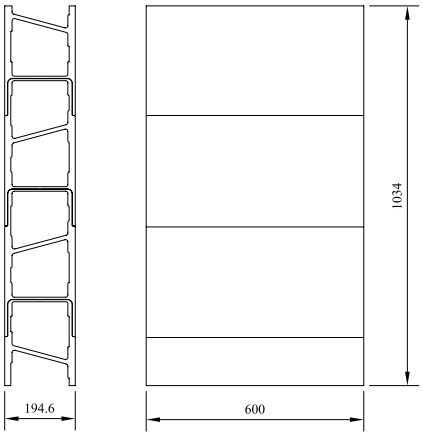

Figure 3.4: Four-element DuraSpan specimen

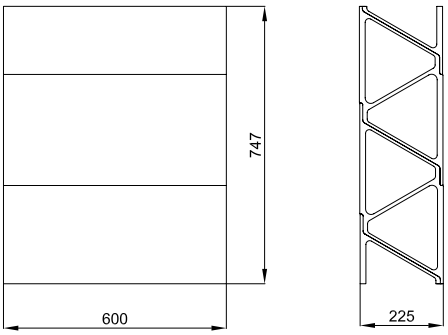

Figure 3.5: Dimensions of ASSET specimens

3.3.2 Materials

Bridge decks

The basic materials used for both bridge decks are E-glass fibers and a polyester resin (isophthalic polyester) and they are produced by pultrusion (see Section 2.3.1). The material properties were investigated at the University of Delaware [26] (DuraSpan) and The Royal Institute of Technology in Stockholm (ASSET) by means of coupon tests. Thus, no prediction concerning the E-modulus, $\widehat{E}$ (considered in the following as system property and not as material property) of the whole profile, or several profiles bonded together, can be made. Bridge deck properties are shown in Table 3.3 and Table 3.4 on the facing page.

	Deck Location	Top sheet 1	Web walls 2	Bottom sheet 3	Equivalent Slab [3] (Bending prop)
Laminate Properties [1]	Lay-up [2]	Web + [0(60) /90(20)/+-45(20)]	[0(33)/+-45(66)]	Web + [0(60) /90(20)/+-45(20)]	
	Thickness (mm)	12.70	6.35 (vert leg) 12.70 (diag leg)	12.70	190.50
	E_L (10^3 MPa)	21.24	17.38	21.24	8.53
	E_T (10^3 MPa)	11.79	9.65	11.79	4.14
	E_Z (10^3 MPa)	4.14	4.14	4.14	0.69
	G_{LT} (10^3 MPa)	5.58	7.17	5.58	0.69
	G_{LZ} (10^3 MPa)	0.60	0.60	0.60	0.69
	G_{ZT} (10^3 MPa)	0.60	0.60	0.60	0.69
	ν_{LT}	0.32	0.3	0.32	0.33
	ν_{LZ}	0.3	0.3	0.3	0.33
	ν_{ZT}	0.3	0.3	0.3	0.33
	εC_L (%)	-1.23	-1.24	-1.23	-
	εT_L (%)	1.23	1.27	1.23	-
	εC_T (%)	-1.27	-1.97	-1.27	-
	εT_T (%)	1.25	1.35	1.25	-
	γ (%)	2.53	2.53	2.53	-
	FC_L(MPa)	-261.210	-215.455	-261.210	-
	FT_L (MPa)	261.210	220.668	261.210	-
	FC_T (MPa)	-149.739	-190.164	-149.739	-
	FT_T (MPa)	147.381	130.316	147.381	-
	FS_{LT} (MPa)	70.650	90.711	70.650	
	ILS (MPa)	41.370	41.370	41.370	-
Bond shear, FB_{LT} (MPa) [5] 4		6.89			

Notes: [1] Laminate stiffnesses and strengths calculated from actual test data of similar thick laminates; failure based on first ply failure criteria

Notation: E_L, E_T,E_Z – extensional moduli; G_{LT},G_{LZ},G_{ZT} – shear moduli
ν_{LT}, ν_{LZ}, ν_{ZT} – poisson's ratios
εC_L, εT_L, εC_T, εT_T, γ – strain allowables (c – compression. T – tension)
FC_L, FT_L, FC_T, FT_T, FS_{LT} – laminate ultimate strengths
ILS – nominal interlaminar shear stress

Subscripts: L – longitudinal direction; T – transverse direction; Z – through thickness

[2] Fiber orientation, [θ°], expressed in percent (%) of laminate thickness
[3] Effective flexural properties for equivalent slab of same thickness
[4] 60% fiber content by weight
[5] 90% of average failure load from preliminary lap shear tests

Table 3.3: Material properties of DuraSpan ® 766 bridge deck (Generation 4), taken from [26].

Laminate properties	Face panels [MPa]	Outer web [MPa]	Inner web [MPa]
E_L	23'000	17'300	16'500
E_T	18'000	22'700	25'600

E_L = E-modulus in pultrusion direction
E_T = E-modulus across pultrusion direction

Table 3.4: Material properties, ASSET deck

Adhesives

Since the DuraSpan specimens were produced in the USA and the ASSET specimens in Denmark, different adhesives were used.

The DuraSpan specimens were manufactured using a two-component urethane adhesive from the Ashland Chemical Company, Pliogrip® 6660. To ease handling on the working site and in the construction hall, the adhesive was designed for a long open-assembly time and the absence of postheat. The open time for applying the adhesive is 45 minutes at 23°C. Table 3.5, shows the properties achieved after four hours.

Characteristics @ 23°C	Pliogrip® 6660
Viscosity, [mPas]	10.000
Density, $[\frac{kg}{m^3}]$	1090
Open Time	45 Minutes
Compressive strength, [MPa]	92
Tensile Strength, [MPa]	16.9
E-modulus, [MPa]	388

Table 3.5: Material properties, adhesive taken from [8]

The ASSET specimens were bonded with a two-component epoxy adhesive, NM BPE Lim 465, produced by Nils Malmgren AB, Sweden [7]. NM BPE Lim 465 was originally designed for strengthening concrete with bonded steel plates and its typical properties at 20°C are shown in Table 3.6 on the following page.

Characteristics @ 25°C	NM BPE Lim 465
Viscosity	Thixotropic
Density, $[\frac{kg}{m^3}]$	1498
Potlife	90 Minutes
Compressive strength [MPa]	103
Tensile strength [MPa]	24
E-modulus, [MPa]	7000

Table 3.6: Material properties, adhesive taken from [7]

3.3.3 Manufacture

Both bridge decks are produced by pultrusion (see Section 2.4, page 13).

Every DuraSpan element has a male and female edge (see Fig. 3.1, page 30). To compose the specimens, the adjacent tubes were mirrored about a horizontal axis, so that the direction of the diagonal web alternates at each element (see Fig. 3.3, page 31), and bonded together. The specimens were manufactured at Martin Marietta Composites in Sparta, North Carolina, USA and transported to the EPFL[1] by plane.

The ASSET specimens were manufactured at Fiberline Composites, Denmark, where the profiles themselves were produced, bonded together and cut to the right size. Prepared in this way, the pieces were transported to the EPFL by lorry.

3.4 Experiment procedure

3.4.1 Compression experiments

Experimental setup and load equipment

The experiments were carried out in the laboratory of the Structural Engineering Institute at the EPFL using the "Trebel 10.000 kN"press. The control unit offers the possibility of conducting either force- or displacement-controlled experiments. The upper and lower steel plates, where the forces are applied on the specimen, have a surface of 80 cm x 80 cm and a thickness of 8 cm. The Trebel press (shown in Fig. 3.8 on the facing page) can handle specimens of up to 6 m in length and was originally developed to test the buckling behavior of columns. The jack is in-ground and has a maximum displacement of 25 cm. A detailed experiment set-up is shown in Fig. 3.6 on the next page for the DuraSpan specimens and Fig. 3.7 on the facing page for the ASSET specimens.

[1] École Polytechnique Fédérale de Lausanne, Switzerland

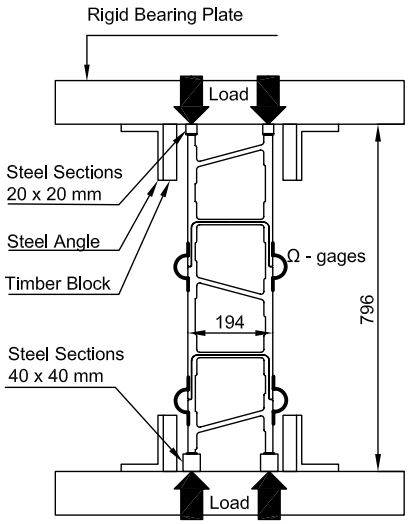

Figure 3.6: Experiment set-up with DuraSpan specimens

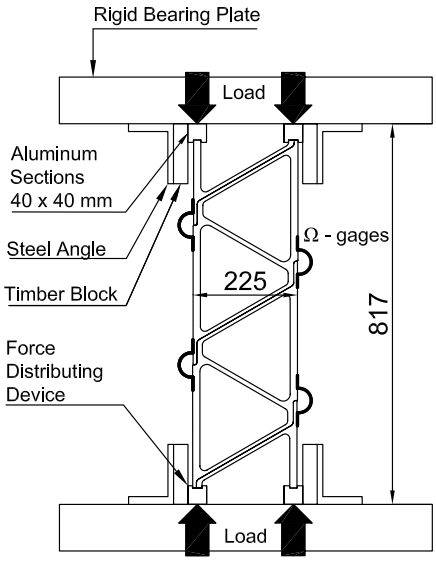

Figure 3.7: Experiment set-up with ASSET specimens

Figure 3.8: Trebel 10.000-kN press

Instrumentation and measurements

The instrumentation used for the experiments consists of a UPM 60 measuring device from Hottinger Baldwin Messtechnik with up to 60 channels, and a laptop to record data. The UPM 60 is a measuring instrument for processing data from strain gages, force gages or inductive strain gages.

Figure 3.9: Installed Ω-gages on DuraSpan specimen

The strain gages used are also from Hottinger Baldwin Messtechnik and have a gage factor of 2.07 %. This factor serves to convert the measured values to a useful unit like μm/m. The temperature coefficient of the gages used is $104 \pm 10 \left[10^{-6}/°C\right]$, which is normally the factor for steel. The reason why strain gages with a temperature coefficient for steel were chosen lies in the anisotropy of the GFRP-profile. Although there are different thermal coefficients in fiber direction and in the transverse direction, studies at the University of Delaware [26] showed that the thermal behavior of pultruded multi-layer bridge decks is similar to that of concrete, and thus steel.

In order to obtain maximum information from the experiments, not only strain gages, but also Ω-gages (Type: PI - 2 - 100; Tokyo Sokki Kenkyujo Co. Ltd., Japan) were installed to measure displacement between the profiles in the adhesively-bonded joints. The basic length of these gages was 50 mm and they were installed on the main axis of both sides of the specimen and over every joint. Figure 3.9 shows a three-element DuraSpan specimen with Ω-gages installed. Before use, each Ω-gage was calibrated.

Figures 3.10 and 3.11 on the facing page show the two different sizes of the concentrically-loaded DuraSpan specimens and the position of the strain gages. Numbers 1-8 are strain gages and are placed on the main axis of the specimen on both sides. Numbers 2 and 4 were placed horizontally to measure the displacement in this direction; the others were bonded vertically. A supplementary (temperature-compensation) strain gage was bonded on a non-loaded GFRP element to accommodate any temperature fluctuations. Fig. 3.12, page 38 shows the position and numbering of strain and Ω-gages on the ASSET specimens.

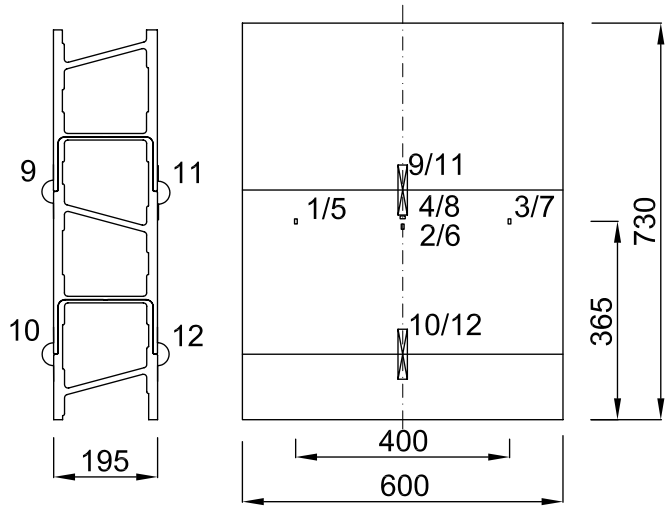

Figure 3.10: Positioning and numbering of gages on three-element DuraSpan specimens

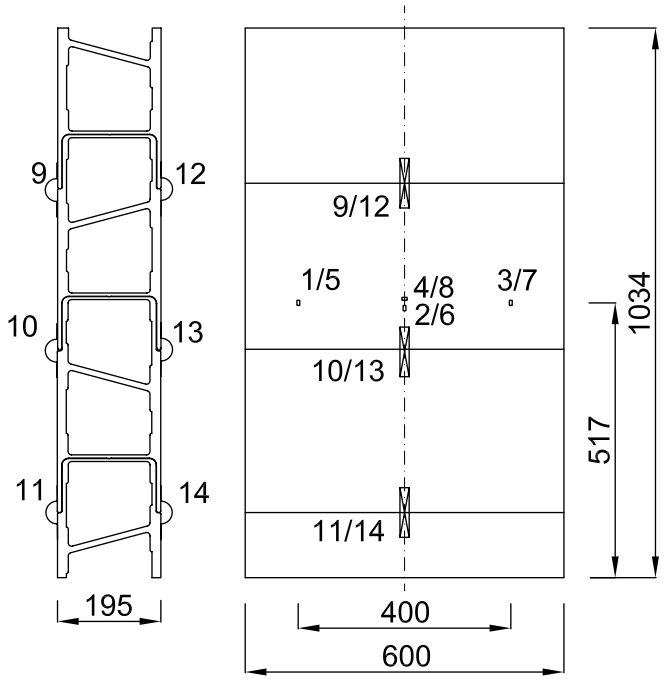

Figure 3.11: Positioning and numbering of gages on four-element DuraSpan specimens

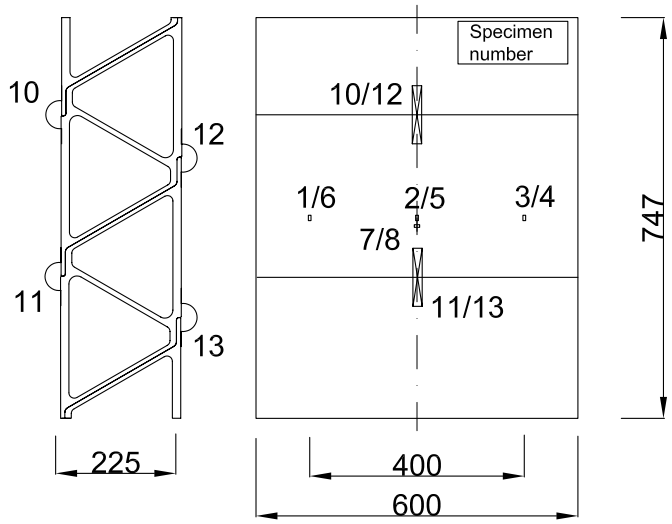

Figure 3.12: Positioning and numbering of gages on Asset specimens

Experiment preparation and procedure

Each specimen was equipped with strain and Ω-gages. The strain gages had to be placed in the predefined position on the surface in such a way that they would work correctly. To meet these requirements, the following procedure was applied to each gage.

- Clean the surface
- Roughen the surface with abrasive paper. First 120 then 320 (first coarse-grained then fine-grained)
- Degrease with acetone
- Draw the lines where to glue the strain gages
- Glue the strain gages
- Connect them with the cables of the data acquisition system
- Test each strain gage with an ohm-meter for functioning

After ensuring the correct positioning and functioning of the strain gages, the specimen was put into the machine and the cables were plugged into the UPM 60. Subsequently, the calibrated Ω-gages were installed. To avoid an oblique position, the specimens were vertically aligned right from the beginning. The inaccuracies of the cutting edges made it necessary to place a force-distributing device between the specimen and the steel plates of the testing machine. Since the cutting edges of the ASSET specimens were more sensitive than those of the DuraSpan specimens a special force-distributing device was necessary (see Fig. 3.14 on the facing page). In the transverse direction, the inaccuracies of the cutting edges were equalized with the help of thin strips of lead. In the

longitudinal direction, steel sheets of a length of 200 mm and different thicknesses (see Fig. 3.13) were placed between the steel bar and the rigid bearing plate of the press. The steel angles, intended to prevent a sudden overturning of the specimen, were fixed allowing a distance of about 2 cm to ensure that there was no fixed-support effect at the edges. Figure 3.6, page 35, shows a drawing of the set-up used for the centric compression experiments.

To attain uniform force introduction, the specimens were loaded until the reaction of the strain gages was visible on the screen (the program allows several gages to be displayed simultaneously), allowing us to monitor load distribution among the gages. The machine was then moved up and the necessary number of shims were placed at the location where the specimen was unevenly loaded . This procedure was repeated several times until the program showed a uniform distribution of the introduced force. The "test load" was approximately 50 kN, corresponding to roughly 8% of the ultimate load. To avoid a sudden failure of the specimen and to investigate post-failure behavior, the experiments were performed-displacement controlled at a rate of 1.5 $\frac{mm}{min}$.

Figure 3.13: Force-introduction point with load-distributing steel sheets for DuraSpan specimens

Figure 3.14: Force-introduction point with load-application device for ASSET specimens

3.4.2 Shear experiments

Experiment set-up and load equipment

The load equipment was identical to that used for the compression experiments. The load-introduction point and supports were modified in order to achieve an in-plane shear loading of the specimens. The set-up was the same for both bridge deck systems and is shown in Fig. 3.15 on the next page for an ASSET specimen.

Instrumentation and measurements

The description of the instrumentation and the measurements given in Section 3.4.1, page 36, also applies for the shear experiments except that there were no Ω-gages. For the DuraSpan deck, the three-element specimens were equipped with 38 strain gages - the four-element specimens with 32. Figures 3.16 and 3.17 on the next page show the two different sizes of the eccentrically-loaded DuraSpan specimens and the positioning of the strain gages. On the ASSET specimens, 40 strain gages were installed (see Fig. 3.18, page 42) on the outer and inner sides of the face sheets in order to determine the axial forces without the influence of the bending moments.

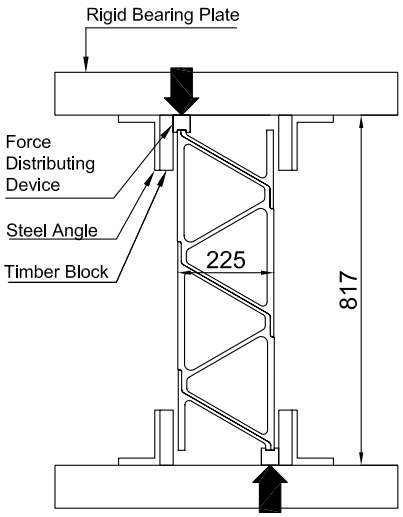

Figure 3.15: Experiment set-up for eccentrically-loaded ASSET specimens

To ensure quick and easy replacement of the specimen after Testing, an unconventional solution was necessary. Due to the high number of strain gages, the standard operation (soldering each cable one after another to the data acquisition system) seemed very difficult. In view of the large quantity of strain gages and the work involved, it was decided to use SCSI-cables from the computer to connect the specimen with the measuring system. This saved a great deal of time and decreased the risk of errors when soldering the cables, since their number was considerably reduced. This system could also be used for all other experiments where strain gages are located closely together.

Experiment preparation and procedure

The preparation of the specimens (strain gages, force-distributing devices, etc.) was described in Section 3.4.1, page 38. The experiment procedure was as described in Section 3.4.1 with one modification. The "test load" was reduced to 5 kN.

The load introduction took place in only one of the two deck face panels of the specimens, and only the opposite face panel was supported. The horizontal forces resulting from the eccentricity of the loading and supporting axes were taken from the support angle sections. The horizontal space between the free end of the specimen and the steel angle was necessary since the specimens were expected to extend in a transverse direction. The dimensions of the steel bar used to introduce the force to the DuraSpan specimens were 40 mm x 40 mm (see Fig. 3.19, page 42). This was the maximum relative displacement between the two face panels until the whole section was under compression. The section of the aluminum bar in the ASSET experiments was also 40 mm x 40 mm but, due to the slot, the relative displacement between the face sheets was only 35 mm (see Fig. 3.14 on the previous page). An adjusted DuraSpan specimen before the experiment can be seen in Fig. 3.20, page 42.

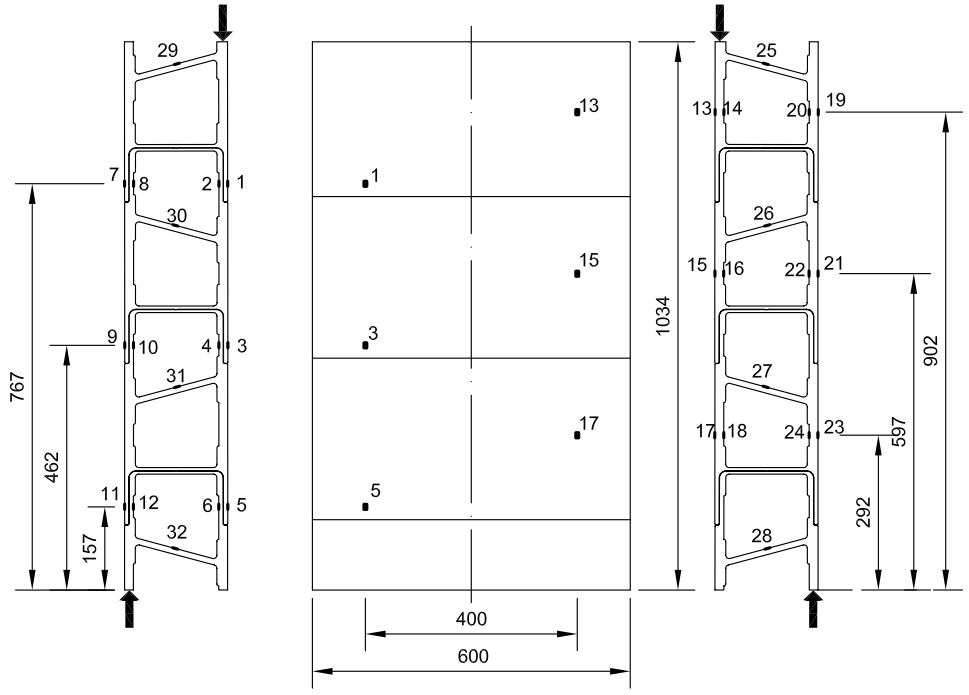

Figure 3.16: Positioning and numbering of strain gages on eccentrically-loaded four-element specimens

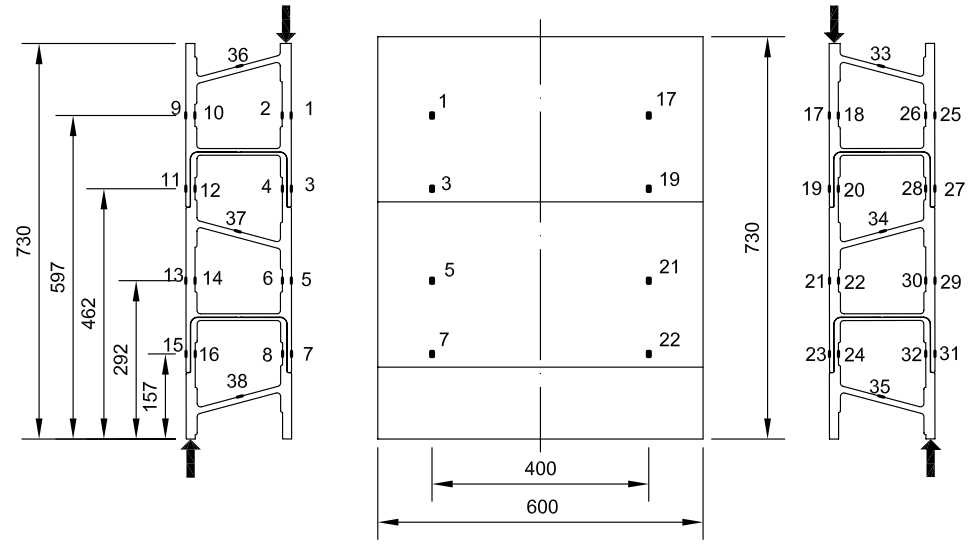

Figure 3.17: Positioning and numbering of gages on eccentrically- loaded three-element specimens

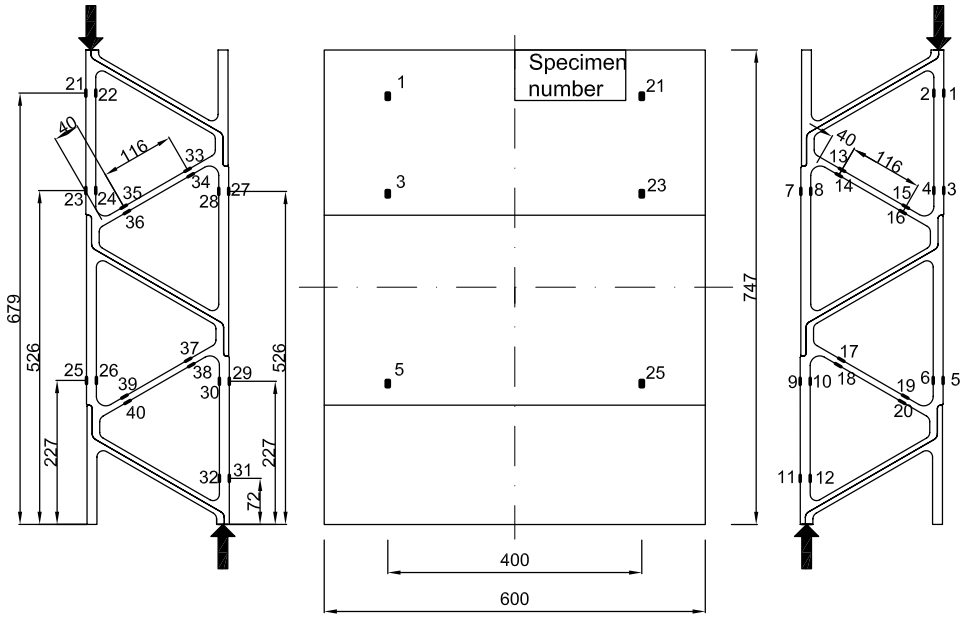

Figure 3.18: Positioning and numbering of gages on eccentrically- loaded Asset specimens

Figure 3.19: Force introduction point with load-distributing steel sheets

Figure 3.20: Adjusted specimen before the experiment

3.5 Experiment results

For both series of experiments, the raw data from the UPM 60 were analyzed using the MATLAB program.

3.5.1 Compression experiments

DuraSpan

The results showed that specimen behavior was as expected before the experiments. Due to the slenderness of the specimens, the failure mode for both sizes was always buckling around the weak axis. The evaluation also showed that the results improved with each specimen. The later specimens were shimmed more accurately, creating a better load distribution.

Figure 3.21: Typical failure pattern of compression experiments (Specimen 3as)

Global load-displacement behavior is represented by specimens 3cs and 4bs in Fig. 3.23, page 45. The behavior of the remaining specimens is similar (see Appendix A.1, page 151). Displacements in the load direction are shown. Both the short and tall specimens exhibited practically the same behavior with comparable stiffness and maximum load (see Table 3.7 on the next page). The range up to approximately 2 mm of displacement was falsified by the experiment set-up. Only by starting from this limit was a full load transmission of the steel plate to the whole element width possible. In addition, Figure 3.26, page 47, shows the global behavior of the short specimens converted into axial stresses (load divided by cross-sectional area of the face panels) and strains (displacement divided by specimen height). The behavior of all specimens was almost linear-elastic up until stability failure. As from approximately 20% of the maximum load, all specimens began to visibly buckle laterally. Lateral deformation then increased constantly (Fig. 3.21). As from approximately 85% of the maximum load, a non-linear deformation increase took place, together with a delamination of individual flanges of the "I-beams" from the deck face panels (Fig. 3.21) and a failure of the most-loaded joint at mid-height of the specimens. Average failure load was 736 kN for the three element specimens and 725 kN for the four element specimens what is ∼15% lower that the elastic limit. The failure mode did not differ between the three-element and the four-element specimens. Fig. 3.21 shows the typical failure of the compression specimens. An example of web delamination and joint failure at mid-height of the specimens is shown in Fig. 3.22 on the following page.

Figure 3.22: Delamination of web and failure of joint (Specimen 3cs).

No. of shapes/ height	No. of specimens	Max. load $[kN]$	E-Modulus global $[MPa]$	E-Modulus strain gages $[MPa]$	E-Modulus Ω-gages $[MPa]$
3/730 mm	3	736 ±19	8109 ±263	14128 ±2440	6847 ±995
4/1034 mm	3	725 ±53	9029 ±644	12091 ±528	9157 ±2319

Table 3.7: Experimental results for the DuraSpan compression experiments. Average values and standard deviation

Contrary to expectations, no local stability failure of the deck face panels with the short specimens took place. Deformation behavior is also shown by strain gages and Ω-gages. The comparison of the results shown by a strain gage and an Ω-gage on the left and right deck face panels of a specimen clearly illustrates the buckling behavior (see Fig. 3.25, page 46). Again, the stress data are related to the cross-sectional area of the deck face panels between the flanges of the "I-beams" where the strain gages were placed. Based on the three deformation behaviors measured in the load direction (Figs. 3.23 on the facing page and 3.25, page 46), three different stiffnesses within the linear-elastic range can be determined, as shown in Table 3.7: a) global stiffness, influenced by the buckling behavior, b) stiffness of the pultruded shapes measured with the strain gages, and c) stiffness measured with the Ω-gages over the adhesively-bonded joints. Global stiffness was determined within the range of -2.5 to -3.0 mm displacement, stiffness of the shapes within the range of -0.05% to -0.07% strain, stiffness over the adhesively-bonded joints within the range of -0.05% to -0.15% strain. The influence of the adhesively-bonded joints on global deck stiffness is remarkable. The stiffness over the joints decreases to approximately 50-70 % of stiffness between the joints.

For development of the calculation method, the average deck system values indicated in Table 3.8 on the next page for compression stiffness, and compression resistance, were derived from the results in Table 3.7 as follows:

- The compression resistance was converted to a 1-m slab width. Indicated are the maximum value and the limit of elastic behavior (85% of the maximum value). As already explained, the average system values of compression resistance represent lower limit values of the effective resistance. The E-Modulus was calculated from the strain- and Ω-gage values ($\frac{2}{3}$ from strain-, $\frac{1}{3}$ from Ω-gages according to the corresponding influence lengths) and almost corresponds to the value indicated by the deck producer (11,790 MPa, see [26]). Due to the buckling behavior, the global E-Modulus in Table 3.7 on the preceding page is too small. The chosen average values correspond to the measured average values of the short specimens. In Figure 3.26, page 47, a corresponding idealized axial stress (σ) - strain (ϵ) behavior is shown, which will be used to determine the bending behavior of the girders described in Chapter 4, page 61. The single specimen diagrams are attached in Appendix A.1, page 151.

Stiffness [MPa]	Max. Load $[\frac{kN}{m}]$	Elastic Limit $[\frac{kN}{m}]$
E-modulus $\widehat{E}$: 11700	1227	1048

Table 3.8: Average deck system properties for in-plane compression, DuraSpan system.

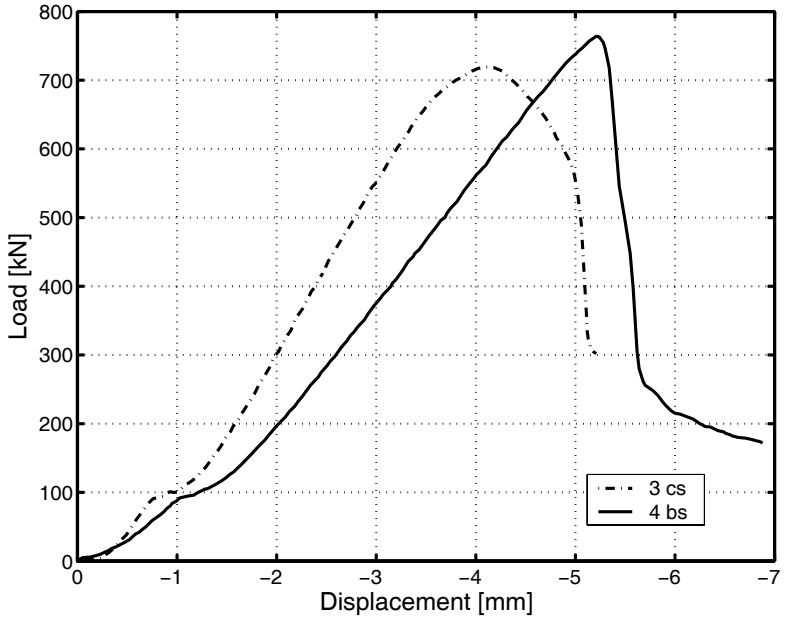

Figure 3.23: Global load-displacement behavior of specimens

Figure 3.24: Failure pattern of specimen 4bs

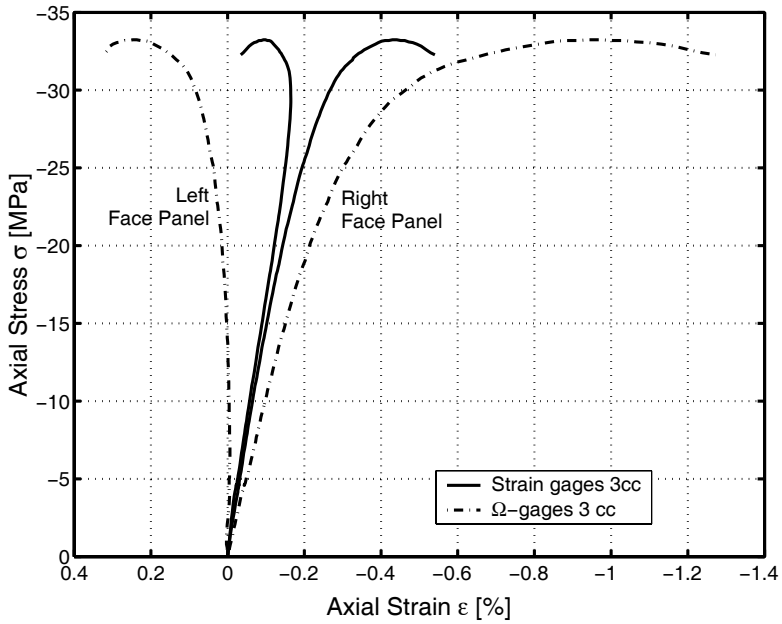

Figure 3.25: Selected strain gages (on pultruded shape) and Ω-gages (over bonded joint) at mid-height, specimen 3cs

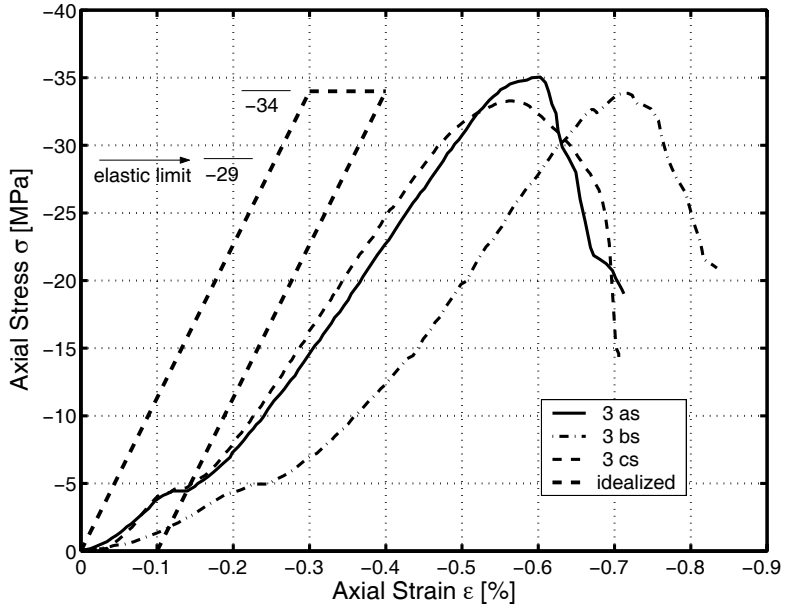

Figure 3.26: Global stress-strain behavior of three-element DuraSpan specimens and idealized behavior

ASSET

Experiments with the ASSET deck showed that the increase of the deck depth of 15% together with the change of the geometry changed the failure mode. With roughly the same specimen height, the ASSET deck did not fail by buckling around the weak axis but by a sort of delamination in the stepped joint (see Fig. 3.31, page 50). The load-displacement behavior of specimens AC1 to AC4, measured by the Trebel press, is shown in Figure 3.28 on the following page. The displacements in the load direction are indicated. Figure 3.29, page 49, shows specimen behavior converted to axial stresses, σ and strains, ϵ. Both values were calculated in the same way as described in Section 3.5.1, page 43. Furthermore, Table 3.9 on page 48 shows average values and standard deviations of the failure loads. All specimens showed linear-elastic behavior up to a brittle failure with a subsequent drop of the load due to the displacement-controlled experiments (Fig. 3.28 on the next page). The range of to approximately 1 mm displacement was distorted by the experiment set-up. Only by starting from this point was a full load transmission of the steel plate to the whole element width possible (same

Figure 3.27: Failure pattern of specimen AC2

effect as with the DuraSpan experiment). In contrast to experiments with the DuraSpan deck , no "limit of elastic behavior" with subsequent non-linear behavior could be observed. Only specimen AC1 behaved slightly differently. The load could be maintained for approximately 2 mm of further deformation; it subsequently decreased sharply.

Specimen	Failure Load $[kN]$	E-Modulus global $[MPa]$	E-Modulus strain gages $[MPa]$	E-Modulus Ω-gages $[MPa]$
AC1	600	10186	20030	12887
AC2	1035	16015	18218	9340
AC3	627	13250	16796	9273
AC4	834	13010	19595	13857
Average	774±203	13115±2381	18659±1462	11339±2381

Table 3.9: In-plane compression behavior, ASSET deck

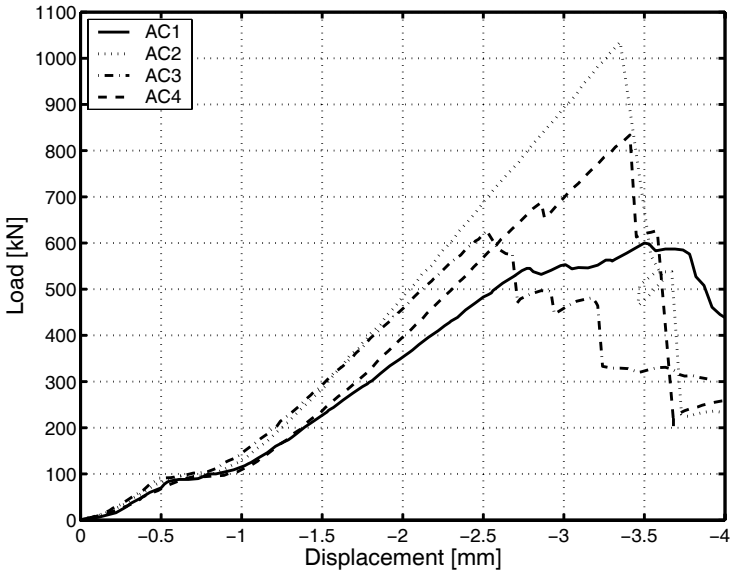

Figure 3.28: In-plane compression: measured load-displacement behavior.

Failures always occurred in one of the truss joints, at the stepped adhesive connection (see Figures 3.27 on the preceding page and 3.31, page 50). At the onset of failure, small debonding cracks parallel to the face panels could be observed in the truss joints. Subsequently, the face panels split and buckled at these locations (see Fig. 3.31, page 50). Failures always occurred in the adherents, never in the adhesives or the interfaces, with the previously mentioned exception of specimen AC1, where failure occurred in two joints simultaneously. Deformation behavior is also shown by the strain and Ω-gages. Fig. 3.30 on the next page illustrates the comparison of a strain- and an Ω-gage measurement result on the left and right deck face panels at mid-height of specimen AC2 (Ω-gage above and below mid-height). The face panels were loaded practically symmetrically.

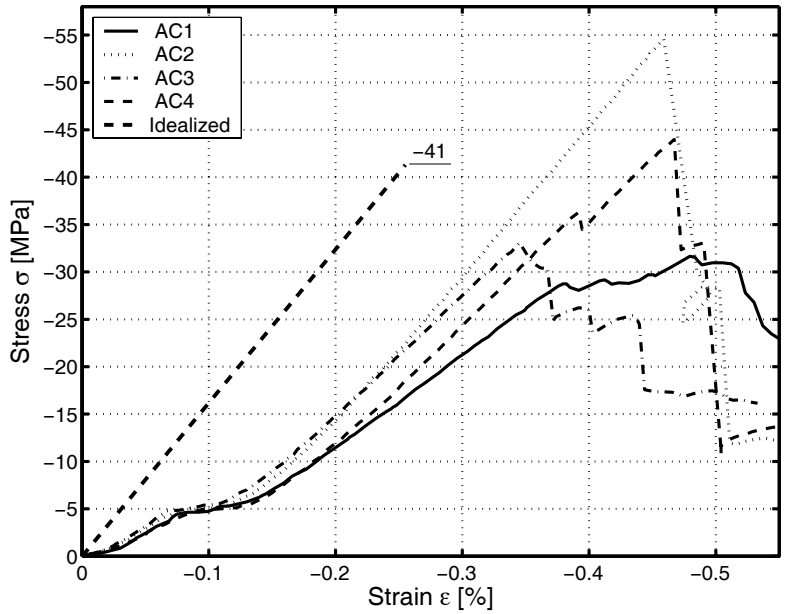

Figure 3.29: In-plane compression: calculated stress strain behavior plus idealized graph.

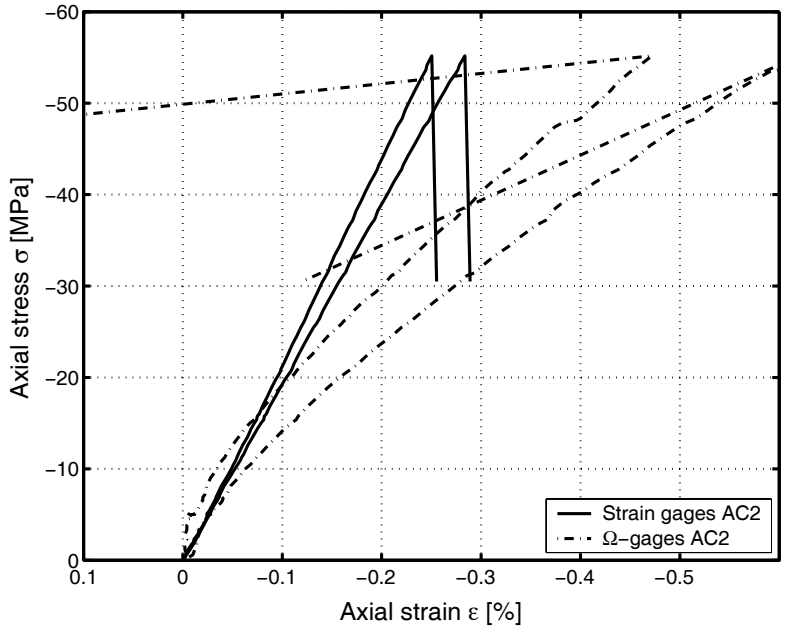

Figure 3.30: Selected strain gages (on pultruded shape)and Ω-gages (over bonded joint) around mid-height, specimen AC2

The other specimens exhibited similar behavior. As for the DuraSpan Specimens, three different transverse compression E-modules could be determined in the linear-elastic ranges (Figs. 3.29 and 3.30 on the preceding page). These are listed in Table 3.9, page 48. The influence of the adhesively-bonded joints on global transverse deck stiffness is much smaller than in the DuraSpan system (Figs. 3.30 on the previous page and Fig. 3.25, page 46). The main reason for this is certainly the epoxy adhesive, which is much stiffer than the polyurethane. The transverse E-Modulus indicated by the deck producer (18 000 MPa, see Table 3.4, page 33) therefore matches the value calculated from the strain-gage measurements and does not take into account the influence of the joints.

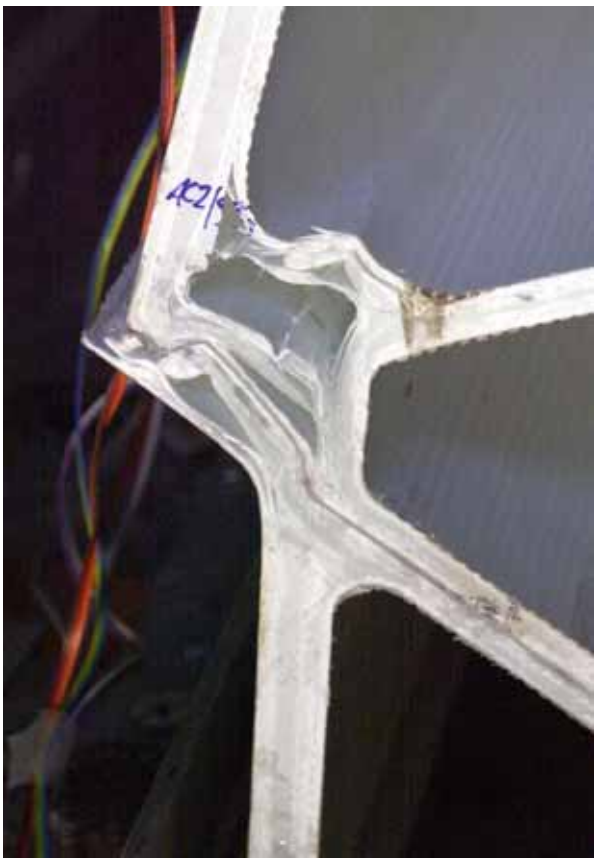

Figure 3.31: Detail of failure, specimen AC2

Summary of the results of the compression experiments

The system properties evaluated in the last two sections which will be used to determine girder behavior are summarized in Table 3.10. The values for the ASSET deck were determined as for the DuraSpan deck (see p. 45).

Deck system	E-modulus $\widehat{E}_{FRP}\ [MPa]$	Resistance $R_c\ [\frac{kN}{m}]$	Failure stress $\sigma_{c,fail}\ [MPa]$	Elastic limit load $R_{c,el}\ [\frac{kN}{m}]$	Elastic limit stress $\sigma_{c,el}\ [MPa]$
DuraSpan	11 700	-1 230	-34	1040	-29
ASSET	16 200	-1 290	-41	-	-

Table 3.10: Evaluated in-plane compression system properties for both bridge decks

The low stiffness over the adhesive joints of both systems reduces the deck's transverse stiffness considerably and thereby the the deck's effectiveness as top chord of the FRP/steel girder.

An idealized axial stress-strain curve (σ-ϵ), derived from the measured and calculated results, is shown in Fig. 3.32. Due to the system ductility observed, a small non-linear deformation of -0.1% strain was considered in the idealized curve for the DuraSpan deck.

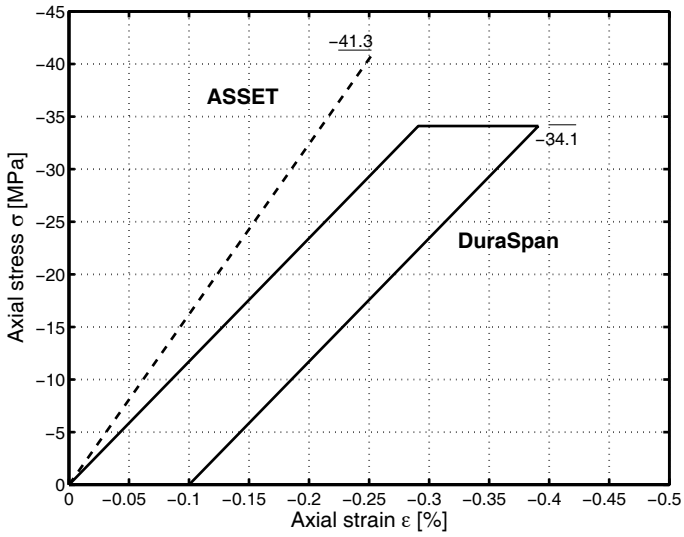

Figure 3.32: Idealized in-plane compression behavior of the two systems.

The in-plane compression behavior of the two systems was comparable, see Table 3.10. Axial failure stresses and E-Modules were of the same order of magnitude. The triangular deck was approximately 12% stiffer and 21% more resistant in compression transverse to pultrusion direction than the trapezoidal deck. The trapezoidal deck behaved in an elastic non-linear manner with an elastic limit at 85% of the compression resistance. The triangular deck behaved strictly linear-elastically up to brittle failure, which was much more abrupt than that of the trapezoidal deck. The idealized compression stress-strain behavior

of the two cross-sections is shown in Figure 3.32 on the previous page. The adhesively-bonded joints of both deck systems were placed at distances of 300 mm. The joints of the trapezoidal system were bonded with a polyurethane adhesive, while an epoxy adhesive was used for those of the triangular system. Compression stiffness over the epoxy joints (11,339 MPa, Table 3.9, page 48) was approximately 70% higher than that over the PU-joints (6,847 MPa, Table 3.7, page 44). The dispersion in the measured failure loads was much higher for the ASSET deck than the DuraSpan deck, probably due to the former's brittle behavior.

3.5.2 Shear experiments

DuraSpan

Global load-displacement behavior is represented by specimens 3aa and 4aa in Fig. 3.34 on the facing page. The remaining specimens demonstrated similar behavior (single-specimen diagrams are attached in Appendix B.1, page 157). The differential shifts of the deck face panels in the load direction are shown. The maximum loads and shifts are represented in Table 3.11 on the facing page. Global load-displacement behavior was converted into shear stress (τ) - shear strain (γ) behavior as follows: on the one hand, the shear force was related to the deck face panels' surface with a resulting shear stress; on the other hand, the shear strain was calculated from the differential shift in load direction and the distance between the deck face panels. Thus:

$$\tau = \frac{F}{b \cdot h} \qquad (3.1)$$

Figure 3.33: Typical failure of three-element specimen (3aa)

Assuming that for small angles $\tan\gamma = \gamma$ one gets:

$$\gamma = \frac{u}{t} \qquad (3.2)$$

with: F = applied force
b = specimen width
h = specimen height
γ = shear strain
u = relative displacement between face panels
t= deck depth

The corresponding shear deformation behavior of the shorter specimens is shown in Fig. 3.35 on the next page. In the linear-elastic range of the deformation curve (γ = 0.007-0.015), a global shear modulus $\widehat{G}$ was determined which can also be seen in Table 3.11.

No. of shapes/height	Max. load $[kN]$	Max. load $[\frac{kN}{m^2}]$	Max. differential shift $[mm]$	G-modulus $\widehat{G}$ $[MPa]$
3/730 mm	-59 ±3	-134 ±7	33 ±8	4.9 ±1.5
4/1034 mm	-69 ±6	-111 ±9	35 ±2	3.3 ±1.2

Table 3.11: In-plane shear stress and strain behavior - experimental results, DuraS pan

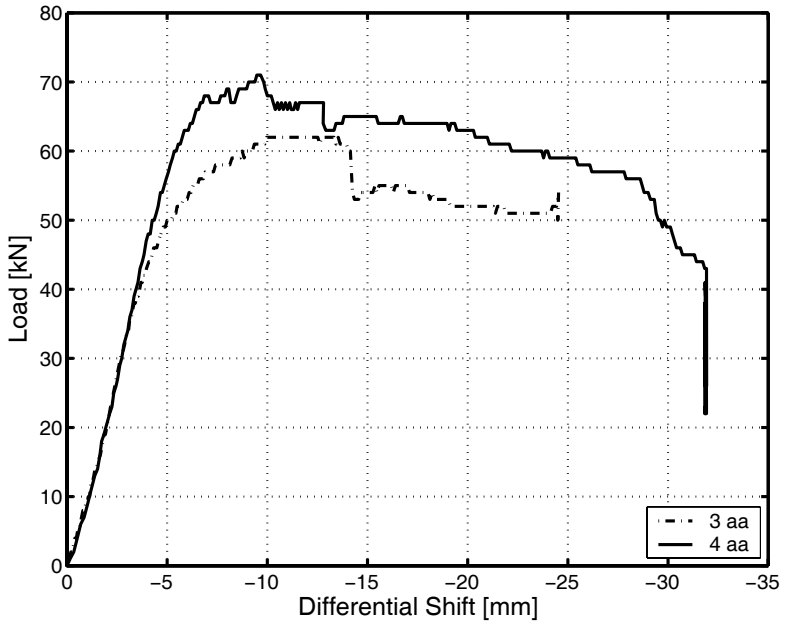

Figure 3.34: Global load-displacement behavior of specimens 3aa and 4aa

The short and tall specimens exhibited different deformation behavior. The deck face sheets of the short specimens remained almost plane and parallel throughout the whole experiment (Fig. 3.33 on the preceding page). On average, first delaminations of the flanges from the deck face sheets were noticed at approximately 70% of maximum load (elastic limit). After this point, the load

increased much more slowly while the loading rate was kept constant. The differential shift of the deck face sheets then began to increase non-linearly until maximum load was reached. Since this was a displacement-controlled experiment, the specimens could subsequently be deformed with an almost constant load. The "I-beam" flanges became increasingly detached, and some of the adhesively-bonded joints opened (Fig. 3.39, page 56). The specimens demonstrated excellent ductility, resulting from system redundancy and not material properties.

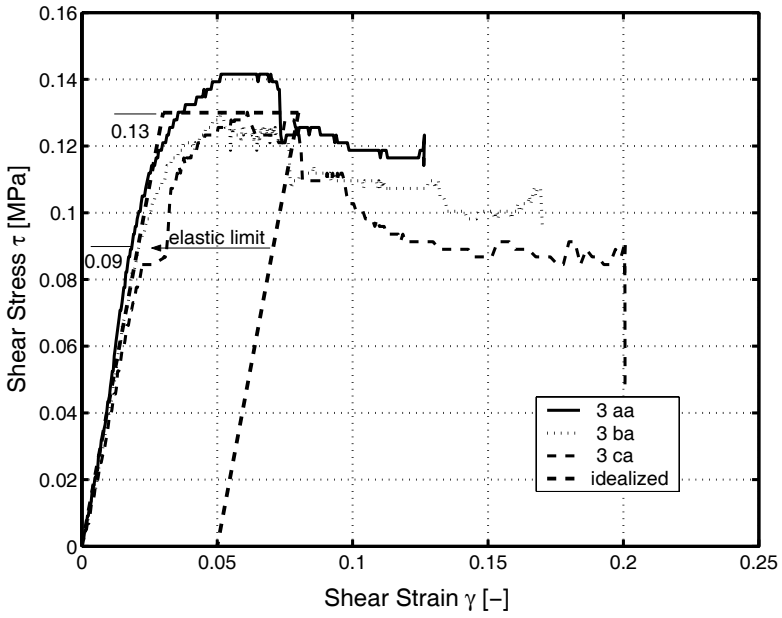

Figure 3.35: Shear stress - shear strain behavior of the short specimens

The load-deformation behavior of the tall specimens initially corresponded to that of the short specimens. However, after the first delaminations, the tall specimens began to buckle laterally (Fig. 3.37 on the next page). At the same time, one of the bonded joints opened (Fig. 3.38 on the facing page). The delamination failures of the "I-beams" were accompanied by an instability-induced failure of the compressed deck face panels. The taller specimens, like the shorter specimens, nevertheless showed good system ductility . Due to the simultaneous buckling-induced failures of the taller specimens, their ultimate failure loads were approximately 20% lower than those of the shorter specimens. Therefore, only the shorter specimens results are considered valid for future design calculations since deck buckling is prevented by connection to steel girders.

From the strain measurement results, the axial forces in the deck face panels were determined using the material properties listed in Table 3.7, page 44. For construction reasons, it was not possible to install strain gages on both sides of the webs and therefore the strains in the neutral axis of the webs could not be determined. For comparison, the internal forces (axial and shear forces, bending moments) were calculated using a simple beam program. Fig. 3.36 on the facing page shows the resulting axial force, shear force and bending

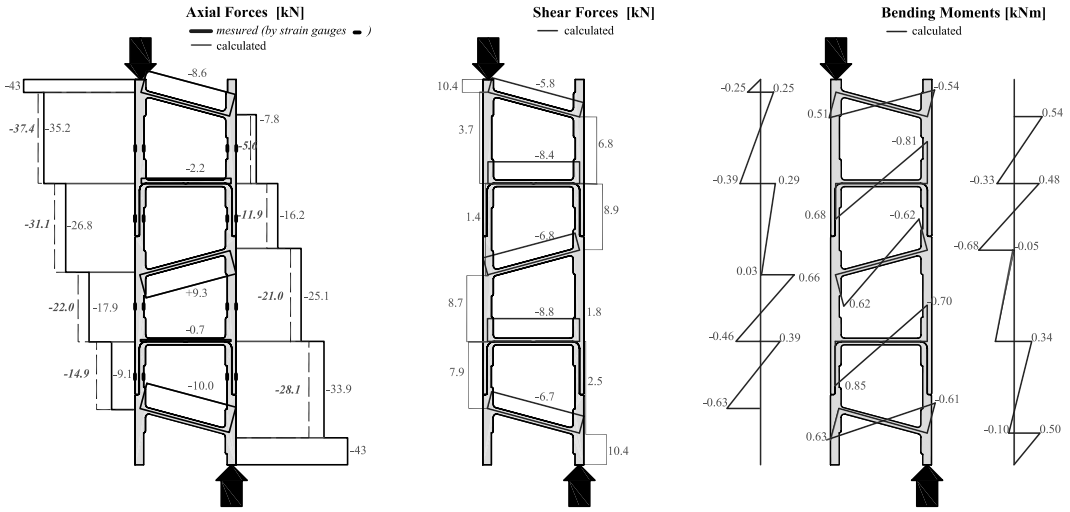

Figure 3.36: Axial force, shear force and bending moment diagrams at the limit of elastic behavior, specimen 3aa)

moment distributions of specimen 3aa at the limit of elastic behavior. From the moment diagram it can be deduced that approximately 85% of the load is transferred through transverse bending of the webs (Vierendeel action). By the truss action of the inclined webs, only ∼15% is transferred. The results of measurements and calculations are of the same order of magnitude. The remaining specimens produced similar results. Single-specimen diagrams are attached in Appendix B.1, page 157.

Figure 3.37: Failure pattern, specimen 4as

Figure 3.38: Failure pattern, specimen 4as; detail adhesively- bonded joint

Figure 3.39: Web delamination and joint failure (specimen 3ca)

ASSET

The differential shifts between deck face panels in the load direction are shown in Fig. 3.41 on the facing page. The average values and standard deviations of the failure loads and maximum shifts are listed in Table 3.12 on the next page. The load-displacement behavior as shown in Fig. 3.41 on the facing page was converted into shear stress (τ) - shear strain (γ) behavior as described in Section 3.5.2, page 52. The resulting shear stress - shear strain behavior is shown in Figure 3.42, page 58. As for the DuraSpan shear experiments, a "global" shear modulus ($\widehat{G}$) for the deck system was determined in the linear-elastic range of the deformation curve (γ = 0.005-0.010), see Table 3.12. All specimens showed linear-elastic behavior up to brittle failure with a subsequent load decrease due to the displacement-controlled experiments (Fig. 3.41 on the next page). Again, no "elastic behavior limit" or non-linear behavior after the first failure could be observed. Failures always occurred abruptly in one of the truss joints at points where the tension-stressed diagonals were attached (see Figs. 3.40 and 3.44, page 59). At the onset of failure, small cracks perpendicular to the tension-stressed diagonals could be observed in the joints. Subsequently, one of the tension-stressed diagonals separated from the truss joint and the face panels buckled. Subsequently, specimens could be further deformed at a very low load level.

Figure 3.40: Failure pattern, specimen AS3

Specimen	Max. load $[kN]$	Max. load $[\frac{kN}{m^2}]$	Differential shift at failure $[mm]$	Global G-modulus $\widehat{G}$ $[MPa]$
AS1	287	640	3.15	47.2
AS2	298	665	2.91	56.8
AS3	241	538	3.47	37.1
AS4	266	593	3.06	47.5
Average	273±25	609± 56	3.15±0.24	47.2±8

Table 3.12: In-plane shear behavior, ASSET deck

Subsequently local debonding failures occurred in truss joints and at upper supports at points subject to maximum out-of-plane tension stresses due to transverse bending. Failures always occurred in the adherents, never in the adhesive joints (see Fig. 3.44, page 59). As for the DuraSpan shear experiments, the results of the strain measurements, axial forces in the deck face panels and webs were determined using the material properties listed in Table 3.12. Thanks to supplementary strain gages on the webs, it was also possible to determine the axial strains there (which was not the case with the DuraSpan shear experiments). Results of the calculation of internal forces with the beam program and measured normal forces are shown in Fig. 3.43 on the following page. From this, it can be deduced that approximately 85% of the load was transferred by truss action (compressive and tensile forces in the diagonals). Less than 15% was transferred by Vierendeel action (transverse bending). However, local moments and high shear forces were calculated in the joints between the intersections of diagonals with face panels which are offset. Results of measurements and calculations are of the same order of magnitude. The remaining specimens showed similar results. Single- specimen diagrams are attached in Appendix B.2, page 162.

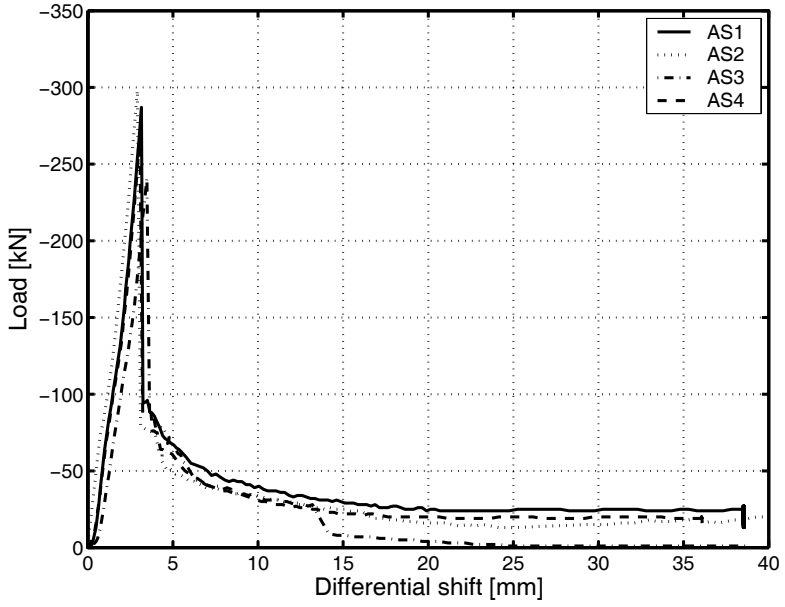

Figure 3.41: Load-displacement behavior measured by shear experiments

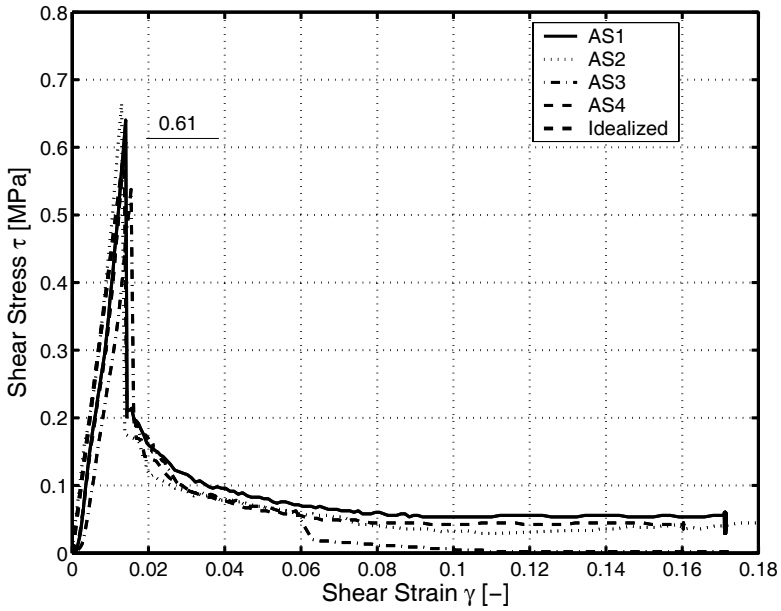

Figure 3.42: Calculated shear stress - shear strain behavior, ASSET deck

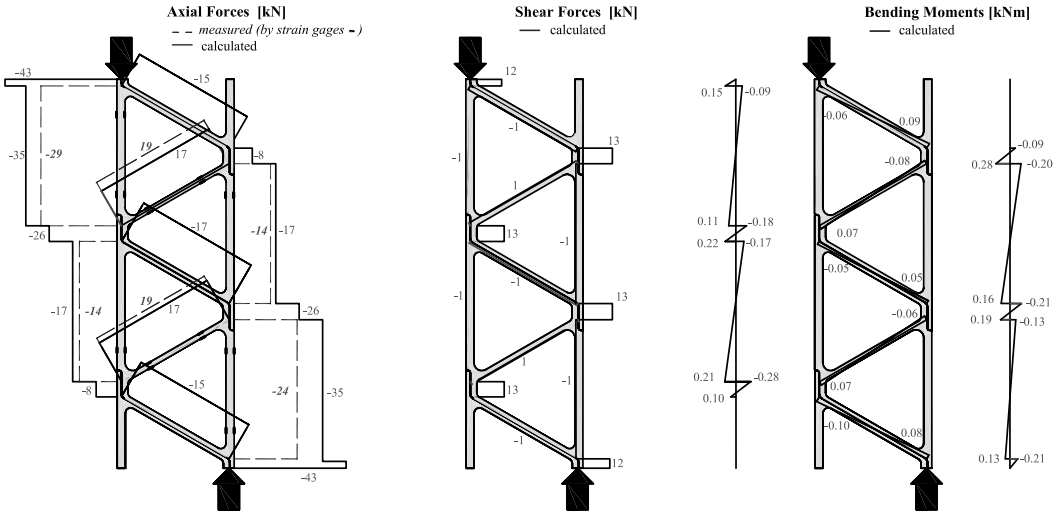

Figure 3.43: Axial force, shear force and bending moment diagrams at 43 kN, specimen 3s

Figure 3.44: Detail of failure, specimen AS3

Summary of the results of the shear experiments

The system properties evaluated in the last two sections which will be used to determine girder behavior are summarized in Table 3.13.

Deck system	G-modulus $\widehat{G}\,[MPa]$	Resistance $R_S \quad [\frac{kN}{m^2}]$	Failure stress $\tau_{fail}\,[MPa]$	Elastic limit load $R_{s,el}\,[\frac{kN}{m^2}]$	Elastic limit stress $\tau_{el}\,[MPa]$
DuraSpan	5	134	0.13	94	0.09
ASSET	47	609	0.61	-	-

Table 3.13: Evaluated in-plane shear system properties for both bridge decks

An idealized shear stress - shear strain curve, τ-γ, was derived from the measured and calculated results and is shown in Fig. 3.45 on the next page. Due to the system ductility observed for the DuraSpan system, a non-linear deformation of 0.05 [-] shear strain was considered in the idealized curve.

The in-plane shear behavior of the two cross-sections was completely different. The DuraSpan deck with trapezoidal cross-section transferred the in-plane shear force from one face panel to the other mainly through transverse bending of cross-sectional elements (Vierendeel action, ∼85%). Only ∼15% of shear force was transferred through axial forces (truss action). The ASSET deck with triangular cross-section, however, showed nearly the opposite results: ∼85% of

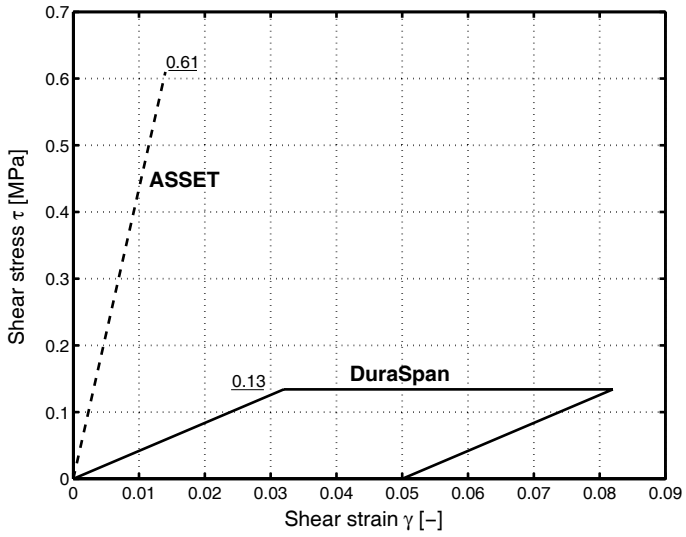

Figure 3.45: Idealized in-plane shear behavior of the two systems

in-plane shear force was transferred by truss action and ∼15% by Vierendeel action. The stiffness and shear resistance of the truss configuration was much higher than those of the trapezoidal configuration: 9.4 times for stiffness and 4.5 times for shear resistance (see Table 3.13 on the preceding page). The behavior of the trapezoidal configuration, on the other hand, showed much higher system ductility than the triangular configuration, which exhibited very brittle behavior. The idealized shear stress-strain behavior of the two cross-sections is shown in Figure 3.45.

4 Four-point bending experiments on composite girders

4.1 Objectives

To fully exploit the advantages of each construction element, it is likely that future projects involving GFRP bridge decks will be carried out using steel main girders as bridge deck support. This combination of steel main girders and GFRP bridge decks is very appropriate for utilizing the composite action between the different materials. The experiments described in this section will provide important information for development of the design method used to determine the degree of composite action in a girder.

With the results from Chapter 3, page 29, the system properties required to estimate the load-bearing capacity of ASSET or DuraSpan composite girders are known, but the exact structural behavior still cannot be determined. Therefore the objective of this series of experiments is the detailed investigation of the structural behavior of composite girders consisting of steel main girders adhesively bonded to ASSET/DuraSpan bridge decks. This includes above all the degree of composite action in the girder, load-bearing capacity, load-deflection behavior, fatigue behavior and transmission of shear forces in the adhesively-bonded joint.

4.2 Experimental program

The basis for the girder experiments described in this section are calculations carried out for a reference bridge of 15m span subjected to EC 1 loads. The span of 15m was chosen because loads in the bridge deck increase with decreasing span. In bridges with spans shorter than 15m composite action has no economical advantage over bridges without composite action. The calculations were done assuming full composite action over the whole girder height, since a design method, which considers partial composite action in those kind of girders, does not exist. The experimental girders then were designed in such a way, that a similar stresse state in the adhesively bonded joint, compared to the stress state in the reference bridge, could be generated. The SLS[1] and ULS[2] loads of the experimental girders are therefore a function of the stresses in the adhesively bonded joint of the reference bridge.

[1] Serviceability Limit State
[2] Ultimate Limit State

This series of experiments involves five specimens, four composite girders and one steel girder. All were single girders of 7.50-m span loaded with two single loads, each 0.75 m distant from the symmetry axis (see Fig. 4.14, page 70, four-point bending). The DuraSpan girders were designated Fix 1 and Fix 2 and the ASSET girders Fix 3 and Fix 4. Fix 1 and Fix 3 were subjected to three load cycles (SLS, ULS and FLS[3]). Fix 2 and Fix 4 were first subjected to 10^7 fatigue cycles, with one cycle up to SLS every 10^6 cycles. After completion of the fatigue experiment, the two girders were subjected to two more load cycles - ULS and FLS. Detailed information is given in Chapter 4.4, page 68. The steel girder was subjected to one load cycle. The designation of the girders in shown in Table 4.1.

	DuraSpan deck	ASSET deck	Steel girder
Girder	Fix 1 | Fix 2	Fix 3 | Fix 4	PM

Table 4.1: Overview of experimental girders

4.3 Experiment specimens

4.3.1 Dimensions

Figures 4.1 on the facing page and 4.2 on the next page show an elevation of the different steel girders. Since the lengths of the single-deck elements were different (see Figs. 4.3 and 4.4, page 64) and a minimum adhesive thickness of 6 mm should be guaranteed, the distance between the hard shims had to be adapted.

Figs. 4.3, page 64 and 4.4, page 64 show an elevation and a cross-section of the DuraSpan/ASSET bridge decks.

[3]Failure Limit State

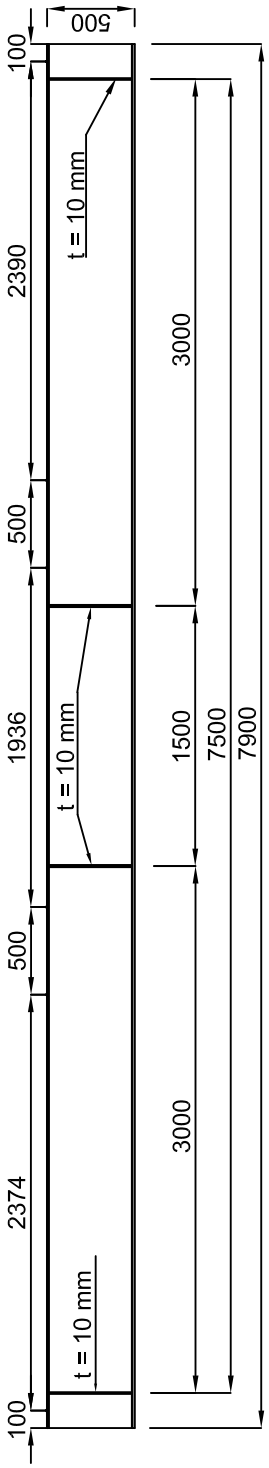

Figure 4.1: Elevation of steel girder with distance between the hard shims on the top flange. Deck type: ASSET

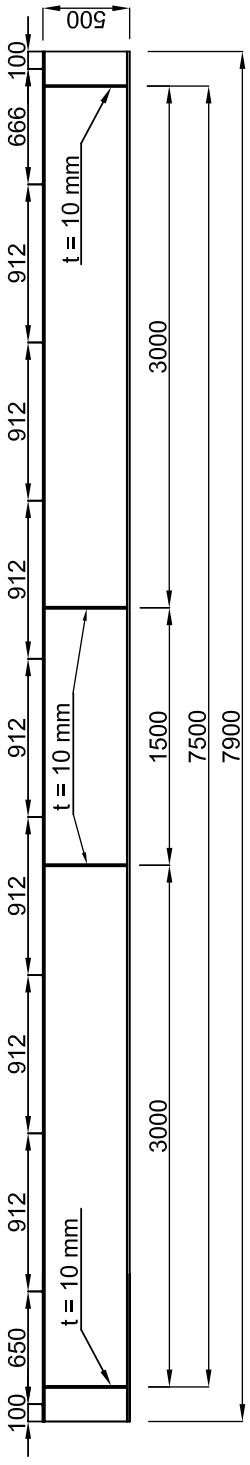

Figure 4.2: Elevation of steel girder with distance between the hard shims on the top flange. Deck type: DuraSpan

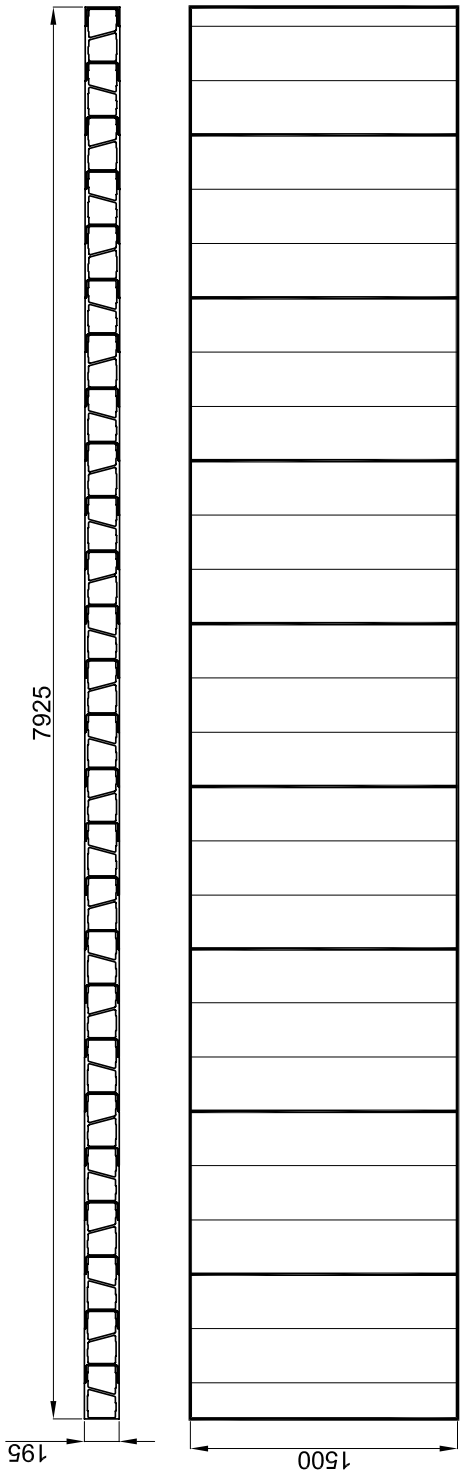

Figure 4.3: Overall dimensions of DuraSpan bridge deck (SikaDur 330 joints shown in bold)

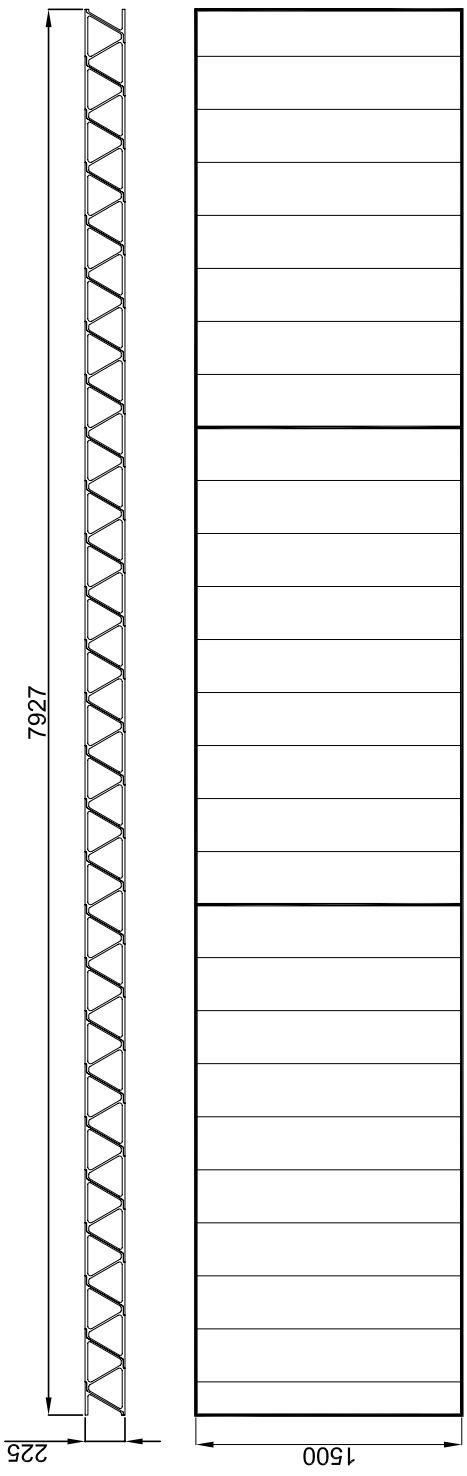

Figure 4.4: Overall dimensions of AS-SET bridge deck (SikaDur 330 joints shown in bold)

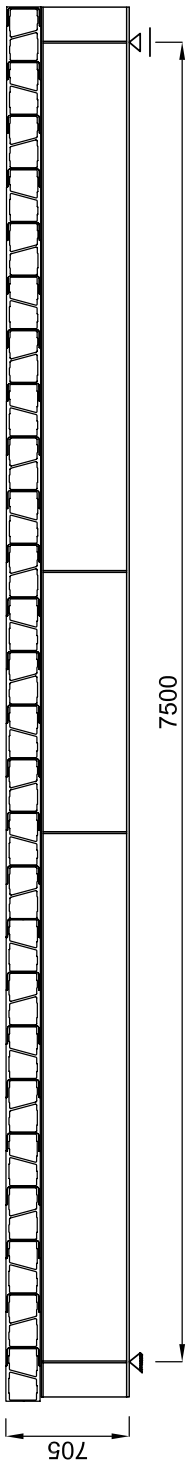

Figure 4.5: Elevation of composite DuraSpan girder

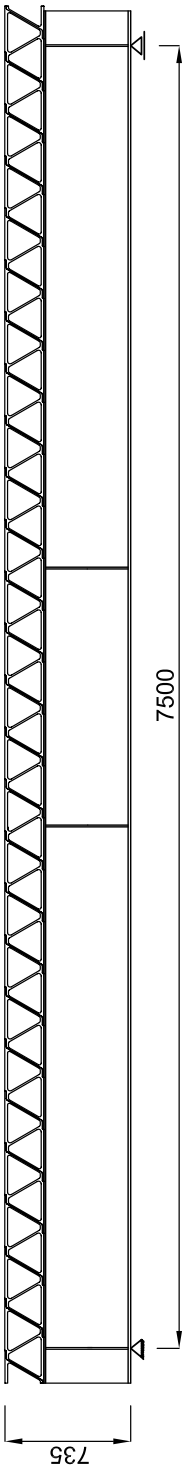

Figure 4.6: Elevation of composite ASSET girder

Figs. 4.7 and 4.8 show a cross-section of the composite girders.

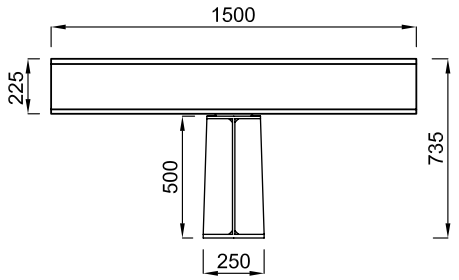

Figure 4.7: Section of ASSET girder

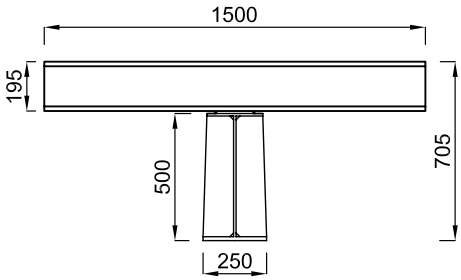

Figure 4.8: Section of DuraSpan girder

4.3.2 Materials

The materials composing the bridge decks and the adhesives are described in Section 3.3.2, page 32, with the exception of SikaDur 330. This is a two- component epoxy adhesive whose properties are presented in Table 4.2.

	SikaDur 330
Mixing ratio	4 : 1
Density, $[\frac{kg}{m^3}]$	1310
Viscosity @ 25°C	Thixotropic
Potlife @ 10°C	90 Minutes
Tensile strength [MPa]	30
Bending E-modulus, [MPa]	3800

Table 4.2: Material properties, SikaDur 330

The steel girders were made from a conventional structural steel, Eurocode 3 designation: S 355. The material properties, evaluated by means of experiements, are $f_y = 382$ MPa[4] and $f_u = 541$ MPa[5].

4.3.3 Manufacture

Bridge deck

The ASSET bridge deck elements were manufactured at Fiberline Composites, Denmark, where the profiles were produced and bonded together to form three parts of ∼2.50-m length and 1.50-m width using NM BPE Lim 465 adhesive (see Fig. 4.4, page 64). The elements were then transported to the EPFL by lorry.

[4] yielding stress
[5] ultimate stress

The DuraSpan bridge deck was manufactured at Martin Marietta Composites, Sparta, North Carolina USA, where the profiles were produced and bonded together to form eight parts of ∼0.94-m length and 1.50-m width using Pliogrip 6660 adhesive (see Fig. 4.3, page 64). The elements were then transported to the EPFL by plane.

Steel girder

The two steel beams used to compose the ASSET girders were manufactured at Ramelet SA, Lausanne, Switzerland. The two steel beams used to compose the DuraSpan girder were manufactured at Zwahlen et Mayr SA, Aigle, Switzerland. To ensure high quality, all joints were welded by a European welding engineer and quality-certificated steel was used.

At the supports and under the concentrated loads stiffeners were placed at both sides of the web.

In order to guarantee a minimum adhesive thickness of 6 mm, hard shims with a height of 6 mm were welded on the top flange of the steel girder (see Figs. 4.9 and 4.10). To keep the adhesive on the steel flange a foam with 10 mm thickness was bonded on the edges of the flanges (soft shim). For manufacture of the composite girder, the space between the foam was filled with adhesive.

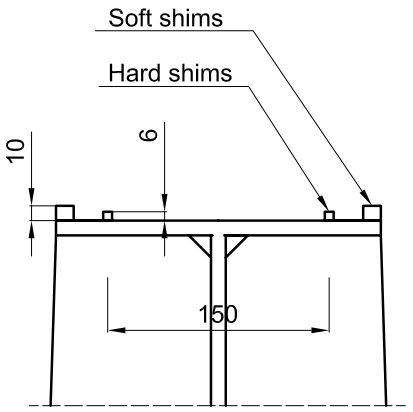

Figure 4.9: Dimensions of soft and hard shims

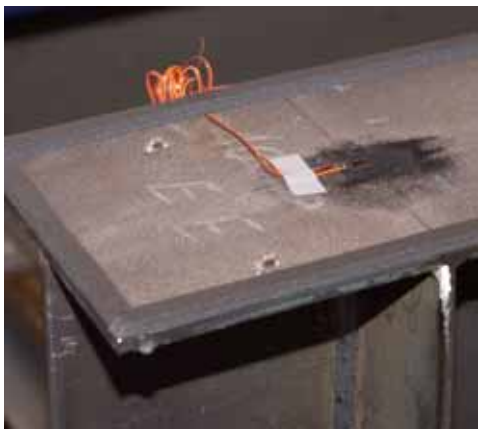

Figure 4.10: Soft and hard shims at girders‘ ends

Composite girder

The two ASSET composite girders were manufactured in the laboratory of the Structural Engineering Institute at EPFL. The bridge deck for each girder was delivered in three prefabricated parts from Fiberline Composites, Denmark. For the joints between the profiles of these parts, NM BPE Lim 465 was used. The second adhesive, SikaDur 330®, was used to bond the prefabricated bridge decks together and make the steel girder ⇔ bridge deck joint. In order to ensure good adhesion, the surface of the bridge deck was roughened with abrasive paper (coarse-grained 120, depth approximately 0.5 mm) and then degreased and the steel girder was sandblasted.

Figure 4.11: Clamped FRP elements of experimental girder Fix 3

To guarantee quick and smooth bonding, four people were involved in the process. One to mix the adhesive, one to prepare the FRP ⇔ FRP joints and two to prepare the steel girder ⇔ FRP joint and place the elements on the steel girder. Before the elements were clamped together, the correct position on the steel girder was verified and a horizontal alignment (water level) was carried out. Fig. 4.11 shows girder Fix 3 after bonding of the bridge deck. To enhance adhesion in the adhesively-bonded joint, a steel girder of $\sim 2\ \frac{kN}{m}$-weight was placed on the bridge deck after all work was completed (see Fig. 4.12 on the facing page). The supports were already 7.50 m apart, which was also the span for the experiment, in order to obtain an unpropped system. To monitor temperature increase during adhesive curing, three thermocouples were installed in the FRP ⇔ steel girder joint.

The manufacture of the two DuraSpan composite girders was slightly different. The geometry of the deck-to-deck joint did not require clamping the elements together. Thermocouples were only installed in the adhesively-bonded joint of the ASSET girders. The bonding of the DuraSpan girders was carried out at Zwahlen et Mayr SA, Aigle, Switzerland.

4.4 Experiment procedure

4.4.1 Experimental set-up and load equipment

The experiments were carried out in the laboratory of the Structural Engineering Institute at EPFL. Due to testing machine availability, girders Fix 1 and Fix 2 (DuraSpan) were tested in hall 2 and Fix 3 and Fix 4 in hall 1. Fig. 4.13 on the next page shows girder Fix 3 with reaction frame and jacks

Figure 4.12: Girder Fix 1 with weight after bonding

in hall 1. Both testing machines comprise the same characteristics, only the capacity of the jacks being different. Jack capacity in hall 1 is 2x1200 kN; in hall 2 2x500 kN. Both systems have a maximum displacement of 250 mm. The control unit offer the possibility of conducting either force- or displacement-controlled experiments. Fatigue testing is also feasible with frequencies up to 2.5 Hz, depending on the total travel. The girders were placed on steel supports with a load-bearing capacity of 1000 kN each. A detailed set-up is shown in Fig. 4.14 on the following page for the ASSET girder. The set-up for the DuraSpan girders was the same and can be seen in Appendix F.2, page 202.

Figure 4.13: Overview of the experimental set-up

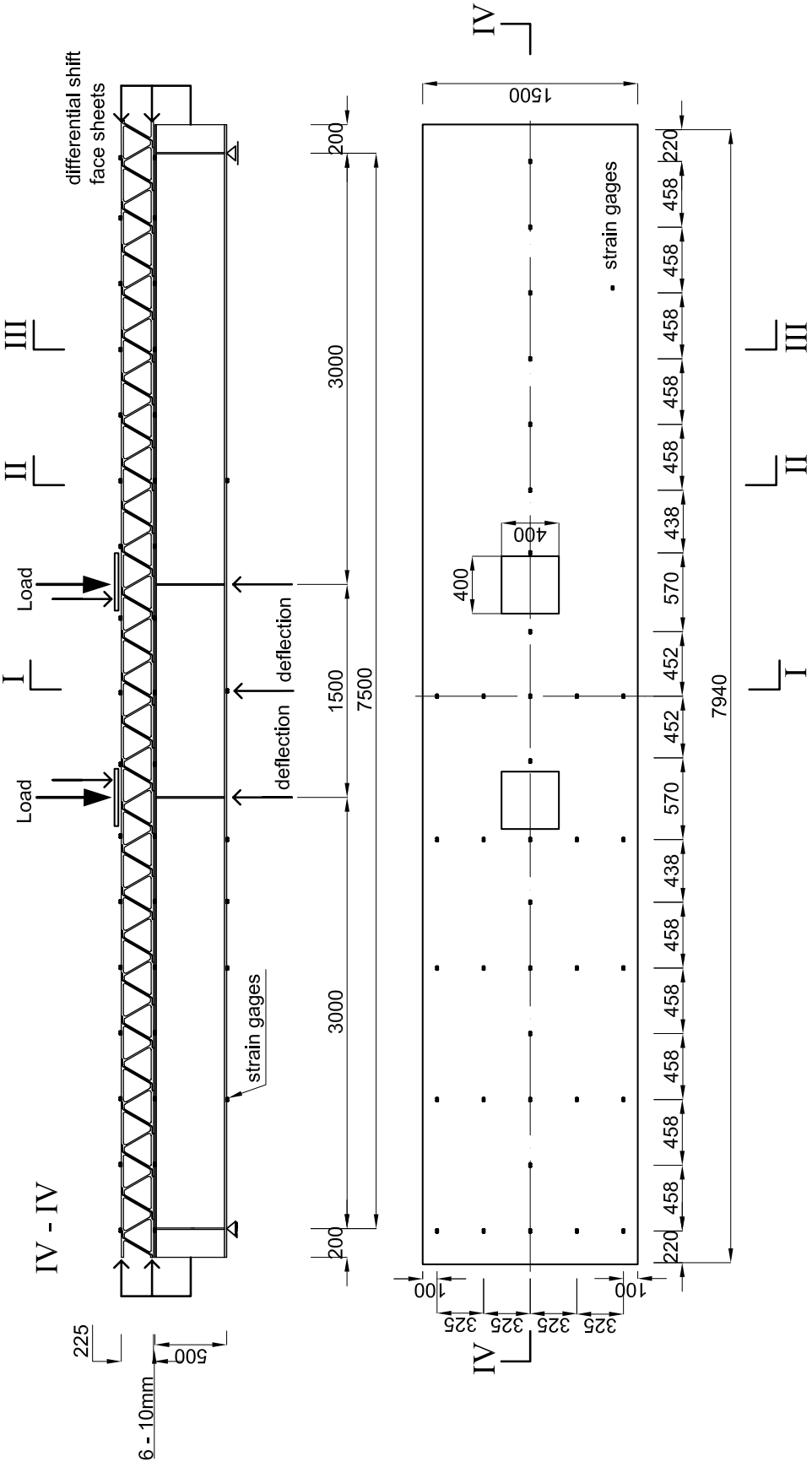

Figure 4.14: Set-up, elevation and top view of ASSET girder.

4.4.2 Instrumentation and measurements

In principle the instrumentation is the same for all girders. The experience with the DuraSpan girders, which were tested first, showed that supplementary strain gages should be added in some cross-sections, so three supplementary strain gages were installed on the lower steel flange of girders Fix 3 and 4. This is the only difference concerning instrumentation. Detailed plans can be found in Appendix F, page 199.

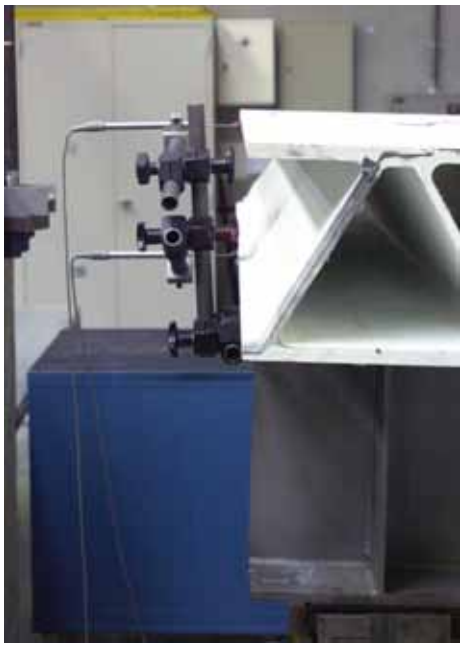

Figure 4.15: End of girder Fix 3 with displacement transducers

The instrumentation used for the experiment consisted of two measuring devices, UPM 60 and Centipede, from Hottinger Baldwin Messtechnik (HBM) with 60/100 channels respectively, and a laptop to record data. Both the UPM 60 and Centipede are measuring instruments for processing data from strain gages, force gages or inductive strain gages.

The strain gages used were the same as described in Section 3.4.1, page 36. Girders Fix 1 and 2 were equipped with 94 strain gages, girders Fix 3 and 4 with 97. Before the experiment, each strain gage was tested for function with an ohmeter (for those in the adhesive joints, this was done before bonding). All gages were installed according to the standard operating procedure described in [59]. The experimental girders were divided into 17 axes with different arrangements of the strain gages. As shown in Figs. 4.16 on the following page and 4.14 on the preceding page, the distance chosen between the axes was relatively small in order to observe exactly what happened in each part of the girder. Since it was very important to obtain information on the behavior of the adhesively-bonded joint, strain gages were installed on every axis on the bridge deck's lower face panel, as well as on the top flange of the steel girder (see Figs. 4.17 on the following page and 4.18, page 73). To judge strain distribution over the section height, two supplementary strain gages were bonded onto the upper face panel of the bridge deck and bottom flange of the steel girder (axes C, E, F, G, J, M). As already mentioned at the beginning of this section, only cross-sections F-F, J-J and M-M of the DuraSpan girders were equipped with strain gages on the bottom steel flange. Another objective of the experiments was to ascertain the effective width of the bridge decks. Axes A, C, E, G and J were therefore equipped with eight supplementary strain gages (see Fig. 4.17 on the following page). The strain gages in axis A were arranged as in Section I-I apart from the gage on the bottom flange (there was none).

Two different types of displacement transducer (also HBM) were installed in order to adapt accuracy to the expected deformation. Type W 20 (4x), with a

working range of ±20 mm, to measure the relative (in-plane) displacement of the deck face panels and type W 100 (5x), with a working range of ±100 mm, to measure deflection. Figure 4.15 on the previous page shows an example of type W 20 at the end of girder Fix 3. The displacement transducers were arranged in such a way that the deflection at mid-span, relative displacement between upper and lower face panels, and a possible crushing of the bridge deck under the single load could be measured (see Fig. 4.14, page 70).

Only in girder Fix 4 were the two thermocouples installed in the bridge deck ⇔ steel girder joint in axes G-G and M-M.

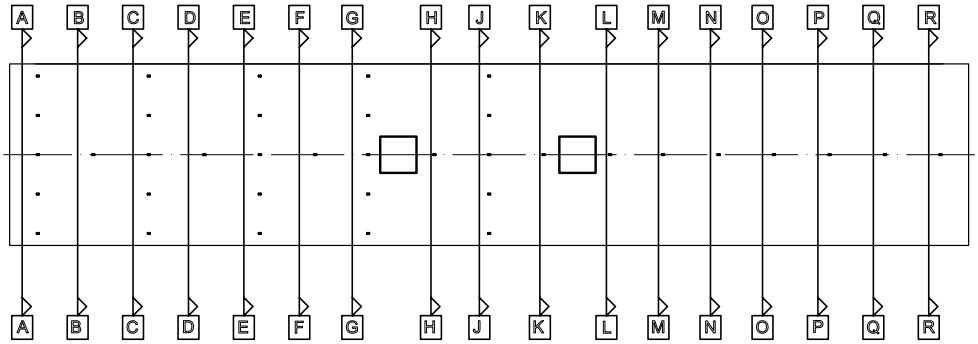

Figure 4.16: Bridge deck with arrangement of section axes and strain gages

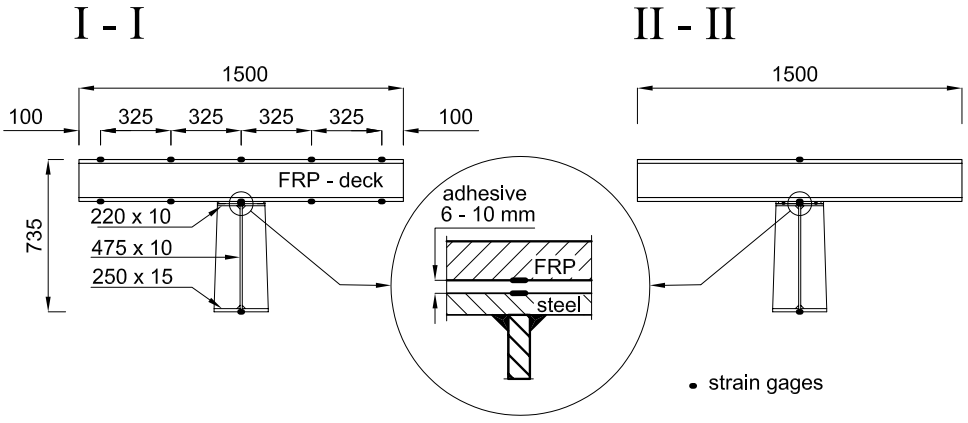

Figure 4.17: Section I-I: Arrangement of strain gages in axes C, E, G, and J. Section II - II: Arrangement of strain gages in axes C, E, F, G, J, M. (C, E and G only ASSET)

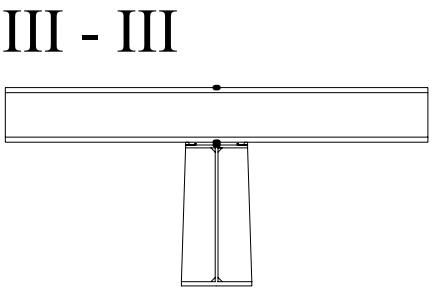

Figure 4.18: Section III - III: Arrangement of strain gages in axes B, D, H, K, L, N, O, P, Q and R.

4.4.3 Experiment preparation and procedure

Figure 4.14, page 70, shows that this involves a four-point bending experiment with 7.50- m span and the single loads situated 0.75 m from the symmetry axis. The distance of 1.50 m was chosen to create an axis-loading according to Eurocode 1. The surface of the load patches (0.4m x 0.4m) is also specified in Eurocode 1. Deformable hard rubber plates of 5- mm thickness were placed between the steel plates under the jacks and GFRP decks. To avoid stability failure of the experimental girder, a horizontal support was created at mid-span (see Fig. 4.19).

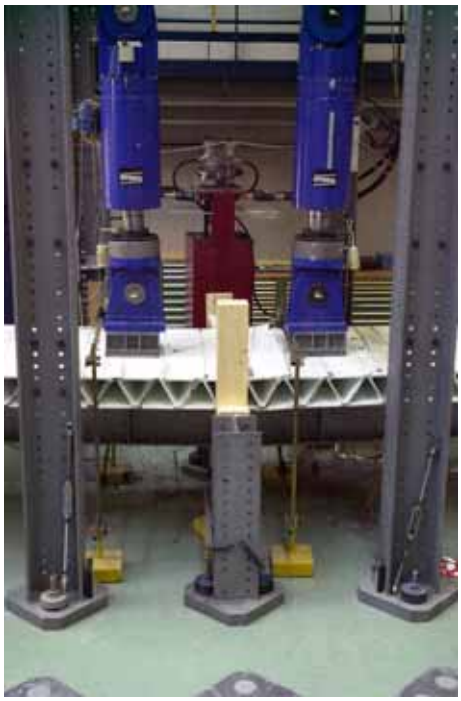

Figure 4.19: Middle part of the experimental girder with horizontal support

Girders Fix 1 and Fix 3 were subjected to three load cycles: 1st cycle SLS (2x90 kN Fix 3, 2x80 kN Fix 1), 2nd cycle ULS (2x120 kN Fix 3, 2x110 kN Fix 1) and 3rd cycle FLS. The load factor between SLS and ULS is therefore 1.35. Girders Fix 2 and Fix 4 were first loaded up to the SLS load (one cycle). 10^7 sinusoidal load cycles of between 2x10 and 2x40 kN then followed at a frequency of 2.0 Hz. An SLS load experiment was carried out after each one million cycles. The corresponding shear stresses calculated in the adhesive joint again matched the variation of stresses in the reference bridge subjected to Eurocode 1 fatigue loads. Following the fatigue experiment, two more load cycles were carried out - one up to ULS load and then up to failure. All static experiments were carried out displacement-controlled at a rate of 1 $\frac{mm}{min}$. The fatigue experiments were carried out force-controlled.

4.5 Experiment results

4.5.1 ASSET girders

Curing behavior of adhesive

The thermocouple measured the temperature increase in the adhesive layer during curing of the adhesive in girder Fix 4. Figure 4.20 shows the measured temperature progression. The ambient temperature of 28.5°C is the temperature at which the diagram starts. The maximum temperature rose to 34°C, thus remaining far below the glass-transition temperature of the deck resin (approximately 85°C).

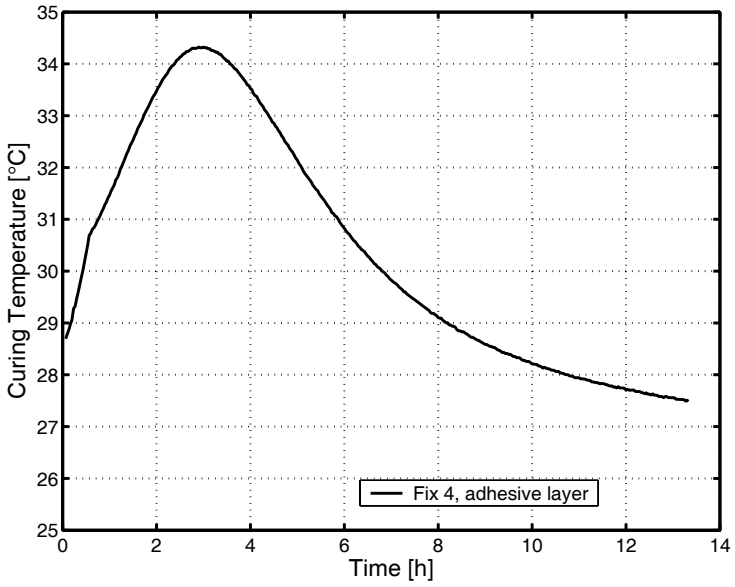

Figure 4.20: Temperature progression in the adhesive layer during curing

Girder behavior at SLS

Deflection and stiffness behavior

The 1st cycle results for girders Fix 3 and Fix 4 and the results for Fix 4 after 10^7 cycles up to SLS loads are listed in Table 4.3 on the facing page. Maximum deflections at mid-span are indicated as well as the calculated girder bending stiffnesses. The stiffnesses, EI_m, were calculated with the measured deflection at 7 mm for both girders using simple beam theory and ignoring shear deformation (see Equation 4.1). Seven mm were chosen in order to have a reliable value for the stiffness near the SLS load level (deflection at SLS $f \cong 8mm$).

$$EI_m = \frac{F \cdot l^3 \cdot \left(3 \cdot \left(\frac{\Phi}{l}\right) - 4 \cdot \left(\frac{\Phi}{l}\right)^3\right)}{24 \cdot f_m} \tag{4.1}$$

With: F = Load per jack
l = Span
Φ = Distance support $\Leftrightarrow$ load
f_m = measured deflection at mid-span

The behavior of the composite girders remained linear-elastic during all SLS experiments and was almost identical (see Fig. 4.32, page 82). During the fatigue experiment, the stiffness, EI_m, of girder Fix 4, calculated from the SLS experiments performed after each million cycles, remained constant up to ten million cycles, as shown in Fig. 4.21.

	Maximum mid-span deflection [mm]		Bending stiffness EI_m $[kN \cdot m^2]$	
Girder	1^{st} cycle	After 10^7 cycles	1^{st} cycle	After 10^7 cycles
Fix 3	8.1	-	186'400	-
Fix 4	7.9	7.4	188'800	192'800
Reference steel	13.8	-	90'500	–

Table 4.3: Maximum deflections and stiffness at mid-span under SLS loading

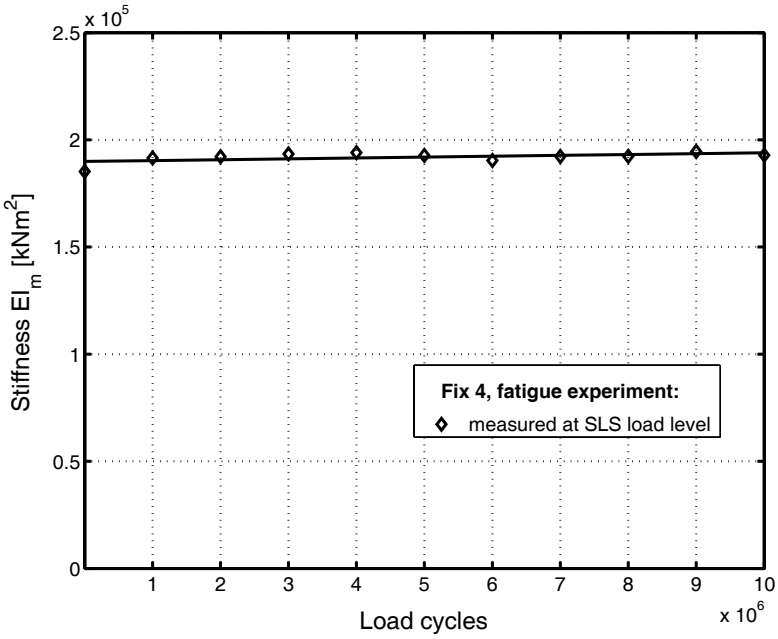

Figure 4.21: Girder stiffness after each million fatigue cycles

Cross-sectional axial stress-strain behavior

The measured axial strain distributions and calculated stresses in the cross-sections at mid-span for the two girders at SLS loads, at the 1st cycle and after ten million cycles for girder Fix 4, are shown in Fig. 4.23. The measured axial strain distributions of both girders were almost identical (see also Appendix D.1, page 173) but did not remain linear through the depth of the cross-section. Between the jacks, where there are no shear forces, the strain distribution remains nearly linear in the deck, but in the areas outside of the jacks, where constant shear forces exist, the strain distribution in the deck is completely different (see Fig. 4.22). This is due to the secondary bending moments in the deck itself. Since there were strain gages only at the outer sides of the face panels, the proportion of the axial forces in the deck could not be determined. Therefore are the lines between the upper and lower face panel only light dotted since they do not show the strain distribution. They should only indicate that the upper and lower face panel are connected by the webs. This is also valid for all Figures of cross-sections C, E, F, G and M, which show the strain distribution (also DuraSpan).

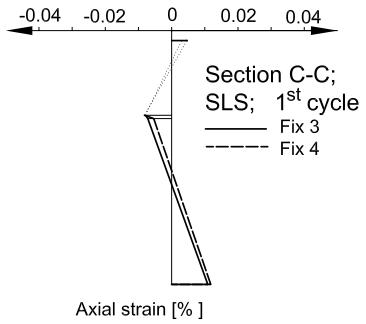

Figure 4.22: Axial strain behavior, axis C-C

The Figures 4.22 and 4.23 show that whether the bridge deck is loaded only in compression or in combination shear/compression makes a big difference to strain distribution. Comparing the same sections under failure load (Section 4.5.1, page 85) makes this even clearer.

Full load transmission could be observed in the adhesively-bonded joint between the top steel flanges and lower deck face panels. The fatigue experiment did not noticeably influence strain distribution in girder Fix 4.

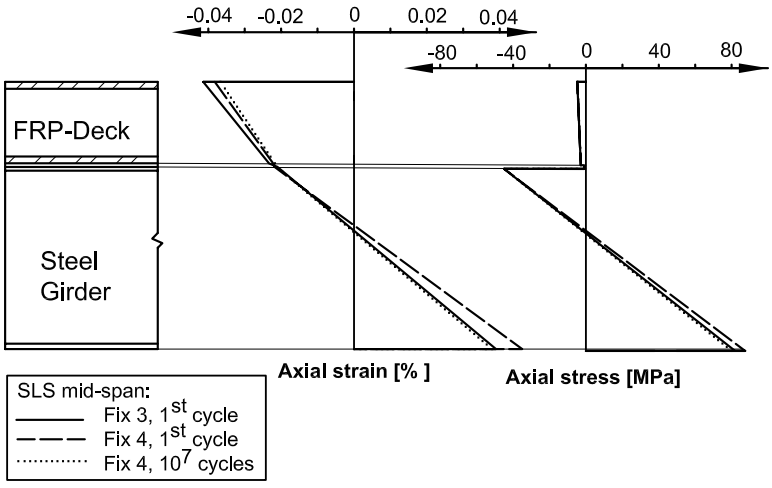

Figure 4.23: Stress and Strain at mid-span under SLS loads (90 kN/jack)

The differential in-plane shifts between the upper and lower deck face panels at the ends of the girders, however, were very small at approximately 0.05 mm (see Fig. 4.39, page 86). Due to the displacement transducers (accuracy ±0.01 mm), the original diagrams were not suitable for assessing the relative displacement of the face panels; therefore only fitted graphs are shown.

Regarding the effective deck width, Fig. 4.24 shows the measured axial strains in the upper and lower deck face panels of girder Fix 3 in the transverse direction at mid-span. Fitted parabolic distribution curves were added. Subjected to SLS loads, the deck was almost evenly loaded and fully participated as part of the top chord. Girder Fix 4 showed similar results (see Appendix D.1.3 page 176). The fatigue experiment did not influence strain distributions. The effect of secondary bending moments in the face sheets, as described in the first paragraph of this section, can also be seen in Appendix D.1.3, page 175 in Figs. D.10-D.16 which represent axes C,E and G.

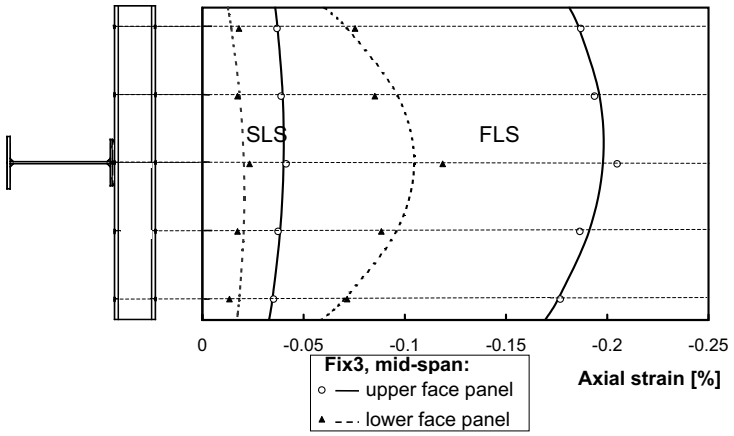

Figure 4.24: Effective width: axial strains and fitted parabolic curves of girder Fix 3 at mid-span.

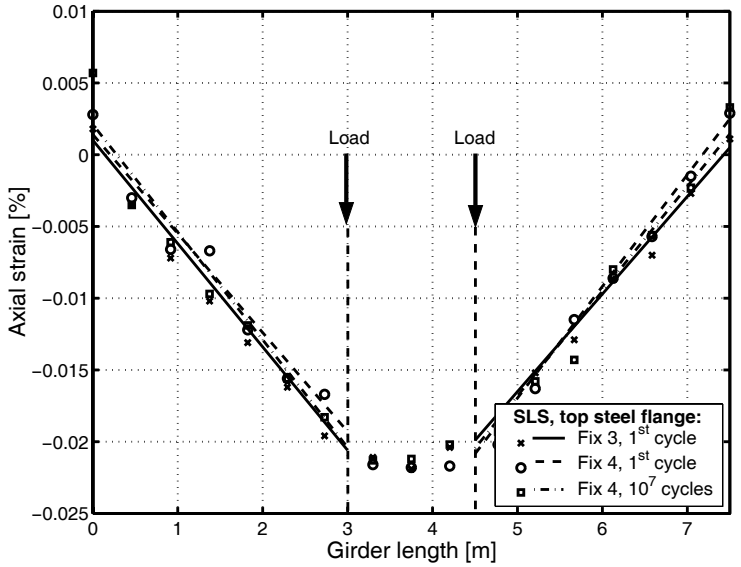

Figure 4.25: Axial strains on top steel flanges at SLS load and fitted straight lines.

Longitudinal axial stress-strain behavior

Figure 4.25 on the previous page illustrates the measured axial strains on the top steel flanges at SLS loads and corresponding fitted straight lines for both girders (correlation factor 0.98). The values closely correspond with the values measured on the lower side of the GFRP deck. The dispersion of the latter is slightly more pronounced (see Appendix D.1, Fig. D.25, page 177). The predicted shear stresses, as shown in Fig. 4.27 on the next page, were determined in accordance with EC 4 part 1 [40], assuming full composite action in the whole girder. For determination of the shear stresses, the composite girder was separated in the adhesively-bonded joint (see Fig. 4.26) and only the sub-system with the steel girder was considered.

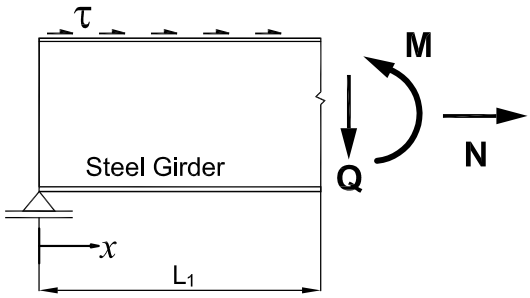

Figure 4.26: Static sub-system for determination of shear stresses

From this the following equation can be derived:

$$\int_0^x \tau_{dx} \stackrel{!}{=} N \tag{4.2}$$

where

$$N = \sum E_a \cdot \epsilon_{a,ex,i} \cdot A_{a,i} \tag{4.3}$$

with: E_a = E-modulus steel
$\epsilon_{a,ex,i}$ = Measured steel strain in the corresponding partial area
$A_{a,i}$ = Partial area of the steel girder

Knowing that the longitudinal shear stresses in the adhesively- bonded joints of the experimental girder must be constant they could easily be calculated. Shear stress distributions in the adhesively-bonded joints are represented in Fig. 4.27 on the next page. In addition, the predicted stress distribution is shown (0.5 MPa constant value between supports and jacks at SLS). The 1st cycle stresses and stresses after the fatigue cycles of the two girders match well.

Due to the secondary bending moments the scattering in the upper face sheet is very pronounced (Fig. 4.28 on the facing page). The fatigue experiment did not influence longitudinal strain distribution in the adhesively-bonded joint.

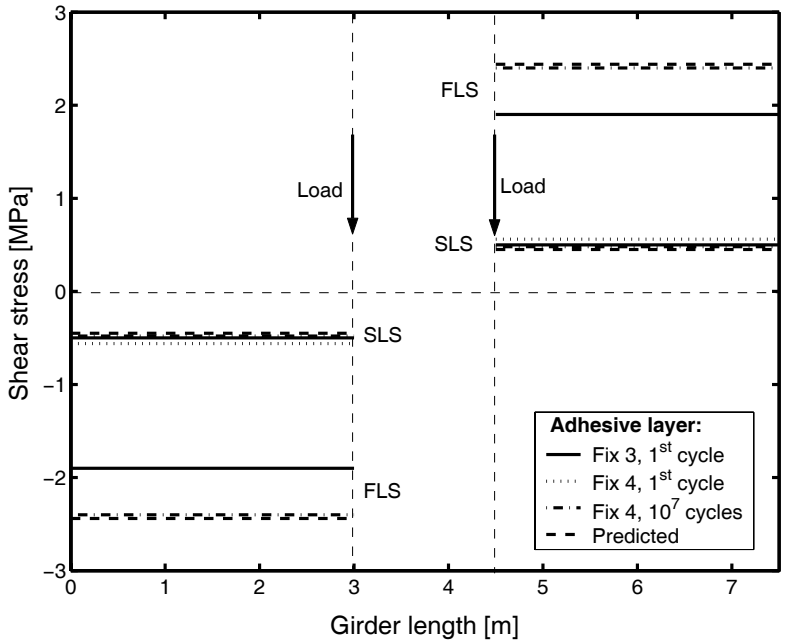

Figure 4.27: Shear stress distributions in the adhesively- bonded joint at SLS and FLS.

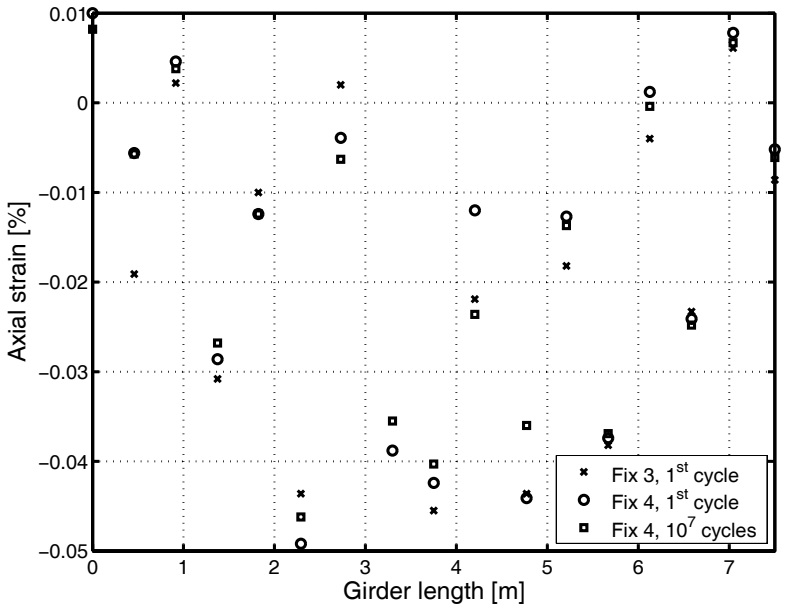

Figure 4.28: Axial strains, upper face panel, SLS

Fatigue behavior

As already mentioned in earlier sections the fatigue experiment did not influence cross-sectional and longitudinal strain behavior. Since the aim was to create a similar stress state in the adhesively-bonded joint of the experimental girder to the stresses in the joint of a 15-m span bridge, investigation of the stresses in the steel girder was not an objective of this experiment. It was not therefore the intention to fail the girder under fatigue loads but to ascertain whether such a girder can bear live loads over a long period of time. The ten million fatigue cycles chosen are a function of the expected service life. They correspond to a bridge with average truck traffic and a service life of 70 years. To clarify, Fig. 4.29 shows only the load deflection behavior of the first and last cycles. The curves match well, what again shows, that fatigue loads do not influence the girder stiffness (same deflection of first and last cycle). All other fatigue diagrams may be found in Appendix D.1.4, page 176. The deflection of all other girders is identical to those shown in Fig. 4.29.

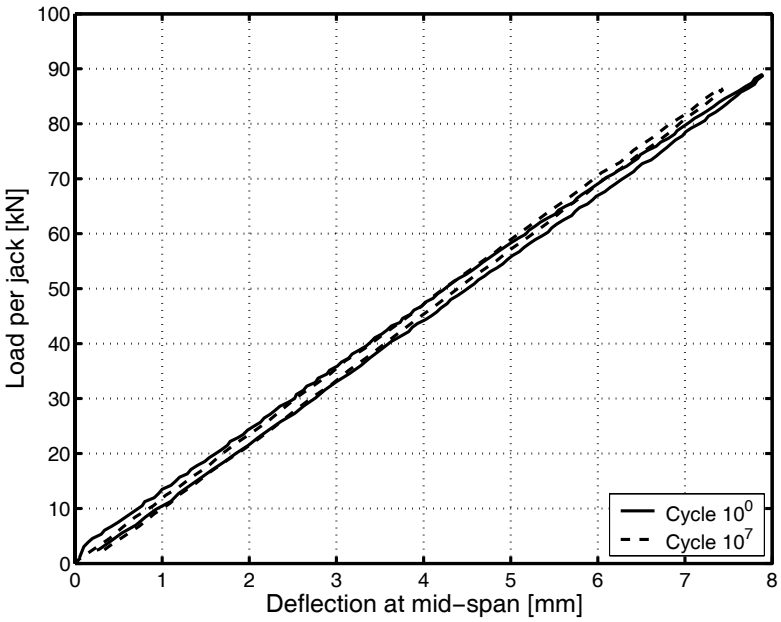

Figure 4.29: Deflection behavior of girder Fix 4 at first cycle and after 10^7 cycles

Girder behavior at ULS

Behavior in all experiments remained linear-elastic up to ULS loads. All measurements (strains and deflections) corresponded to SLS measurements increased linearly by the load factor ($\gamma = 1.35$). As subsequent failure experiments showed, the decks behaved linear-elastically up to failure.

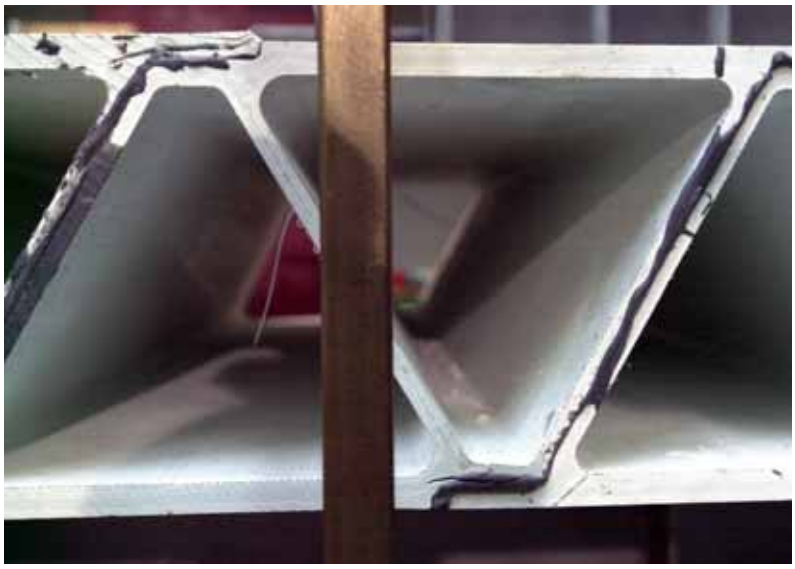

Figure 4.30: First and second failures in the upper and lower deck panels near axis H-H, girder Fix 4.

Girder behavior at FLS

Deflection, stiffness and failure behavior

The failure experiments were carried out for girder Fix 3 at the 3rd cycle and for girder Fix 4 after ten million fatigue cycles. Table 4.4 on the next page shows the main results, failure loads and maximum deflections at failure. Girder behavior corresponded with the experiments at SLS (1st cycle, Fix 3 and Fix 4) and ULS (2nd cycle, Fix 3) in these load ranges. Exceeding the ULS load, both girders showed almost identical linear-elastic behavior up to approximately 90% of failure loads (see Fig. 4.32 on the following page). Subsequently, girder stiffness began to decrease slightly due to yielding of the bottom steel flanges (see Fig. 4.33, page 83). After the first audible cracks in the decks at approximately 95% of failure loads, the girders were unloaded in order to study the unloading and reloading paths and residual plastic deformations. The different paths were almost identical and parallel to the initial elastic loading paths (see Fig. 4.32 on the following page). Residual plastic deformations were very small at approximately 3 mm for both girders. After reloading, a first failure occurred abruptly in both

Figure 4.31: First failure of girder Fix 4 in a stepped joint of the upper face panel.

	Failure load [kN/jack]		Deflection at mid-span [mm]	
Girder	3^{rd} cycle	After 10^7 cycles	3^{rd} cycle	After 10^7 cycles
Fix 3	373	-	39	-
Fix 4	-	400	-	41
Reference steel	263	-	75	-

Table 4.4: Experimental results at Failure State

girders. A crack occurred in the short flange of a stepped truss joint of the upper face panel, close to one of the load patches (axis G-G Fix 3 and axis H-H Fix4), as can be seen in Fig. 4.31 on the previous page. The epoxy joint in the bridge deck (between the profiles) at this location remained undamaged. This failure mode matched that of the in-plane compression experiments on the small-size specimens. The failure of the upper face panel in both girders was a combination of the compression force resulting from global bending behavior and a local failure at load- introduction points (see Fig. 4.31 on the preceding page). The local failure in girder Fix 4 started at ∼365kN. This shows the difference of displacement transducers D3 - D4 (configuration see Appendix F, page 199) in Fig. 4.34, page 84 for girder Fix 4, where a considerable decrease in deck depth was observed. Girder Fix 3 demonstrated similar behavior (see Appendix D.1.2, page 174).

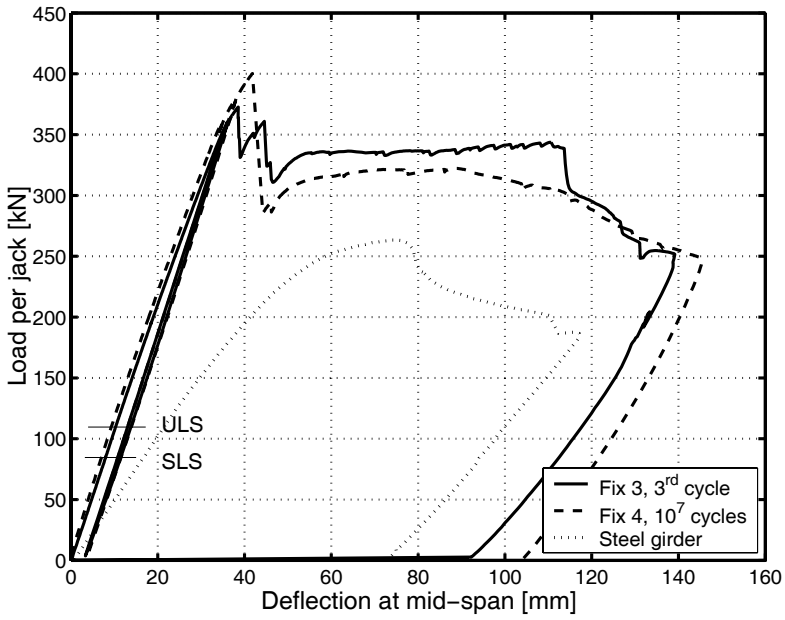

Figure 4.32: Load-deflection behavior of girders at mid-span

The ultimate failure load was 373 kN for girder Fix 3 and 400 kN for Fix 4. Directly after failure in the upper face panel, a second failure occurred in the same deck section in the lower face panel (see Fig. 4.30 on the previous page) due to a force redistribution into the lower face panel. Again, the short

flange of the stepped joint of the bridge deck failed, not the adhesively-bonded joint. Subsequently, the lower panel detached from the top steel flange at this point and the flange started to deform plastically (buckling), as can be seen in Fig. 4.35 on the following page. Fig. 4.36, page 85 shows, that the separation of lower deck panel and top steel flange took place in the adhesively bonded joint without damaging the first layer of the deck. During first and second failures, the load dropped to a lower level due to the displacement-control. Subsequently, the girder could be deformed further at an almost constant load up to approximately 115-mm deflection for Fix 3 and 100-mm for Fix 4. At this deflection, a third deck-joint failure developed near the opposite jack in girder Fix 3 (axis K-K). The load dropped down again and then decreased continuously. Both girders exhibited the same behavior after failure, but with Fix 4 the load decreased more evenly as there was no third deck failure. The experiments were stopped at approximately 140 mm of deflection, which corresponded to a ratio of span/54. The unloading path was parallel to that of the reference steel girder, as can be seen in Fig. 4.32 on the facing page. A large plastic deformation remained after unloading at 93 mm for girder Fix 3 and 105 mm for Fix 4. Detailed failure pictures of the leading axis of the ASSET girders can be seen in Appendix E.2, page 185.

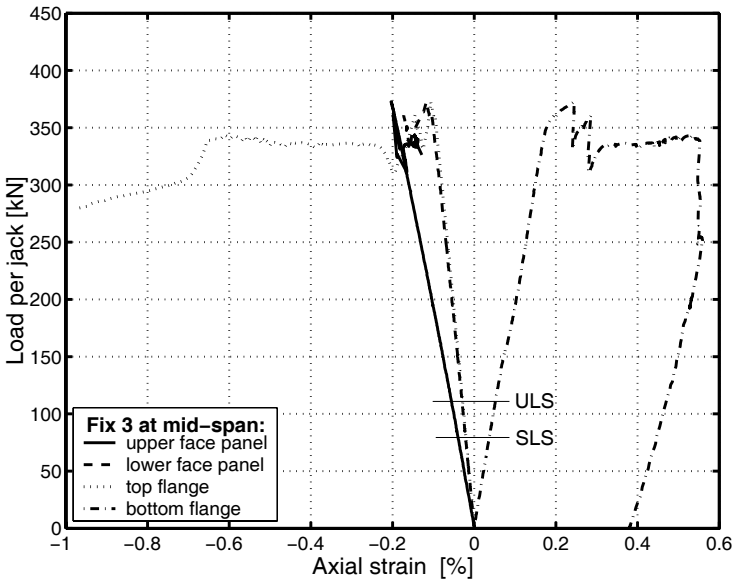

Figure 4.33: Load-strain behavior of girder Fix 3 at mid-span (yielding strain of steel: $\epsilon_y = \pm 0.18\%$)

Figure 4.32 on the facing page also shows the behavior of the reference steel girder. The top flange began to yield at approximately 185 kN per jack. At approximately 250 kN per jack, the yielding top flange began to buckle at one point between the jacks, very similar to Fig. 4.35 on the next page. The load then decreased after reaching a maximum of 263 kN per jack and 75 mm of vertical deflection. The experiment was stopped at 117 mm of deflection at mid-span. Figures of the failure behavior of the steel girder can be seen in Appendix E.1, page 183.

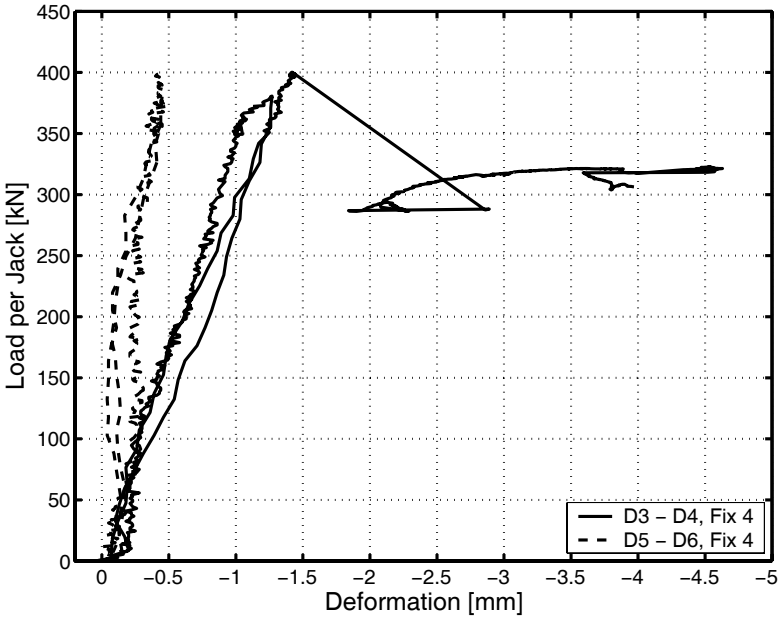

Figure 4.34: Variation of deck depth in the load axes

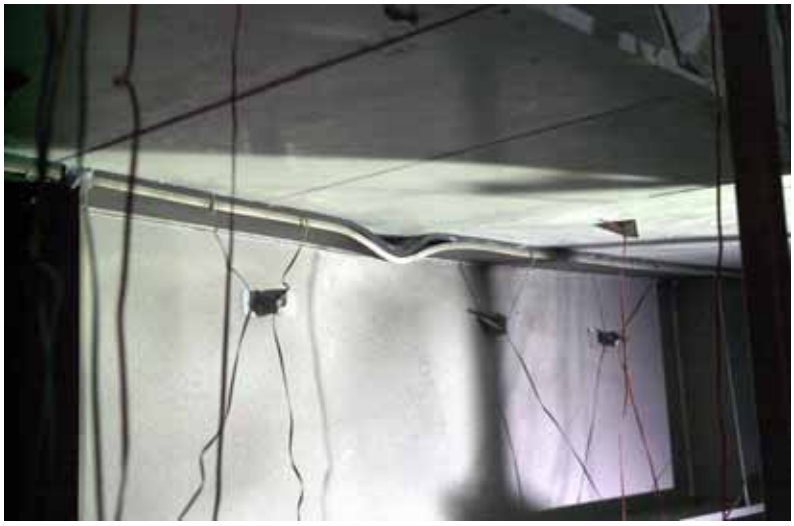

Figure 4.35: Local detachment of deck at mid-span and buckling of top steel flange, girder Fix 4.

Figure 4.36: Detail adhesive bond after failure, back view axis J - J (The failed adhesive was taken away for the photo)

Cross-sectional axial stress-strain behavior

The measured axial strain distributions and the resulting calculated stresses in the cross-sections at mid-span for girder Fix 3 at the 3rd cycle and for Fix 4 after ten million cycles at the onset of failure are shown in Fig. 4.38 on the next page. The measured strains of both girders matched in the deck and adhesively-bonded joint. The strains in the bottom steel flange of girder Fix 4 were slightly higher than in Fix 3. As already described in Section 4.5.1, page 76, the cross-section's behavior changes between the jacks and at locations where shear forces are constant. Compared to the SLS, the strains increased linearly (see Fig. 4.37). Differential in-plane shifts between the upper and lower deck face panels remained small at approximately 0.3 mm at FLS loads (see. Fig. 4.39 on the following page). Again, full load transmission could be observed in the adhesively- bonded joints between the top steel flanges and lower deck face panels (no relative displacement between steel girder and bridge deck could be measured; configuration of displacement transducers see Appendix F.1 Fig. F.1, page 199). The linear-elastic development of the strains at mid-span during the FLS experiments is also illustrated in Fig. 4.33, page 83 for girder Fix 3. The bottom flange began to yield shortly before failure while the top flange had not yet attained the yielding strain (0.18%). After deck failure, however, the top flange also began to yield.

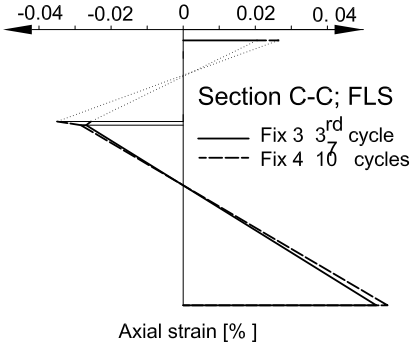

Figure 4.37: Axial strain behavior, axis C-C at FLS

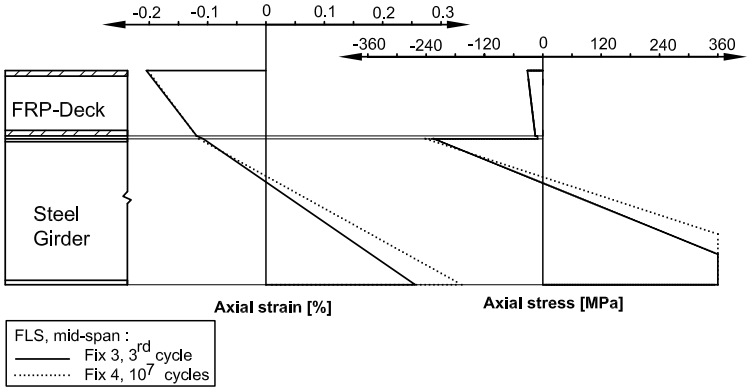

Figure 4.38: Axial stress and strain distribution in the mid-span cross-section at FLS

With regard to effective deck width, axial strain distributions in the transverse deck direction changed in relation to SLS results (see Fig. 4.24, page 77). A decrease in axial strain towards the edge areas of the face panel was observed. The decrease was more pronounced in the lower than in the upper panel. Girder Fix 4 showed similar results after the fatigue experiment.

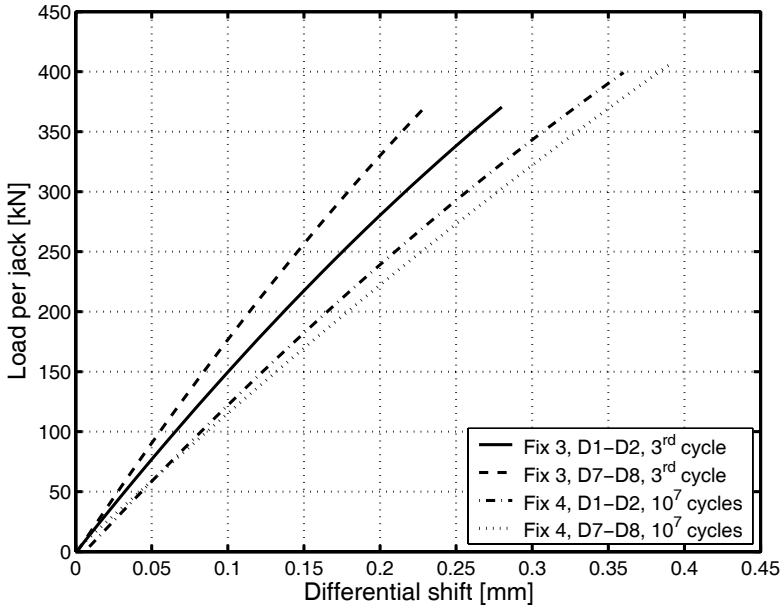

Figure 4.39: Differential shifts between deck face panels.

Longitudinal axial stress-strain behavior

Since the sectional strains increased linear-elastically up to failure (see Fig. 4.33, page 83) and the top flanges did not yield, the axial strains along the top steel flanges, shown in Fig. 4.40 on the next page, increased proportionally to the corresponding SLS strains in Fig. 4.25, page 77. The strains in the upper face panel however did not increase linearly to SLS as could be expected.

Fig. 4.41 shows that the influence of the secondary bending moments is not negligible. Although there is still scattering between each cross-sectional axis, a certain linearity is recognizable. The calculated longitudinal shear stresses at FLS were 1.9 MPa for girder Fix 3 and 2.4 MPa for Fix 4, as shown in Fig. 4.27, page 79. In addition, the predicted stress distribution is shown (2.4 MPa constant value between supports and jacks, assuming full composite action). Again, the longitudinal shear stresses were low and the fatigue experiment did not influence them noticeably.

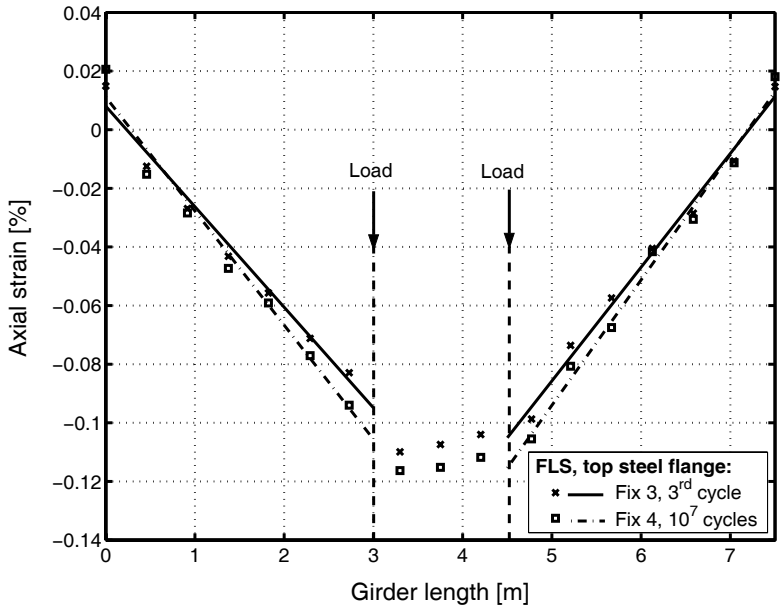

Figure 4.40: Axial strains on top steel flanges at FLS and fitted straight lines.

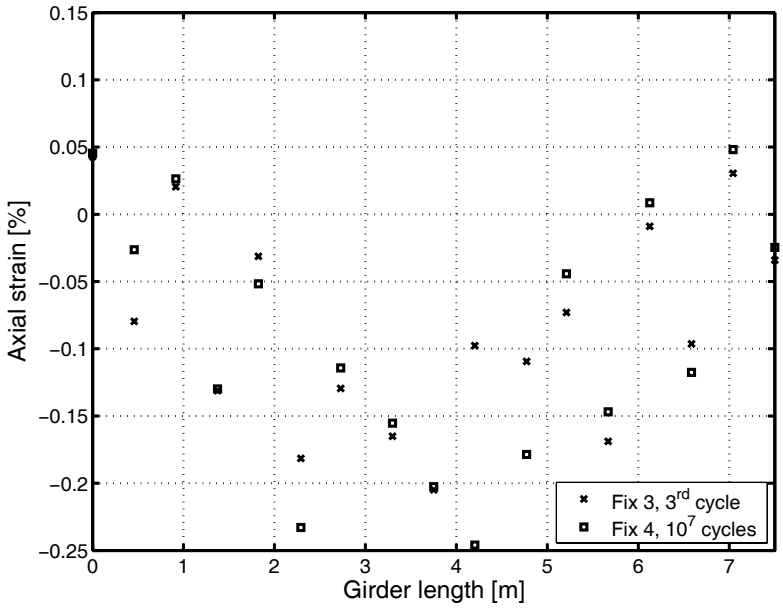

Figure 4.41: Axial strains, upper face sheet

4.5.2 DuraSpan girders

Behavior of girders at SLS

Deflection and stiffness behavior

The main results of the SLS experiments are summarized in Table 4.5. Indicated are the measured maximum deflections at mid-span and the calculated bending stiffnesses, EI_m, for girder Fix 1, resulting from the initial SLS experiment (1^{st} cycle). The same values are listed for girder Fix 2, resulting from the initial SLS experiment (1^{st} cycle) and the FLS experiment after 10^7 fatigue cycles at SLS load level. The stiffnesses, EI_m, of the hybrid girders were calculated as explained in Section 4.5.1, page 74. The behavior of the girders remained linear-elastic during all SLS experiments and was almost identical, as shown in Fig. 4.50, page 93. Compared to the reference steel girder, deflections of girder Fix 1 were 31% lower while those of girder Fix 2 were 29% lower (1^{st} cycles). During the fatigue experiment, the stiffness, EI_m, of girder Fix 2, calculated from the SLS experiments performed after each million cycles, remained constant up to ten million cycles; the deflections did not increase (see Fig. 4.42 on the facing page).

	Maximum mid-span deflection $[mm]$		Bending stiffness EI_m $[kN \cdot m^2]$	
Girder	1^{st} cycle	After 10^7 cycles	1^{st} cycle	After 10^7 cycles
Fix 1	10.3	-	128,800	-
Fix 2	10.7	10.2	122,900	130,300
Reference steel	13.8	-	90,500	–

Table 4.5: Maximum deflections and stiffnesses at mid-span under SLS loading

Cross-sectional axial stress-strain behavior

The measured axial strain distribution and calculated stress distribution in the cross-sections at mid-span for the two girders at SLS loads, for the 1^{st} cycle and after ten million cycles for girder Fix 2, are shown in Fig. 4.44 on the next page. The measured axial strain distributions of both girders were almost identical (see also Appendix D.2, page 178) but did not remain linear throughout the depth of the cross-section. Strains in the upper deck face panels decreased to values approximately 10% below those in the lower deck face panels. Accordingly, differential in-plane shifts between upper and lower deck face panels of 0.84-0.88

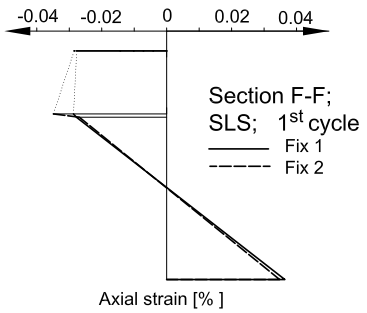

Figure 4.43: Axial strain behavior, axis F-F at SLS

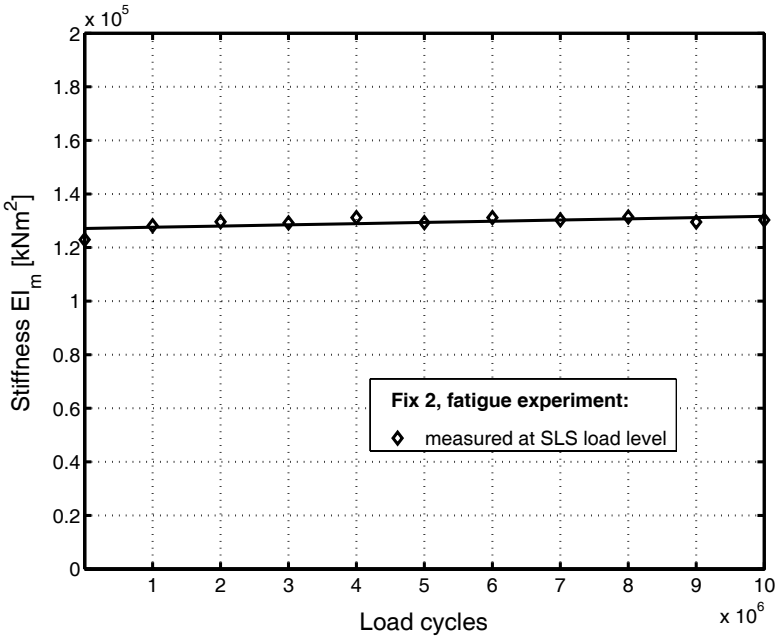

Figure 4.42: Girder stiffness after each million fatigue cycles

mm could be measured at girder ends as shown in Fig. 4.54, page 96. Therefore, only partial composite action in the deck itself could be observed. In the areas outside of the jacks, where constant shear forces exist, the strain distribution in the deck is different (see Fig. 4.43 on the preceding page). This is due to the secondary bending moments in the deck itself. Since there were strain gages only at the outer sides of the face panels, the proportion of the normal forces in the deck could not be determined. The strain distribution over the full section height can only be shown for axes F-F, J-J and M-M but these sections do not illustrate the maximum and minimum strains in the upper face sheet. The strains over the whole girder length in the upper face sheets are shown in Fig. 4.47, page 91.

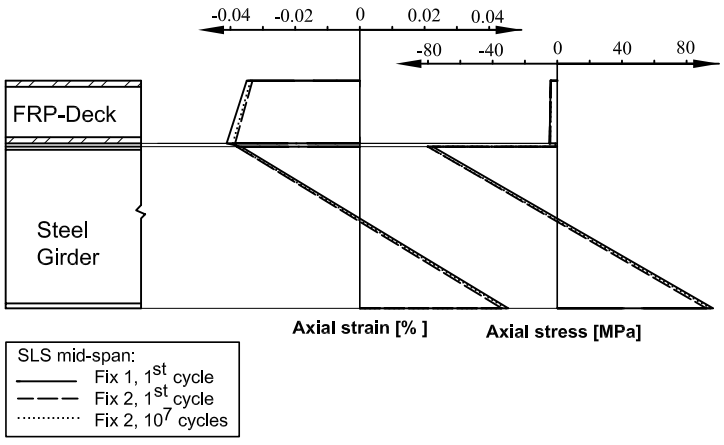

Figure 4.44: Stresses and strains at mid-span under SLS loads (80 kN/jack)

As for the ASSET girders, full load transmission could be observed in the adhesively-bonded joints between the top steel flanges and lower deck face panels. Regarding the effective deck width, Fig. 4.45 shows the axial strains measured in the upper and lower deck face panels of girder Fix 1 in the transverse direction at mid-span. Fitted parabolic distribution curves were added. Subjected to SLS loads, the deck was almost evenly loaded and fully participated as part of the top chord. Girder Fix 2 showed similar results. The fatigue experiment did not noticeably influence strain distribution in girder Fix 2.

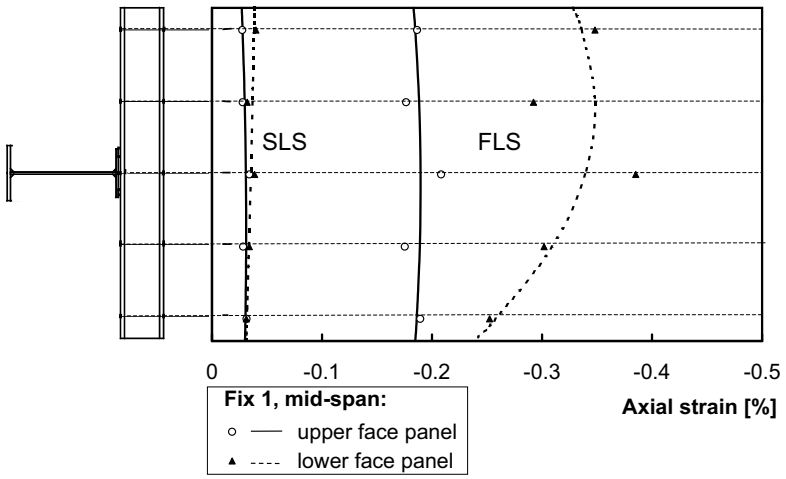

Figure 4.45: Effective width: axial strains and fitted parabolic curves of girder Fix 1 at mid-span.

Longitudinal axial stress-strain behavior

Figure 4.46 on the facing page illustrates the axial strains measured on the top steel flanges at SLS loads and corresponding fitted straight lines for both girders. The values match well values measured on the lower side of the GFRP deck; the dispersion of the latter is slightly more pronounced (see Fig. D.46, page 182). Due to secondary bending moments, scattering in the upper face panel is very pronounced (Fig. 4.47 on the facing page) and, in contrast to the lower face panel, no linear strain distribution, could be observed. The 1st cycle strains of the two girders and strains after the fatigue cycles match well. The predicted and measured stresses in the adhesively-bonded joint match well for the SLS. The stresses were determined as described in Section 4.5.1, page 78, and can be seen in Fig. 4.48. The fatigue experiment did not influence longitudinal strain distribution in the adhesive bond.

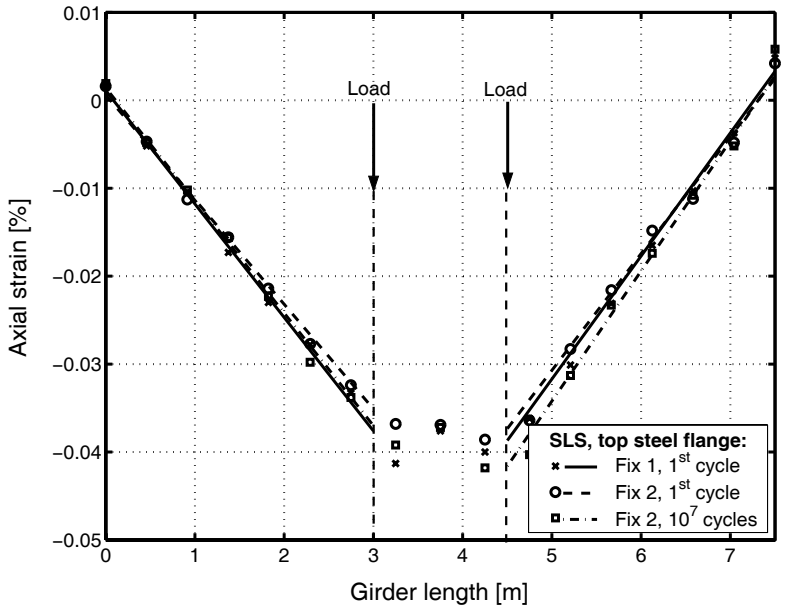

Figure 4.46: Axial strains on top steel flanges at SLS load and fitted straight lines.

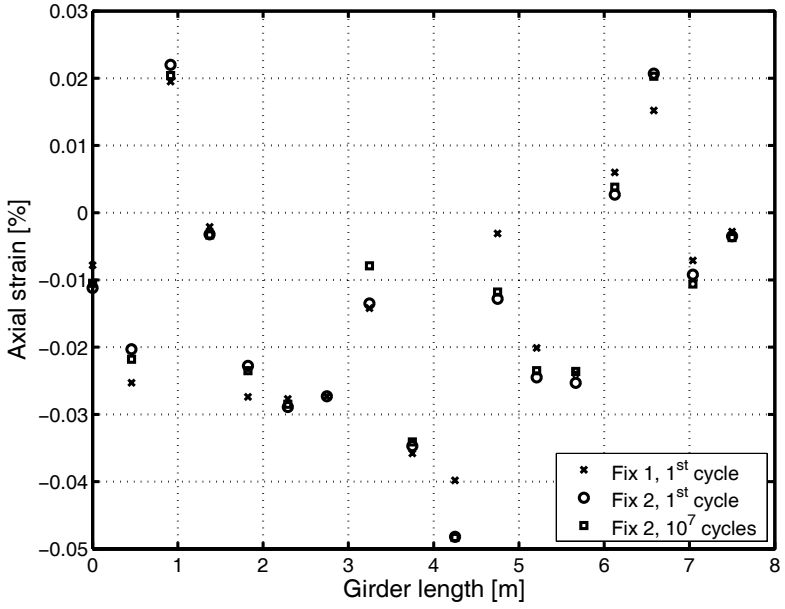

Figure 4.47: Axial strains, upper face sheet

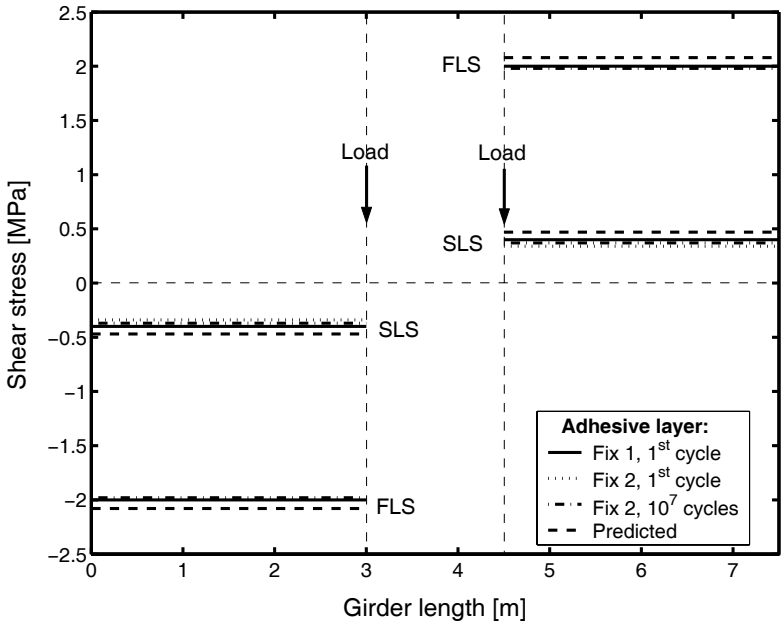

Figure 4.48: Shear-stress distributions in the adhesively- bonded joint at SLS and FLS.

Creep behavior

During the four-hour creep period at full SLS loads, the maximum deflection of girder Fix 1 increased less than 0.5 mm and returned to the initial state fifteen minutes after unloading (see Fig. 4.49). The duration of four hours appears relatively short, but experiments conducted at the CCLab[6] showed that under SLS loads, the major part of creep deformations occur in the first hour after load application [67]. The four-hour period thus seems sufficient. Nevertheless additional creep experiments over a longer period of time are necessary in order to affirm the results of the experiments in this study.

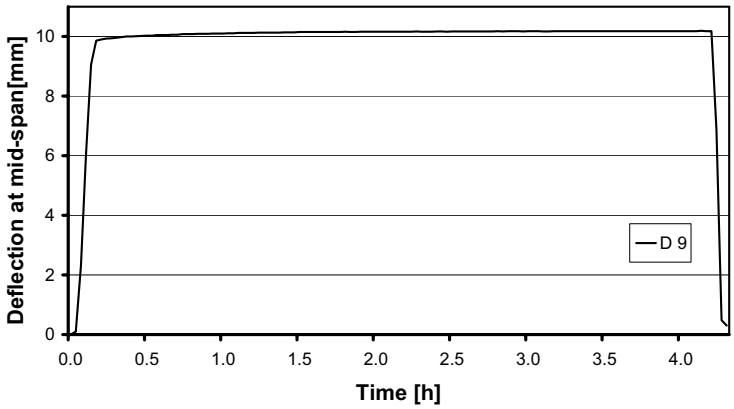

Figure 4.49: Deflection behavior under creep-loading (2x80kN)

[6]Composite Construction Laboratory

Fatigue behavior

As already mentioned in previous sections, the fatigue experiment did not influence cross-sectional and longitudinal strain behavior. The objective of the fatigue experiment was explained in Section 4.5.1, page 80. To clarify, Fig. 4.50 shows load deflection behavior of only the first and the last cycles. All other fatigue diagrams can be found in Appendix D.2.4, page 180. The deflections of the girder for cycles 10^6 - 10^7 are identical. The deflection of the first cycle was slightly higher (5%). It may be said that up to 55kN loading paths are absolutely parallel, but the graph of the first cycle experiment subsequently shows a small break. Although the difference is not very great, it should be mentioned because the graphs of all subsequent fatigue experiments are congruent.

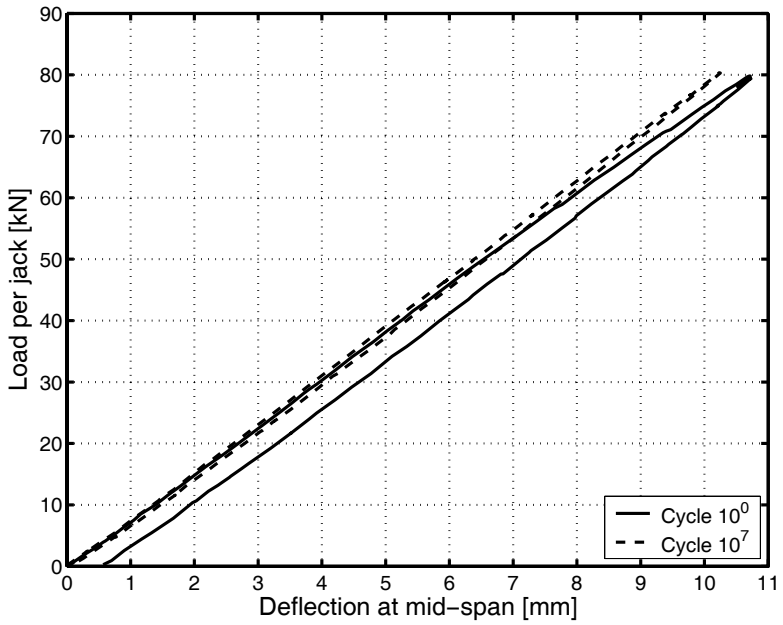

Figure 4.50: Deflection behavior of girder Fix 2 at first cycle and after 10^7 cycles

Behavior of girders at ULS

Behavior in all experiments remained linear-elastic up to ULS loads. All measurements (strains and deflections) which corresponded to SLS measurements increased linearly by the load factor ($\gamma = 1.35$). Therefore, the same remarks apply as for SLS behavior.

Behavior of girders at FLS

Deflection, stiffness and failure behavior

The failure experiments were carried out for girder Fix 1 at the 3rd cycle and girder Fix 2 after ten million fatigue cycles. Table 4.6 on the facing page shows the main results. The behavior of the girders in the elastic range matched the experiments at SLS (1st cycle, Fix 1 and 2) and ULS (2nd cycle, Fix 1). Subsequently, both girders showed almost identical and very ductile behavior (see Fig. 4.53 on the next page). The limit of elastic behavior of the girders was noticed during the FLS experiments at 130 kN per jack for girder Fix 1 and at 140 kN per jack for Fix 2 (see Fig. 4.53 on the facing page), since there was a small visible break in both graphs. Exceeding the elastic limits of the deck, first local delamination failures occurred due to Vierendeel action (similar to system experiments in Chapter 3, page 29). The differential in-plane shifts between the deck face panels at girder ends increased in parallel to Figure 4.53 on the facing page (see Fig. 4.54, page 96). At a load of 280 kN per jack, the bottom steel flange of girder Fix 1 began to yield, at 305 kN per jack the top steel flange yielded too as shown in Fig. 4.59, page 99. The corresponding loads for Fix 2 were 230 kN and 320 kN respectively. Vertical

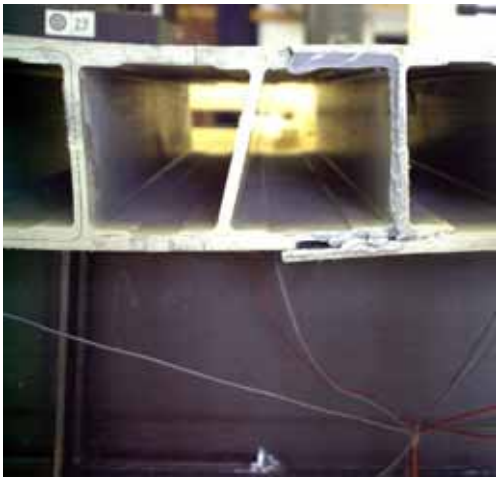

Figure 4.52: Initial failure of girder Fix 2 in epoxy joint of lower deck face panel between jacks.

Figure 4.51: Deflection of girder Fix 2 at onset of failure, undulated deformation of upper face panel due to Vierendeel action.

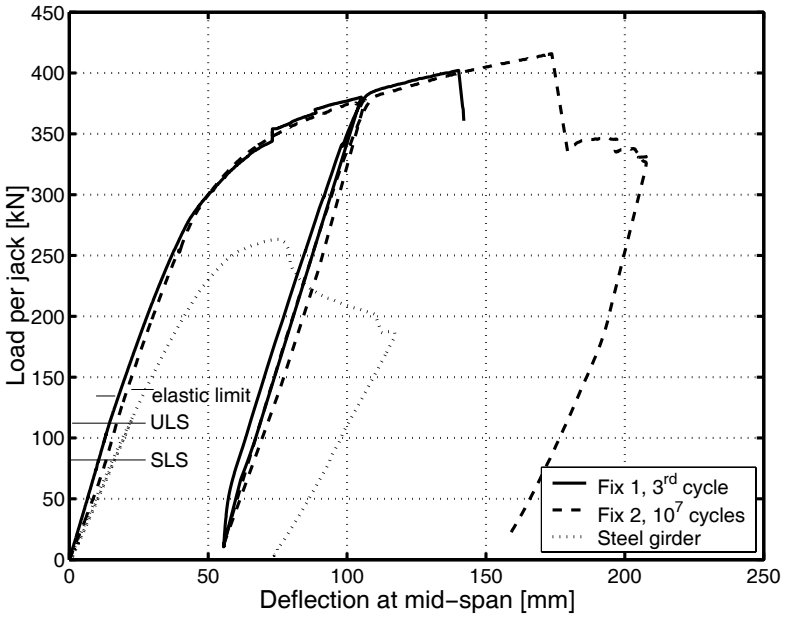

Figure 4.53: Load-deflection behavior of girders at mid-span

deflections, local delamination failures and differential in-plane shifts between face panels then increased non-linearly. Horizontal cracks formed in the upper part of the vertical webs, on the outside at the girder ends due to Vierendeel action. In addition, an undulated deformation, again due to Vierendeel action, could be observed in the upper deck face panels (see Fig. 4.51 on the preceding page). At a load of approximately 380 kN per jack, both girders were unloaded in order to study the unloading and reloading paths and residual plastic deformations. The unloading and reloading paths were almost identical and parallel to the initial elastic loading paths (see Fig. 4.53). Residual plastic deformations were approximately 55 mm for both girders. At a load of 405 kN per jack for girder Fix 1 and 415 kN per jack for Fix 2, one of the transverse epoxy joints (Fix 1 axis H-H see Appendix E.3.1 Fig. E.23, page 193; Fix 2 axis G-G see Fig. 4.52 on the facing page) in the lower deck face panels between the jacks failed in combination shear/compression in each girder. Vertical mid-span deflections at onset of failure were 140 mm for Fix 1 and 172 mm for Fix 2 (see Figs. 4.53 and 4.51 on page 94).

	Failure load $[kNjack]$		Deflection at mid-span $[mm]$	
Girder	3^{rd} cycle	After 10^7 cycles	3^{rd} cycle	After 10^7 cycles
Fix 1	405	-	140	-
Fix 2	-	415	-	172
Reference steel	263	-	75	-

Table 4.6: Experimental results at Failure State

The maximum differential in-plane shifts between the upper and lower face panel were 12.5 mm for Fix 1 and 13.5 mm for Fix 2 (see Fig. 4.54). Recapitulating, the fatigue experiment had no effect on failure load or failure behavior.

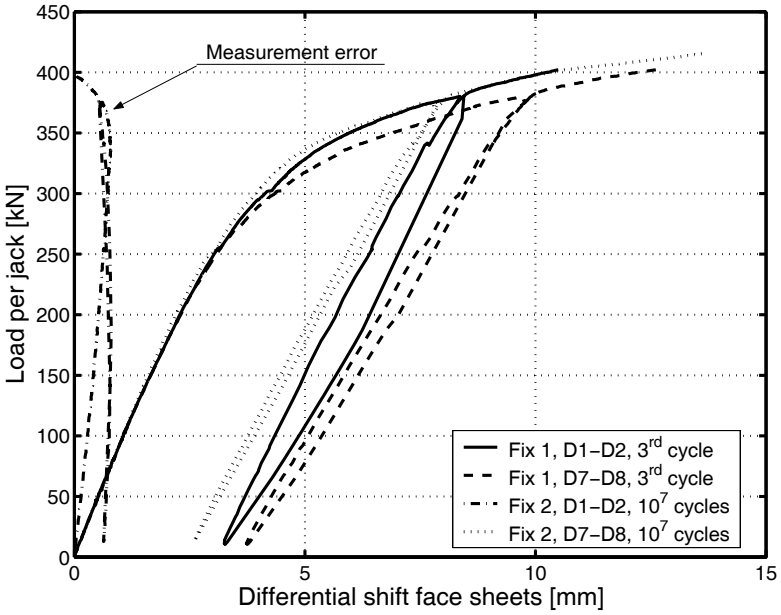

Figure 4.54: Differential shifts between deck face panels.

As the experiments were conducted displacement-controlled, the loads decreased immediately after these failures. The Fix 1 experiment was stopped at this point, while the Fix 2 experiment was continued displacement-controlled. The load of Fix 2 decreased to 340 kN per jack (see Fig. 4.53 on page 95). With increasing vertical deflection, the adhesive connection between the deck and upper steel flange began to open in the area between the jacks (see Fig. 4.55 on the facing page). Thereby, failure occurred in the outer layer of the FRP deck, not in the adhesive as it was the case for the ASSET girders. The top steel flange, which was no longer fixed, showed considerable plastic out-of-plane deformations (buckling), similar to those of the reference girder. Subsequently, two supplementary hinges formed in the deck due to further failures in the transverse joints and resulted in the upward buckling of the deck (see Fig. 4.56 on the next page, residual deformation after unloading). The additional joint failures occurred at jack locations in an epoxy joint on one side and a polyurethane joint on the other. The experiment was stopped at 207 mm of vertical deflection, corresponding to 1/36 of the span.

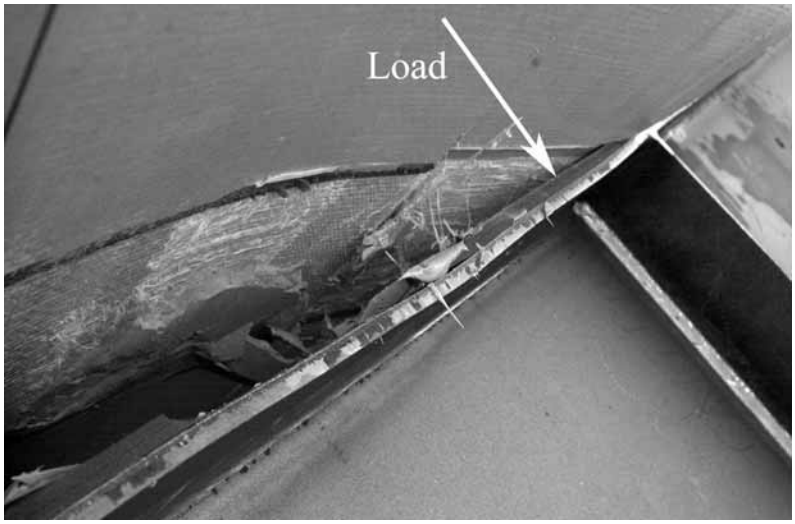

Figure 4.55: Detachment of the deck between jacks after initial failure. Large plastic deformation of the top steel flange, girder Fix 2.

Figure 4.56: Secondary failure of girder Fix 2: buckling of the deck between jacks (residual deformation after demounting).

Cross-sectional axial stress-strain behavior

The measured axial strain distributions and calculated axial stresses in the cross-sections at mid-span for girder Fix 1 at the 3rd cycle and Fix 2 after 10^7cycles at onset of initial failure are shown in Fig. 4.58. The strains in section F-F increased linearly to the SLS (see Fig. 4.43, page 88 and Fig. 4.57). The measured strain distributions of both girders were almost identical but, again, did not remain linear through the depth of the cross-section. The loss in the upper face panels increased to values 30-40 % below values measured in the lower deck face panels. The divergence started to increase non-linearly with the yielding of the steel flanges (see Fig. 4.59 on the next page). The load was fully transmitted through the adhesively-bonded joint, which signifies full composite action (no relative displacement between steel girder and bridge deck could be measured; configuration of displacement transducers see Appendix F.2 Fig. F.20, page 203). Only partial composite action was achieved in the decks themselves. No influence of the fatigue loading on strain distributions could be observed. As previously mentioned, the steel girders yielded completely, the upper part in compression, the lower part in tension (see. Fig. 4.59 on the next page).

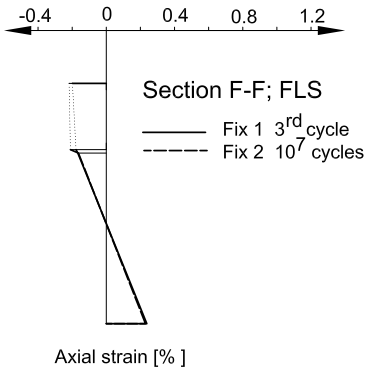

Figure 4.57: Axial strain behavior, axis F-F at FLS

Regarding the effective deck width, the axial strain distributions in the transverse deck direction changed in comparison with SLS results (see. Fig. 4.45, page 90, results for Fix 1). A decrease was observed in the edge areas of the lower face panel. The lesser loaded upper face panel, however, continued to fully participate. Girder Fix 2 showed similar results after the fatigue experiment. At FLS, the measured results showed considerable dispersion. This may be due to the simultaneous occurrence of the previously mentioned Vierendeel action in the face panels. Evaluation of displacement transducers D3 - D6 showed no indications of a local failure of the deck near the load patches.

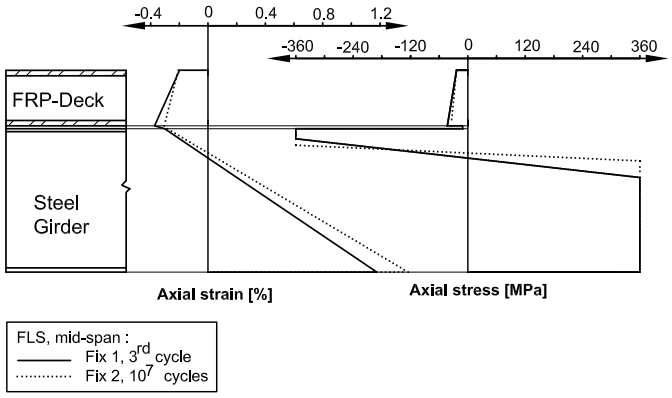

Figure 4.58: Stresses and strains at mid-span under FLS loads (∼400 kN/jack)

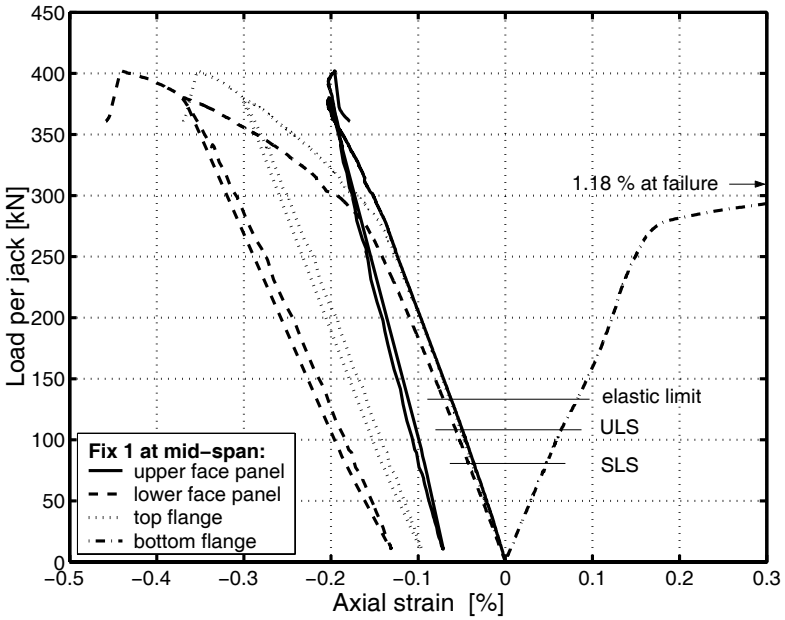

Figure 4.59: Axial strains axis J - J, girder Fix 1. (Yielding strain steel: $\epsilon_y = \pm 0.18\%$)

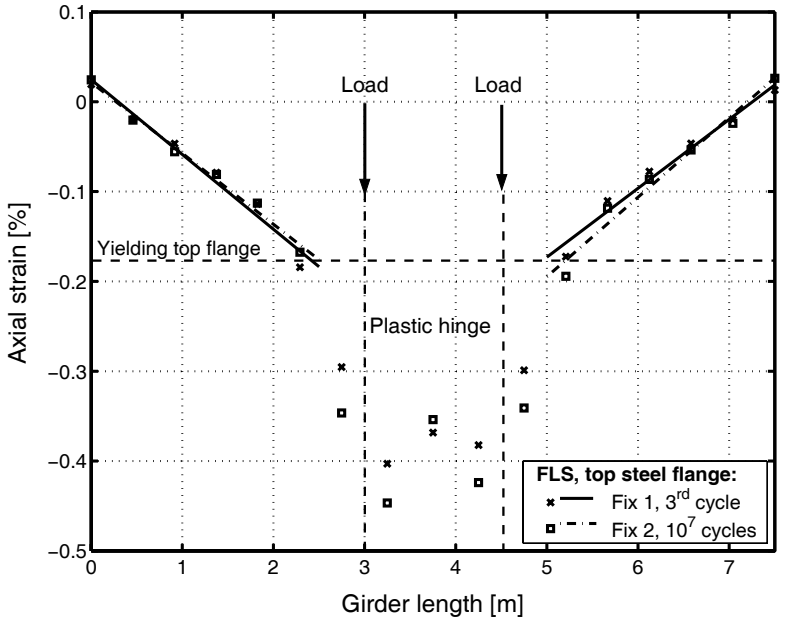

Figure 4.60: Axial strains on top steel flanges at FLS and fitted straight lines.

Longitudinal axial stress-strain behavior

In the still elastic girder parts between the supports and jacks, the axial strains, measured on the top steel flanges, increased linearly and proportionally to the corresponding SLS strains in Fig. 4.46, page 91. In the part of the girders between the jacks where the steel girders yielded, however, strains increased non-linearly with the formation of large plastic hinges (see Fig. 4.51, page 94 and 4.60 on the preceding page). The shear stresses at FLS, calculated in the linear-elastic parts, were on the order of 2.0 MPa and matched the predicted value almost (see Fig. 4.48, page 92).

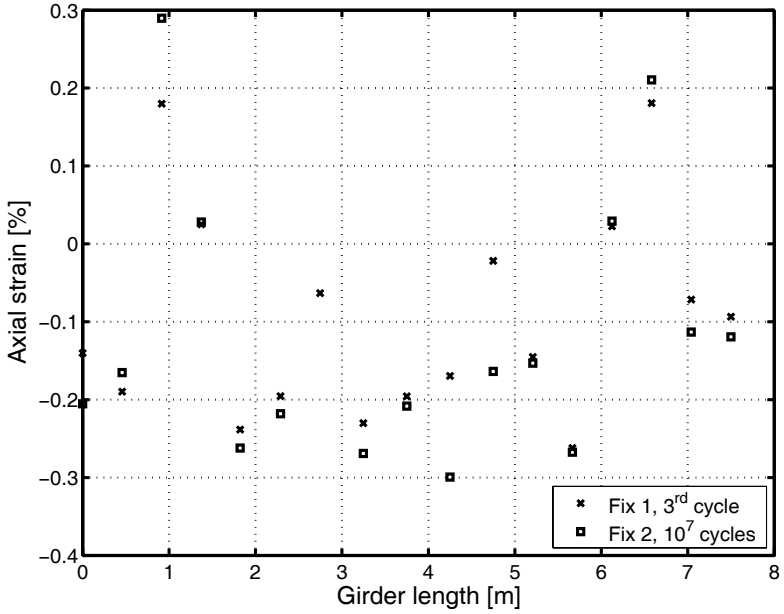

Figure 4.61: Axial strains, upper face sheet

4.5.3 Summary of the results of the girder experiments

Composite action

Prediction of the composite girders' behavior assumed full composite action between all components of the cross-sections for both deck systems. As the experiments showed, the adhesively-bonded joints between bridge decks and steel girders were sufficiently stiff and resistant to guarantee full composite action between the top steel flanges and lower deck face panels at all load levels up to failure. Participation of the upper deck face panels, however, was slightly reduced in the ASSET girders and considerably reduced in the DuraSpan girders. Consistent with the much higher in-plane shear stiffness of the ASSET deck, the upper face panel showed a much less pronounced decrease in participation than the DuraSpan deck, as seen in Fig. 4.62. The same conclusions can be drawn from comparison of the differential shifts between the upper and lower deck face panels at girder ends. The ASSET deck showed a maximum differential shift of only 0.3 mm at failure. The corresponding DuraSpan deck values were approximately 50 times higher, as shown in Fig. 4.63 on the next page. Fig. 4.63 on the following page also illustrates the very high ductility of the Vierendeel mechanism in the DuraSpan deck compared to the fairly brittle truss mechanism in the ASSET deck.

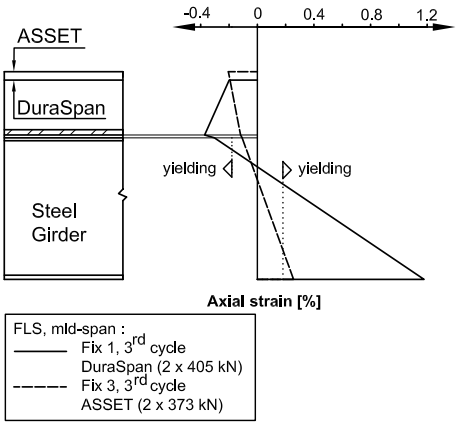

Figure 4.62: Comparison of axial strain distributions in the mid-span cross-section at FLS.

Compared to the reference steel girder values, deflections at SLS of the ASSET girders decreased by approximately 50% (average value), while failure loads increased by approximately 46% (average value) due to composite action. The DuraSpan girders were slightly more deformable (only 23% decrease) but more resistant (56% increase). Fig. 4.64 on the next page shows the difference in deflection of the three tested systems. The pure steel girder with considerable deflections, the DuraSpan girder with lower deflection and the ASSET girder with the lowest deflection due to composite action and the high in-plane shear stiffness of the bridge deck.

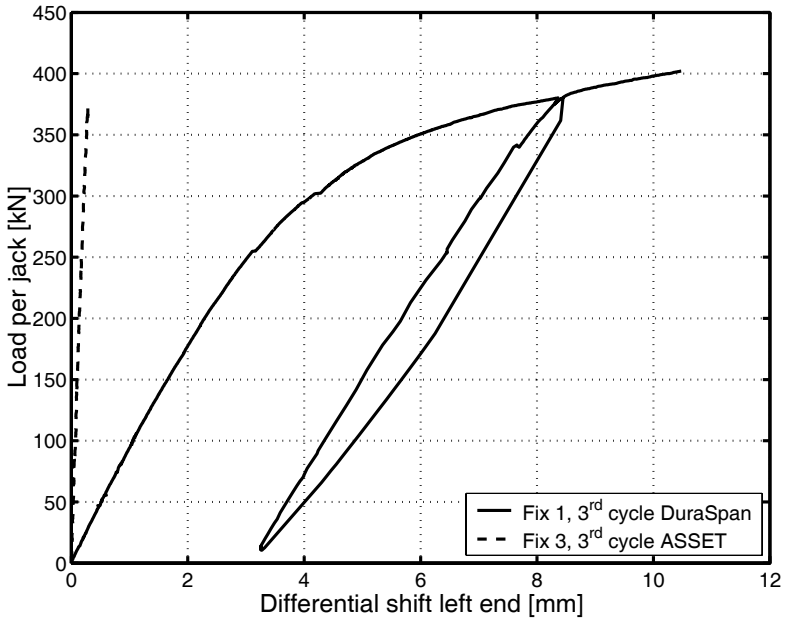

Figure 4.63: Comparison of differential shifts between deck face panels.

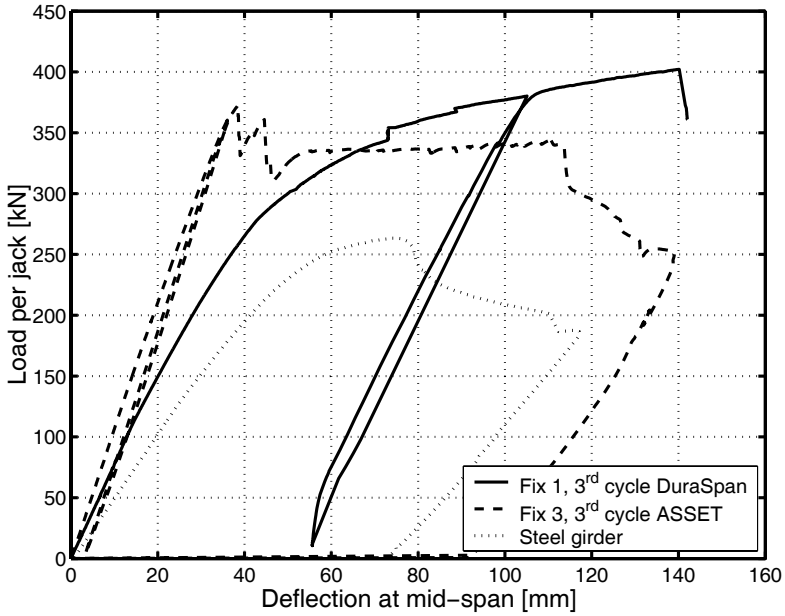

Figure 4.64: Comparison of load-deflection behavior at mid-span (FLS experiments).

Effective deck width

The ASSET decks of both girders fully participated as top chord over the whole 1.50-m width at SLS and ULS. At FLS, however, the panels showed decreased participation towards the edges. The decrease was more pronounced in the lower panel than the upper one. The DuraSpan decks showed similar behavior: full effective width at SLS and ULS, reduced effective width at FLS.

Fatigue behavior

Again, as was noticed for the DuraSpan girder Fix 2, intermediate SLS experiments after each million cycles and final failure experiments performed on the ASSET girder Fix 4 showed no indications of degradation or damage to the girder nor to the adhesive bond as a result of the 10 million fatigue cycles.

Failure behavior

As for the ASSET girders, the upper deck face panels failed at a lower stress than predicted. From the system experiments, a failure stress of -41 MPa was expected, as shown in Table 3.10, page 51. The calculated stresses of -33 MPa from the experiments were 20% below this value (see Fig. 4.38, page 86). The stepped joints, which failed first, were only 60 mm from one of the load patches of the two jacks. Therefore a direct influence of the load patch on the stress states in the joints was probable, which led to premature joint failure. Experiments on the small-size specimens showed that the stress state in these joints is very complex due to eccentricities of the panel and diagonal axes and therefore the joints were very sensitive to brittle failure. The first failures in the upper panels led to a deviation of the axial forces into the lower panels, which were then overloaded and failed again in the stepped joints at the same cross-sections where the first failures occurred. Compared to the reference steel girder, however, the decks still maintained some compression resistance (see Fig. 4.32, page 82). Only with the occurrence of the further deck failures did the loads approach the failure load of the reference steel girder, but at girder deflections which were about twice as great as for the reference steel girder at failure. Compared to the DuraSpan girders, the behavior of the ASSET girders was much more brittle, as can be seen in Fig. 4.64 on the preceding page. Without the premature failure in the upper deck panel, however, a more ductile behavior and a slightly higher failure load could be expected.

Due to only partial composite action in the GFRP decks themselves, the lower face panels of the two DuraSpan girders were considerably more heavily loaded than the upper face panels. The initial failures in both girders occurred, therefore, in a transverse joint of the lower face panels in the area with maximum moments between the jacks. The resulting maximum axial compression stresses at failure in the lower face panels were -51 MPa for girder Fix 1 and -45 MPa for girder Fix 2 (see Fig. 4.58, page 98). These values exceeded those of average compression stress at failure obtained from the deck system experiments (see Table 3.10, page 51, -34 MPa). The higher-than-expected stresses at failure can be explained by the fixation of the lower face panels onto steel girders, which prevented them from buckling. The secondary de-

tachment and buckling failure of the deck of girder Fix 2 can be explained as follows: the yielding top steel flange and the failed lower face panel were unable to provide further resistance. Therefore, the remaining compression forces deviated upwards through the diagonal webs into the still-intact upper face panel. These upward-directed forces caused out-of-plane tensile stresses in the adhesively-bonded joint in the area between the jacks (area without shear loading). These stresses obviously exceeded the through-the-thickness strength of the outer deck layer and caused the previously described opening of the connection between the jacks. At the same time, the additional two hinges formed underneath the jacks. Compared to the reference steel girder, the deck was still able to maintain a residual compression resistance (see Fig. 4.64, page 102).

Adhesive girder-to-deck connection

The longitudinal shear stresses in the adhesive girder-to-deck connection between supports and jacks were evenly distributed and very small at all three load levels up to failure. Shear stresses at failure were of the order of only 1.9 - 2.4 MPa and therefore far from ultimate stresses (see Figs. 4.27, page 79 and 4.48, page 92). The absence of peeling stresses made the stress state even more favorable.

Concerning the ASSET girders, the resulting maximum shear stress of girder Fix 3 was approximately 20% below the predicted value of 2.4 MPa, mainly due to the premature failure in the upper deck panel and the reduced effective width in the lower panel. The maximum shear stress of girder Fix 4 matched the predicted value due to the higher failure load. Although the adhesive layers were a comparatively thick 6 - 10 mm, full composite action was achieved and no creep deformation due to the fatigue experiment occurred. The ten million fatigue cycles showed no visible or measurable degradations or damage. In this respect, the ASSET and DuraSpan girders exhibited the same behavior.

The shear stresses at failure in the DuraSpan girders were of the order of 2.0 MPa and therefore also far from ultimate stresses. The ten million fatigue cycles showed no visible or measurable degradations or damage.

Both bridge decks were able to prevent buckling of the top steel flanges. Thus, compared to the reference steel girder, maximum deflections at failure could be increased considerably.

The final failures in the adhesively-bonded joint provoked by the out-of plane-stresses showed that, regardless of the same surface preparation, the failure occurred once directly in the joint (ASSET girders) and once in the outer layer of the face panel (DuraSpan girders). One reason for this could be the different fillers in the matrix, since the matrix in both bridge decks is an isophthalic polyester.

5 Analytical description of girder behavior

5.1 Existing analytical design methods

A certain number of dimensioning and calculation methods for composite girders with flexible shear connections are described in literature (e.g. [42], [41]). Not all are suitable for calculation of the girders described in this thesis since the objectives are to determine cross-sectional stress-strain distribution and deflections.

The "partial connection method"explained in EC 4 [42] allows engineers to determine the moment of resistance and thus ultimate limit state, but not deflections. Deflections are calculated assuming full composite action since slipping between the concrete deck and steel girder at SLS is very low. Since "slipping" of the face panels of the FRP bridge decks is considerable (see Fig 4.63, page 102), even at SLS loads, this method cannot be applied for steel/FRP composite girders.

Another design method for mechanically-jointed beams is presented in EC 5 [41]. The basis of this design method was developed in the mid fifties by Karl Möhler [84] and has since been improved by J. Natterer in [91] for example with respect to timber girders. The advantage of this method is not only that cross-sectional stress-strain distribution in girders with flexible shear connection, but also their deflection, can be determined. For this reason it was decided to adapt this method for composite girders consisting of steel main girders and FRP bridge decks.

5.2 Prediction of composite girder behavior at SLS and ULS

5.2.1 Considerations based on Natterer

The method developed by J. Natterer and M. Hoeft provides more results than the "mechanically jointed beams method" described in EC 5 since stresses in all cross-sectional parts can be calculated, but it is also more complicated. Both methods are only valid for single girders and special load configurations. The main difference between them is that the basic differential equations for the method described in EC 5 are derived for a sinusoidal-distributed load, while Natterer extended these equations for different loading conditions - including symmetric single loads at any location. Natterer also improved the method so that different other cross-sections than those indicated in EC 5 are allowed (see Fig. 5.1 on the following page). The derivation and solution of the differential equations for two single loads should enable this method to

provide more precise results for the girders studied in this thesis. Nevertheless for all other common load configurations (constant and linear-distributed load, sinusoidal- distributed load, one single load, etc.), the differential equations have also been solved. Thus, the load-bearing behavior of composite girders subjected to other load conditions than those presented in this study can also be calculated. Natterer's work is based on certain assumptions, the most important of which are summarized below.

1. Hooke's law is respected $\Rightarrow \sigma = E \cdot \epsilon$
2. Bernouilli's law is respected for each single cross-section
3. The single cross-sections are rectangular over the whole girder length
4. The girder is only loaded in bending
5. The complete cross-section must have at least one symmetry axis
6. The shear stiffness $\widehat{G}$ of the joint has to be constant and must have linear load/deformation behavior
7. Shear deformations of the single cross-sections are neglected

Point 6 does not appear to be fulfilled for the DuraSpan deck, when considering the idealized shear diagram on page 60, but the differential shifts of the face panels in the girder experiments (page 96) showed that up to 140 kN, the bridge deck is still in the elastic region (concerning in-plane shear, compare also Fig. 3.34, page 53). All other items are assumed to be respected.

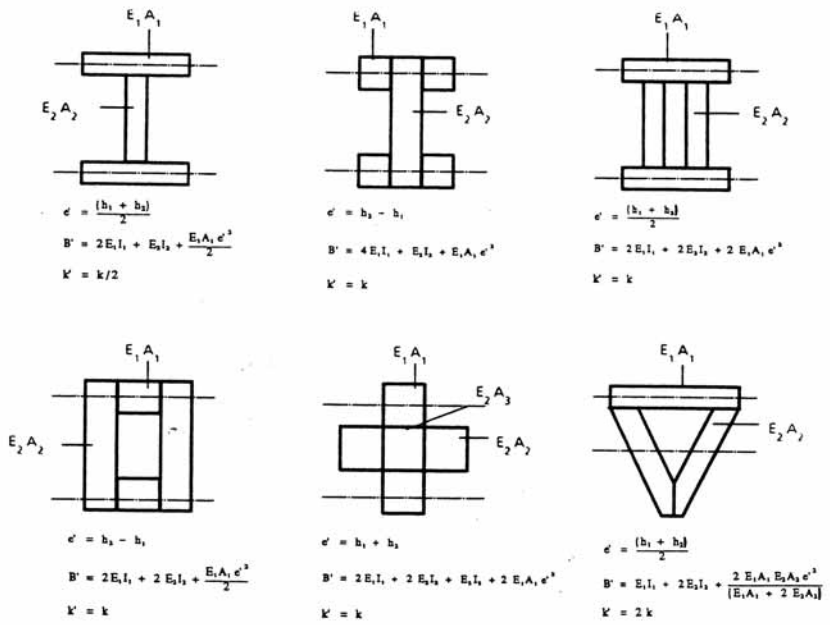

Figure 5.1: Cross-sections considered in [91], apart from section shown in Fig. 5.2 on the next page

The following recapitulates the basis of the derivation of the differential equations and the differential equations themselves in order to justify their application.

The general conditions mentioned above are respected but the cross-section of the steel/FRP composite girder is different (see Figs. 5.2 and 5.3) from the one analyzed by Natterer. Therefore it has to be determined whether the design method can be applied or not. Fig. 5.2 shows a general 2-part cross-section as was analyzed by Natterer. In Fig. 5.3 a cross-section of the girders investigated in this thesis is shown. The differences become clear when comparing the two cross-sections:

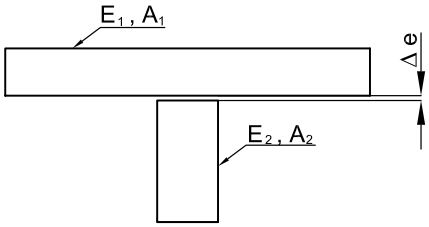

Figure 5.2: Cross-section analyzed by Natterer

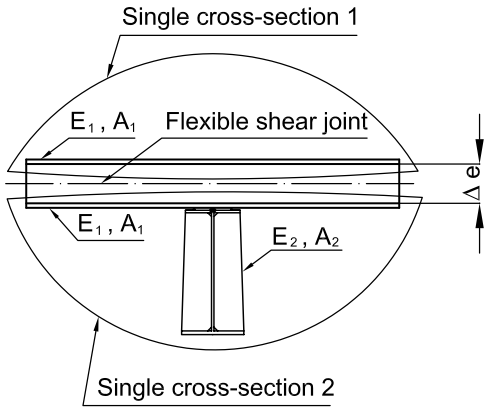

Figure 5.3: Cross-section of steel/FRP composite girder

1. Natterer had to divide the cross-section into two single cross-sections in the shear joint, therefore each single cross-section comprises only one material (E_1 and E_2 in Fig. 5.2). When dividing the steel/FRP cross-section in the flexible shear joint (see Fig. 5.3) it can be seen that single cross-section 2 comprises two different materials. This problem will be dealt with and solved in Section 5.2.2, page 113. As explained in Section 4.5.2, page 98, full composite action was achieved in the adhesively-bonded joint, hence the flexible shear joint in the steel/FRP girder is not the adhesively- bonded connection, but the bridge deck with its flexible webs (compare also Fig. 4.54, page 96). The assumption of full composite action in the adhesively bonded joint is a major factor for the application of this method on steel/FRP composite girders. The verification of this assumption will be shown in Chapter 6, page 141.

2. The other noticeable difference is the distance $\triangle e$ in the shear joint between the two single cross-sections. This distance easily attains 200 mm for FRP bridge decks but in Natterer's work only ∼20 mm are considered. Natterer verified that this difference does not affect the validity of the differential equations; it only influences the lever arm between the normal forces of the single cross-sections.

Therefore it may be concluded that the differential equations derived for concrete/wood composite girders in [91] are also valid for steel/FRP composite girders.

For derivation of the differential equations for the flexible shear connection, the equilibrium equations ($\sum V^1$, $\sum H^2$, $\sum M^3$) for the single cross-sections are drawn up (see Figs. 5.4 and 5.5). After inclusion of the geometrical deformation conditions and several conversions, the differential equations for the deflection $w_{(x)}$ and deformation $u_{(x)}$ in the joint are obtained.

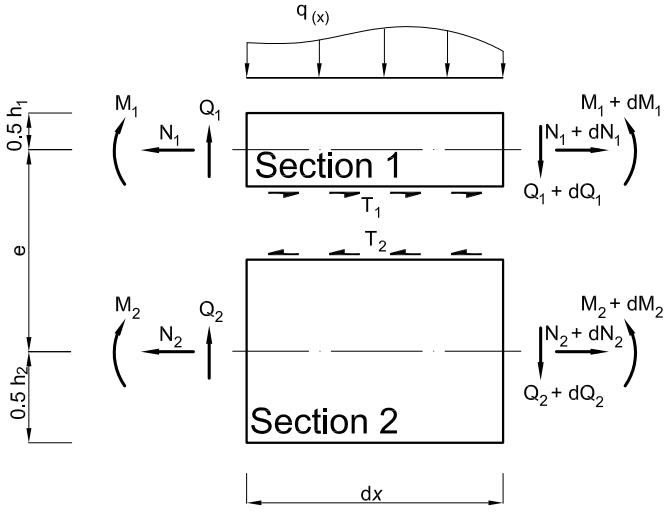

Figure 5.4: Inner forces at a girder element of length dx

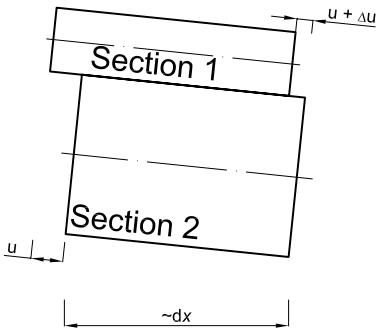

Figure 5.5: Geometry at girder ends

Differential equation for deflection:

$$w^{VI} - b^2 \cdot w^{IV} = \frac{1}{(E_1 I_1 + E_2 I_2)} \cdot \left(q'' - \omega^2 \cdot q\right) \tag{5.1}$$

Differential equation for deformations at girder ends:

$$u''' - b^2 \cdot u' = \frac{q \cdot e}{(E_1 I_1 + E_2 I_2)} \tag{5.2}$$

[1] sum of vertical forces
[2] sum of horizontal forces
[3] sum of moments

with:

$$\omega^2 = \frac{(E_1 A_1 + E_2 A_2) \cdot k}{E_1 A_1 \cdot E_2 A_2} \tag{5.3}$$

$$b^2 = \omega^2 + \frac{k \cdot e^2}{E_1 I_1 + E_2 I_2} \tag{5.4}$$

and

with: k = Shear stiffness of joint in $[\frac{N}{mm^2}]$
e = Difference between neutral axes of the single cross-sections (see Fig. 5.4 on the preceding page)

Natterer derived differential equations for nearly all common load configurations but calculation of the load-bearing capacity of the experimental girders only requires that shown in Fig. 5.6.

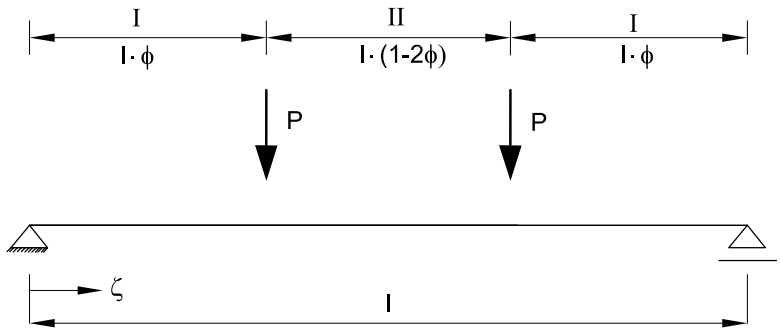

Figure 5.6: Single girder with symmetrical load pair at any location

Boundary conditions:

① $w_{I,(\zeta=0)} = 0$
② $M_{I,(\zeta=0)} = 0$
③ $M_{I,i,(\zeta=0)} = 0$
④ $w_{I,(\zeta=1)} = 0$
⑤ $M_{I,(\zeta=1)} = 0$
⑥ $M_{I,i,(\zeta=1)} = 0$

Continuity conditions:

⑦ $Q_{I,(\zeta=l\cdot\Phi)} = Q_{II,(\zeta=l\cdot\Phi)} + P$
⑧ $u_{I,(\zeta=l\cdot\Phi)} = u_{II,(\zeta=l\cdot\Phi)}$
⑨ $M_{I,(\zeta=l\cdot\Phi)} = M_{II,(\zeta=l\cdot\Phi)}$
⑩ $u'_{I,(\zeta=l\cdot\Phi)} = u'_{II,(\zeta=l\cdot\Phi)}$
⑩+① $w_{I,(\zeta=l\cdot\Phi)} = w_{II,(\zeta=l\cdot\Phi)}$
⑩+② $w'_{I,(\zeta=l\cdot\Phi)} = w'_{II,(\zeta=l\cdot\Phi)}$

By using the boundary and continuity conditions in Formulas 5.1 and 5.2, page 108, the differential equations can be solved. For the static system shown in Fig. 5.6 on the preceding page, the deformation equations can be expressed as follows:

Region I, $0 \leq \zeta \leq \Phi$:

$$w_{I(\zeta)} = \frac{P \cdot l^3}{B} \left\{ \frac{a^2}{1-a^2} \left[\frac{1}{\lambda^2} \cdot \zeta - \frac{1}{\lambda^3} \frac{\sinh(\lambda \cdot \zeta)}{\cosh\left(\frac{\lambda}{2}\right)} \cdot \cosh[\lambda(\Phi - 0.5)] \right] + \frac{1}{2} \cdot \zeta \left(\Phi - \Phi^2 - \frac{\zeta^2}{3} \right) \right\} \tag{5.5}$$

$$u_{I(\zeta)} = \frac{P \cdot e \cdot l^2}{B} \cdot \frac{1}{1-a^2} \cdot \frac{1}{\lambda^2} \left[1 - \frac{\cosh(\lambda \cdot \zeta)}{\cosh\left(\frac{\lambda}{2}\right)} \cosh[\lambda(\Phi - 0.5)] \right] \tag{5.6}$$

Region II, $\Phi \leq \zeta \leq 1 - \Phi$:

$$w_{II(\zeta)} = \frac{P \cdot l^3}{B} \left\{ \frac{a^2}{1-a^2} \left[\frac{1}{\lambda^2} \cdot \Phi - \frac{1}{\lambda^3} \frac{\sinh(\lambda \cdot \Phi)}{\cosh(\frac{\lambda}{2})} \cdot \cosh[\lambda(\zeta - 0.5)] \right] + \frac{\Phi}{2} \cdot \left(\zeta - \zeta^2 - \frac{\Phi^2}{3} \right) \right\} \tag{5.7}$$

$$u_{II(\zeta)} = -\frac{P \cdot e \cdot l^2}{B} \cdot \frac{1}{1-a^2} \frac{1}{\lambda^2} \left[\frac{\sinh(\lambda \cdot \Phi)}{\cosh\left(\frac{\lambda}{2}\right)} \sinh[\lambda(\zeta - 0.5)] \right] \tag{5.8}$$

Region III, $1 - \Phi \leq \zeta \leq 1$:

$$w_{III(\zeta)} = w_{I(\zeta)} \cdot (1 - \zeta) \tag{5.9}$$

With

$$B = E_1 I_1 + E_2 I_2 + \frac{E_1 A_1 \cdot E_2 A_2 \cdot e^2}{E_1 A_1 + E_2 A_2} \tag{5.10}$$

The interrelation between the inner forces in the single cross-sections and equations 5.5 - 5.9 on the preceding page can be derived using the equations already used for derivation of the differential equations. Since the derivation of these equations is not an aim of this thesis, they are only indicated here. The detailed derivation is shown in [91]. Assuming that most of the shear force in the girder will be taken by the web of the steel flange, only formulas for the normal forces and bending moments are indicated.

Using equations 5.11 and 5.12, the inner forces, and thus the cross-sectional stress/strain distribution of the single cross-sections 1 and 2, can be determined. For the load configuration of the experimental girders, equations 5.7 and 5.8 on the preceding page must be applied.

$$\Rightarrow N_{II(\zeta)} = P \cdot l \frac{a^2}{e} \left(\Phi - \frac{1}{\lambda} \cdot \frac{\sinh(\lambda \cdot \Phi)}{\cosh(\frac{\lambda}{2})} \cdot \cosh(\lambda[\zeta - 0.5]) \right) \tag{5.11}$$

$$\begin{aligned} \Rightarrow M_{II,i,(\zeta)} = & P \cdot l \cdot a_i \Bigg((1 - a^2)\Phi + a^2 \cdot \frac{1}{\lambda} \cdot \frac{\sinh(\lambda \cdot \Phi)}{\cosh(\frac{\lambda}{2})} \\ & \cdot \cosh(\lambda[\zeta - 0.5]) \Bigg) \end{aligned} \tag{5.12}$$

With

$$\frac{a^2}{1 - a^2} = \frac{E_1 A_1 \cdot E_2 A_2 \cdot e^2}{(E_1 A_1 + E_2 A_2)(E_1 I_1 + E_2 I_2)}$$

$$a_i = \frac{E_i I_i}{E_1 I_1 + E_2 I_2}$$

$$\lambda^2 = b^2 \cdot l^2$$

and

$\frac{a^2}{1-a^2}$	material and geometrical constant
λ	shear influence constant
b^2	see Equation 5.4, page 109
e	see Fig. 5.4, page 108
l	Span

To enable application of the design method for other girders than the experimental girders, the solution of the differential Equations 5.1 and 5.2, page 108, is also given for a constant distributed load (see Fig. 5.7).

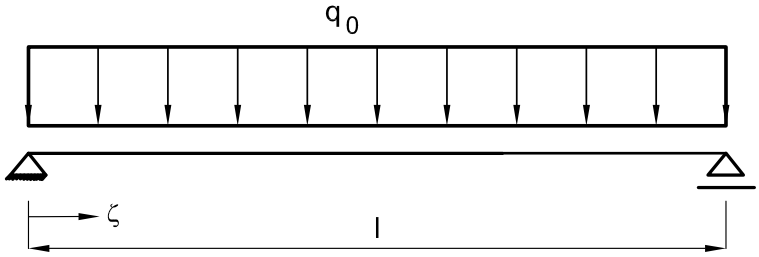

Figure 5.7: Simple girder with constant distributed load

$$w_{(\zeta)} = \frac{q_0 \cdot l^4}{B}\left\{\frac{a^2}{1-a^2}\left[\frac{1}{2\cdot\lambda^2}\cdot(\zeta-\zeta^2)+\frac{1}{\lambda^4}\left(\frac{\cosh[\lambda(\zeta-0.5)]}{\cosh(\frac{\lambda}{2})}-1\right)\right] + \frac{1}{24}\cdot\left(\zeta-2\zeta^3+\zeta^4\right)\right\} \tag{5.13}$$

$$u_{(\zeta)} = \frac{q_0 \cdot e \cdot l^3}{B}\cdot\left\{\frac{1}{1-a^2}\left(\frac{1}{2\cdot\lambda^2}\cdot(1-2\zeta)-\frac{1}{\lambda^3}\cdot\frac{\sinh(\lambda[\zeta-0.5])}{\cosh\left(\frac{\lambda}{2}\right)}\right)\right\} \tag{5.14}$$

The inner forces are determined as follows:

$$N_{(\zeta)} = q_0 \cdot l^2 \cdot \frac{a^2}{e}\left[\frac{1}{2}(\zeta-\zeta^2)-\frac{1}{\lambda^2}\cdot\left(1-\frac{\cosh(\lambda[\zeta-0.5])}{\cosh(\frac{\lambda}{2})}\right)\right] \tag{5.15}$$

$$M_{i(\zeta)} = q_0 \cdot l^2 \cdot a_i\left\{\frac{1}{2}(\zeta-\zeta^2)(1-a^2)+\frac{a^2}{\lambda^2}\left(1-\frac{\cosh(\lambda[\zeta-0.5])}{\cosh(\frac{\lambda}{2})}\right)\right\} \tag{5.16}$$

The stresses in the single cross-sections can be determined as described in the following section.

5.2.2 Derivation of equations for steel/FRP composite girders

In this section the author will derive the necessary equations for calculation of the cross-sectional stress/strain distribution and deflections of steel/FRP composite girders based on the differential equations shown in Section 5.2, page 105. For this, the following system parameters are necessary:

1. The geometry
2. The E-modulus of both materials
3. The in-plane shear stiffness of the flexible joint

⇒ 1: The geometry can be taken as given, since it was decided by the engineer.

⇒ 2: The E- modulus of steel is known and the appropriate values for the FRP-decks were derived in Chapter 3 and are summarized in Section 3.5.1, page 51.

⇒ 3: Since the adhesively-bonded joints in all four experimental girders provided full composite action, the in-plane shear stiffness of the bridge decks itself is decisive. This was also derived in Chapter 3. The summary appears on page 59. The connection of the two face panels of the bridge deck by means of the webs is considered as "flexible joint" . In order to use equations 5.11 and 5.12, page 111, the in-plane shear stiffness $\widehat{G}$ has to be modified since stiffness k is defined as the force which provokes 1-mm relative displacement between the two face panels of the bridge deck (see also Fig. 5.8). Assuming that for small angles $tan\alpha = \alpha$, this gives:

$$\widehat{K} = \widehat{G} \cdot \alpha = \widehat{G} \cdot \frac{1}{h} \qquad \left[\frac{N}{mm^3}\right] \tag{5.17}$$

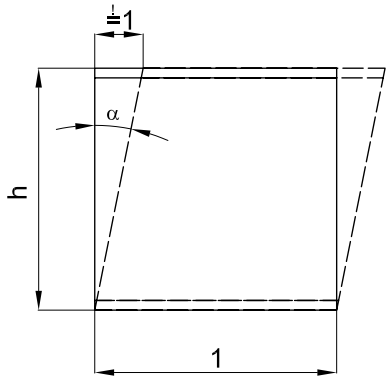

Figure 5.8: Geometry of bridge deck for determining in-plane shear stiffness K (not to scale)

$\widehat{K}$ is the in-plane shear stiffness normalized on a surface of 1 mm^2. In order to describe exactly the stiffness of a specific girder, $\widehat{K}$ has to be

multiplied by the effective width of the bridge deck. In conjunction with Equation 5.4, page 109 this gives:

$$\Rightarrow b^{*2} = \frac{(E_1 A_1 + E_2 A_2) \cdot \widehat{K} \cdot b_{ef}}{E_1 A_1 \cdot E_2 A_2} + \frac{\widehat{K} \cdot b_{ef} \cdot e^2}{(E_1 I_1 + E_2 I_1)} \tag{5.18}$$

The problem already addressed in single cross-section 2 (see Fig. 5.3, page 107) can easily be solved by converting the lower face panel of the bridge deck into an equivalent steel section. For this the modular ratios of steel and FRP are needed.

$$n_0 = \frac{E_a}{\widehat{E}_{FRP}} \tag{5.19}$$

n_0= Modular ratio for short-term loading

Multiplied by this factor, single cross-section 2 looks as follows:

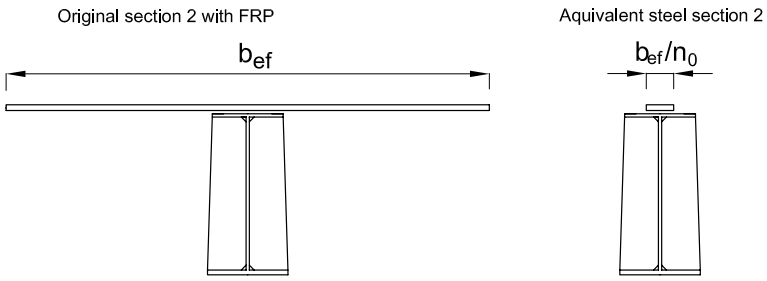

Figure 5.9: Original and transferred single cross-section 2

With the in-plane shear stiffness k and single cross-section 2 transferred to a homogeneous steel section, the static properties (I_1, I_2) of both single cross-sections are known and the inner forces $N_{II(\zeta)}$ and $M_{i,II(\zeta)}$ can be determined. By superposition of the resulting bending and normal stresses, the maximum values in each part of the girder are obtained (see Equations 5.20 - 5.22 on the next page).

$$\sigma_{II,1,j} = \sigma^N_{II,1} + \sigma^M_{II,1,j} = \frac{N_{II}}{A_1} + \frac{M_{II,1}}{W_{1,j}} \tag{5.20}$$

With:

$\sigma_{II,1,j}$	Stress in single cross-section 1 for region II at location j
$\sigma^N_{II,1}$	Normal stresses for region II
$\sigma^M_{II,1,j}$	Bending stresses in single cross-section i for region II at location j
N_{II}	Normal forces in the single cross-sections; single cross section 1

	negative, single cross section 2 positive; according to Equation 5.11, page 111
A_1	Area of single cross-section 1
$M_{II,1}$	Bending moment in single cross-section 1 for region II
$W_{1,j}$	Moment of resistance in single cross-section 1 at location j

To obtain the stresses in the FRP part of single cross-section 2, the stresses have to be divided by the modular ratio for short-term loading, n_0.

$$\sigma_{II,2,j,FRP} = \sigma^N_{II,2,FRP} + \sigma^M_{II,2,j,FRP} = \frac{N_{II}}{A_2 \cdot n_0} + \frac{M_{II,2}}{W_{2,j} \cdot n_0} \tag{5.21}$$

The stresses in the steel part of single cross-section 2 can be calculated analogically to Equation 5.20 on the preceding page.

$$\sigma_{II,2,j,a} = \sigma^N_{II,a} + \sigma^M_{II,2,j,a} = \frac{N_{II}}{A_2} + \frac{M_{II,2}}{W_{2,j}} \tag{5.22}$$

5.2.3 Numerical examples

In this section, the cross-sectional stress/strain behavior and deflection behavior of the experimental girders studied in Chapter 4 will be determined using the equations derived in the previous two sections. Using equations 5.11 and 5.12, page 111, the inner forces of the single cross-sections can be determined. Since the design method is only valid for linear- elastic material properties, the cross-sections are verified at a load level of 133 kN/jack, corresponding to 400 kNm (note: ULS = 110/120 kN/jack). The DuraSpan girders behaved linear-elastically up to ∼140kN/jack. The ASSET girders behaved linear elastically up to failure at ∼380 kN. The linear-elastic system properties of the DuraSpan bridge deck are also respected as shown in Section 5.2.3, page 121.

The in-plane shear moduli for the tested deck systems were determined using Equation 5.8, page 113.

$$\widehat{K}_{Dura} = \frac{\widehat{G}_{Dura}}{h_{Dura}} = \frac{5}{195} = 2.56 \cdot 10^{-2} \quad \frac{N}{mm^3}$$

$$\widehat{K}_{ASSET} = \frac{\widehat{G}_{ASSET}}{h_{ASSET}} = \frac{47}{225} = 20.88 \cdot 10^{-2} \quad \frac{N}{mm^3}$$

	Shear stiffness K $[\frac{N}{mm^3}]$
ASSET	$20.88 \cdot 10^{-2}$
DuraSpan	$2.56 \cdot 10^{-2}$

Verification of ASSET girder

Calculation of inner forces at mid-span

With:

$E_1 = 16\,200 \quad MPa$
$A_1 = 23\,400 \quad mm^2$
$I_1 = 474\,552 \quad mm^4$
$l = 7\,500 \quad mm$
$e = 467 \quad mm$
$\Phi = 0.4$

$E_2 = 210\,000 \quad MPa$
$A_2 = 12\,505 \quad mm^2$
$I_2 = 5.703 \cdot 10^8 \quad mm^4$
$\widehat{K} = 20.88 \cdot 10^{-2} \quad \frac{N}{mm^3}$
$b_{ef} = 1500 \quad mm$
$\zeta = 0.5$

$$\begin{aligned} N_{II(\zeta=0.5)} &= P \cdot l \frac{a^2}{e} \left(\Phi - \frac{1}{\lambda} \cdot \frac{\sinh(\lambda \cdot \Phi)}{\cosh(\frac{\lambda}{2})} \cdot \cosh(\lambda[\zeta - 0.5]) \right) \\ &= 133\,000 \cdot 7\,500 \cdot \frac{0.376}{467} \left(0.4 - \frac{1}{9.41} \cdot \frac{\sinh(9.41 \cdot 0.4)}{\cosh(\frac{9.41}{2})} \cdot 1 \right) \\ &= 288\,100 \quad N \end{aligned}$$

$$\begin{aligned} M_{II,1(\zeta=0.5)} &= P \cdot l \cdot a_1 \left((1 - a^2)\Phi + a^2 \cdot \frac{1}{\lambda} \cdot \frac{\sinh(\lambda \cdot \Phi)}{\cosh(\frac{\lambda}{2})} \cdot \cosh(\lambda[\zeta - 0.5]) \right) \\ &= 133\,000 \cdot 7\,500 \cdot 6.419 \cdot 10^{-5} \left[(1 - 0.376) \cdot 0.4 + \frac{0.376}{9.41} \cdot 0.39 \cdot 1 \right] \\ &= 16\,975 \quad Nmm \end{aligned}$$

With:

$$a_1 = \frac{E_1 I_1}{E_1 I_1 + E_2 I_2} = \frac{16\,200 \cdot 474\,552}{16\,200 \cdot 474\,552 + 210\,000 \cdot 5.703 \cdot 10^8} = 6.419 \cdot 10^{-5}$$

$$\frac{a^2}{1-a^2} = \frac{E_1A_1 \cdot E_2A_2 \cdot e^2}{(E_1A_1 + E_2A_2)(E_1I_1 + E_2I_2)}$$
$$= \frac{16\,200 \cdot 23\,400 \cdot 210\,000 \cdot 12\,505 \cdot 467^2}{(16\,200 \cdot 23\,400 + 210\,000 \cdot 12\,505)(16\,200 \cdot 474\,552 + 210\,000 \cdot 5.703 \cdot 10^8)}$$
$$= 0.603$$
$$\Rightarrow a^2 = 0.376$$

$$b^{*2} = \frac{(E_1A_1 + E_2A_2) \cdot \widehat{K} \cdot b_{ef}}{E_1A_1 \cdot E_2A_2} + \frac{\widehat{K} \cdot b_{ef} \cdot e^2}{(E_1I_1 + E_2I_2)}$$
$$= \frac{(16\,200 \cdot 23\,400 + 210\,000 \cdot 12\,505) \cdot 20.88 \cdot 10^{-2} \cdot 1500}{16\,200 \cdot 23\,400 \cdot 210\,000 \cdot 12\,505}$$
$$+ \frac{20.88 \cdot 10^{-2} \cdot 1500 \cdot 467^2}{16\,200 \cdot 474\,552 + 210\,000 \cdot 5.703 \cdot 10^8}$$
$$= 1.516 \cdot 10^{-6} \quad \frac{1}{mm^2}$$

$$\Rightarrow \lambda^2 = l^2 \cdot b^2 = 7\,500^2 \cdot 1.516 \cdot 10^{-6} = 88.4$$

$$M_{II,2(\zeta=0.5)} = P \cdot l \cdot a_2 \left((1-a^2)\Phi + a^2 \cdot \frac{1}{\lambda} \cdot \frac{\sinh(\lambda \cdot \Phi)}{\cosh(\frac{\lambda}{2})} \cdot \cosh(\lambda[\zeta - 0.5]) \right)$$
$$= 133\,000 \cdot 7\,500 \cdot 0.999 \left[(1 - 0.376) \cdot 0.4 + \frac{0.376}{9.41} \cdot 0.39 \cdot 1 \right]$$
$$= 2.644 \cdot 10^8 \quad Nmm$$

With:

$$a_2 = \frac{E_2I_2}{E_1I_1 + E_2I_2} = \frac{210\,000 \cdot 5.703 \cdot 10^8}{16\,200 \cdot 474\,552 + 210\,000 \cdot 5.703 \cdot 10^8} = 0.999$$

Calculation of axial stresses at mid-span

The maximum stresses in each cross-section can be calculated using Equations 5.20 - 5.22, page 115.

$$\sigma_{\mathbf{II,1,max}} = \sigma^N_{II,1} + \sigma^M_{II,1,max} = -\frac{N_{II}}{A_1} + \frac{M_{II,1}}{W_{1,max}}$$
$$= -\frac{288\,100}{23\,400} - \frac{16\,980}{60\,840} = \mathbf{-12.6} \quad \mathbf{MPa}$$

With:

$$W_{1,max} = \frac{I_1}{d_{max}} = \frac{474\,552}{\frac{15.6}{2}} = 60\,840 \quad mm^3$$

and

d_{max} maximum distance from neutral axis of single cross-section 1

The maximum stresses in the FRP part of single cross-section 2 is calculated as follows:

$$\sigma_{\mathbf{II,2,max,FRP}} = \sigma^N_{II,2,FRP} + \sigma^M_{II,2,max,FRP} = \frac{N_{II}}{A_2 \cdot n_0} + \frac{M_{II,2}}{W_{2,max,FRP}}$$
$$= \frac{288\,100}{12\,505 \cdot 12.96} - \frac{2.643 \cdot 10^8}{2.281 \cdot 10^6 \cdot 12.96} = \mathbf{-7.2} \quad \mathbf{MPa}$$

With:

$$W_{2,max,FRP} = \frac{I_2}{d_{max,FRP}} = -\frac{5.703 \cdot 10^8}{250} = -2.281 \cdot 10^6 \quad mm^3$$

$$n_0 = \frac{E_a}{E_{FRP}} = \frac{210\,000}{16200} = 12.96$$

and

d_{FRP} distance from neutral axis of single cross-section 2 to the lower face panel

The maximum stresses in the top steel flange:

$$\sigma_{\mathbf{II,2,max,a,o}} = \sigma^N_{II,2,a} + \sigma^M_{II,2,max,a} = \frac{N_{II}}{A_2} + \frac{M_{II,2}}{W_{2,max,a,o}}$$

$$= \frac{288\,100}{12\,505} - \frac{2.643 \cdot 10^8}{2.376 \cdot 10^6} = \mathbf{-88.2} \quad \mathbf{MPa}$$

With:

$$W_{2,max,a,o} = \frac{I_2}{d_{max,a,o}} = -\frac{5.703 \cdot 10^8}{240} = -2.376 \cdot 10^6 \quad mm^3$$

and

$d_{a,o}$ distance of neutral axis of single cross-section 2 $\Leftrightarrow$ top steel flange

The maximum stresses in the bottom steel flange:

$$\sigma_{\mathbf{II,2,max,a,u}} = \sigma^N_{II,2,a} + \sigma^M_{II,2,max,a} = \frac{N_{II}}{A_2} + \frac{M_{II,2}}{W_{2,max,a,u}}$$

$$= \frac{288\,100}{12\,505} + \frac{2.643 \cdot 10^8}{2.193 \cdot 10^6} = \mathbf{143.5} \quad \mathbf{MPa}$$

With:

$$W_{2,max,a,o} = \frac{I_2}{d_{max,a,u}} = \frac{5.703 \cdot 10^8}{260} = 2.193 \cdot 10^6 \quad mm^3$$

and

$d_{a,u}$ distance of neutral axis of single cross-section 2 $\Leftrightarrow$ lower steel flange

Figure 5.10 on the following page shows in graphical form the calculated stress distribution at mid-span versus the measured values in girders Fix 3 and Fix 4. As Table 5.1, page 121, shows, good correlation between the calculated and measured values can be observed. Only for the upper face panel of Fix 4 were increased stresses apparent but these are still within the acceptable range of measurement. However, the difference in stresses is very low ($\leq$3 MPa).

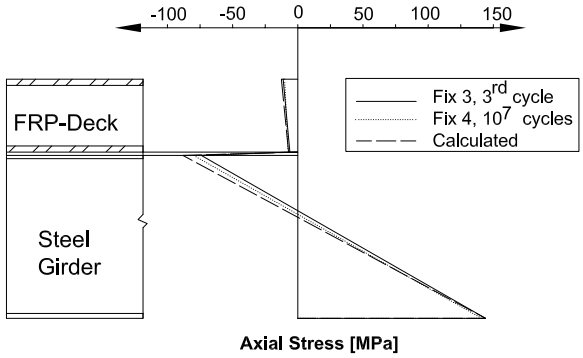

Figure 5.10: Calculated and measured cross-sectional stress distributions for ASSET girders at mid-span and 133kN/jack

Calculation of deflections at mid-span

Deflections are calculated using Equation 5.7, page 110.

$$\begin{aligned}
\mathbf{w_{II(\zeta=0.5)}} &= \frac{P \cdot l^3}{B} \cdot \left\{ \frac{a^2}{1-a^2} \left[\frac{1}{\lambda^2} \cdot \Phi - \frac{1}{\lambda^3} \cdot \frac{sinh(\lambda \cdot \Phi)}{\cosh(\frac{\lambda}{2})} \cosh(\lambda[\zeta - 0.5]) \right] \right. \\
&\quad \left. + \frac{\Phi}{2} \left(\zeta - \zeta^2 - \frac{\Phi^2}{3} \right) \right\} \\
&= \frac{133\,000 \cdot 7\,500^3}{1.9202 \cdot 10^{14}} \cdot \left\{ 0.603 \left[\frac{0.4}{88.5} - \frac{1}{9.41^3} \frac{\sinh(9.41 \cdot 0.4)}{\cosh(\frac{9.41}{2})} \right] \right. \\
&\quad \left. + \frac{0.4}{2} \left(0.5 - 0.5^2 - \frac{0.4^2}{3} \right) \right\} = \mathbf{12.2} \quad \mathbf{mm}
\end{aligned}$$

With:

$$\begin{aligned}
B &= E_1 I_1 + E_2 I_2 + \frac{E_1 A_1 \cdot E_2 A_2 \cdot e^2}{E_1 A_1 + E_2 A_2} \\
&= 16\,200 \cdot 474\,552 + 210\,000 \cdot 5.703 \cdot 10^8 + \frac{16\,200 \cdot 23\,400 \cdot 210\,000 \cdot 12\,505 \cdot 467^2}{16\,200 \cdot 23\,400 + 210\,000 \cdot 12\,505} \\
&= 1.9202 \cdot 10^{14} \quad Nmm^2
\end{aligned}$$

To clarify the calculated and measured values, they are presented below in tabular form.

	Absolute Values [MPa]			Normalized Values [%]		
	Fix 3	Fix 4	**Calc.**	Fix 3	Fix 4	**Calc.**
Upper face panel	-11.2	-10.1	**-12.6**	+11	+20	**100**
Lower face panel	-6.1	-7.5	**-7.1**	+14	-6	**100**
Top steel flange	-74	-80	**-88.2**	+16	+9	**100**
Bottom steel flange	144	141	**144**	± 0	-2	**100**
Deflection [mm]	12.5	11.1	**12.2**	+2	-9	**100**

Table 5.1: Calculated and measured values in ASSET girders and normalized values

Verification of DuraSpan girder

The procedure is the same as for the ASSET girder.

Calculation of inner forces at mid-span

With:

$E_1 = 11\,700 \quad MPa$
$A_1 = 27\,000 \quad mm^2$
$I_1 = 729\,000 \quad mm^4$
$l = 7\,500 \quad mm$
$e = 442 \quad mm$
$\Phi = 0.4$
$\sigma_{c,el} = 29 \quad MPa$

$E_2 = 210\,000 \quad MPa$
$A_2 = 12\,204 \quad mm^2$
$I_2 = 5.51 \cdot 10^8 \quad mm^4$
$\widehat{K} = 2.56 \cdot 10^{-2} \quad \frac{N}{mm^3}$
$b_{ef} = 1500 \quad mm$
$\zeta = 0.5$

$$N_{II(\zeta=0.5)} = P \cdot l \frac{a^2}{e} \left(\Phi - \frac{1}{\lambda} \cdot \frac{\sinh(\lambda \cdot \Phi)}{\cosh(\frac{\lambda}{2})} \cdot \cosh(\lambda[\zeta - 0.5]) \right)$$

$$= 133\,000 \cdot 7\,500 \cdot \frac{0.322}{442} \left(0.4 - \frac{1}{3.21} \cdot \frac{\sinh(3.21 \cdot 0.4)}{\cosh \frac{3.21}{2}} \cdot 1 \right)$$

$$= 144\,982 \quad N$$

$$\Rightarrow \quad N_{II(\zeta=0.5)} = 144\,982 \quad N$$

$$M_{II,1(\zeta=0.5)} = P \cdot l \cdot a_1 \left((1 - a^2)\Phi + a^2 \cdot \frac{1}{\lambda} \cdot \frac{\sinh(\lambda \cdot \Phi)}{\cosh(\frac{\lambda}{2})} \cdot \cosh(\lambda[\zeta - 0.5]) \right)$$

$$= 133\,000 \cdot 7\,500 \cdot 7.373 \cdot 10^{-5} \left[(1 - 0.322) \cdot 0.4 + \frac{0.322}{3.213} \cdot 0.6438 \cdot 1 \right]$$

$$= 24\,695 \quad Nmm$$

With:

$$a_1 = \frac{E_1 I_1}{E_1 I_1 + E_2 I_2} = \frac{11\,700 \cdot 729\,000}{11\,700 \cdot 729\,000 + 210\,000 \cdot 5.508 \cdot 10^8} = 7.373 \cdot 10^{-5}$$

$$\begin{aligned}
\frac{a^2}{1-a^2} &= \frac{E_1 A_1 \cdot E_2 A_2 \cdot e^2}{(E_1 A_1 + E_2 A_2)(E_1 I_1 + E_2 I_2)} \\
&= \frac{11\,700 \cdot 27\,000 \cdot 210\,000 \cdot 12\,204 \cdot 442^2}{(11\,700 \cdot 27\,000 + 210\,000 \cdot 12\,204)(11\,700 \cdot 729\,000 + 210\,000 \cdot 5.508 \cdot 10^8)} \\
&= 0.475 \\
&\Rightarrow a^2 = 0.322
\end{aligned}$$

$$\begin{aligned}
b^{*2} &= \frac{(E_1 A_1 + E_2 A_2) \cdot c \cdot b_{ef}}{E_1 A_1 \cdot E_2 A_2} + \frac{\widehat{K} \cdot b_{ef} \cdot e^2}{E_1 I_1 + E_2 I_1} \\
&= \frac{(11\,700 \cdot 27\,000 + 210\,000 \cdot 12\,204) \cdot 2.56 \cdot 10^{-2} \cdot 1500}{11\,700 \cdot 27\,000 \cdot 210\,000 \cdot 12\,204} \\
&\quad + \frac{2.56 \cdot 10^{-2} \cdot 1500 \cdot 442^2}{11\,700 \cdot 729\,000 + 210\,000 \cdot 5.508 \cdot 10^8} \\
&= 2.014 \cdot 10^{-7} \quad \frac{1}{mm^2}
\end{aligned}$$

$$\lambda^2 = l^2 \cdot b^{*2} = 7\,500^2 \cdot 2.014 \cdot 10^{-7} = 10.31$$

$$\begin{aligned}
M_{II,2(\zeta=0.5)} &= P \cdot l \cdot a_2 \left((1-a^2)\Phi + a^2 \cdot \frac{1}{\lambda} \cdot \frac{\sinh(\lambda \cdot \Phi)}{\cosh(\frac{\lambda}{2})} \cdot \cosh(\lambda[\zeta - 0.5]) \right) \\
&= 133\,000 \cdot 7\,500 \cdot 0.999 \left[(1 - 0.322) \cdot 0.4 + \frac{0.322}{3.213} \cdot 0.644 \cdot 1 \right] \\
&= 3.349 \cdot 10^8 \quad Nmm
\end{aligned}$$

With:

$$a_2 = \frac{E_2 I_2}{E_1 I_1 + E_2 I_2} = \frac{210\,000 \cdot 5.508 \cdot 10^8}{11\,700 \cdot 729\,0 + 210\,000 \cdot 5.508 \cdot 10^8} = 0.999$$

Calculation of axial stresses at mid-span

$$\sigma_{\mathbf{II,1,max}} = \sigma^N_{II,1} + \sigma^M_{II,1,max} = -\frac{N_{II}}{A_1} + \frac{M_{II,1}}{W_{1,max}}$$

$$= -\frac{144\,982}{27\,000} - \frac{24\,691}{81\,000} = \mathbf{-5.7} \quad \mathbf{MPa} \quad > \quad \sigma_{\mathbf{c,el}} = \mathbf{-29} \quad \mathbf{MPa}$$

With:

$$W_{1,max} = \frac{I_1}{d_{max}} = \frac{729\,000}{\frac{18}{2}} = 81\,000 \quad mm^3$$

Maximum stresses in the FRP part of single cross-section 2:

$$\sigma_{\mathbf{II,2,max,FRP}} = \sigma^N_{II,2,FRP} + \sigma^M_{II,2,max,FRP} = \frac{N_{II}}{A_2 \cdot n_0} + \frac{M_{II,2}}{W_{2,max,FRP}}$$

$$= \frac{144\,982}{12\,204 \cdot 17.95} - \frac{3.348 \cdot 10^8}{2.152 \cdot 10^6 \cdot 17.95}$$

$$= \mathbf{-8.0} \quad \mathbf{MPa} \quad > \quad \sigma_{\mathbf{c,el}} = \mathbf{-29} \quad \mathbf{MPa}$$

With:

$$W_{2,max,FRP} = \frac{I_2}{d_{max,FRP}} = -\frac{5.508 \cdot 10^8}{256} = -2.152 \cdot 10^6 \quad mm^3$$

$$n_0 = \frac{E_a}{E_{FRP}} = \frac{210\,000}{11700} = 17.95$$

Maximum stresses in the top steel flange:

$$\sigma_{\mathbf{II,2,max,a,o}} = \sigma^N_{II,2,a} + \sigma^M_{II,2,max,a} = \frac{N_{II}}{A_2} + \frac{M_{II,2}}{W_{2,max,a,o}}$$

$$= \frac{144\,982}{12\,204} - \frac{3.348 \cdot 10^8}{2.239 \cdot 10^6} = \mathbf{-137.7} \quad \mathbf{MPa}$$

With:

$$W_{2,max,a,o} = \frac{I_2}{d_{max,a,o}} = -\frac{5.508 \cdot 10^8}{246} = -2.239 \cdot 10^6 \quad mm^3$$

Maximum stresses in the bottom steel flange:

$$\sigma_{\mathbf{II,2,max,a,u}} = \sigma^N_{II,2,a} + \sigma^M_{II,2,max,a} = \frac{N_{II}}{A_2} + \frac{M_{II,2}}{W_{2,max,a,u}}$$

$$= \frac{144\,982}{12\,204} + \frac{3.348 \cdot 10^8}{2.168 \cdot 10^6} = \mathbf{166.3} \quad \mathbf{MPa}$$

With:

$$W_{2,max,a,o} = \frac{I_2}{d_{max,a,u}} = \frac{5.508 \cdot 10^8}{254} = 2.168 \cdot 10^6 \quad mm^3$$

and

$d_{max,a,u}$ distance of neutral axis of single cross-section 2 $\Leftrightarrow$ lower steel flange

Figure 5.11 on the next page shows in graphical form the calculated stress distribution at mid-span versus the measured values in girders Fix 1 and Fix 2. As Table 5.2 on the facing page, shows, good correlation between the calculated and measured values can be ascertained. The less accurate values in the upper face panel can be explained by the high secondary bending moments in the bridge deck. For future work, strain gages should be installed on the outer and inner side of the upper face panel.

Calculation of deflections at mid-span

The deflections are calculated using Equation 5.7, page 110.

$$\mathbf{w_{II(\zeta=0.5)}} = \frac{P \cdot l^3}{B} \cdot \left\{ \frac{a^2}{1-a^2} \left[\frac{1}{\lambda^2} \cdot \Phi - \frac{1}{\lambda^3} \cdot \frac{sinh(\lambda\Phi)}{\cosh(\frac{\lambda}{2})} \cosh(\lambda[\zeta - 0.5]) \right] \right.$$

$$\left. + \frac{\Phi}{2} \left(\zeta - \zeta^2 - \frac{\Phi^2}{3} \right) \right\}$$

$$= \frac{133\,000 \cdot 7\,500^3}{1.707 \cdot 10^{14}} \cdot \left\{ 0.474 \left[\frac{0.4}{10.32} - \frac{1}{3.21^3} \frac{\sinh(3.21 \cdot 0.4) \cdot \cosh 0.4}{\cosh(\frac{3.21}{2})} \right] \right.$$

$$\left. + \frac{0.4}{2} \left(0.5 - 0.5^2 - \frac{0.4^2}{3} \right) \right\} = \mathbf{16.0} \quad \mathbf{mm}$$

With:

$$B = E_1 I_1 + E_2 I_2 + \frac{E_1 A_1 \cdot E_2 A_2 \cdot e^2}{E_1 A_1 + E_2 A_2}$$

$$= 11\,700 \cdot 729\,000 + 210\,000 \cdot 5.51 \cdot 10^8 + \frac{11\,700 \cdot 27\,000 \cdot 210\,000 \cdot 12\,204 \cdot 442^2}{11\,700 \cdot 27\,000 + 210\,000 \cdot 12\,204}$$

$$= 1.706 \cdot 10^{14} \quad Nmm^2$$

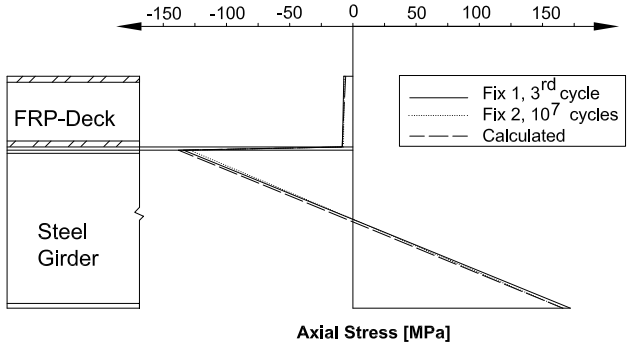

Figure 5.11: Calculated and measured cross-sectional stress distributions for DuraSpan girders at mid-span and 133kN/jack

For girder Fix 1 the deflections could be predicted with with good accuracy (+9%). Girder Fix 2, however, showed 23% bigger deflections in the experiment than predicted.

Results for the DuraSpan girders are also presented in tabular form.

	Absolute Values [MPa]			Normalized Values [%]		
	Fix 1	Fix 2	**Calc.**	Fix 1	Fix 2	**Calc.**
Upper face panel	-7.2	-6.9	**-5.7**	-26	+21	**100**
Lower face panel	-8.3	-7.5	**-8.0**	-4	+6	**100**
Top steel flange	-134	-129	**-138**	+3	+6	**100**
Bottom steel flange	172	166	**166**	+4	± 0	**100**
Deflection [mm]	17.5	19.8	**16.0**	+9	+23	**100**

Table 5.2: Calculated and measured values in DuraSpan girders and normalized values

5.3 Verification of composite girders based on EC5

The main difference between the method explained in Chapter 5.2 and the simplified one in the Eurocode lies in the derivation of the differential equations. As already explained, the equations in the Eurocode are strictly speaking only valid for single-span girders under sinusoidal load, but they also give a good approximation for systems with a linear- distributed load. Therefore the results for girders under four- point bending, like those investigated in this study,

are even less accurate. Another significant difference is the calculation of the stresses in the single cross-sections. In EC 5 the stresses can be calculated directly, while in the method derived in Chapter 5.2, the inner forces in the single cross-sections must be known before the stresses can be calculated.
Below the main steps for calculation of a composite girder in the linear-elastic range in accordance with EC 5 are presented. The necessary material and system properties are the E-modulus of steel, in-plane compression ($\widehat{E}$) and shear modula ($\widehat{G}$) of the bridge deck and the moments of inertia.
The first step involves determination of the composite action between the two cross-sectional parts. This is realized using Equation 5.23. A γ close to 0 indicates a very flexible connection - values close to 1 indicate a very stiff connection ($\Rightarrow \gamma = 1$ full composite action). In the EC 5, three different sections can be calculated with up to 2 flexible joints. Each single cross-section i has its own γ, while γ_2 always indicates the reference stiffness ($\gamma_2 = 1$).

$$\gamma_i = \frac{1}{1 + \dfrac{\pi^2 \cdot E_i \cdot A_i \cdot s_i}{K_i \cdot l^2}} \tag{5.23}$$

With:

γ_i	stiffness factor for the part of composite action	$[-]$
E_i	E-modulus of single cross-sections i	$[MPa]$
A_i	cross-sectional surface of single cross-sections i	$[mm^2]$
s_i	distance between discrete connections (nails, screws...)	$[mm]$
K_i	instantaneous slip modulus according to EC5	$[N/mm]$
l	span	$[mm]$

In the second step, an effective bending stiffness $(EI)_{ef}$ of the girder is determined.

$$(EI)_{ef} = \sum_{i=1}^{2} (E_i I_i + \gamma_i E_i A_i \cdot a_i^2) \tag{5.24}$$

With

$$a_1 = \frac{E_2 A_2 (h_1 + h_2)}{2(\gamma_1 \cdot E_1 A_1 + E_2 A_2)} \tag{5.25}$$

$$a_2 = \frac{h_1 + h_2}{2} - a_1 \tag{5.26}$$

and

h_1, h_2	Single cross-section height
a_i	Distance of neutral axis of cross-section A_i from the neutral axis of composite girder (see Fig. 5.12 on the next page) [20]

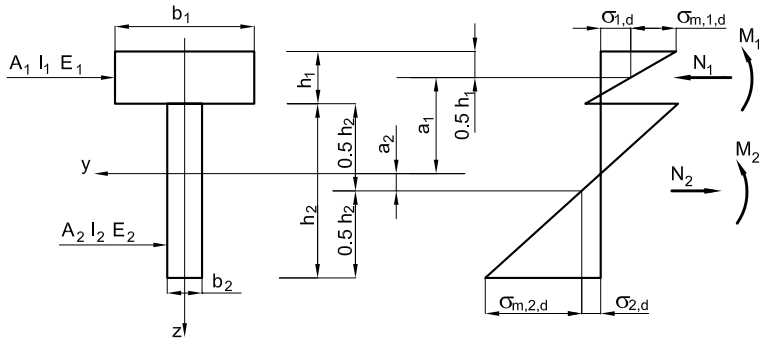

Figure 5.12: Idealized cross-section according to EC 5

The stresses in the cross-section can now be calculated using Equation 5.27

$$\sigma_{i,m,d} = \sigma_{i,d} + \sigma_{m,i,d} \tag{5.27}$$

With

$$\sigma_{i,d} = \frac{M_d}{(EI)_{ef}} \cdot \gamma \cdot a_i \cdot E_i \tag{5.28}$$

$$\sigma_{m,i,d} = \frac{M_d}{(EI)_{ef}} \cdot \frac{h_i}{2} \cdot E_i \tag{5.29}$$

and

$\sigma_{i,d}$	Design value of normal stresses resulting from the pair of normal forces in the full cross-section
$\sigma_{m,i,d}$	Design value of normal stresses resulting from bending moments in the single cross-section

The deflections can be determined using $(EI)_{ef}$ and the appropriate formulas from literature (e.g. [101]). For the girders investigated in this work this gives:

$$_{max}f = \frac{P \cdot l^3}{(EI)_{ef} \cdot 24}(3 \cdot 0.4 - 4 \cdot 0.4^3) \tag{5.30}$$

5.3.1 Derivation of equations for steel/FRP composite girders based on EC 5

In principle only the stiffness factor γ needs to be adapted, since the problem of two different materials in single cross-section 2 has already been solved in Section 5.2.2. The reason γ has to be adapted is the connection of the single cross-sections. While in typical wood-wood composite girders nails or screws are used for connection (discrete), FRP bridge decks provide a type of continuous connection, since $\widehat{G}$ was determined for the surface of the specimens and then normalized on 1 mm^2. The factor s_i in Equation 5.23 on the preceding page takes into account the effect of the discrete connection and allows the

in-plane shear stiffness of a certain joint to be determined. In steel/FRP composite girders, in-plane shear stiffness is affected by the bridge deck's effective width. Therefore the in-plane shear stiffness $\widehat{K}$ of joint has to be multiplied by the effective width of the bridge deck in order to obtain a realistic value for a particular girder. For this reason factor s_i in Equation 5.23, page 126, is replaced by the reciprocal value of the effective width b_{ef} of the bridge deck. Another slight modification concerns a_i. As can be seen in Fig. 5.12 on the previous page, the joint between the two components is infinitesimally small for traditional wood/wood composite girders. This is not the case for girders consisting of a steel main girder and FRP bridge deck. To take into account the web height of the bridge deck, $h_1 + h_2$ in Equations 5.25 and 5.26 have to be replaced by the height H of the complete section (see Fig. 5.13).

$$\gamma_i^* = \frac{1}{1 + \dfrac{\pi^2 \cdot E_i \cdot A_i}{\widehat{K}_i \cdot b_{ef} \cdot l^2}} \tag{5.31}$$

Equations 5.24 - 5.29 give:

$$(EI)_{ef}^* = \sum_{i=1}^{2} \left(E_i I_i + \gamma^* E_i A_i \cdot (a_i^*)^2 \right) \tag{5.32}$$

With

$$a_2^* = \frac{1}{2} \frac{\gamma_1^* E_1 A_1 H}{\sum \gamma_i^* E_i A_i} \tag{5.33}$$

$$a_1^* = -(H - \frac{h_1}{2} - z_{s,2} - a_2^*) \tag{5.34}$$

and

H height of the complete cross-section

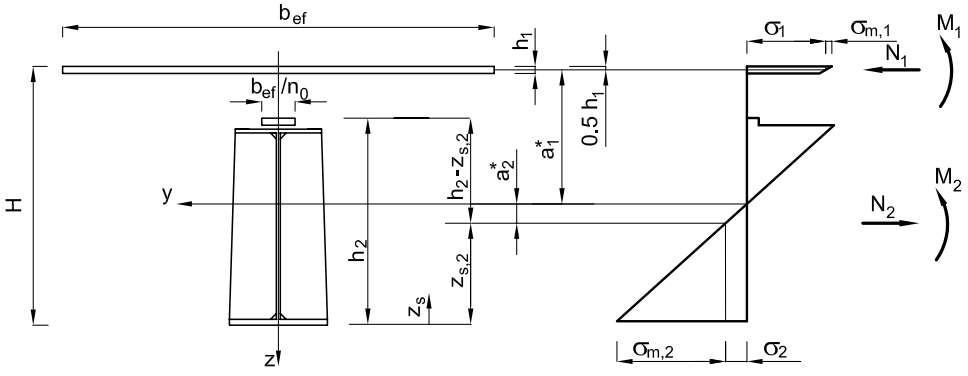

Figure 5.13: Cross-sectional geometry and stress distribution

For the stresses one receives:

$$\sigma_i^* = \frac{M}{(EI)_{ef}^*} \cdot \gamma_i^* \cdot a_i^* \cdot E_i \tag{5.35}$$

$$\sigma_{m,1}^* = \frac{M}{(EI)_{ef}^*} \cdot \frac{h_1}{2} \cdot E_i \tag{5.36}$$

$$\sigma_{m,2}^* = \frac{M}{(EI)_{ef}^*} \cdot z_{s,2} \cdot E_i \tag{5.37}$$

$$\sigma_{i,m}^* = \sigma_i^* + \sigma_{m,i}^* \tag{5.38}$$

With

$z_{s,2}$ neutral axis of single cross-section 2 (see Fig. 5.13)

For the case that single cross-section 2 is bi-symmetric $z_{s,2}$ simplifies to $\frac{h_2}{2}$. Deflections see Equation 5.30, page 127.

5.3.2 Numerical examples

In this section the cross-sectional stress/strain behavior and deflection behavior of the experimental girders investigated in Chapter 4 will be determined using the modified equations based on EC 5. The described method allows only maximum stresses in the single cross-sections to be determined, as seen in Fig. 5.12, page 127. Thus, stress distribution over the cross-sectional height cannot be shown. For this reason results are presented only in tabular form.

Verification of ASSET girder at mid-span

$E_1 = 16\,200 \quad MPa$ | $E_2 = 210\,000 \quad MPa$
$A_1 = 23\,400 \quad mm^2$ | $A_2 = 12\,505 \quad mm^2$
$I_1 = 474\,552 \quad mm^4$ | $I_2 = 5.703 \cdot 10^8 \quad mm^4$
$l = 7\,500 \quad mm$ | $\widehat{K}_1 = 20.88 \cdot 10^{-2} \quad \frac{N}{mm^3}$
$H = 735 \quad mm$ | $b_{ef} = 1500 \quad mm$
$z_{s,2} = 260 \quad mm$ | $\gamma_2 = 1 \qquad$ (Reference stiffness)
$M = 4.0 \cdot 10^8 \quad Nmm$ | $P = 133\,000 \quad N$

$$\gamma_1^* = \frac{1}{1 + \dfrac{\pi^2 \cdot E_1 \cdot A_1}{\widehat{K}_1 \cdot b_{ef} \cdot l^2}} = \frac{1}{1 + \dfrac{\pi^2 \cdot 16\,200 \cdot 23\,400}{20.88 \cdot 10^{-2} \cdot 1\,500 \cdot 7\,500^2}} = 0.825$$

$$a_2^* = \frac{\gamma_1^* E_1 A_1 H}{2(\gamma_1^* E_1 A_1 + \gamma_2 E_2 A_2)} = \frac{0.825 \cdot 16\,200 \cdot 23\,400 \cdot 735}{2(0.825 \cdot 16\,200 \cdot 23\,400 + 1 \cdot 210\,000 \cdot 12\,505)} = 39 \quad mm$$

$$a_1^* = -(H - \frac{h_1}{2} - z_{s,2} - a_2^*) = -(735 - \frac{15.6}{2} - 260 - 39) = -428 \quad mm$$

$$\begin{aligned}(EI)_{ef}^* &= \sum_{i=1}^{2} \left(E_i I_i + \gamma_i^* E_i A_i \cdot (a_i^*)^2\right) \\ &= 16\,200 \cdot 474\,552 + 0.825 \cdot 16\,200 \cdot 23\,400 \cdot 428^2 \\ &\quad + 210\,000 \cdot 5.703 \cdot 10^8 + 210\,000 \cdot 12\,505 \cdot 39^2 = 1.811 \cdot 10^{14} \quad Nmm^2\end{aligned}$$

$$\sigma_1^* = \frac{M}{(EI)_{ef}^*} \cdot \gamma_1^* \cdot a_1^* \cdot E_i = \frac{4.0 \cdot 10^8}{1.811 \cdot 10^{14}} \cdot 0.825 \cdot (-428) \cdot 16\,200 = -12.6 \quad MPa$$

$$\sigma_2^* = \frac{M}{(EI)_{ef}^*} \cdot \gamma_2 \cdot a_2^* \cdot E_2 = \frac{4.0 \cdot 10^8}{1.811 \cdot 10^{14}} \cdot 1 \cdot 39 \cdot 210\,000 = 18.1 \quad MPa$$

$$\sigma_{m,1}^* = \frac{M}{(EI)_{ef}^*} \cdot \frac{h_1}{2} \cdot E_1 = \frac{4.0 \cdot 10^8}{1.811 \cdot 10^{14}} \cdot \frac{15.6}{2} \cdot 16\,200 = 0.3 \quad MPa$$

$$\sigma_{m,2}^* = \frac{M}{(EI)_{ef}^*} \cdot z_{s,2} \cdot E_2 = \frac{4.0 \cdot 10^8}{1.811 \cdot 10^{14}} \cdot 1 \cdot 260 \cdot 210\,000 = 120.6 \quad MPa$$

$$\Rightarrow \sigma_{\mathbf{1,max}}^* = \sigma_1^* - \sigma_{m,1}^* = -12.6 - 0.3 = \mathbf{-12.9} \quad \mathbf{MPa}$$

$$\Rightarrow \sigma_{\mathbf{2,max}}^* = \sigma_2^* + \sigma_{m,2}^* = 18.1 + 120.6 = \mathbf{138.7} \quad \mathbf{MPa}$$

Deflection:

$$_{\mathbf{max}}\mathbf{f} = \frac{P \cdot l^3}{(EI)_{ef} \cdot 24}(3{\cdot}0.4{-}4{\cdot}0.4^3) = \frac{133\,000 \cdot 7500^3}{1.811 \cdot 10^{14} \cdot 24}(3{\cdot}0.4{-}4{\cdot}0.4^3) = \mathbf{12.2} \quad \mathbf{mm}$$

Verification of the experimental girders using the adapted design method according to EC 5 showed that for stiff (in terms of in-plane shear stiffness) FRP bridge decks this method also provides results with good accuracy for stresses in the steel girder and deflections. Calculated stresses in the upper face panel however are slightly higher than those measured in the experimental girders.

	Absolute Values [MPa]			Normalized Values [%]		
	Fix 3	Fix 4	**Calc.**	Fix 3	Fix 4	**Calc.**
Upper face panel	-11.2	-10.1	**-12.9**	+13	+22	**100**
Bottom steel flange	144	141	**139**	+4	+2	**100**
Deflection [mm]	12.5	11.1	**12.2**	+2	-9	**100**

Table 5.3: Results for the ASSET girders, calculated with the method based on EC 5, and normalized values

Verification of DuraSpan girder at mid-span

$E_1 = 11\,700 \quad MPa$ $\qquad$ $E_2 = 210\,000 \quad MPa$
$A_1 = 27\,000 \quad mm^2$ $\qquad$ $A_2 = 12\,204 \quad mm^2$
$I_1 = 729\,000 \quad mm^4$ $\qquad$ $I_2 = 5.508 \cdot 10^8 \quad mm^4$
$l = 7\,500 \quad mm$ $\qquad$ $\widehat{K}_1 = 2.56 \cdot 10^{-2} \quad \frac{N}{mm^3}$
$H = 704 \quad mm$ $\qquad$ $b_{ef} = 1500 \quad mm$
$z_{s,2} = 254 \quad mm$ $\qquad$ $\gamma_2 = 1 \qquad$ (Reference stiffness)
$M = 4.0 \cdot 10^8 \quad Nmm$ $\qquad$ $P = 133\,000 \quad N$

$$\gamma_1^* = \frac{1}{1 + \dfrac{\pi^2 \cdot E_1 \cdot A_1}{\widehat{K}_1 \cdot b_{ef} \cdot l^2}} = \frac{1}{1 + \dfrac{\pi^2 \cdot 11\,700 \cdot 27\,000}{2.56 \cdot 10^{-2} \cdot 1\,500 \cdot 7\,500^2}} = 0.409$$

$$a_2^* = \frac{\gamma_1^* E_1 A_1 H}{2(\gamma_1^* E_1 A_1 + \gamma_2 E_2 A_2)} = \frac{0.409 \cdot 11\,700 \cdot 27\,000 \cdot 704}{2(0.409 \cdot 11\,700 \cdot 27\,000 + 1 \cdot 210\,000 \cdot 12\,204)} = 17 \quad mm$$

$$a_1^* = -(H - \frac{h_1}{2} - z_{s,2} - a_2^*) = -(704 - \frac{18}{2} - 254 - 17) = -424 \quad mm$$

$$\begin{aligned}(EI)_{ef}^* &= \sum_{i=1}^{2} \left(E_i I_i + \gamma_i^* E_i A_i \cdot (a_i^*)^2\right) \\ &= 11\,700 \cdot 729\,000 + 0.409 \cdot 11\,700 \cdot 27\,000 \cdot 424^2 \\ &\quad + 210\,000 \cdot 5.508 \cdot 10^8 + 210\,000 \cdot 12\,204 \cdot 17^2 = 1.397 \cdot 10^{14} \quad Nmm^2\end{aligned}$$

$$\sigma_1^* = \frac{M}{(EI)_{ef}^*} \cdot \gamma_1^* \cdot a_1^* \cdot E_i = \frac{4.0 \cdot 10^8}{1.397 \cdot 10^{14}} \cdot 0.409 \cdot (-424) \cdot 11\,700 = -5.8 \quad MPa$$

$$\sigma_2^* = \frac{M}{(EI)_{ef}^*} \cdot \gamma_2 \cdot a_2^* \cdot E_2 = \frac{4.0 \cdot 10^8}{1.397 \cdot 10^{14}} \cdot 1 \cdot 17 \cdot 210\,000 = 10.2 \quad MPa$$

$$\sigma^*_{m,1} = \frac{M}{(EI)^*_{ef}} \cdot \frac{h_1}{2} \cdot E_1 = \frac{4.0 \cdot 10^8}{1.397 \cdot 10^{14}} \cdot \frac{18}{2} \cdot 11\,700 = 0.3 \quad MPa$$

$$\sigma^*_{m,2} = \frac{M}{(EI)^*_{ef}} \cdot z_{s,2} \cdot E_2 = \frac{4.0 \cdot 10^8}{1.397 \cdot 10^{14}} \cdot 1 \cdot 254 \cdot 210\,000 = 152.8 \quad MPa$$

$$\Rightarrow \sigma^*_{\mathbf{1,max}} = \sigma^*_1 - \sigma^*_{m,1} = -5.8 - 0.3 = \mathbf{-6.1} \quad \mathbf{MPa}$$

$$\Rightarrow \sigma^*_{\mathbf{2,max}} = \sigma^*_2 + \sigma^*_{m,2} = 10.2 + 152.8 = \mathbf{163} \quad \mathbf{MPa}$$

Deflection:

$$_{\mathbf{max}}\mathbf{f} = \frac{P \cdot l^3}{(EI)_{ef} \cdot 24}(3{\cdot}0.4 - 4{\cdot}0.4^3) = \frac{133\,000 \cdot 7500^3}{1.397 \cdot 10^{14} \cdot 24}(3{\cdot}0.4 - 4{\cdot}0.4^3) = \mathbf{15.8} \quad \mathbf{mm}$$

Results in tabular form

	Absolute Values [MPa]			Normalized Values [%]		
	Fix 1	Fix 2	**Calc.**	Fix 1	Fix 2	**Calc.**
Upper face panel	-7.2	-6.9	**-6.1**	-18	-13	**100**
Bottom steel flange	172	166	**163**	+5	+2	**100**
Deflection [mm]	17.5	19.8	**15.8**	+11	+25	**100**

Table 5.4: Results for the DuraSpan girders, calculated with the method based on EC 5, and normalized values

As Table 5.4 shows, the design method based on the EC 5 is also suitable for calculating load carrying behavior of composite girders with bridge decks having a low in-plane shear stiffness. Stresses in the lower steel flange can be determined with good accuracy but, as for the ASSET girders, the ones in the upper face panel are less accurate compared to the measured results from the experimental girders. The deflections could be determined with good accuracy for girder Fix 1. For girder Fix 2 a similar deviation of 25% as after the method based on Natterer has to be mentioned.

Calculation of two girders with two different bridge decks showed therefore, that there is a certain variation of the results of the upper face panel. This effect could already be determined for the calculations based on Natterer in Section 5.2.2.

5.4 Prediction of failure load of composite girders

The failure load cannot be determined using the design methods described in previous sections since they are only valid for linear-elastic behavior. The experiments showed that both girder systems are more or less in the plastic region at failure load. This problem can only be solved by an iteration of the cross-sectional strain distribution. Based on the system properties evaluated in Chapter 3, the failure load of composite girders with the tested deck systems can be determined.

Failure in FRP decks with only partial shear connection between the upper and lower face panels can occur in very different modes, depending on the shear to compression stiffness ratio, the shear to compression resistance ratio, the loading type and bridge span. Decks with a high shear resistance can fail in compression in the lower face panel for $\gamma \Rightarrow 0$ (no composite action); in compression in both face panels simultaneously for $\gamma \approx 0.5$ (partial composite action); and in compression in the upper face panel for $\gamma = 1$ (full composite action). Thereby, the maximum bending moment will be reached in the case of $\gamma \approx 0.5$ where both face panels are fully used. Decks with very low shear resistance can fail in compression in the lower face panel for $\gamma = 0$; in compression in the lower face panel or in shear in the deck core for $\gamma \approx 0.5$ (simultaneously if the shear behavior is "pseudo-plastic"); and in shear in the deck core for $\gamma = 1$. At this project stage it was not yet possible to develop a general method of ultimate failure load prediction, which covers all these cases. However, for the two deck types used, DuraSpan ($\gamma = 0.41 \Rightarrow 0.5$, low shear resistance with "pseudo-plastic"behavior, see Fig. 3.45, page 60) and ASSET ($\gamma = 0.83 \Rightarrow 1$, high shear resistance with elastic-brittle behavior, see also Fig. 3.45), the ultimate failure load of the girders was predicted using assumptions regarding failure modes and axial strains at failure in the face panels shown in Fig. 5.14.

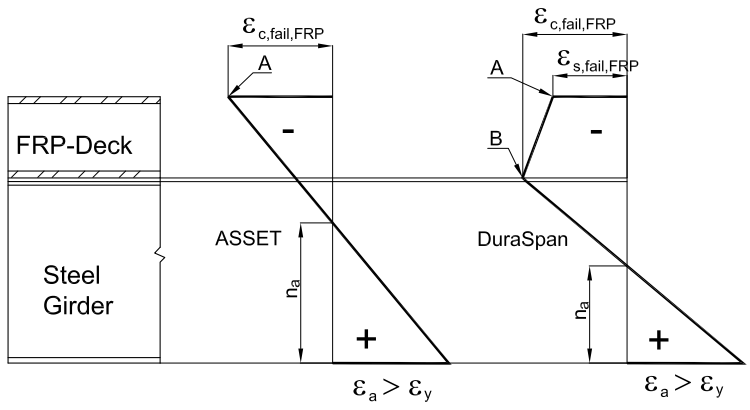

Figure 5.14: Prediction of axial strain distributions for ultimate failure load.

With:

$\epsilon_{c,fail,FRP}$	compressive failure strain of deck face panel
$\epsilon_{s,fail,FRP}$	axial strain at shear failure in the core of the deck
ϵ_a	axial strain in bottom steel flange
n_a	neutral axis

Since the span of the girder has a decisive influence on the failure mode it has to be verified, whether the assumptions taken in Fig. 5.14 on the preceding page apply to the experimental girders. For that reason the maximum force in the upper face panel has to be calculated.

The maximum compression force in the upper face panel can be determined using Equations 5.39 and 5.40. The controlling force is the smaller one (see Equation 5.41).

$$F_{Rs,FRP} = R_s \cdot b_{ef}(\Phi \cdot l) \tag{5.39}$$

$$F_{Rc,FRP} = \frac{R_c}{2} \cdot b_{ef} \tag{5.40}$$

$$F_{max,FRP} = min \begin{cases} F_{Rs,FRP} \\ F_{Rc,FRP} \end{cases} \tag{5.41}$$

With:

$F_{Rs,FRP}$	maximum force which can be introduced in the upper face panel by in-plane shear stiffness
$F_{Rc,FRP}$	maximum compression force which can be borne by upper face panel
R_c	in-plane compression resistance of bridge deck (Section 3.5.1, page 51)
R_s	in-plane shear resistance of bridge deck (Section 3.5.2, page 59)
b_{ef}	effective width of bridge deck
Φ	see Fig. 5.6, page 109
l	span

Equation 5.41 indicates also where failure will occur - in the upper or lower face panel. If Equation 5.39 gives a greater force than Equation 5.40, failure will occur in the upper face panel as it is the case for the ASSET girders (see Fig. 5.14 on the preceding page). If $F_{Rs,FRP} \leq F_{Rc,FRP}$ then, failure occurs in the lower face panel as it the case for the DuraSpan girders (see Fig. 5.14).

With the boundary conditions derived for each girder in Equations 5.39 and 5.40, cross-sectional strain distribution and thus failure load can be determined. Concerning the ASSET girders, only $F_{Rc,FRP}$ (applied at point A in Fig. 5.14) is needed since the strain distribution along the section height is assumed as linear. Concerning the DuraSpan girders, $F_{Rs,FRP}$ applied at point A and $F_{Rc,FRP}$ applied at point B are needed to clearly determine failure load. In both cases, the inner forces have to be in equilibrium.

$$\sum_{i=1}^{n} F_i = \sum C_i + \sum T_i \stackrel{!}{=} 0 \tag{5.42}$$

With:

C_i	compression forces
T_i	tensile forces

Equation 5.42 has only one solution, which can be obtained by varying the neutral axis n_a. The sum of moments around one point of the cross-section, together with the static system, give the failure load. Failure load of composite girders treated in this thesis can therefore be determined as shown in Equation 5.43. This procedure will be explained by means of the girders investigated in Chapter 4.

$$_{max}F = \frac{_{max}M}{\Phi \cdot l} = \frac{\sum C_i \cdot z_i + \sum T_i \cdot z_i}{\Phi \cdot l} \tag{5.43}$$

With:

$_{max}F$	ultimate load
$_{max}M$	ultimate bearable bending moment
z_i	lever arm of axial forces

Figs. 4.24, page 77 and 4.45, page 90 show, that strain distribution over the width of the bridge deck cannot be assumed as linear for the FLS since strains decrease towards the edges. Therefore, the effective width of the bridge deck has to be reduced. The effective width depends, as the failure load, on many parameters as for example in-plane shear stiffness of face panels, plastic behavior of materials or span of the girders [40]. In this research project it was not possible to consider all those parameters and to develop a general method for determination of effective width of FRP bridge decks. For that reason the effective width of the affected face panels is reduced globally by the factor **0.9**. This concerns the upper and lower face panel of the ASSET deck and the lower face panel of the DuraSpan deck. Here once again the diagrams of the effective width of both girders.

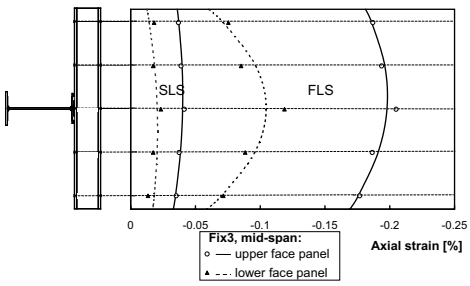

Figure 5.15: Effective width ASSET girder Fix 3

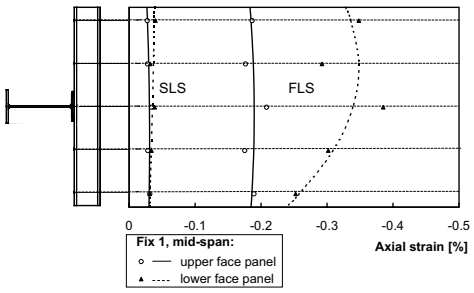

Figure 5.16: Effective width DuraSpan girder Fix 1

5.4.1 Numerical examples

Since the presented method should predict failure load of steel/FRP composite girders using ASSET or DuraSpan bridge decks, used failure stresses are the ones determined in Section 3.5.1, page 51 and not the calculated stresses resulting from girder experiments.

Failure load ASSET girder

$E_a = 210\,000 \quad MPa$
$R_s = 609 \quad \frac{kN}{m^2}$
$b_{ef} = 0.9 \cdot 1500 = 1350 \quad mm$
$\Phi \cdot l = 3000 \quad mm$
$t_{fl} = 15.6 \quad mm$

$\widehat{E}_{FRP} = 16\,200 \quad MPa$
$R_c = 1290 \frac{kN}{m}$
$\sigma_{c,fail} = 41 \quad MPa$
$\epsilon_y = 0.18 \quad \%$

$$F_{Rs,FRP} = R_s \cdot b_{ef} \cdot \Phi \cdot l = 609 \cdot 1.35 \cdot 3.0 = 2466 \quad kN$$

$$F_{Rc,FRP} = \frac{R_c}{2} \cdot bef = \frac{1290}{2} \cdot 1.35 = 871 \quad kN$$

$$\Rightarrow F_{Rc,FRP} < F_{Rs,FRP} \qquad \Rightarrow \text{Failure in upper face panel}$$

Compressive failure strain:

$$\epsilon_{c,fail,FRP} = \frac{\sigma_{c,fail}}{\widehat{E}_{FRP}} = \frac{41}{16\,200} = 0.25 \quad \%$$

After determination of location of failure (upper or lower face panel) and the corresponding failure strain, the strain distribution along the cross-sectional height is known. An iteration of neutral axis n_a leads to the following distribution:

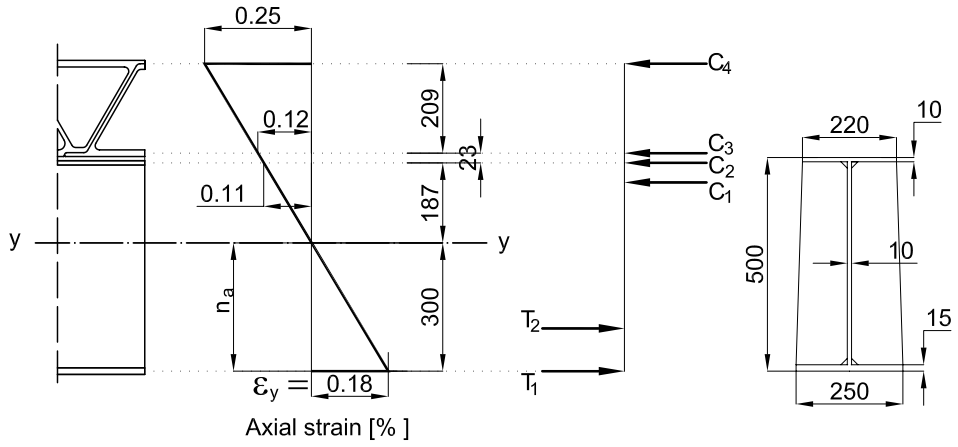

Figure 5.17: State of equilibrium of inner forces, ASSET girder

Equilibrium of inner forces with Equation 5.42, page 135.

$$\begin{aligned}\sum_{i=1}^{n} F_i &= T_1 + T_2 + C_1 + C_2 + C_3 + C_4 \\ &= 380 \cdot 250 \cdot 15 + \frac{1}{2} \cdot 380 \cdot 300 \cdot 10 \\ &\quad - \frac{1}{2} \cdot 1.10 \cdot 10^{-3} \cdot 2.1 \cdot 10^5 \cdot 10 \cdot 187 - 1.10 \cdot 10^{-3} \cdot 2.1 \cdot 10^5 \cdot 10 \cdot 220 \\ &\quad - 1.20 \cdot 10^{-3} \cdot 16\,200 \cdot 15.6 \cdot 1\,350 - 871 \cdot 10^3 \\ &= -10 \quad kN \approx 0\end{aligned}$$

The load-bearing capacity can now be determined by accumulating the sum of moments around any point. In this example the neutral axis of the lower steel flange was chosen.

$$\begin{aligned}\overset{\curvearrowleft}{M_0} &= -570 \cdot \frac{1}{3} \cdot 0.300 + 216 \cdot \left(0.300 + \frac{2}{3} \cdot 0.187\right) \\ &\quad + 508 \cdot 0.488 + 409 \cdot 0.511 + 871 \cdot 0.72 \\ &= 1119 \quad kNm\end{aligned}$$

$\Rightarrow$ Maximum load bearing capacity: $\quad \mathbf{_{max}M = 1119 \quad kNm}$

Dividing $_{max}M$ by $\Phi \cdot l$ gives the calculated failure load of the ASSET girder.

$$\Rightarrow \quad \mathbf{_{max}F_{ASSET}} = \frac{_{max}M}{\Phi \cdot l} = \frac{1119}{0.4 \cdot 7.5} = \mathbf{373 \quad kN}$$

	Absolute Values [kN]		Normalized Values [%]	
	Experiment	**Calculation**	Experiment	**Calculation**
Fix 3	373	**373**	±0	**100**
Fix 4	400	**373**	+7	**100**

Table 5.5: Calculated and measured failure loads of the ASSET girder and normalized values

Table 5.5 shows that the failure loads of composite girders using the ASSET deck can be predicted with the proposed method with good accuracy. For girder Fix 4 the failure load was even underestimated.

Failure load DuraSpan girder

$E_a = 210\,000 \quad MPa$
$\widehat{E}_{FRP} = 11\,700 \quad MPa$
$R_s = 134 \quad \frac{kN}{m^2}$
$R_c = 1230 \quad \frac{kN}{m}$
$\Phi \cdot l = 3000 \quad mm$
$\epsilon_y = 0.18 \quad \%$
$b_{ef,u} = 1500 \quad mm$
$b_{ef,l} = 0.9 \cdot 1500 = 1350 \quad mm$
$\sigma_{c,fail} = 34 \quad MPa$
$\tau_{fail} = 0.13 \quad MPa$
$t_{fl} = 18 \quad mm$

$$F_{Rs,FRP} = R_s \cdot b_{ef,u} \cdot \Phi \cdot l = 134 \cdot 1.5 \cdot 3.0 = 603 \quad kN$$

$$F_{Rc,FRP} = \frac{R_c}{2} \cdot b_{ef,l} = \frac{1230}{2} \cdot 1.35 = 830 \quad kN$$

$$\Rightarrow F_{Rc,FRP} > F_{Rs,FRP} \qquad \Rightarrow \text{Failure in lower face panel}$$

Compressive failure strain:

$$\epsilon_{c,fail,FRP} = \frac{\sigma_{c,fail}}{\widehat{E}_{FRP}} = \frac{34}{11\,700} = 0.29 \quad \%$$

Axial strain at shear failure:

$$\epsilon_{s,fail,FRP} = \frac{\tau_{fail}(\Phi \cdot l)}{t_{fl} \cdot \widehat{E}_{FRP}} = \frac{0.13 \cdot (0.4 \cdot 7500)}{18 \cdot 11\,700} = 0.19 \quad \%$$

After iteration the strain distribution shown in Fig. 5.18 results.

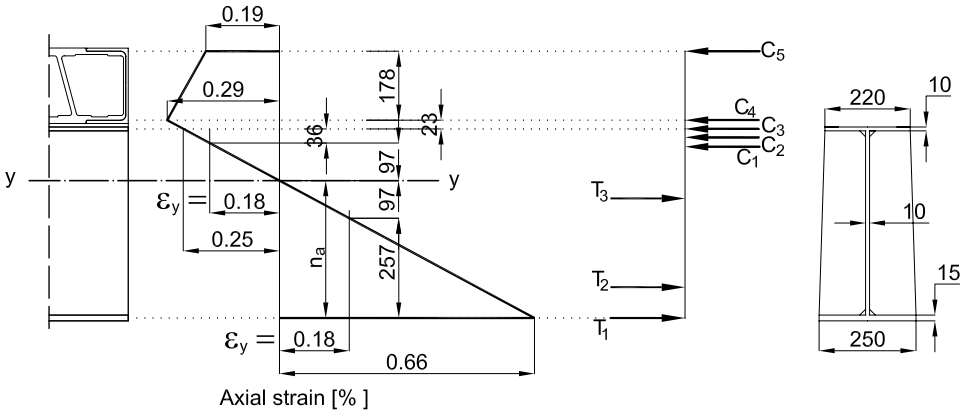

Figure 5.18: State of equilibrium of inner forces, DuraSpan girder

Equilibrium of inner forces:

$$\begin{aligned}\sum_{i=1}^{n} F_i &= T_1 + T_2 + T_3 + C_1 + C_2 + C_3 + C_4 + C_5 \\ &= 380 \cdot 250 \cdot 15 + 380 \cdot 257 \cdot 10 + \frac{1}{2} \cdot 380 \cdot 97 \cdot 10 \\ &\quad - \frac{1}{2} \cdot 380 \cdot 97 \cdot 10 - 380 \cdot 10 \cdot 36 - 380 \cdot 10 \cdot 220 - 830 \cdot 10^3 - 603 \cdot 10^3 \\ &= -4 \quad kN \approx 0\end{aligned}$$

Load bearing capacity:

$$\begin{aligned}\overset{\curvearrowleft}{M_0} &= -977 \cdot \frac{1}{3} \cdot 0.257 - 184 \cdot \left(0.257 + \frac{1}{3} \cdot 0.097\right) \\ &\quad + 184 \cdot \left(0.354 + \frac{2}{3} \cdot 0.097\right) + 137 \cdot \left(0.451 + \frac{1}{2} \cdot 0.036\right) + 836 \cdot 0.487 \\ &\quad + 830 \cdot 0.51 + 603 \cdot 0.688 = 1250 \quad kNm\end{aligned}$$

$\Rightarrow$ Maximum load bearing capacity: $\mathbf{_{max}M = 1250 \quad kNm}$

Calculated failure load of DuraSpan girder:

$$\Rightarrow \quad \mathbf{_{max}F_{Dura}} = = \frac{_{max}M}{\Phi \cdot l} = \frac{1250}{0.4 \cdot 7.5} = \mathbf{417} \quad \mathbf{kN}$$

	Absolute Values [kN]		Normalized Values [%]	
	Experiment	**Calculation**	Experiment	**Calculation**
Fix 1	400	**417**	-4	**100**
Fix 2	415	**417**	~ 0	**100**

Table 5.6: Calculated and measured failure loads of the DuraSpan girder and normalized values

Table 5.6 shows that also the failure load of composite girders with low in-plane shear stiffness can be predicted with the proposed method with good accuracy. The load bearing capacity is slightly ($\sim$4%) over estimated.

5.5 Comparison girder experiments ⇔ theoretical results

5.5.1 SLS and ULS load level

Since all experiments behaved linear-elastically up to ∼140 kN/jack, one can assume that the following conclusions for ULS are also valid for SLS.

The results based on the exact solution of the differential equations for the investigated static system from Section 5.2.2, page 113 correspond very closely to the conducted experiments. Very stiff (ASSET) or relatively flexible (DuraSpan) bridge decks in terms of in-plane shear stiffness do not seriously influence the accuracy of the results of the investigated method. Nevertheless a certain deviation to the calculated values must be noticed for the upper face panel of both bridge deck system. This effect is probably caused by the high secondary bending moments the upper face panels. Therefore, in future girder experiments, strain gages should be installed on both sides of the upper face panel. This deviation in the upper face panel was not as pronounced in the ASSET girders, which can be explained by the very small relative displacements of the face panels of this system.

The results of the method shown in Section 5.3, based on EC 5, also describe the load-bearing behavior with good accuracy, but the same deviations of the results of the upper face panels must be noticed. Since the absolute values in terms of stresses are small (< 3 MPa) the conclusion can be drawn, that this method is also suitable to estimate the load bearing behavior of steel/FRP composite girders. Compared to the results from the exact solution of the differential equations, only the maximum stresses in each cross-section can be determined; thus stress/strain distribution over the cross-section height is unknown.

5.5.2 Failure limit state, FLS

As can be seen in Table 5.5, page 137, and Table 5.6 on the preceding page, the predicted failure loads match well for the ASSET and DuraSpan girders. Failure load of DuraSpan girders is over estimated of $\sim 4\%$. The proposed method is therefore well suited for determining the failure load of composite girders with ASSET or DuraSpan bridge decks. Calculation for the DuraSpan girder showed, that this method can also take into account partial composite action of the bridge deck for a given span. This is very important for future work, when the failure load of composite girders with different spans shall be determined.

At all three load levels, no relative displacement in the adhesive layer between the structural components was observed during the experiments. The assumption of full composite action in the two design methods concerning the adhesive layer is therefore justifiable. An analytical verification is shown in Chapter 6 on the next page.

6 Influence of adhesive type and thickness

6.1 Introduction

A major factor in Chapter 5 is the assumption of full composite action in the adhesively-bonded joint. For the investigated girder systems this could be verified, since there was no relative displacement in the joint. These results cannot of course be applied to systems with different adhesives or adhesive thicknesses. To make this possible, a parameter study was carried out for two different adhesives and thicknesses between 10 and 50 mm. A minimum thickness of 10 mm was chosen in order to compensate manufacturing or rolling tolerances of the steel girder. Since steel/FRP composite girders are considered for multi-girder bridges, the minimum adhesive thickness is also necessary to equalize different vertical positions of the steel girders. Thicknesses greater than 50 mm were not considered because they were estimated as not being relevant for practical applications.

6.2 Adhesives

The two investigated adhesives should have different material properties in order to obtain information as to wether the assumption of full composite action in the adhesively-bonded joint is also valid for soft adhesives. For this reason the adhesives SikaDur 330 and SikaForce 7851 were chosen. SikaDur 330 was already described in Section 4.3.2, page 66, since it was used to manufacture the composite girders. SikaForce 7851 also has two components but it is a polyurethane adhesive. The main characteristics are presented in Table 6.1.

	SikaForce 7851
Mixing ratio	1.72 : 1
Density, $[\frac{kg}{m^3}]$	1100
Viscosity @ 25°C	Thixotropic
Potlife @ 25°C	15 Minutes
Tensile strength [MPa]	22
Lapshear strength [MPa]	15

Table 6.1: Material properties, SikaForce 7851

The E-modulus and G-modulus had to be investigated by means of experiments [28]. Since the adhesive is always under compression in single-span composite girders, the given E-modulus is also considered in compression. The G-modulus was determined by the "napkin-ring"test [46]. The SikaDur 330 adhesive behaved so stiffly, that no useful data concerning the G-modulus could be derived from the experiments. The G-modulus of SikaDur 330 was thus analytically determined by assuming isotropic behavior. Comparable calculations have already been carried out by A. Bassetti in [17]. The G-modulus for SikaDur 330 was determined as follows:

With:

$E_{c,330} = 3050 \quad MPa \qquad\qquad \nu = 0.35$

we get

$$G_{330} = \frac{E}{2(1+\nu)} = \frac{3050}{2(1+0.35)} \cong 1100 \quad MPa \tag{6.1}$$

	SikaDur 330 [MPa]	SikaForce 7851 [MPa]
E-modulus	3050	370
G-modulus	1100	355

Table 6.2: Summary of adhesive properties, taken from [28]

6.3 Stiffness K

In order to have results comparable to those from the bridge decks, the shear stiffness of the adhesives is also calculated for a relative displacement of 1 mm and normalized on a surface of 1 mm^2 (see Fig. 6.1 on the facing page).

The shear stress in a section of $1mm^2$ and $1mm$ of deformation is equivalent to the in-plane shear stiffness K. By assuming that for small angles $tan\alpha = \alpha$, we get:

$$\tau = K = G \cdot \alpha = G \cdot \frac{1}{t} \tag{6.2}$$

6.4 Parameter study

The parameter study was carried out by varying t from 10-40mm for both adhesives.

Figure 6.2 on the next page shows that with increasing adhesive thickness, the stiffness of the joint decreases. The loss of stiffness is more pronounced in the range between 10 and 20 mm than between 20 and 40 mm.

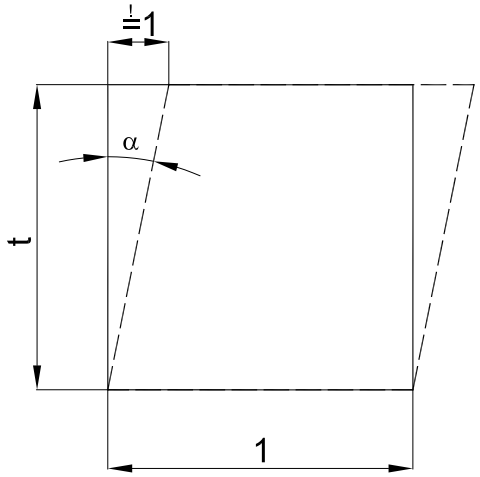

Figure 6.1: Deformed adhesive element; t = adhesive thickness (not to scale)

The flexible SikaForce 7851 shows relatively low values right from the beginning, but when comparing these values with the stiffness of the ASSET ($K = 20.88 \cdot 10^{-2} N/mm^3$) or the DuraSpan ($K = 2.56 \cdot 10^{-2} N/mm^3$) deck, it must be said that even at 50 mm thickness, the adhesive is still sufficiently stiff to provide full composite action.

This study only considers short-term loads. Long-term effects such as creep have to be investigated separately. Creep does not seem to be decisive since shear stresses under dead loads are very small (c.f. SLS: $_{max}\tau = 0.5 \quad MPa$). The stresses under dead load can even be reduced when designing an un-propped system. Un-propped means, that the dead load of the structure does not act on the composite girder but on the steel girder.

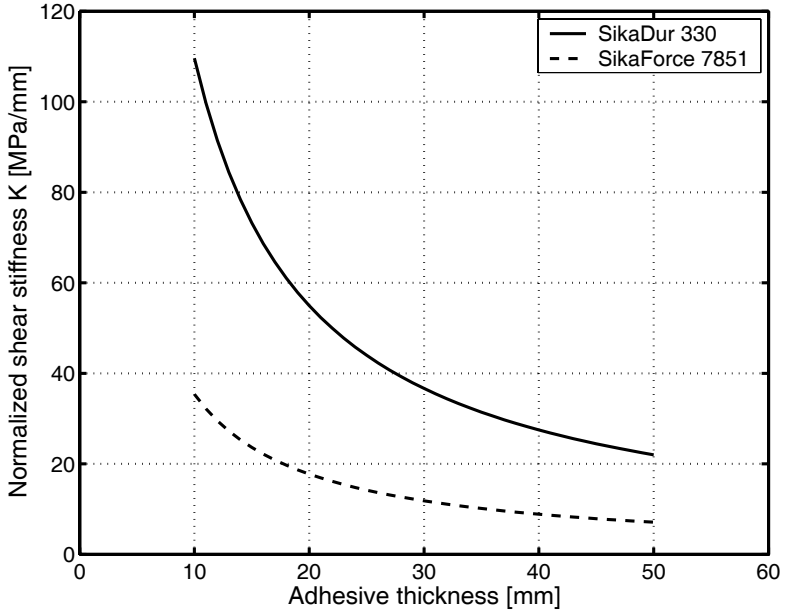

Figure 6.2: Change in adhesive shear stiffness with increasing adhesive thickness

6.5 Numerical examples

The stiffness factor K is not very expressive, therefore the stiffnesses of the adhesively-bonded joints of the experimental girders investigated in Chapter 4 are calculated using the method described in Section 5.3.1. To show the stiffness of the adhesively-bonded joint, only single cross-section 2 is considered for the calculation (see Fig. 6.3). For this calculations only the face panel of the ASSET deck was considered.

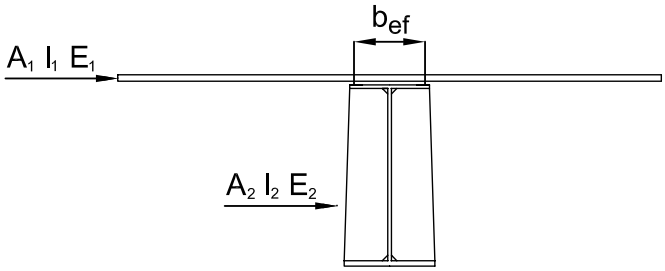

Figure 6.3: Cross-section for calculation of the stiffness of adhesively-bonded joint

The degree of composite action in a girder can easily be described by the factor γ. As already explained in Section 5.3.1, a γ of 1 signifies full composite action between structural components, while the value 0 signifies no composite action at all. The degree of composite action due to the adhesively-bonded joint is calculated for both adhesives - SikaDur 330 and SikaForce 7851. To show the degree of composite action with high adhesive thicknesses, γ is also calculated for a thickness of 40 mm.

Composite action using SikaDur 330

$E_1 = 16\,200 \quad MPa$ $\qquad$ $A_1 = 23\,400 \quad mm^2$

$b_{ef} = 196 \quad mm$ (adhesive width) $\qquad$ $K_{10} = 110 \quad \frac{N}{mm^3}$

$l = 7\,500 \quad mm$ $\qquad$ $K_{50} = 21 \quad \frac{N}{mm^3}$

$$\gamma_{10}^{*} = \frac{1}{1 + \frac{\pi^2 \cdot E_i \cdot A_i}{K_i \cdot b_{ef} \cdot l^2}} = \frac{1}{1 + \frac{\pi^2 \cdot 16\,200 \cdot 23\,400}{110 \cdot 196 \cdot 7\,500^2}} = 0.997$$

$$\gamma_{50}^{*} = \frac{1}{1 + \frac{\pi^2 \cdot E_i \cdot A_i}{K_i \cdot b_{ef} \cdot l^2}} = \frac{1}{1 + \frac{\pi^2 \cdot 16\,200 \cdot 23\,400}{21 \cdot 196 \cdot 7\,500^2}} = 0.981$$

Composite action using SikaForce 7851

$E_1 = 16\,200 \quad MPa$ $\qquad$ $A_1 = 23\,400 \quad mm^2$
$b_{ef} = 196 \quad mm$ (adhesive width) $\qquad$ $K_{10} = 37 \quad \frac{N}{mm^3}$
$l = 7\,500 \quad mm$ $\qquad$ $K_{50} = 8 \quad \frac{N}{mm^3}$

$$\gamma_{10}^{*} = \frac{1}{1 + \dfrac{\pi^2 \cdot E_i \cdot A_i}{K_i \cdot b_{ef} \cdot l^2}} = \frac{1}{1 + \dfrac{\pi^2 \cdot 16\,200 \cdot 23\,400}{37 \cdot 196 \cdot 7\,500^2}} = 0.991$$

$$\gamma_{50}^{*} = \frac{1}{1 + \dfrac{\pi^2 \cdot E_i \cdot A_i}{K_i \cdot b_{ef} \cdot l^2}} = \frac{1}{1 + \dfrac{\pi^2 \cdot 16\,200 \cdot 23\,400}{8 \cdot 196 \cdot 7\,500^2}} = 0.959$$

The results show that even for a soft adhesive of 50 mm thickness nearly full composite action is achieved. For the experimental girders with 10-mm adhesive thickness and adhesive SikaDur 330, full composite action can be determined in the joint as was already expected from the experiments. Nevertheless, the long-term behavior of thick adhesive joints has to be investigated.

7 Conclusions

7.1 Adhesively-bonded deck-to-girder connections

The girder experiments showed that the manufacturing method for adhesively-bonded FRP/steel composite girders proposed in this thesis is reliable and effective; even multi-girder systems can be constructed. Furthermore the adhesively-bonded joint provided full composite action. The composite action between the GFRP bridge decks and steel girders increases the stiffness and the resistance and reduces the deflections of the composite girders considerably. The possible deck contribution depends mainly on the in-plane deck stiffness in the longitudinal direction of the bridge axis. The adhesively-bonded joint between the two different GFRP bridge deck systems and steel girders behaved well under quasi-static and fatigue loading. The joint did not fail and showed no damage after ten million fatigue cycles. A ductile failure mode could be achieved due to deck compression failure during yielding of the steel girder. For other adhesive thicknesses than the one tested in the experimental girders and for a second (polyurethane) adhesive, it could be shown that the assumption of full composite action is justifiable even for high adhesive thicknesses and soft adhesives. This was verified by the parameter study carried out in Chapter 6.

7.2 Design method for steel/FRP composite girders

A design method, based on the work of J. Natterer [91], was developed which allows determination of the cross-sectional stress/strain distribution for SLS and ULS and the deflections of steel/FRP composite girders in the elastic region. This design method developed in Section 5.2 can take into account the degree of composite action originating from the GFRP bridge deck regardless of the deck's in-plane shear stiffness (high or low).

The design method based on EC 5, developed in Section 5.3.1, provides results similar to the values measured in the experiments and is therefore also well suited for determining the load-bearing behavior of steel/FRP composite girders. This method is easier to use but allows only determination of maximum stresses in the single cross-sections; thus strain distribution over the full cross-sectional height cannot be calculated. Nevertheless, for a first estimation of the load-bearing behavior of a steel/FRP composite girder, this method can be recommended.

In Section 5.4, it was shown that the failure load of adhesively-bonded steel/FRP composite girders using the tested deck systems can be determined with very good accuracy. A ductile failure behavior of the composite girder can be achieved by designing the steel girder in such a way that it yields before failure of the bridge deck.

7.3 Experimental technique to determine deck-system properties

In order to act efficiently as part of the top chord in a bridge girder, FRP bridge-deck systems need sufficient compression and shear stiffness and resistance in the bridge direction. With the help of the experimental technique proposed in Chapter 3, these system properties could be determined for the investigated bridge decks. The described set-up for the compression and shear experiments was used to determine the system properties of pultruded FRP bridge- deck profiles, but is not limited to these. With a **S**tandard **O**peration **P**rocedure, still to be developed, other bridge-deck types (e.g. sandwich decks) could also be tested in order to determine system properties.

In pultruded bridge deck systems, stiffness is affected by the multitude of adhesively- bonded joints between the pultruded profiles and by the pultruded profiles themselves. The investigation clearly showed that epoxy bonded joints are much stiffer than polyurethane bonded joints and that configurations with the former show considerably less loss in deck stiffness than with the latter.

Concerning in-plane shear resistance and stiffness, the experiments revealed that not the material properties of the single deck parts (web, flange) are determined, but the geometrical configuration. From this it follows that systems which bear the in-plane shear load by truss action are much more efficient for girders with composite action than those bearing the load with Vierendeel action, but on the other hand, they have no system ductility (brittle failure mode!).

7.4 Contribution of the thesis to composite steel/FRP girders

This thesis provides engineers with a tool to determine in practice, and without difficult FEM analysis or experiments, the load-bearing behavior of adhesively-bonded steel/FRP composite girders. The design method developed allows the in-plane shear stiffness of bridge decks to be taken into account and all significant parameters (cross-sectional stress/strain distribution, deflections for SLS and ULS and the failure load with the appropriate the stress/strain distribution) to be determined.

The author's contribution to the state of the art of adhesively- bonded steel/FRP composite girders can be described as follows:

- It was shown, that adhesive bonding is a feasible and reliable connection technique to build steel/FRP composit girders;

- An experimental technique for determination of the system properties of FRP bridge decks was developed. The proposed method for determining the in-plane compression and shear modulus and the in-plane compression and shear resistance can easily be applied to other bridge decks, even sandwich decks. The availability of these two system properties is a

major condition for calculation the load-bearing behavior of steel/FRP composite girders;

- The cross-sectional stress/strain distribution and deflection of steel/FRP composite girders can be determined by applying the proposed design method for SLS and ULS. Another design method to predict the failure load of composite girders with ASSET or DuraSpan bridge decks was also developed. The particularity of both methods is that the in-plane shear stiffness of FRP bridge decks can be taken into account. The more-or-less flexible in-plane shear stiffness constitutes a partial "shear connection" between the upper and lower face panels. To date, no other analytical model exists for determining this behavior.

7.5 Future work

The results of this work, especially of the girder experiments, are based on a relatively small number of specimens. To achieve a better statistical basis, more experiments are certainly needed in the future.

Since the domain of steel/FRP composite girders is very new, this study cannot cover all aspects. Some remaining tasks for future research to develop a dimensioning method for steel/FRP bridges using the girders described in this thesis are:

- Investigations concerning load-deformation behavior transverse to the bridge axis of multi-girder bridges;
- The effect of concentrated loads close to abutments and their influence on the transmission of shear loads into the joint and bridge deck itself;
- The load-bearing capacity under negative bending moments (multi-span-girders);
- The influence of different adhesives on load-bearing capacity and creep behavior;
- The development of partial safety factors for steel/FRP composite girders.

Appendix A

Diagrams for compression experiments

A.1 DuraSpan

The measured results are shown in Fig. A.1 - A.18, page 151. Fig. A.1 - A.6 on the next page show the load and the deformation measured by the press. Fig. A.7, page 153 - A.12, page 153 show the load versus the strains measured by strain gages and Fig. A.13, page 154 - A.18, page 154 show the load and deformation of the Ω-gages.

A.1.1 Load-deformation behavior

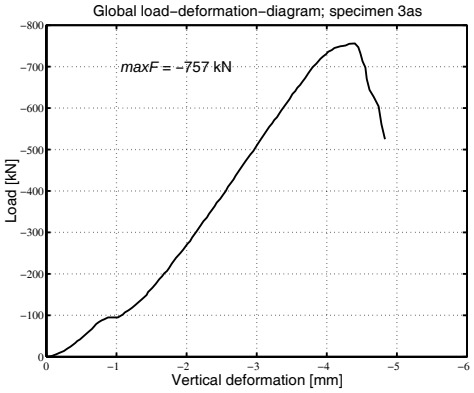

Figure A.1: Load-deformation behavior, specimen 3as

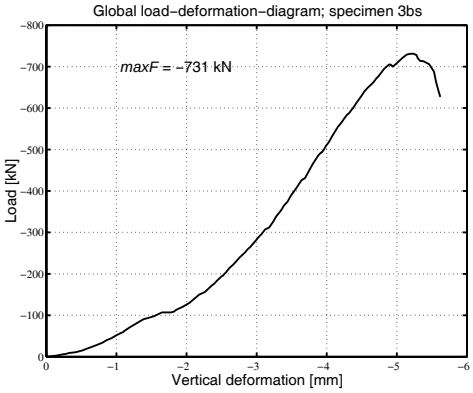

Figure A.2: Load-deformation behavior, specimen 3bs

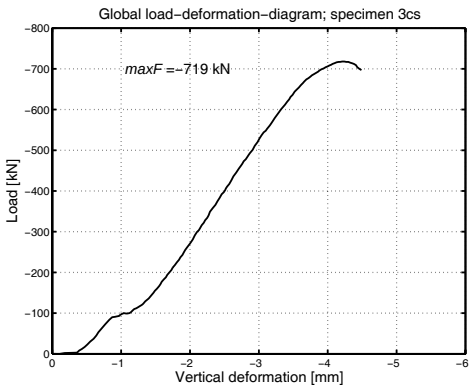

Figure A.3: Load-deformation behavior, specimen 3cs

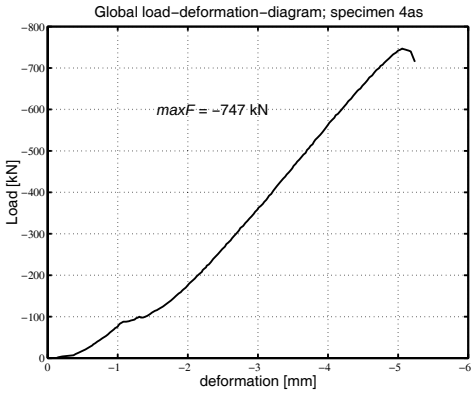

Figure A.4: Load-deformation behavior, specimen 4as

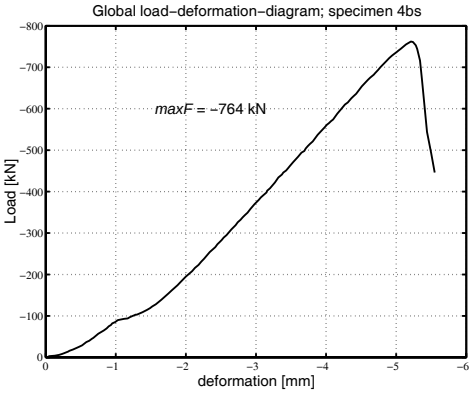

Figure A.5: Load-deformation behavior, specimen 4bs

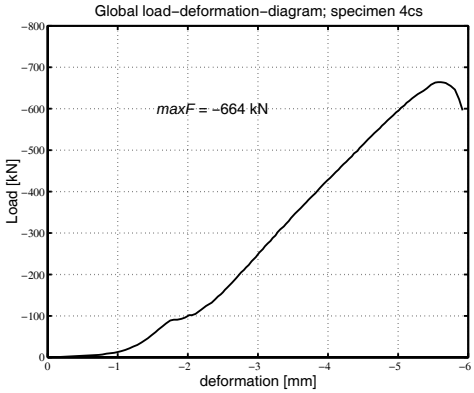

Figure A.6: Load-deformation behavior, specimen 4cs

A.1.2 Load-strain behavior strain gages

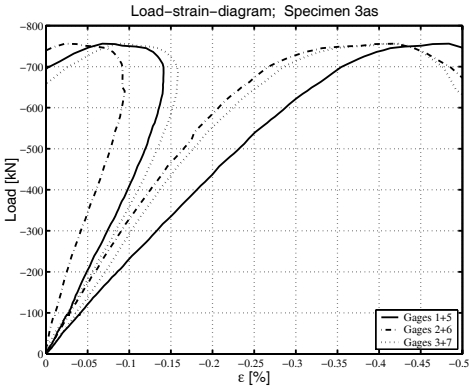

Figure A.7: Load-strain behavior strain gages, specimen 3as

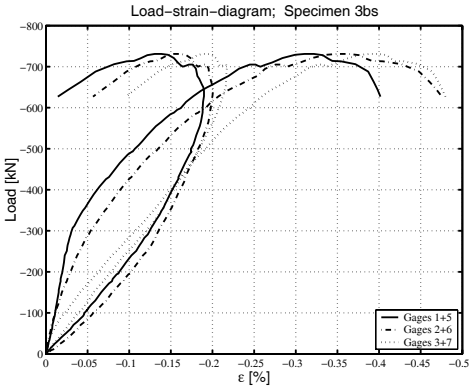

Figure A.8: Load-strain behavior strain gages, specimen 3bs

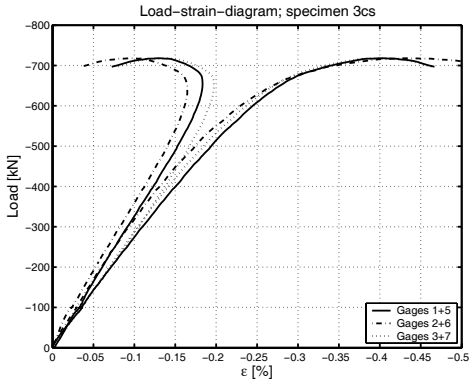

Figure A.9: Load-strain behavior strain gages, specimen 3cs

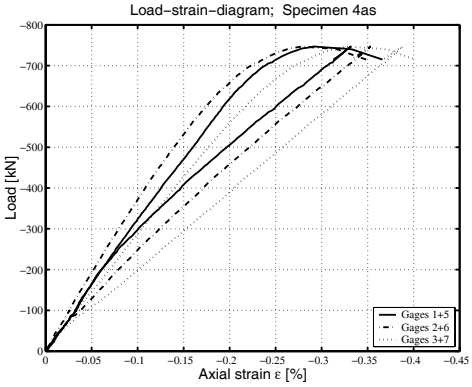

Figure A.10: Load-strain behavior strain gages, specimen 4as

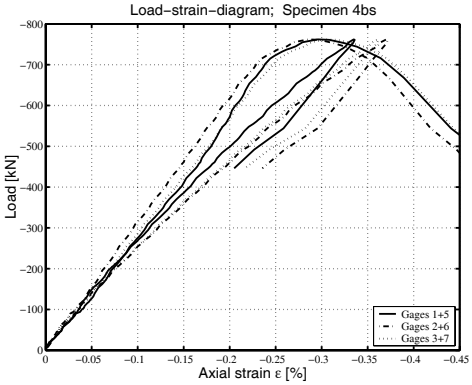

Figure A.11: Load-strain behavior strain gages, specimen 4bs

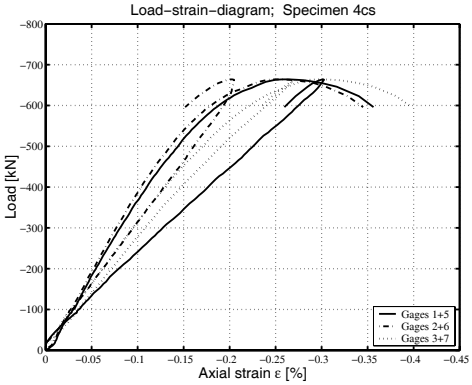

Figure A.12: Load-strain behavior strain gages, specimen 4cs

A.1.3 Load-deformation behavior Ω-gages

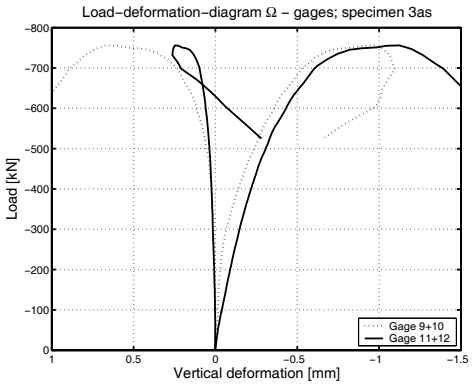

Figure A.13: Load-deformation behavior Ω - gages, specimen 3as

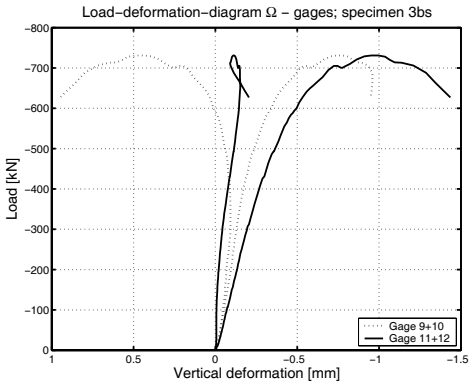

Figure A.14: Load-deformation behavior Ω - gages, specimen 3bs

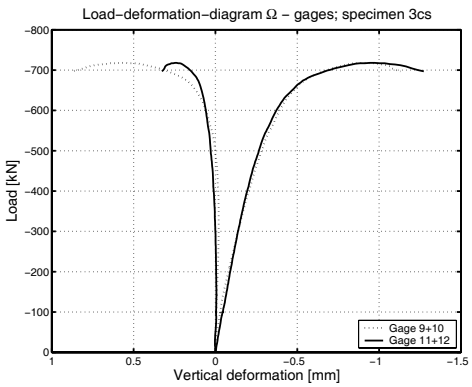

Figure A.15: Load-deformation behavior Ω - gages, specimen 3cs

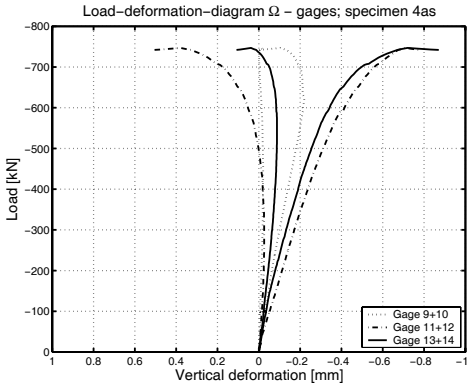

Figure A.16: Load-deformation behavior Ω - gages, specimen 4as

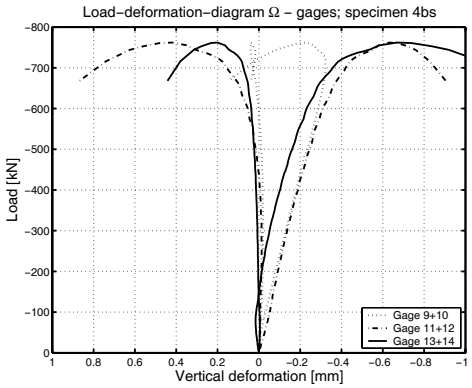

Figure A.17: Load-deformation behavior Ω - gages, specimen 4bs

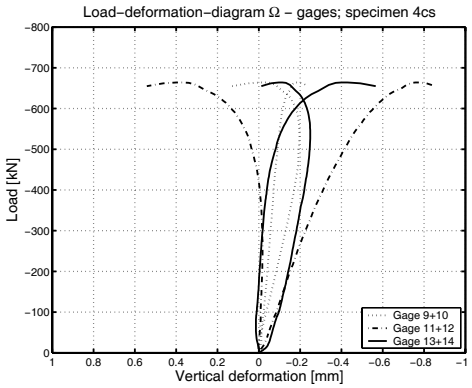

Figure A.18: Load-deformation behavior Ω - gages, specimen 4cs

A.2 ASSET

A.2.1 Load-deformation behavior

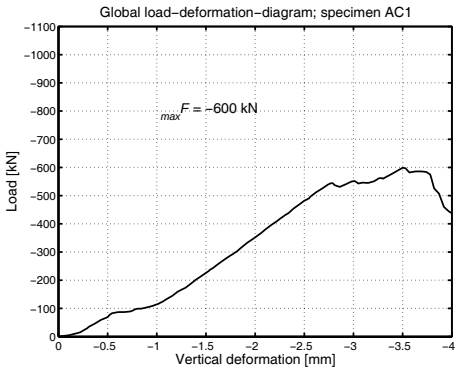

Figure A.19: Load-deformation behavior, specimen AC1

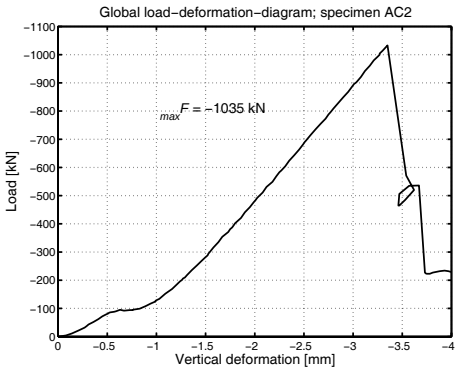

Figure A.20: Load-deformation behavior, specimen AC2

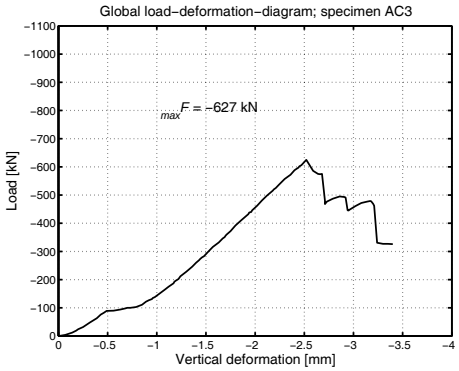

Figure A.21: Load-deformation behavior, specimen AC3

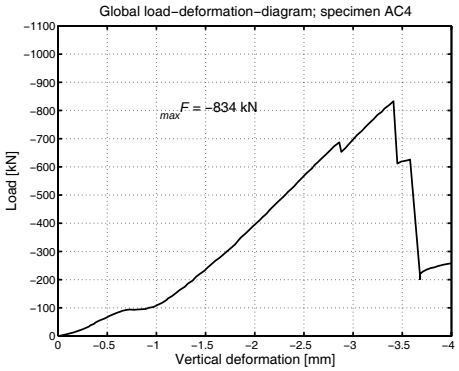

Figure A.22: Load-deformation behavior, specimen AC4

A.2.2 Load-strain behavior strain gages

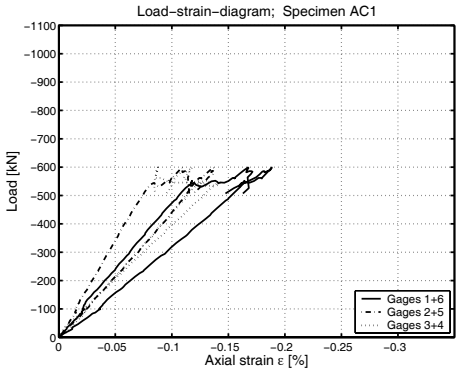

Figure A.23: Load-strain behavior strain gages, specimen AC1

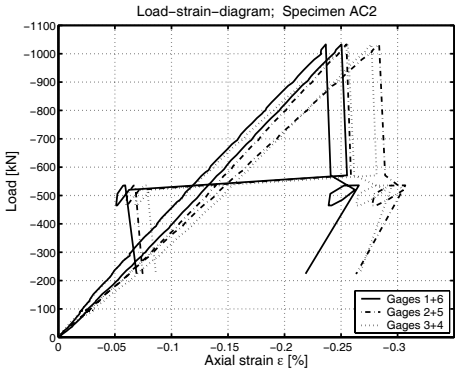

Figure A.24: Load-strain behavior strain gages, specimen AC2

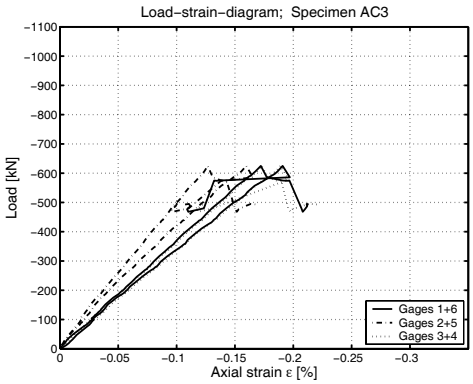

Figure A.25: Load-strain behavior strain gages, specimen AC3

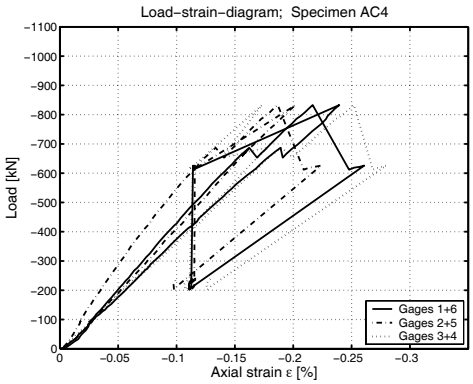

Figure A.26: Load-strain behavior strain gages, specimen AC4

A.2.3 Load-deformation behavior Ω-gages

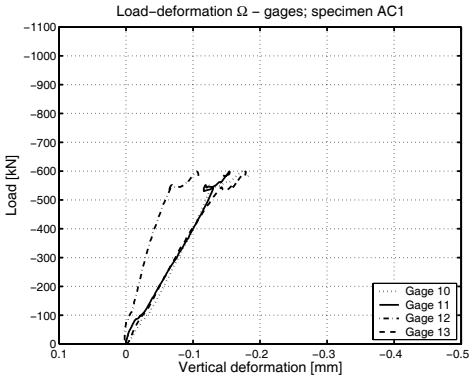

Figure A.27: Load-deformation behavior Ω - gages, specimen AC1

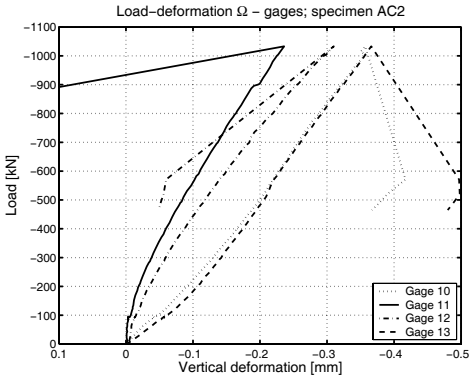

Figure A.28: Load-deformation behavior Ω - gages, specimen AC2

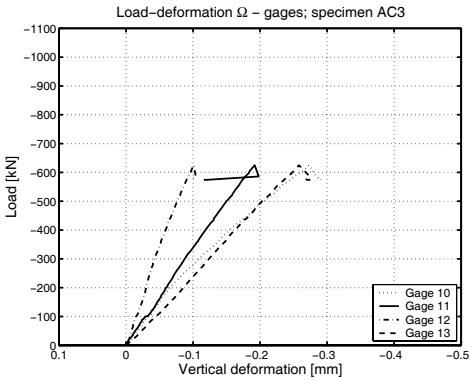

Figure A.29: Load-deformation behavior Ω - gages, specimen AC3

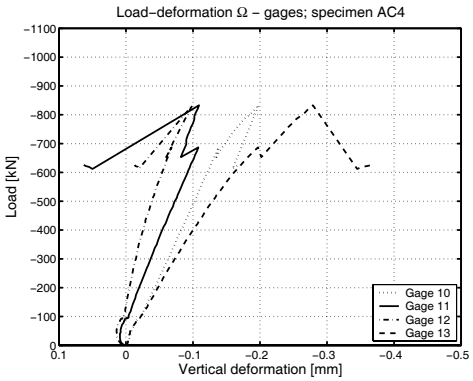

Figure A.30: Load-deformation behavior Ω - gages, specimen AC4

Appendix B

Diagrams for shear experiments

B.1 DuraSpan

B.1.1 Load-deformation behavior

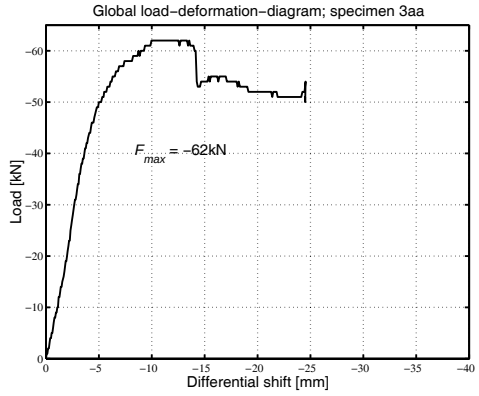

Figure B.1: Load-deformation behavior, specimen 3aa

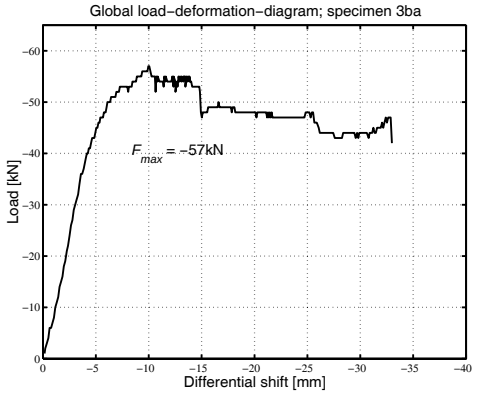

Figure B.2: Load-deformation behavior, specimen 3ba

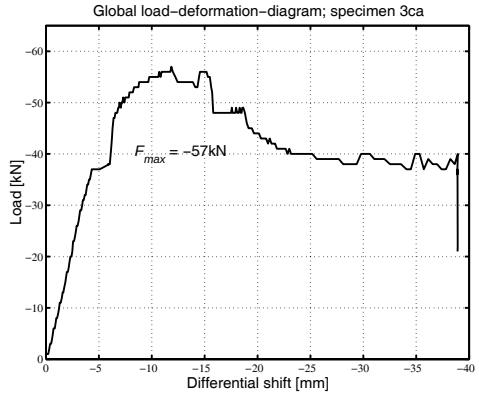

Figure B.3: Load-deformation behavior, specimen 3ca

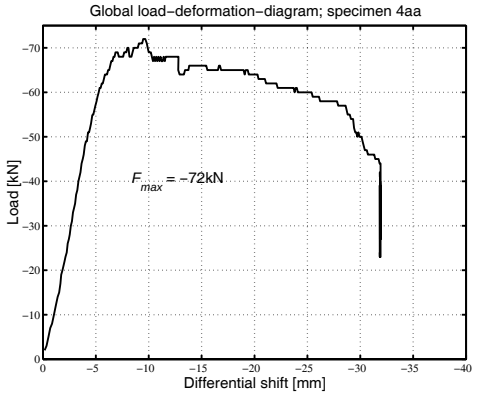

Figure B.4: Load-deformation behavior, specimen 4aa

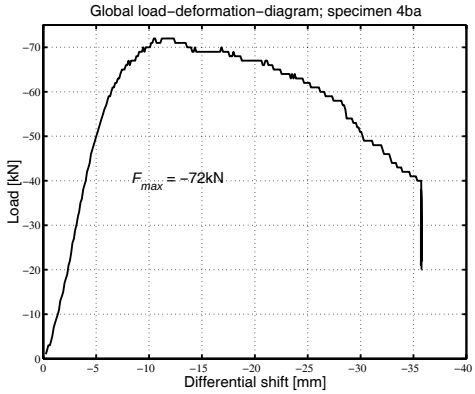

Figure B.5: Load-deformation behavior, specimen 4ba

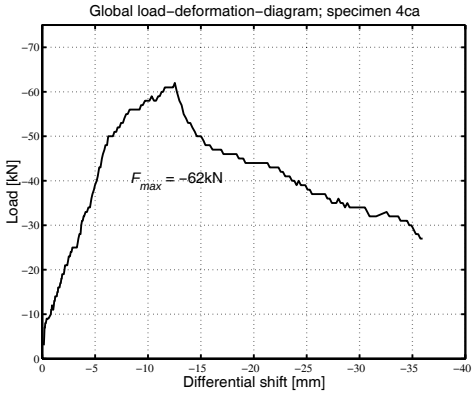

Figure B.6: Load-deformation behavior, specimen 4ca

B.1.2 Load-strain behavior strain gages

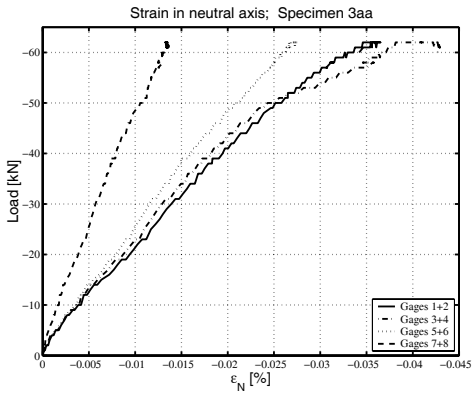

Figure B.7: Strains in neutral axis, specimen 3aa, gages 1-8

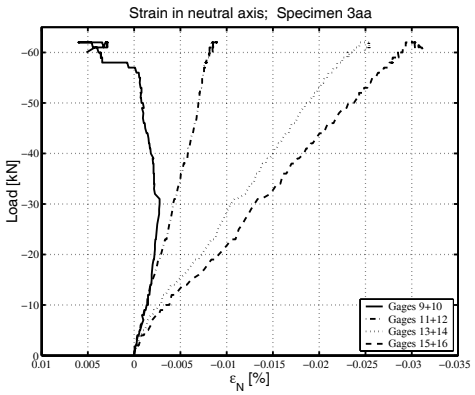

Figure B.8: Strains in neutral axis, specimen 3aa, gages 9-16

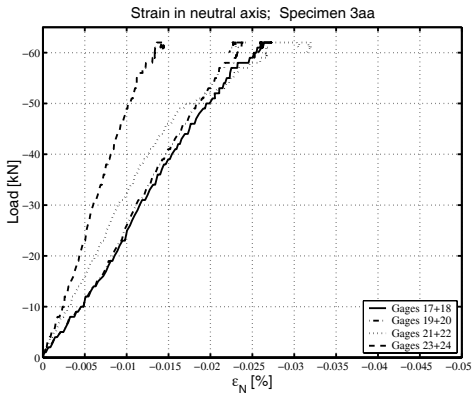

Figure B.9: Strains in neutral axis, specimen 3aa, gages 17-24

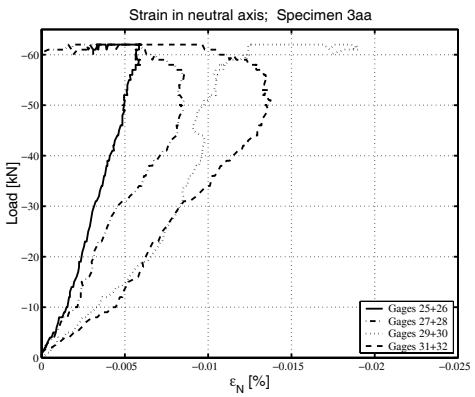

Figure B.10: Strains in neutral axis, specimen 3aa, gages 25-32

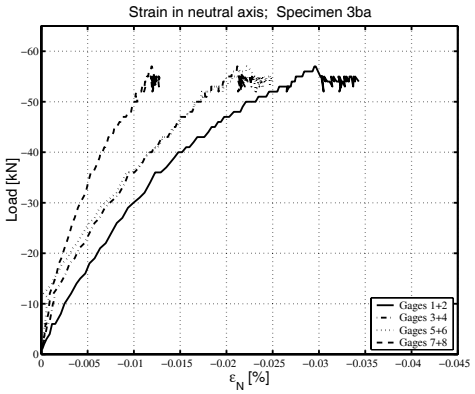

Figure B.11: Strains in neutral axis, specimen 3ba, gages 1-8

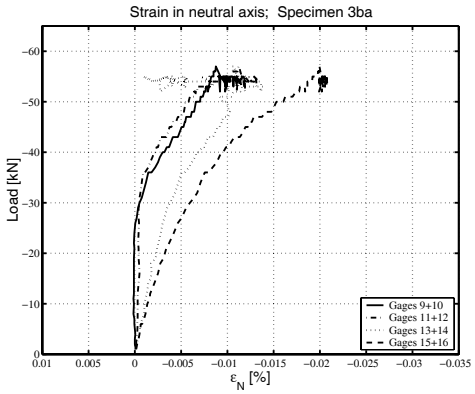

Figure B.12: Strains in neutral axis, specimen 3ba, gages 9-16

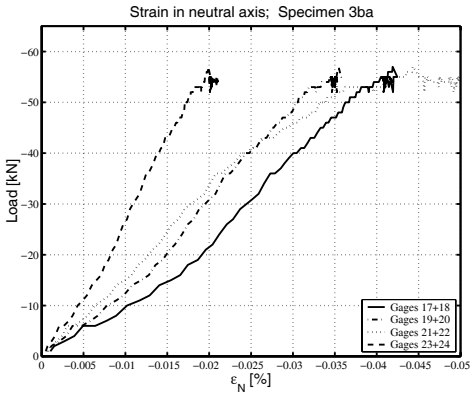

Figure B.13: Strains in neutral axis, specimen 3ba, gages 17-24

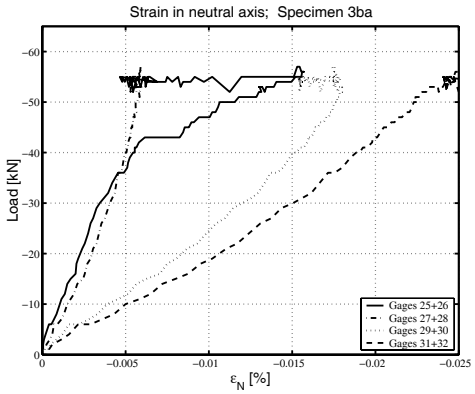

Figure B.14: Strains in neutral axis, specimen 3ba, gages 25-32

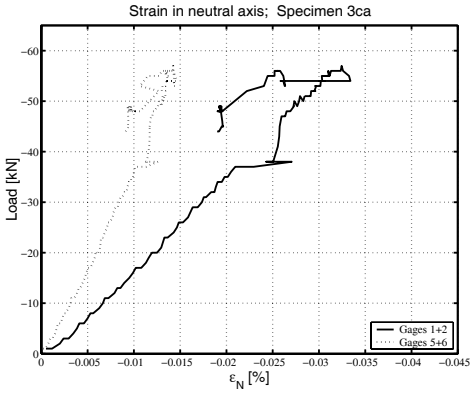

Figure B.15: Strains in neutral axis, specimen 3ca, gages 1-6

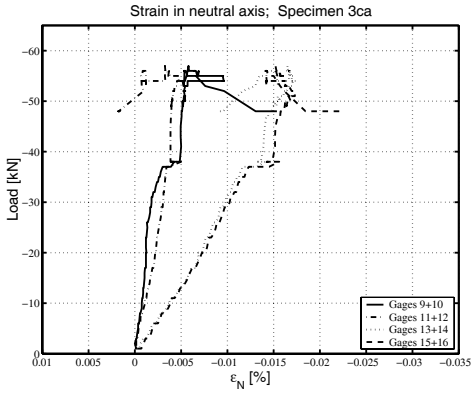

Figure B.16: Strains in neutral axis, specimen 3ca, gages 9-16

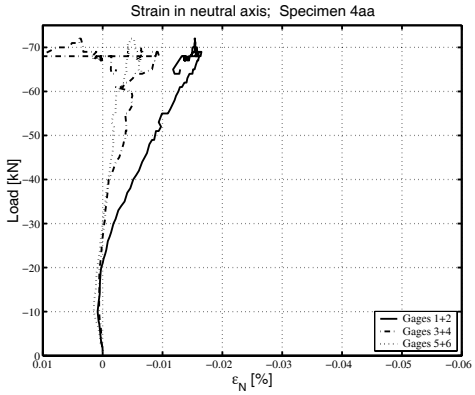

Figure B.17: Strains in neutral axis, specimen 4aa, gages 1-6

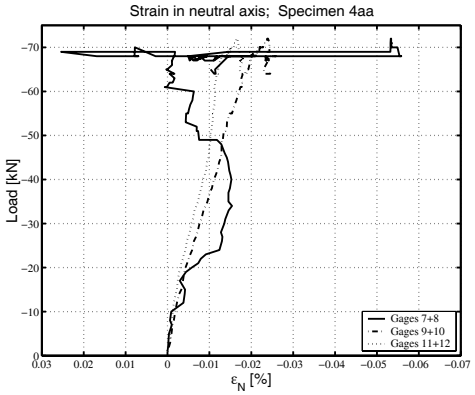

Figure B.18: Strains in neutral axis, specimen 4aa, gages 7-12

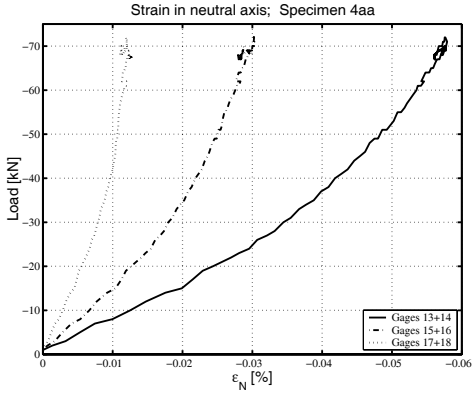

Figure B.19: Strains in neutral axis, specimen 4aa, gages 13-18

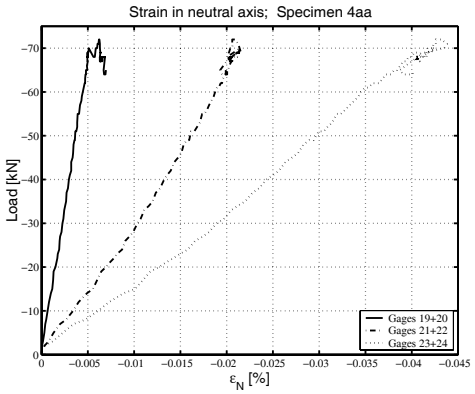

Figure B.20: Strains in neutral axis, specimen 4aa, gages 19-24

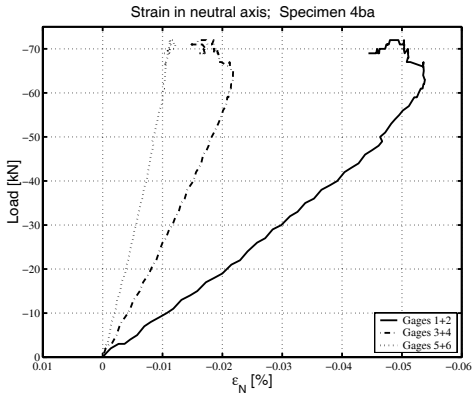

Figure B.21: Strains in neutral axis, specimen 4ba, gages 1-6

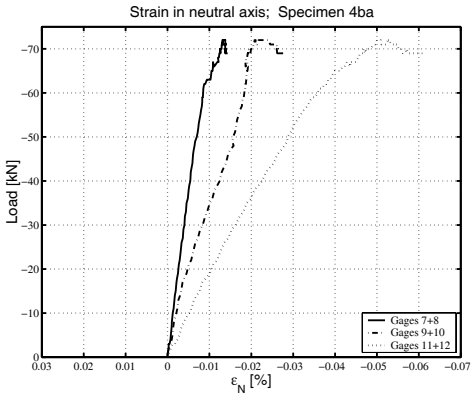

Figure B.22: Strains in neutral axis, specimen 4ba, gages 7-12

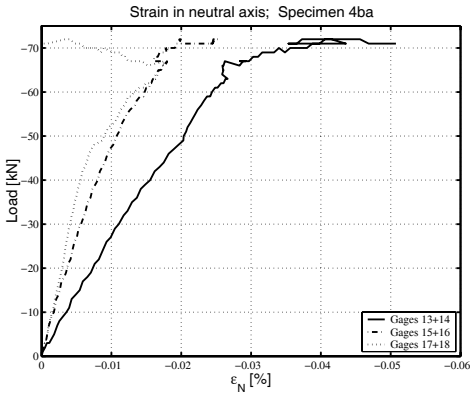

Figure B.23: Strains in neutral axis, specimen 4ba, gages 13-18

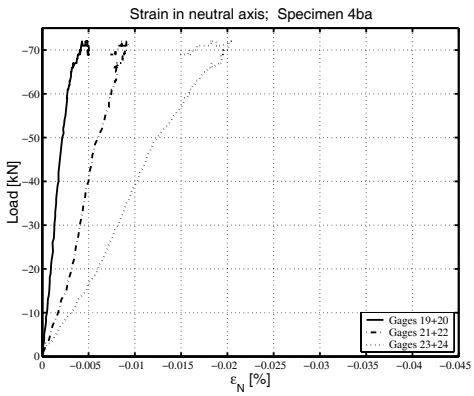

Figure B.24: Strains in neutral axis, specimen 4ba, gages 19-24

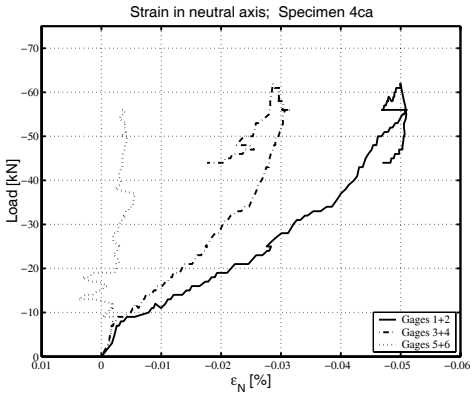

Figure B.25: Strains in neutral axis, specimen 4ca, gages 1-6

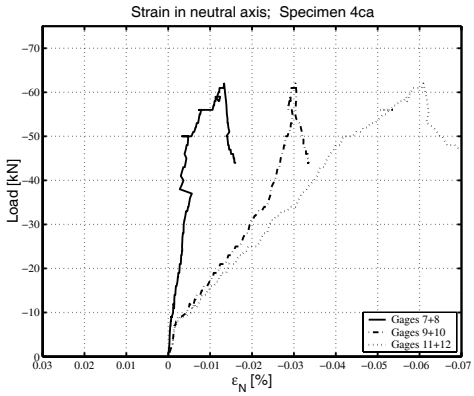

Figure B.26: Strains in neutral axis, specimen 4ca, gages 7-12

B.2 ASSET

B.2.1 Load-deformation behavior

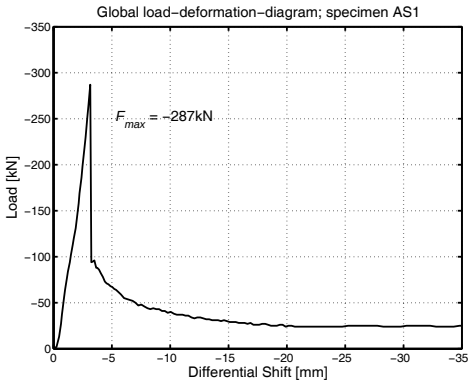

Figure B.27: Load-deformation behavior, specimen AS1

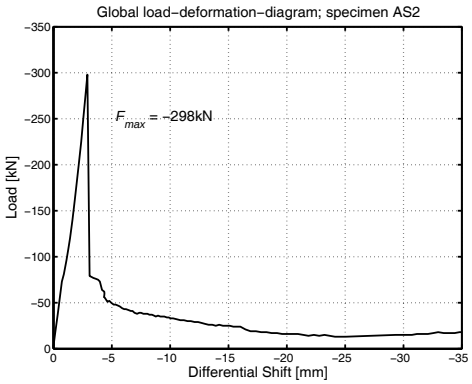

Figure B.28: Load-deformation behavior, specimen AS2

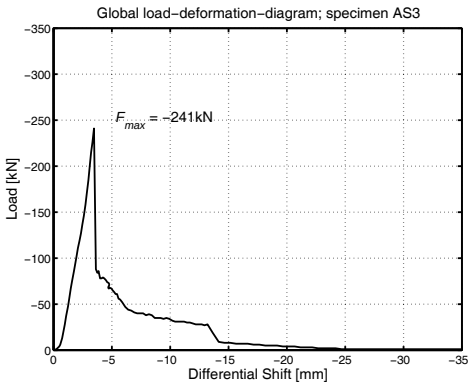

Figure B.29: Load-deformation behavior, specimen AS3

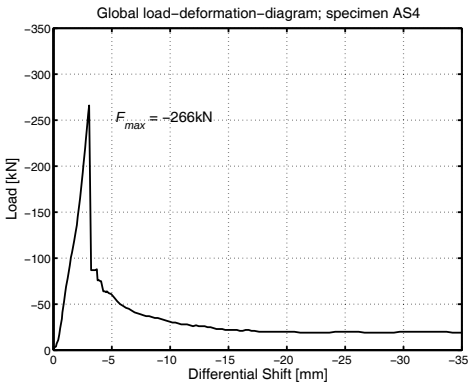

Figure B.30: Load-deformation behavior, specimen AS4

B.2.2 Load-strain behavior strain gages

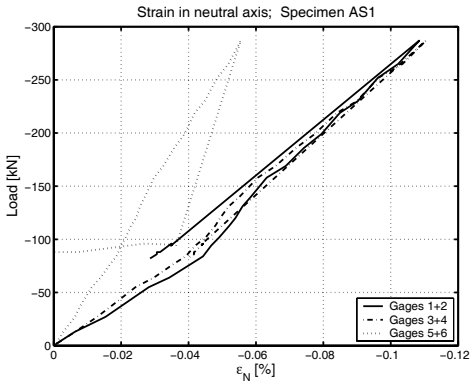

Figure B.31: Strains in neutral axis, specimen AS1, gages 1-6

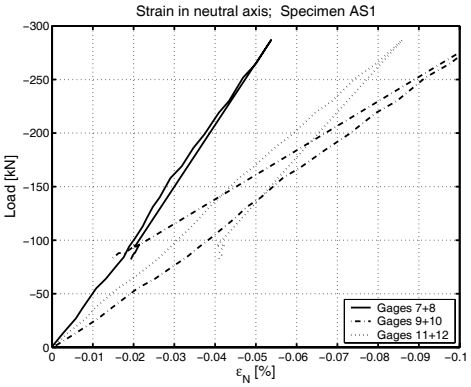

Figure B.32: Strains in neutral axis, specimen AS1, gages 7-12

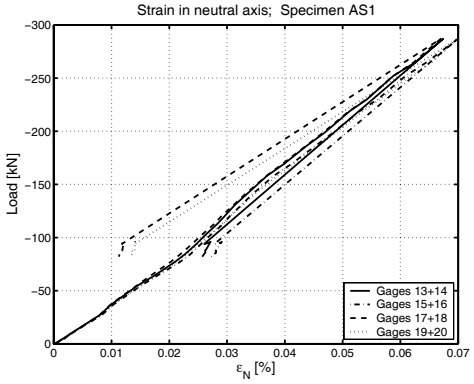

Figure B.33: Strains in neutral axis, specimen AS1, gages 13-20

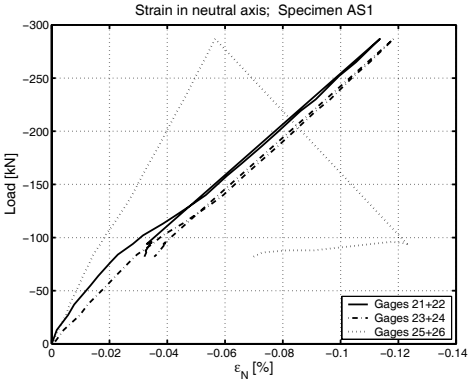

Figure B.34: Strains in neutral axis, specimen AS1, gages 21-26

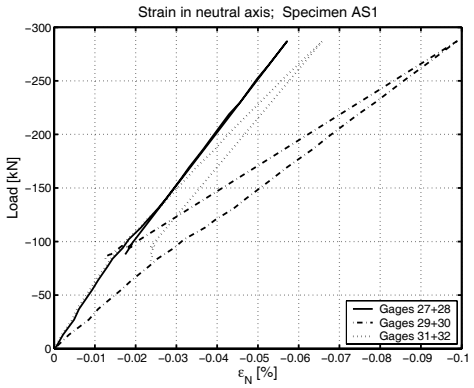

Figure B.35: Strains in neutral axis, specimen AS1, gages 27-32

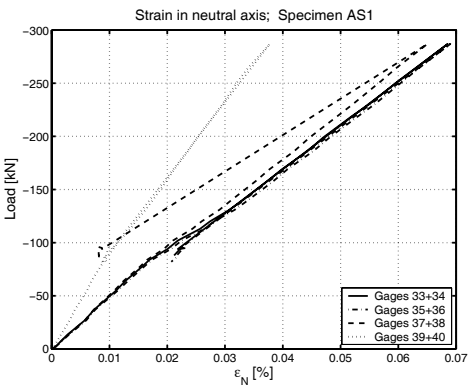

Figure B.36: Strains in neutral axis, specimen AS1, gages 33-40

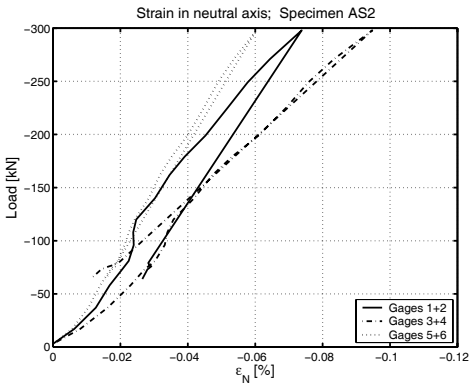

Figure B.37: Strains in neutral axis, specimen AS2, gages 1-6

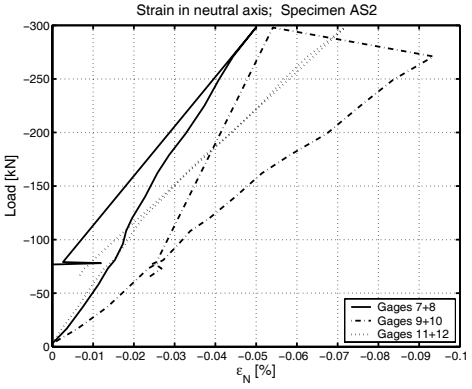

Figure B.38: Strains in neutral axis, specimen AS2, gages 7-12

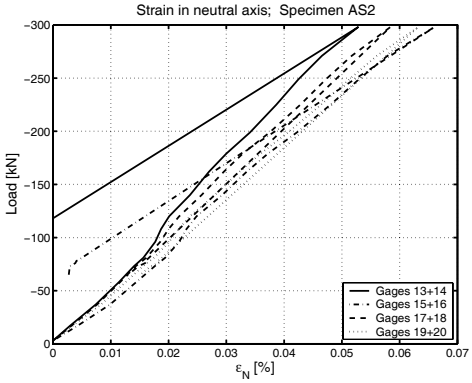

Figure B.39: Strains in neutral axis, specimen AS2, gages 13-20

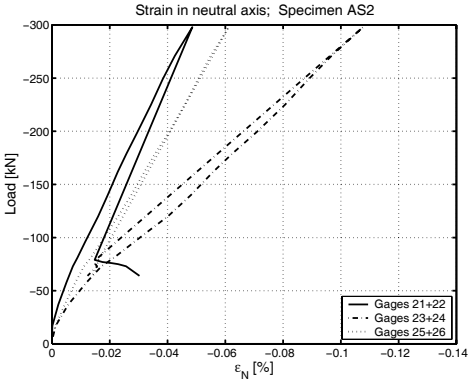

Figure B.40: Strains in neutral axis, specimen AS2, gages 21-26

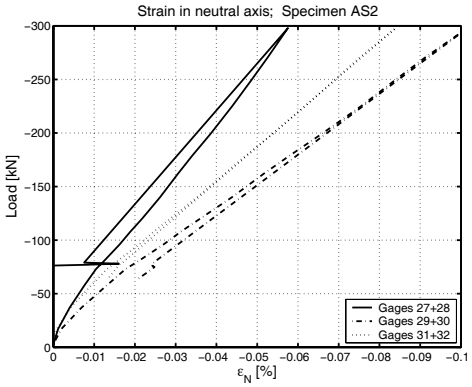

Figure B.41: Strains in neutral axis, specimen AS2, gages 27-32

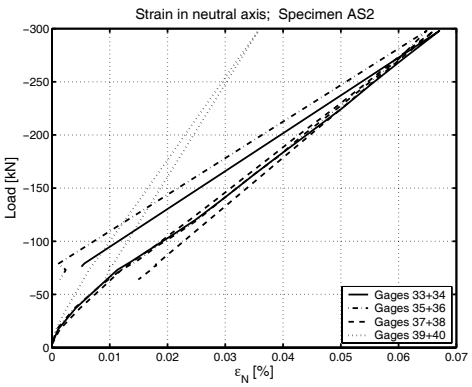

Figure B.42: Strains in neutral axis, specimen AS2, gages 33-40

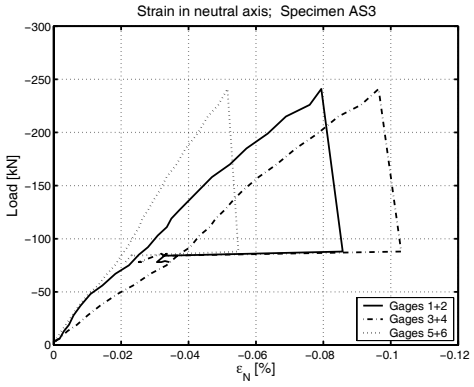

Figure B.43: Strains in neutral axis, specimen AS3, gages 1-6

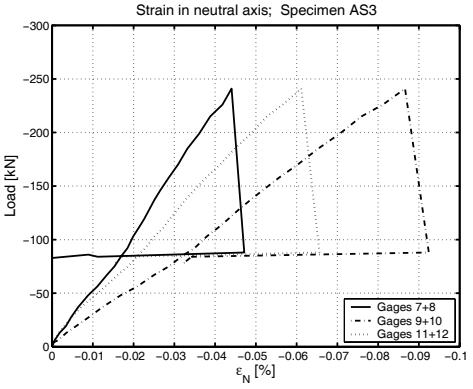

Figure B.44: Strains in neutral axis, specimen AS3, gages 7-12

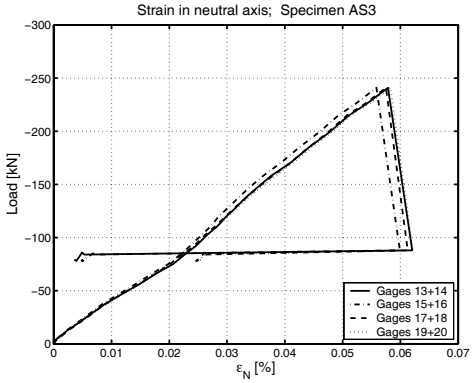

Figure B.45: Strains in neutral axis, specimen AS3, gages 13-20

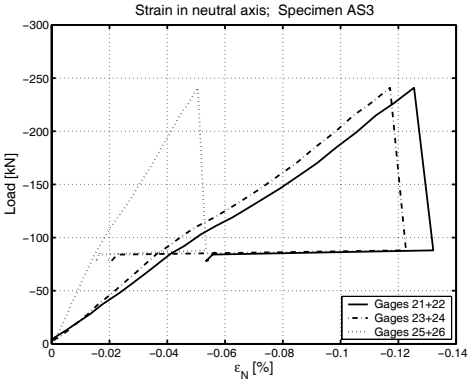

Figure B.46: Strains in neutral axis, specimen AS3, gages 21-26

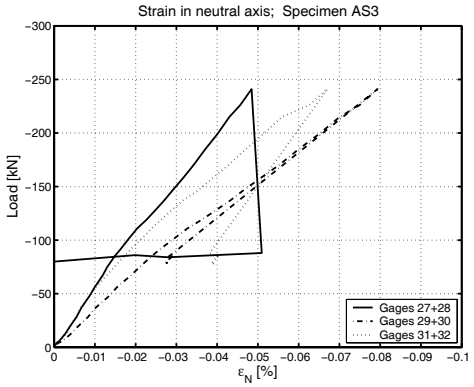

Figure B.47: Strains in neutral axis, specimen AS3, gages 27-32

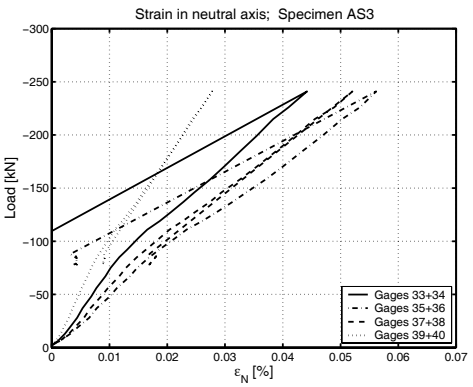

Figure B.48: Strains in neutral axis, specimen AS3, gages 33-40

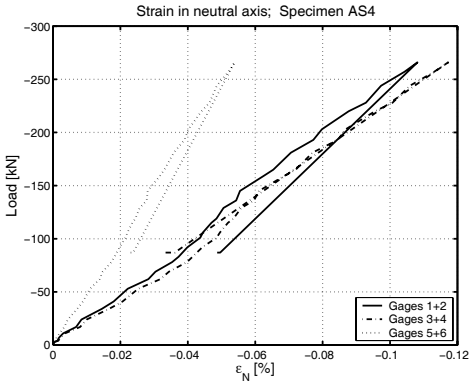

Figure B.49: Strains in neutral axis, specimen AS4, gages 1-6

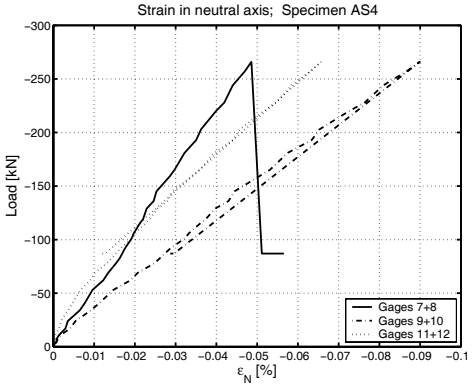

Figure B.50: Strains in neutral axis, specimen AS4, gages 7-12

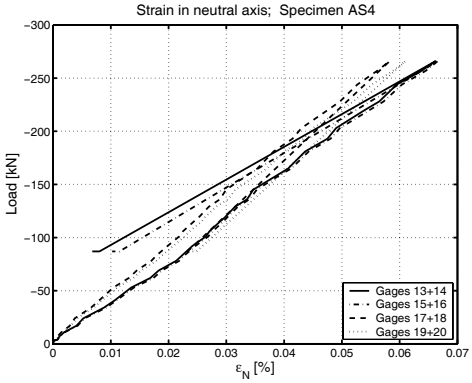

Figure B.51: Strains in neutral axis, specimen AS4, gages 13-20

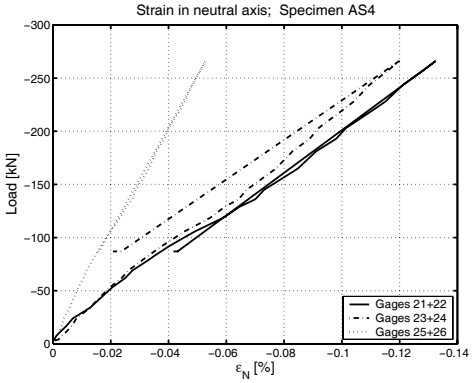

Figure B.52: Strains in neutral axis, specimen AS4, gages 21-26

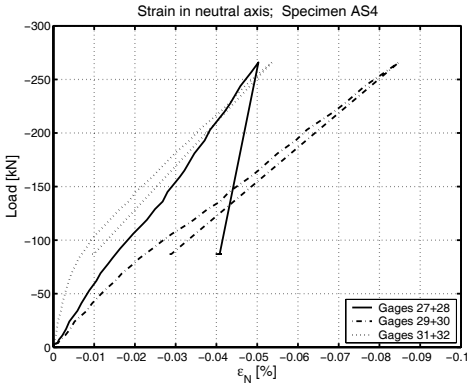

Figure B.53: Strains in neutral axis, specimen AS4, gages 27-32

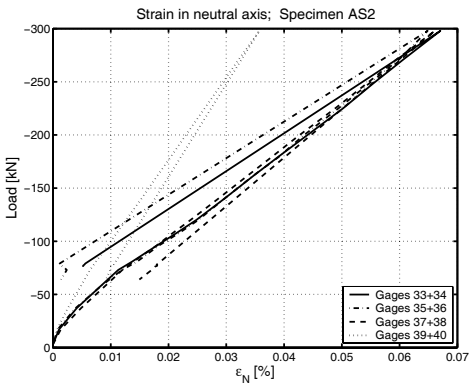

Figure B.54: Strains in neutral axis, specimen AS4, gages 33-40

Appendix C

Failure pictures compression/shear experiments

C.1 ASSET specimens

Compression experiments

Figure C.1: Failure pattern AC-1

Figure C.2: Failure pattern AC-2

Figure C.3: Failure pattern AC-3

Figure C.4: Failure pattern AC-4

Shear experiments

Figure C.5: Failure pattern AS-1

Figure C.6: Failure pattern AS-2

Figure C.7: Failure pattern AS-3

AS-4 not available.

C.2 DuraSpan specimens

Available failure pictures:

Compression experiments

Figure C.8: Failure pattern 4bs

Figure C.9: Failure pattern 3bs

Shear experiments

Figure C.10: Failure pattern 3aa

Figure C.11: Failure pattern 3ba

Figure C.12: Failure pattern 4aa

Figure C.13: Failure pattern 4ba

Appendix D

Diagrams for girder experiments

D.1 ASSET girders

D.1.1 Cross-sectional axial strain behavior, SLS

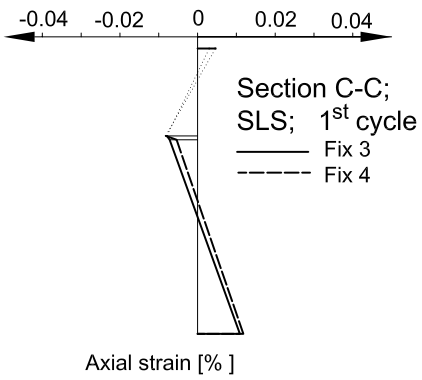

Figure D.1: Axial strain behavior, axis C-C

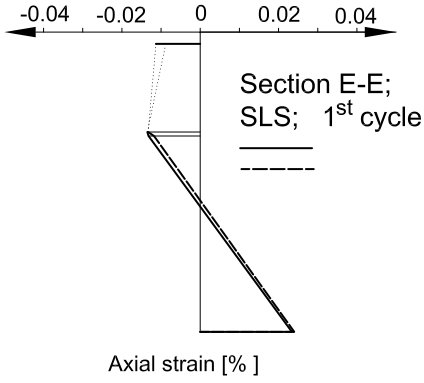

Figure D.2: Axial strain behavior, axis E-E

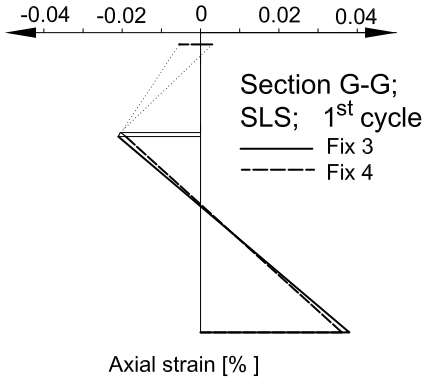

Figure D.3: Axial strain behavior, axis G-G

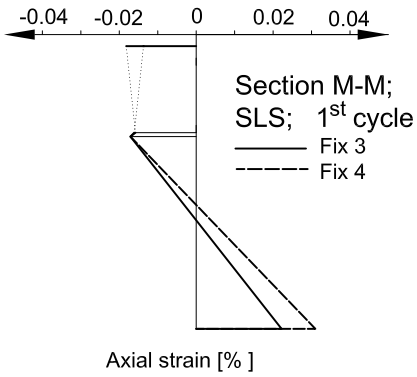

Figure D.4: Axial strain behavior, axis M-M

D.1.2 Cross-sectional axial strain behavior, FLS

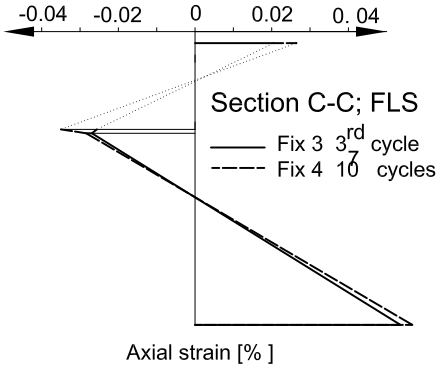

Figure D.5: Axial strain behavior, axis C-C

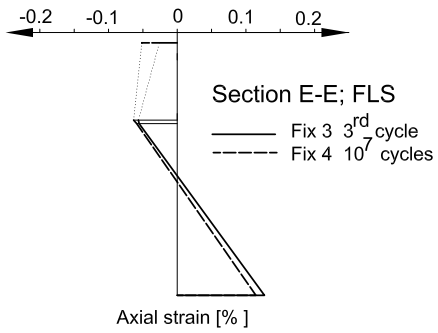

Figure D.6: Axial strain behavior, axis E-E

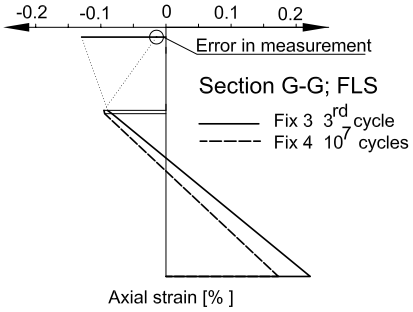

Figure D.7: Axial strain behavior, axis G-G

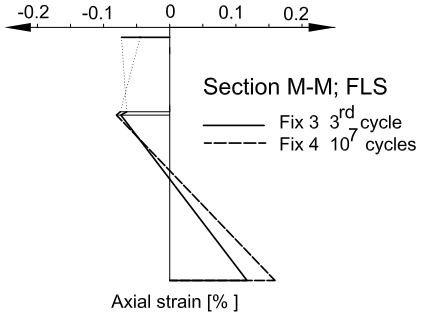

Figure D.8: Axial strain behavior, axis M-M

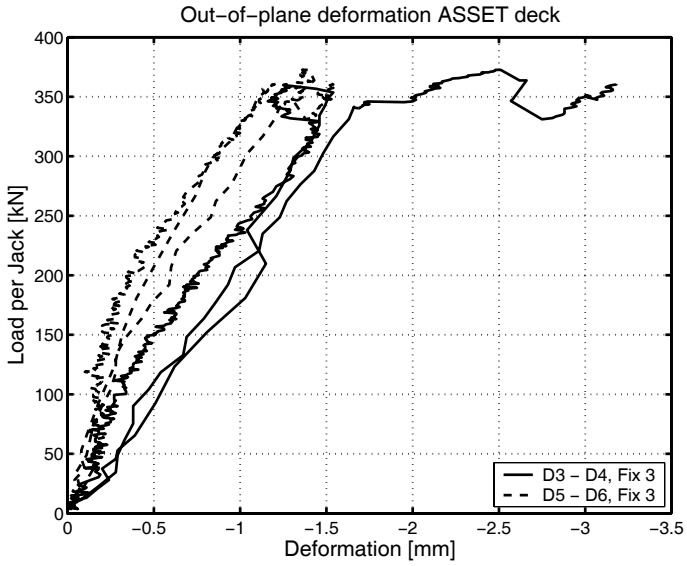

Figure D.9: Variation of deck depth in the load axes

D.1.3 Effective width

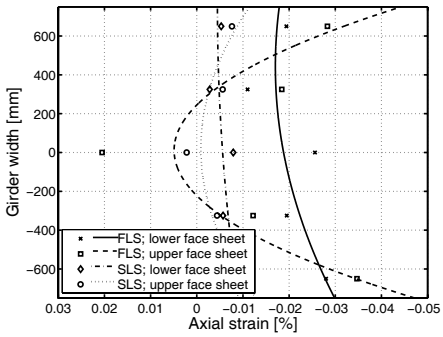

Figure D.10: Effective width Fix 3, axis C-C

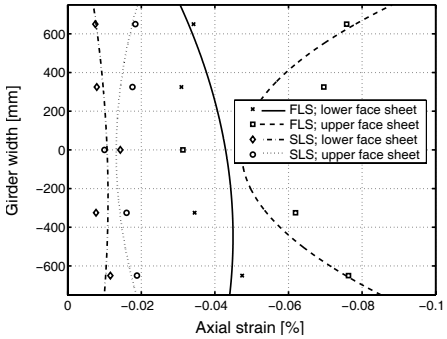

Figure D.11: Effective width Fix 3, axis E-E

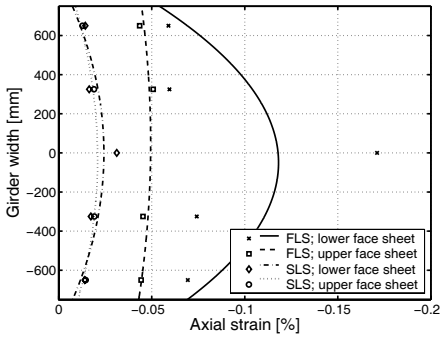

Figure D.12: Effective width Fix 3, axis G-G

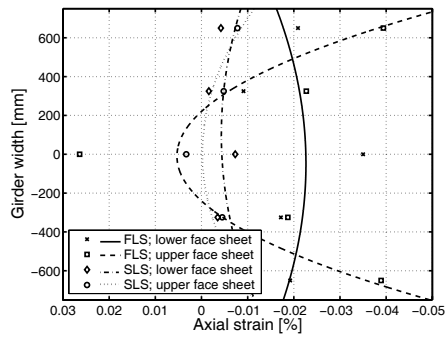

Figure D.13: Effective width Fix 4, axis C-C

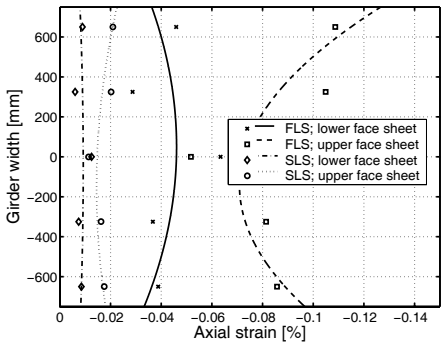

Figure D.14: Effective width Fix 4, axis E-E

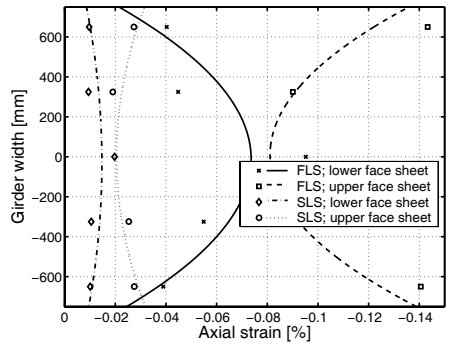

Figure D.15: Effective width Fix 4, axis G-G

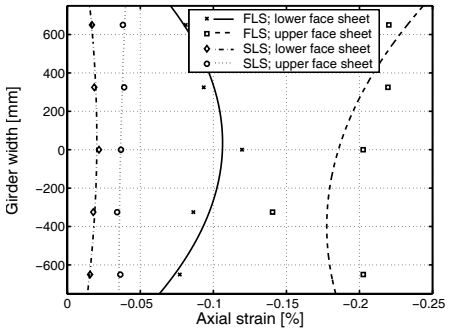

Figure D.16: Effective width Fix 4, axis J-J

D.1.4 Fatigue behavior

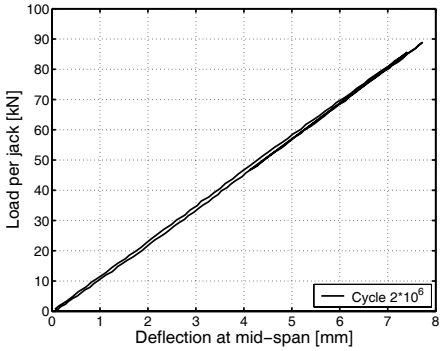

Figure D.17: Load deflection behavior after $2*10^6$ cycles

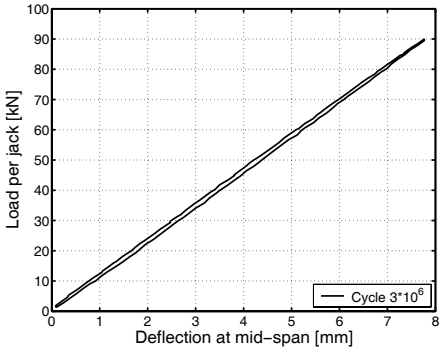

Figure D.18: Load deflection behavior after $3*10^6$ cycles

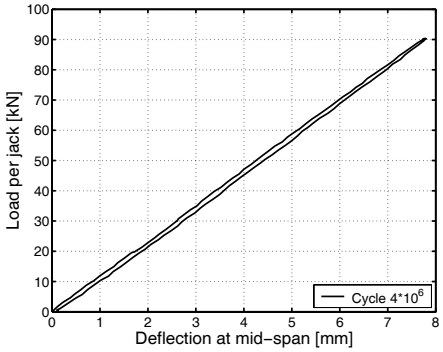

Figure D.19: Load deflection behavior after $4*10^6$ cycles

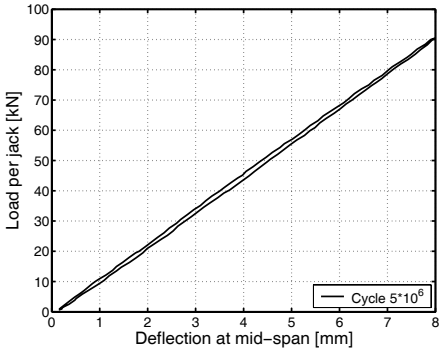

Figure D.20: Load deflection behavior after $5*10^6$ cycles

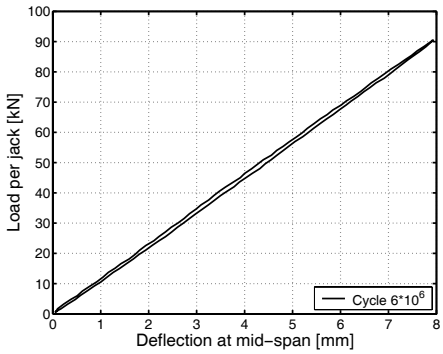

Figure D.21: Load deflection behavior after $6*10^6$ cycles

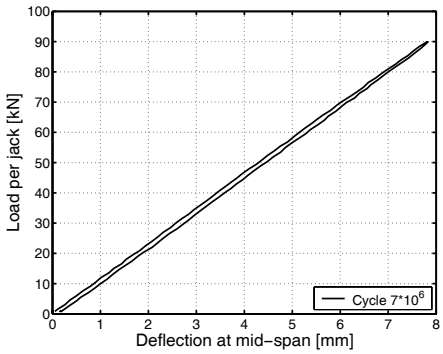

Figure D.22: Load deflection behavior after $7*10^6$ cycles

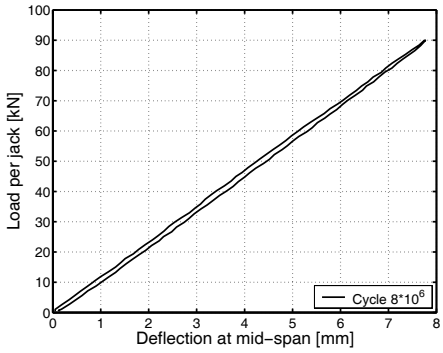

Figure D.23: Load deflection behavior after $8*10^6$ cycles

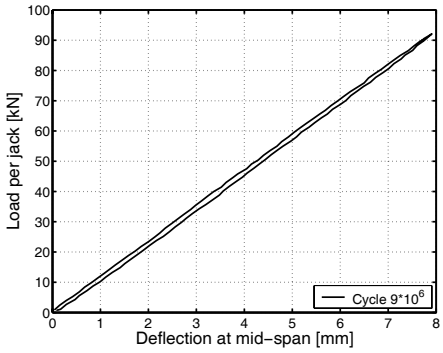

Figure D.24: Load deflection behavior after $9*10^6$ cycles

D.1.5 Longitudinal axial strain behavior, SLS

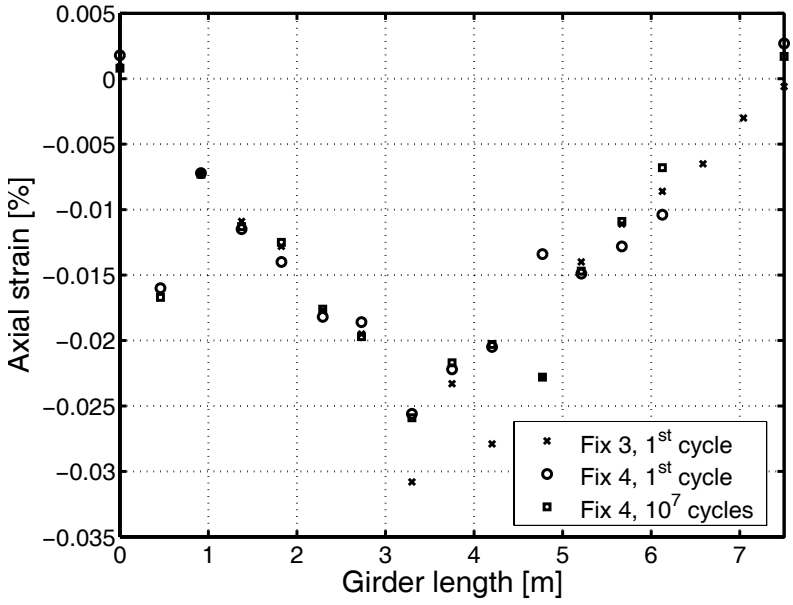

Figure D.25: Axial strains lower face sheet

D.1.6 Longitudinal axial strain behavior, FLS

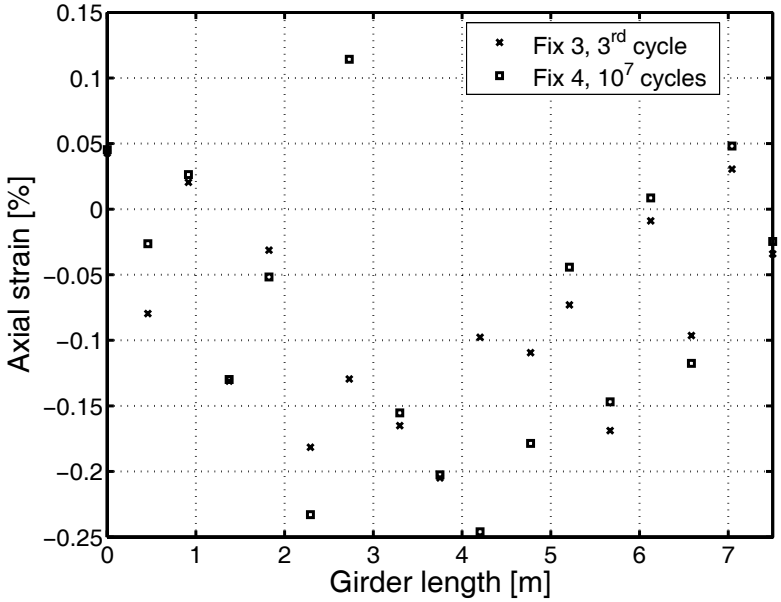

Figure D.26: Axial strains lower face sheet

D.2 DuraSpan girders

D.2.1 Cross-sectional axial strain behavior, SLS

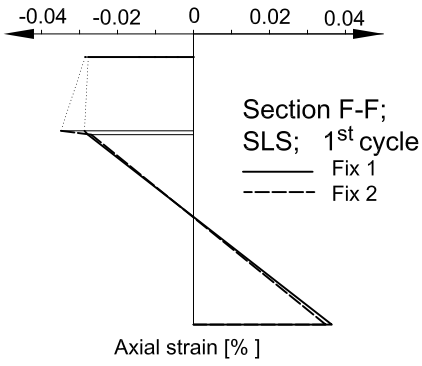

Figure D.27: Axial strain behavior, axis F-F

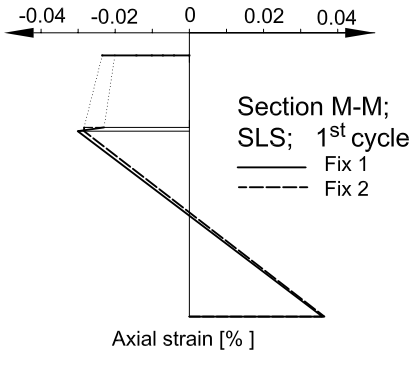

Figure D.28: Axial strain behavior, axis M-M

D.2.2 Cross-sectional axial strain behavior, FLS

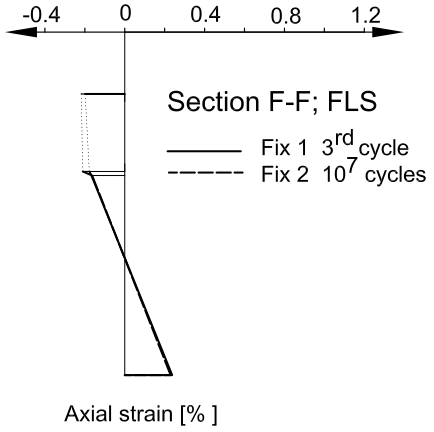

Figure D.29: Axial strain behavior, axis F-F

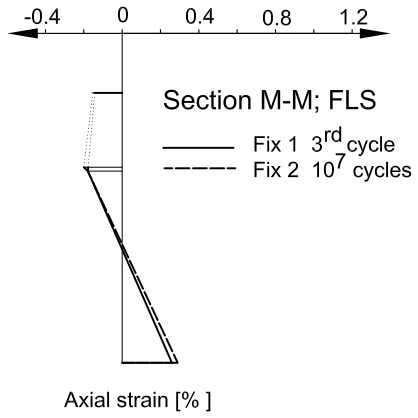

Figure D.30: Axial strain behavior, axis M-M

D.2.3 Effective width

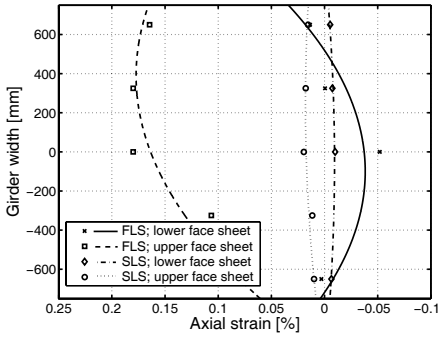

Figure D.31: Effective width Fix 1, axis C-C

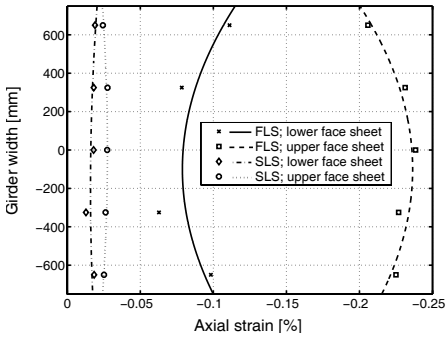

Figure D.32: Effective width Fix 1, axis E-E

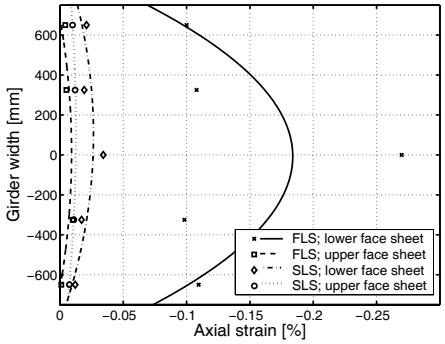

Figure D.33: Effective width Fix 1, axis G-G

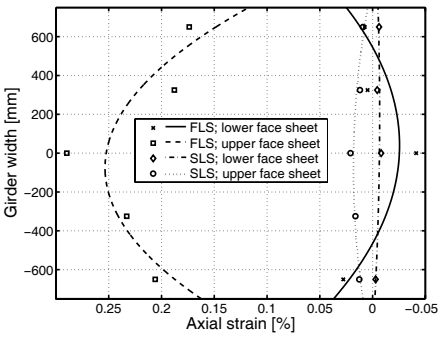

Figure D.34: Effective width Fix 2, axis C-C

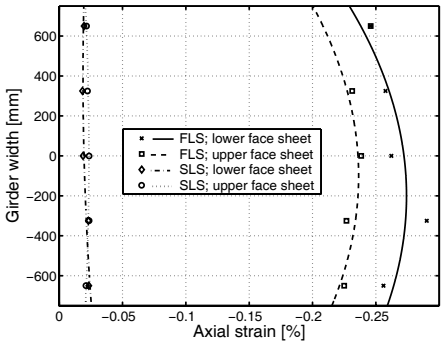

Figure D.35: Effective width Fix 2, axis E-E

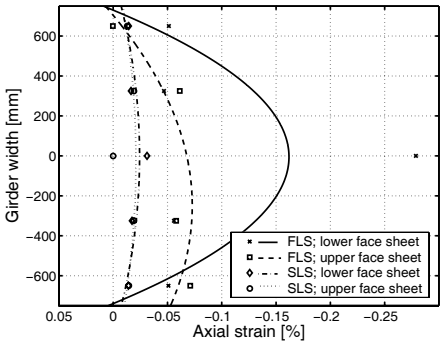

Figure D.36: Effective width Fix 2, axis G-G

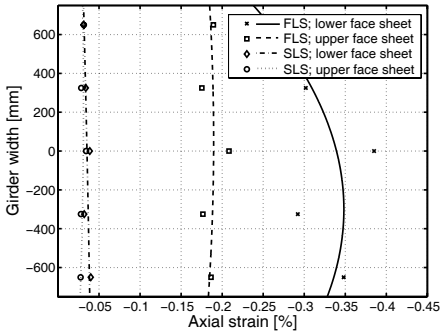

Figure D.37: Effective width Fix 2, axis J-J

D.2.4 Fatigue behavior

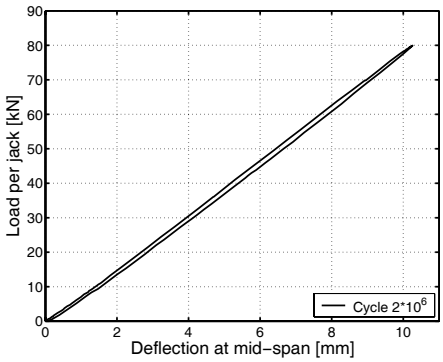

Figure D.38: Load deflection behavior after $2*10^6$ cycles

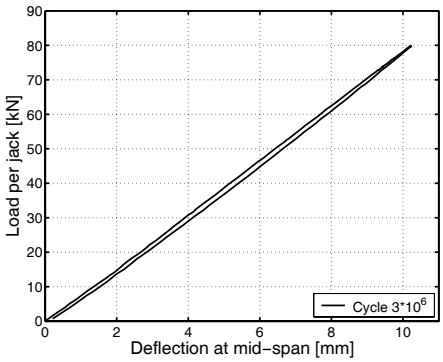

Figure D.39: Load deflection behavior after $3*10^6$ cycles

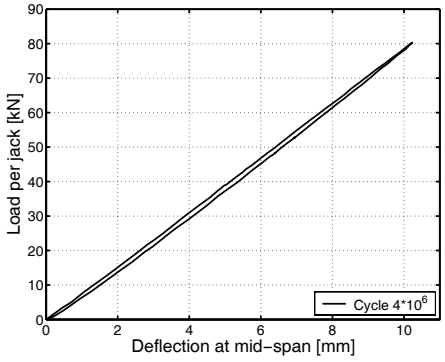

Figure D.40: Load deflection behavior after $4*10^6$ cycles

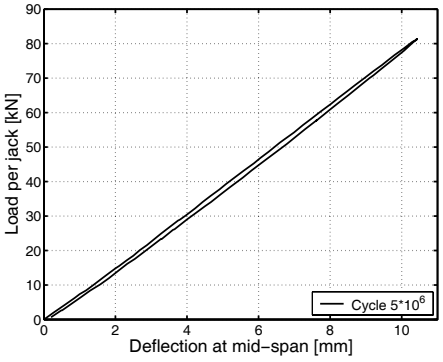

Figure D.41: Load deflection behavior after $5*10^6$ cycles

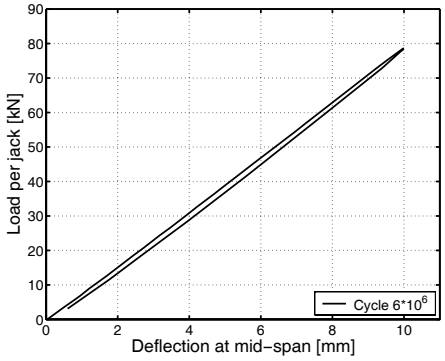

Figure D.42: Load deflection behavior after $6*10^6$ cycles

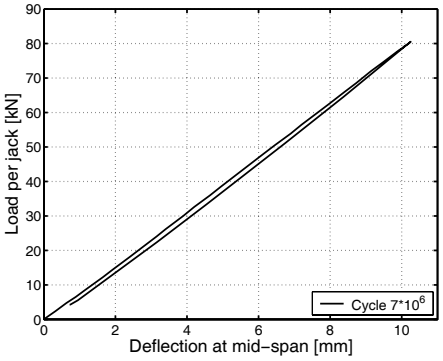

Figure D.43: Load deflection behavior after $7*10^6$ cycles

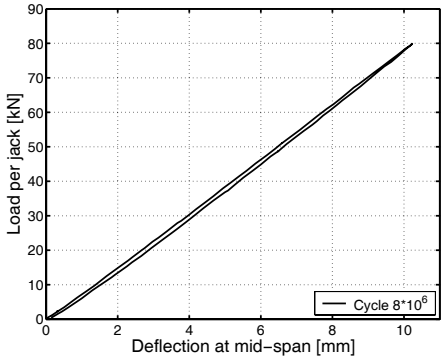

Figure D.44: Load deflection behavior after $8*10^6$ cycles

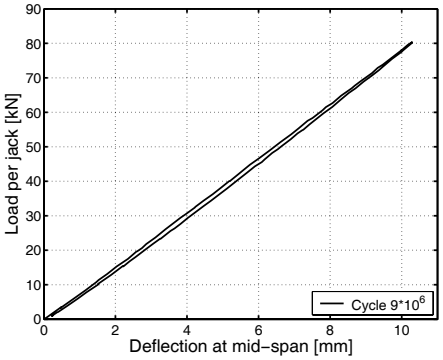

Figure D.45: Load deflection behavior after $9*10^6$ cycles

D.2.5 Longitudinal axial strain behavior

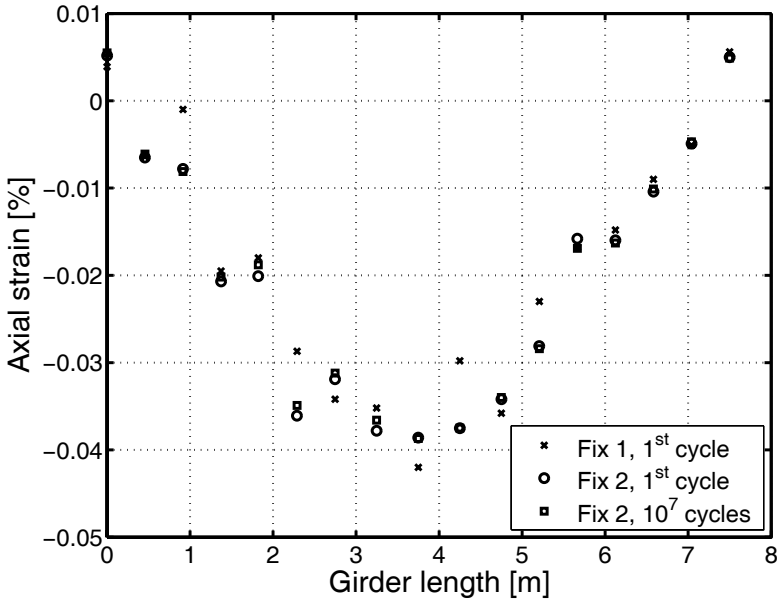

Figure D.46: Axial strains lower face sheet, SLS

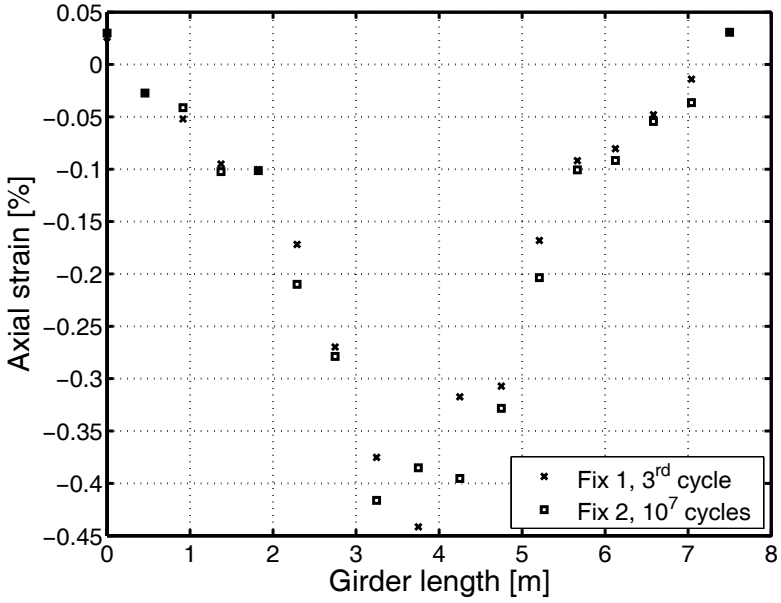

Figure D.47: Axial strains lower face sheet, FLS

Appendix E

Failure pictures girder experiments

E.1 Steel girder

Figure E.1: Set-up of steel-girder experiment - overview

Figure E.2: Buckling of upper steel flange (left side)

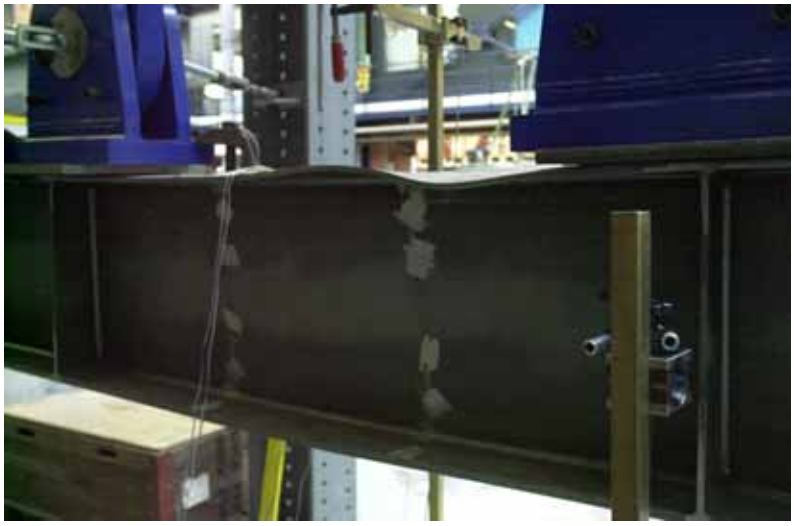

Figure E.3: Buckling of upper steel flange (left side)

Figure E.4: Buckling of upper steel flange (left side)

Figure E.5: Buckling of upper steel flange (right side)

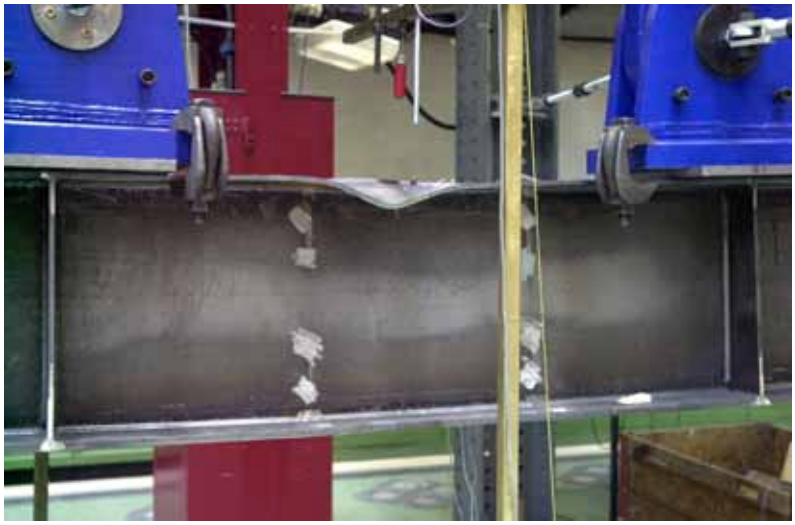

Figure E.6: Buckling of upper steel flange (right side)

E.2 ASSET girders

E.2.1 Pictures Fix 3

Figure E.7: Location of first failure (Axis G - G) after end of experiment with large delamination

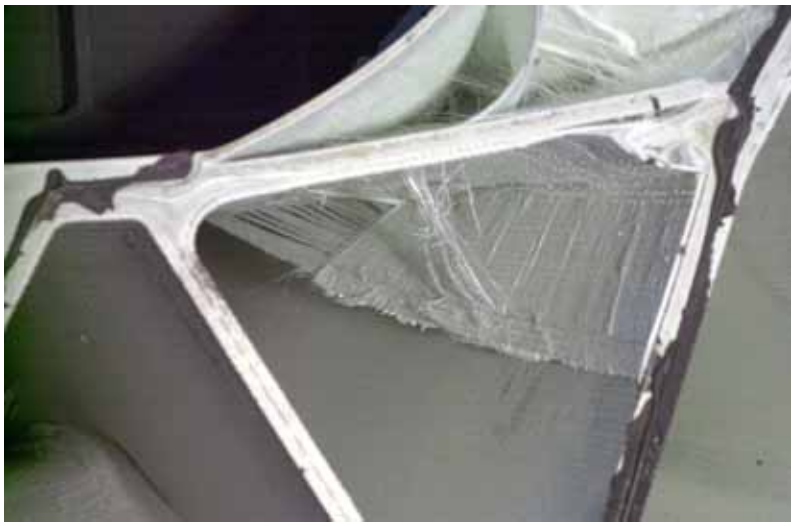

Figure E.8: Failure axis G - G with delamination of inner mat of the upper face panel

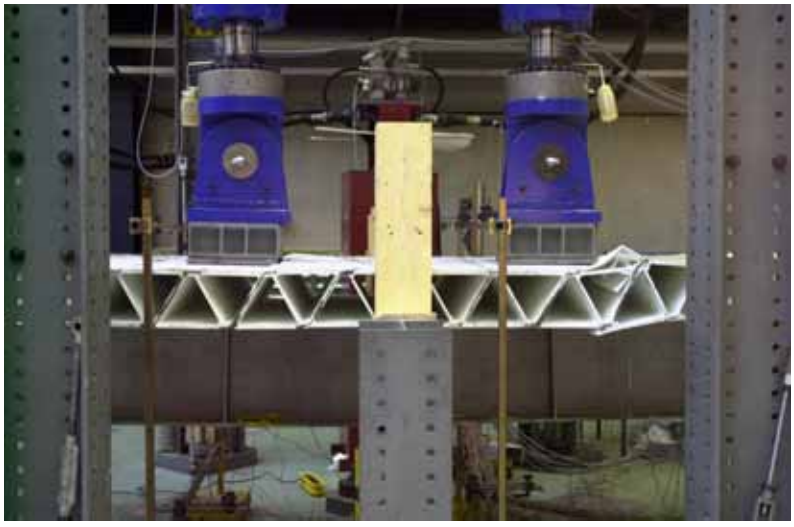

Figure E.9: Back view mid-span with first and second failure in axis G-G and third failure in axis K-K

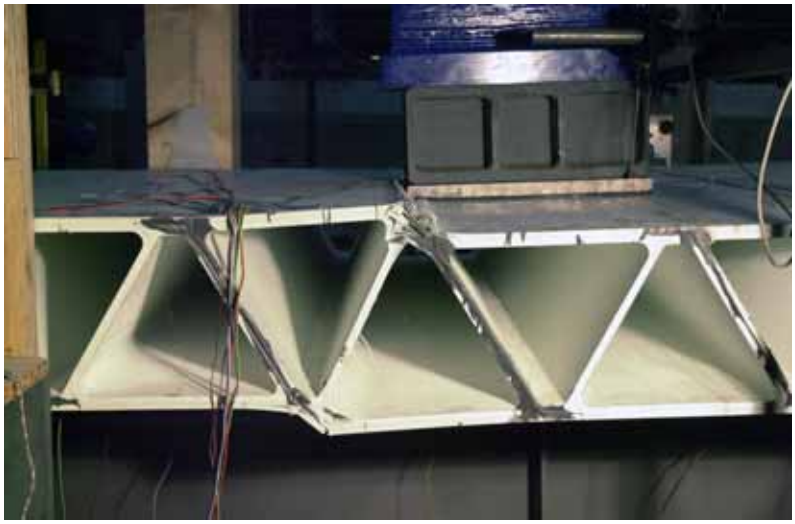

Figure E.10: Front view with third failure in axis K - K

Figure E.11: Under view of axis K - K with buckling of top steel flange at location with detached bridge deck

Figure E.12: Upper and lower face panel, axis G - G

Figure E.13: Delamination of the bridge deck from the steel girder, Axis K - K

Figure E.14: Failure of upper face panel axis K - K

E.2.2 Pictures Fix 4

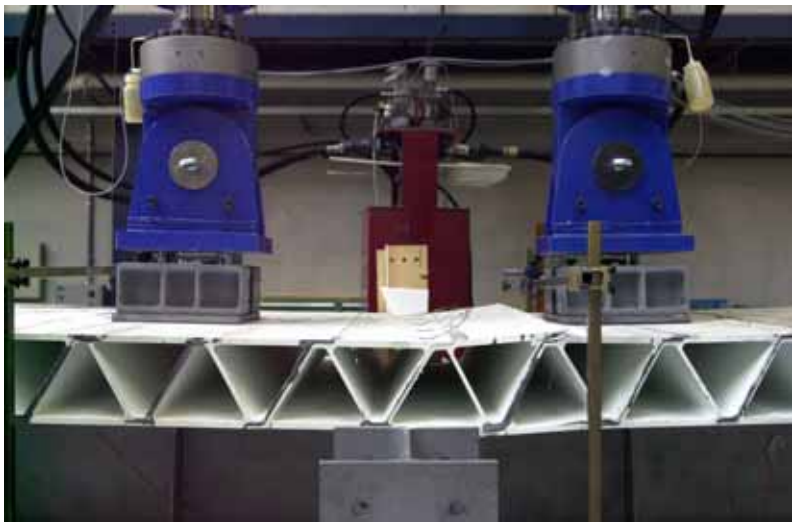

Figure E.15: Back view mid-span, failure in axis H - H

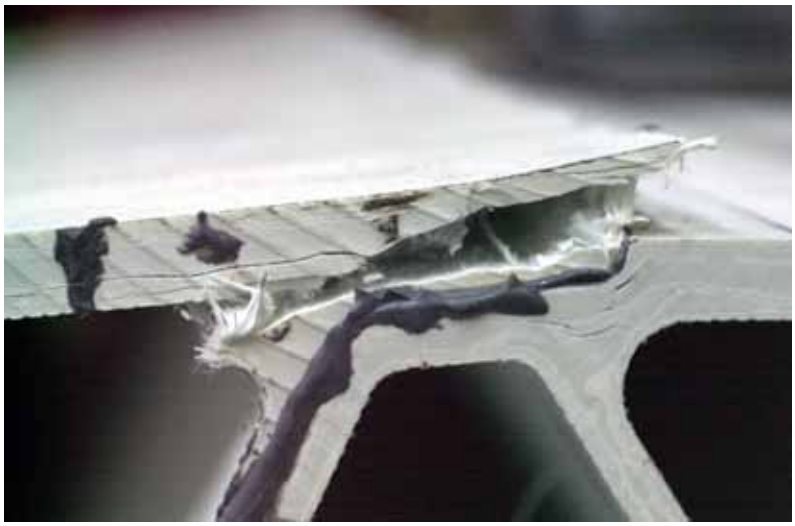

Figure E.16: Detail failure of upper face panel, axis H - H, back view

Figure E.17: Detail failure of upper face panel, axis H - H, front view

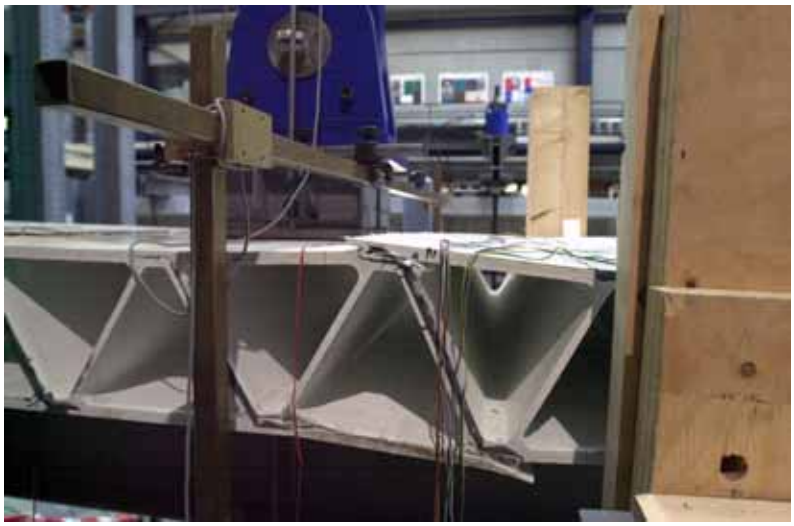

Figure E.18: Front view axis H - H

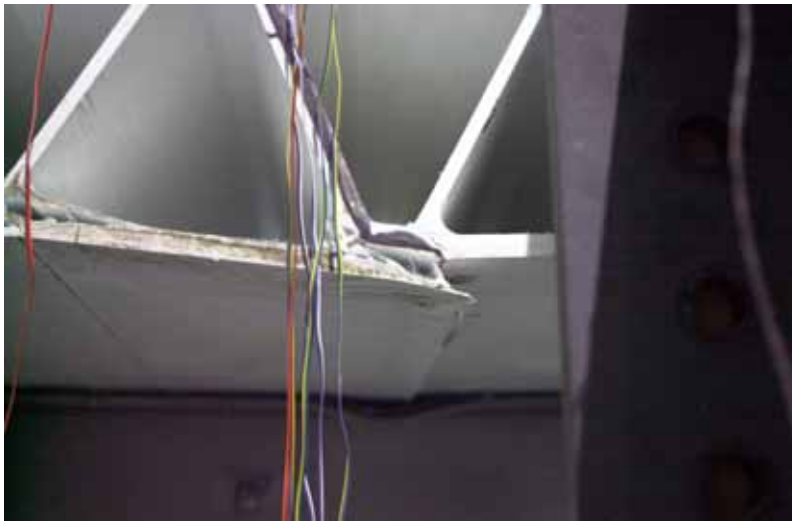

Figure E.19: Front view axis H - H with buckling of top steel flange

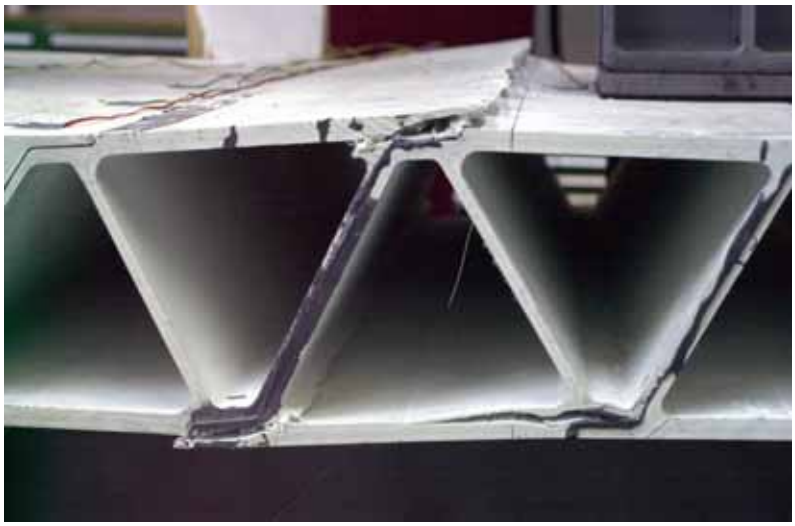

Figure E.20: Back view axis H - H

Figure E.21: Small cracks near location of failure, axis L - L

E.3 DuraSpan girders

E.3.1 Pictures Fix 1

Figure E.22: Front view with horizontal support at mid-span

Figure E.23: Front view with failure in axis H - H

Figure E.24: Side view from right with visible large deflection at ∼280 kN/jack

Figure E.25: Bottom view with large deflection and plastic hinges under the jacks

Figure E.26: Crack due to secondary bending moments in the upper face sheet, axis G - G

E.4 Pictures Fix 2

Figure E.27: Undulated deformation of the upper face sheet due to Vierendeel action (at the onset of failure)

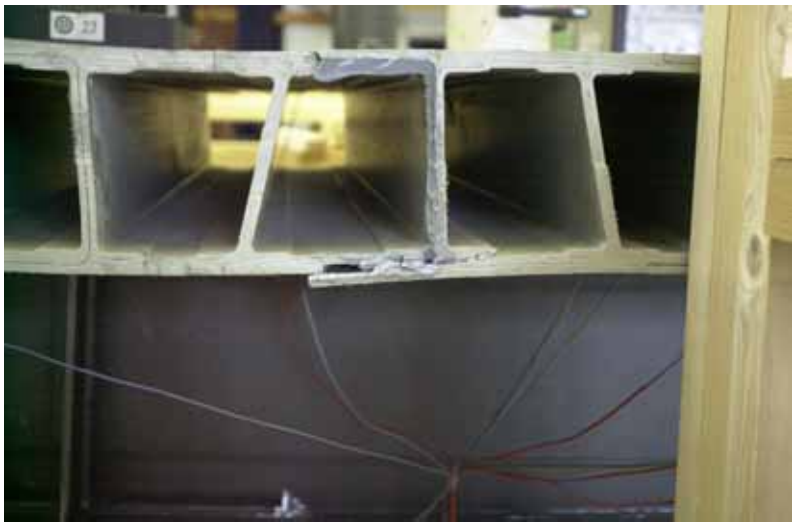

Figure E.28: Initial failure in axis K - K in the epoxy adhesive joint of the lower deck face sheet between the jacks.

Figure E.29: Side view from right with large deformations at the onset of failure

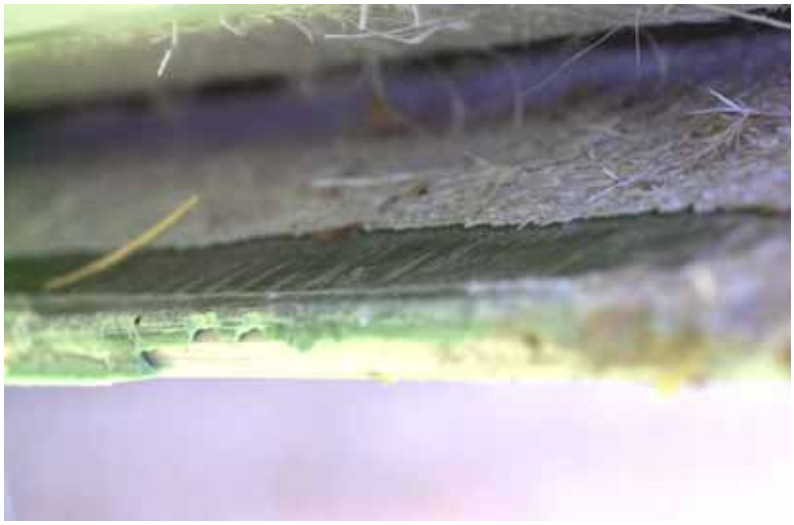

Figure E.30: Failure in a polyurethane joint (axis H - H) showing adhesion problems at the profile edge

Figure E.31: Failure in the upper face sheet of an epoxy joint (near axis J - J) showing good adhesion but locations with no adhesive

Figure E.32: Same axis as in Fig. E.31 but lower face sheet. Combined compression/shear failure

Figure E.33: Detail of a polyurethane joint with failure in the first layer of the FRP (the adhesive joint stays intact)

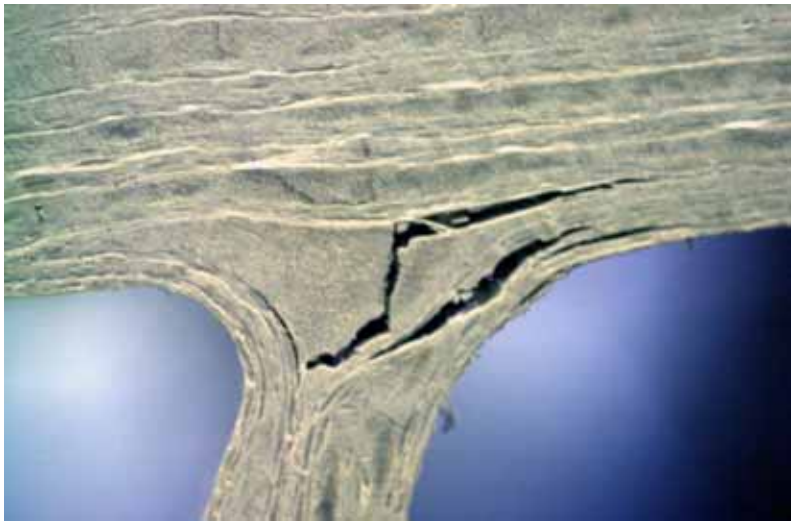

Figure E.34: Crack due to secondary bending moments in the upper face sheet, axis G - G

Appendix F

Plans of instrumentation; girder experiments

F.1 ASSET girders

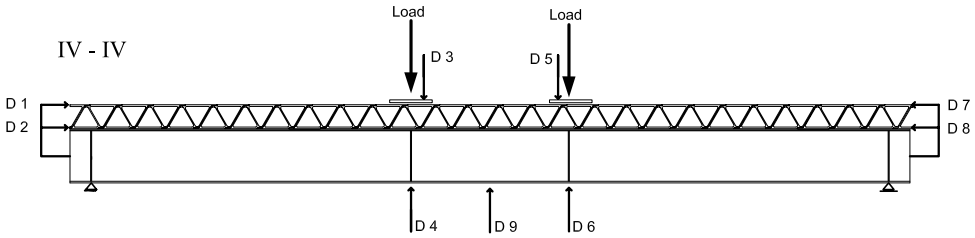

Figure F.1: Displacement transducers

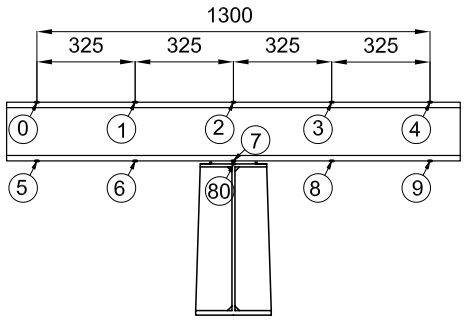

Figure F.2: Strain gages section A - A

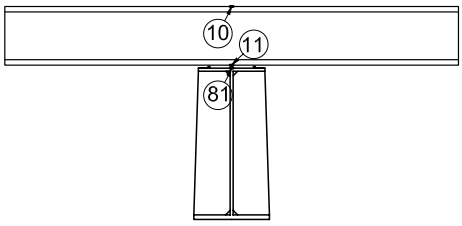

Figure F.3: Strain gages section B - B

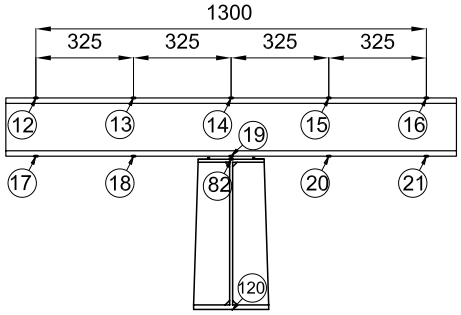

Figure F.4: Strain gages section C - C

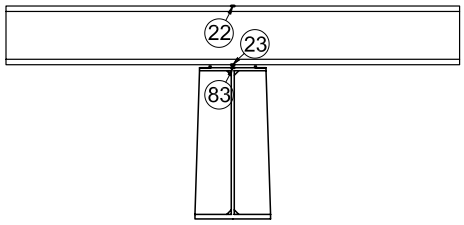

Figure F.5: Strain gages section D - D

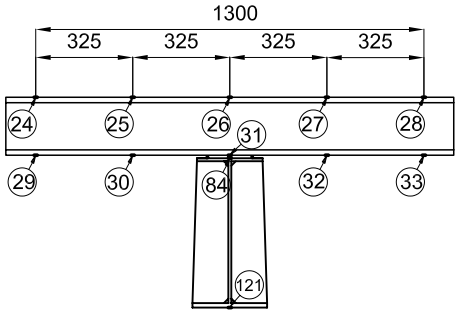

Figure F.6: Strain gages section E - E

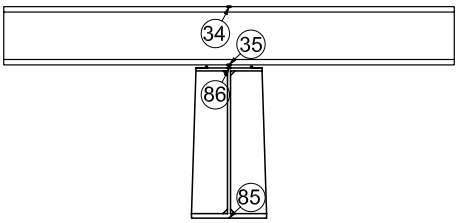

Figure F.7: Strain gages section F - F

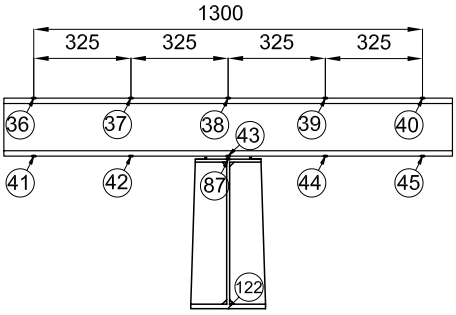

Figure F.8: Strain gages section G - G

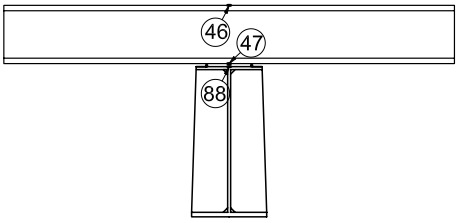

Figure F.9: Strain gages section H - H

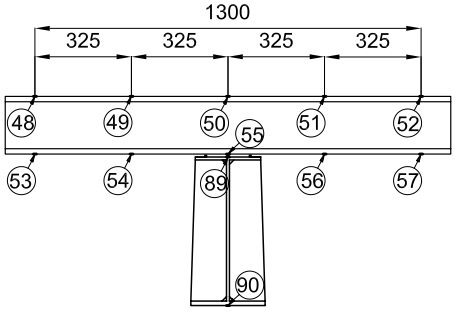

Figure F.10: Strain gages section J - J

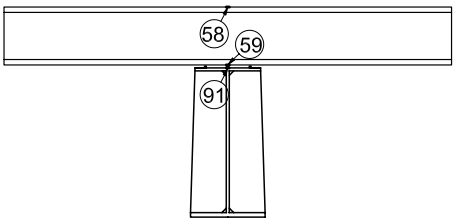

Figure F.11: Strain gages section K - K

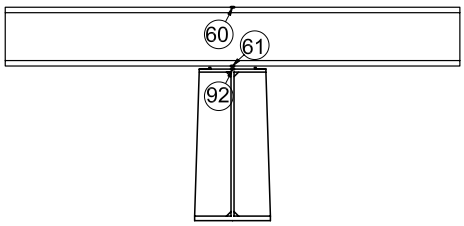

Figure F.12: Strain gages section L - L

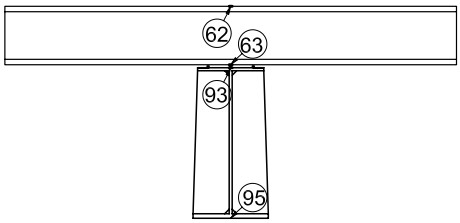

Figure F.13: Strain gages section M - M

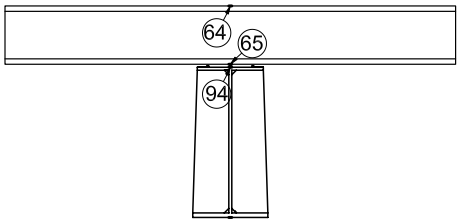

Figure F.14: Strain gages section N - N

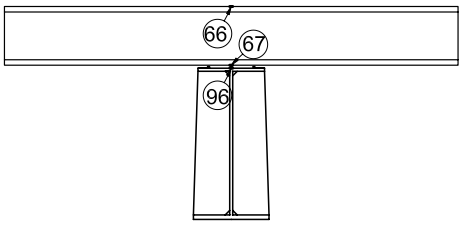

Figure F.15: Strain gages section O - O

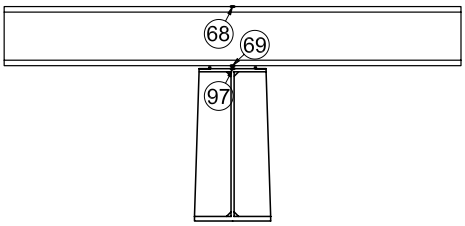

Figure F.16: Strain gages section P - P

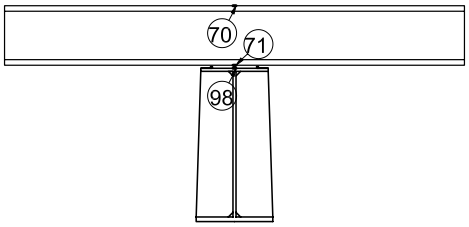

Figure F.17: Strain gages section Q - Q

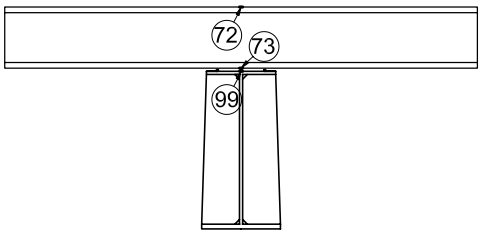

Figure F.18: Strain gages section R - R

F.2 DuraSpan girders

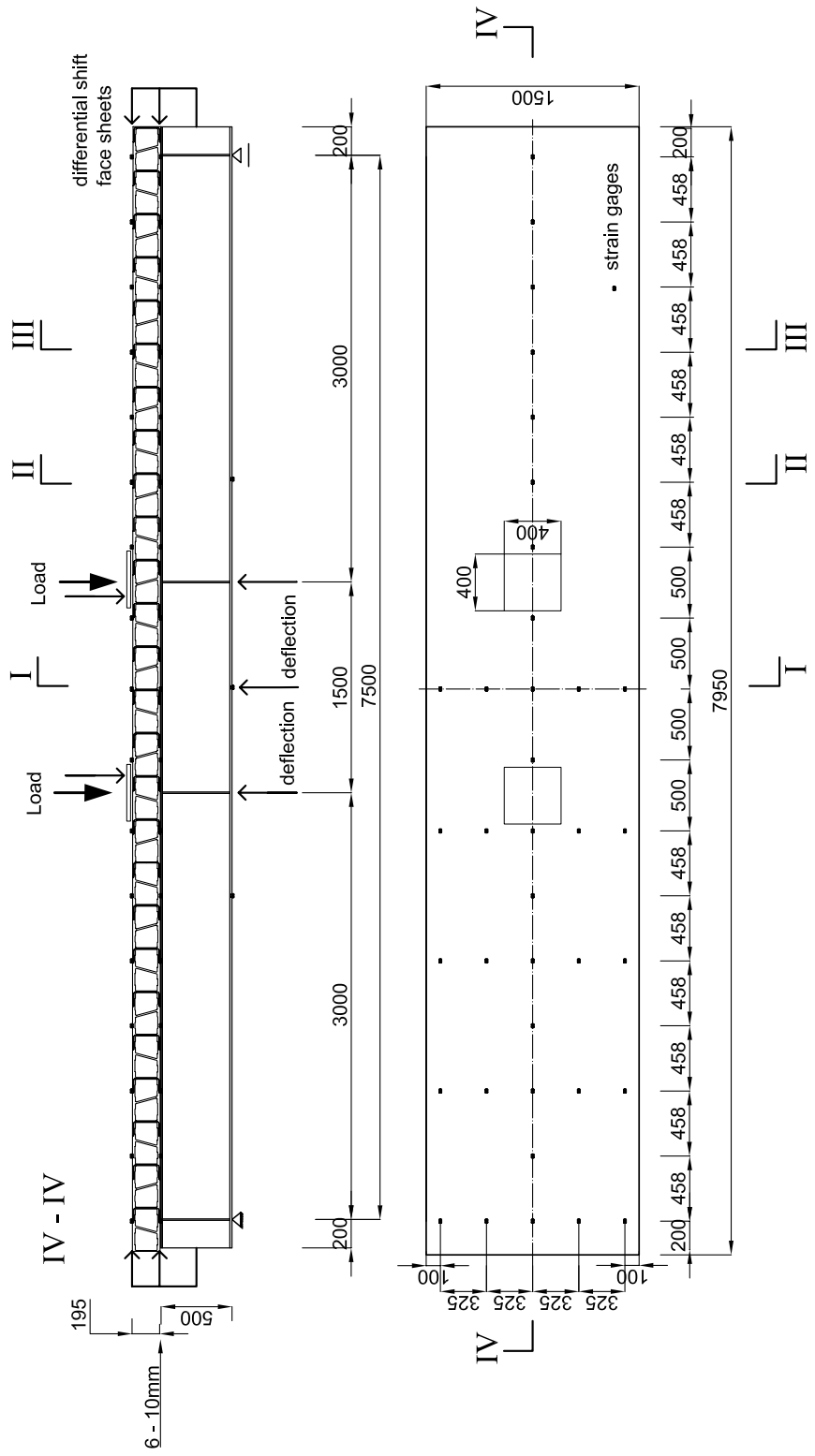

Figure F.19: Set-up, elevation and top view of DuraSpan girder.

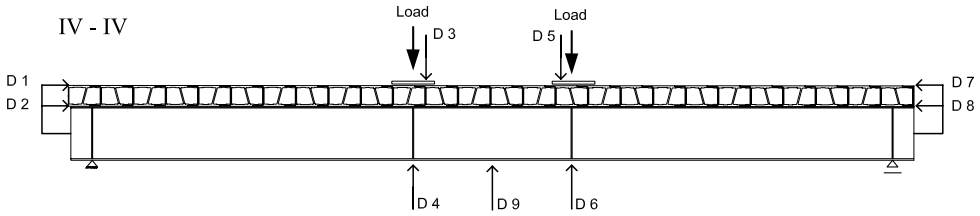

Figure F.20: Displacement transducers

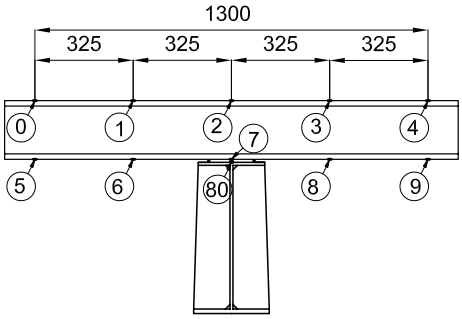

Figure F.21: Strain gages section A - A

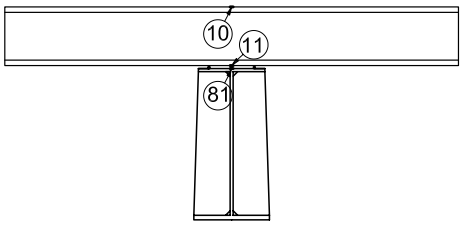

Figure F.22: Strain gages section B - B

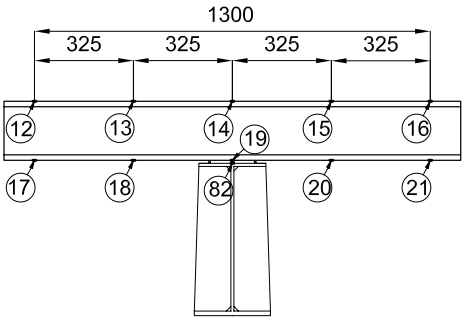

Figure F.23: Strain gages section C - C

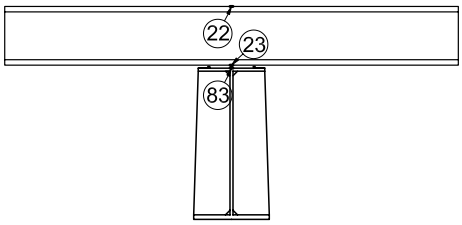

Figure F.24: Strain gages section D - D

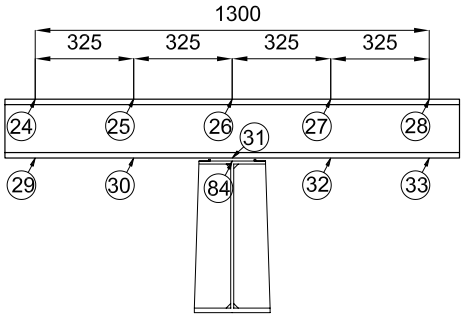

Figure F.25: Strain gages section E - E

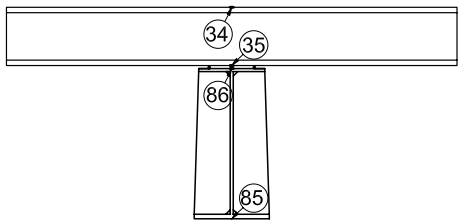

Figure F.26: Strain gages section F - F

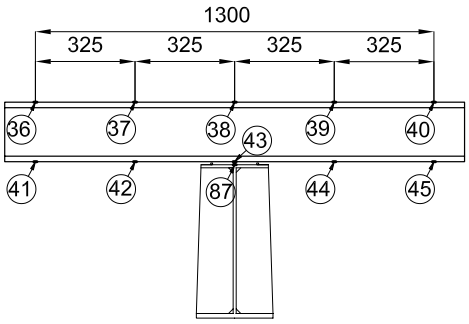

Figure F.27: Strain gages section G - G

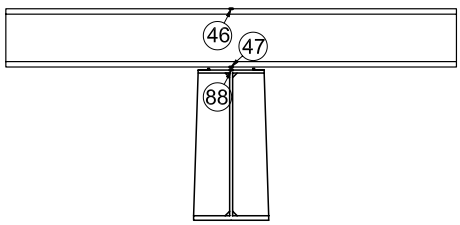

Figure F.28: Strain gages section H - H

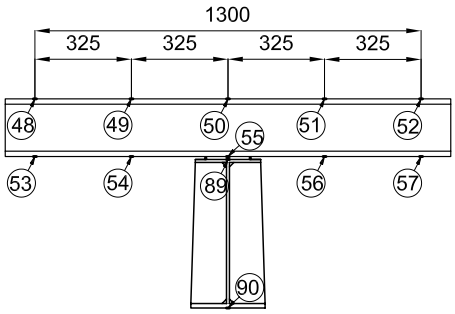

Figure F.29: Strain gages section J - J

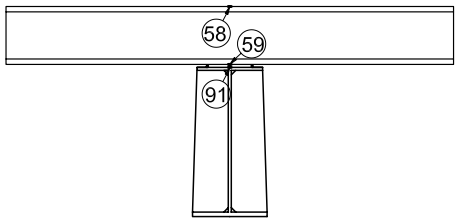

Figure F.30: Strain gages section K - K

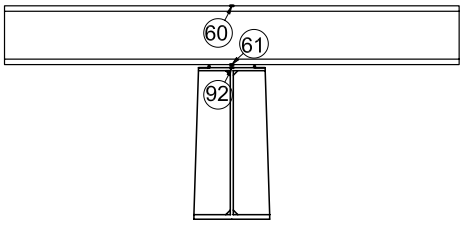

Figure F.31: Strain gages section L - L

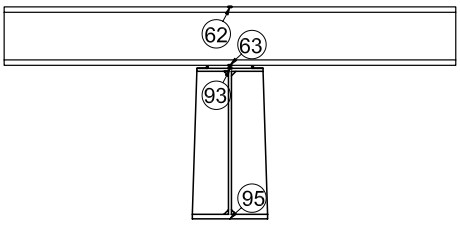

Figure F.32: Strain gages section M - M

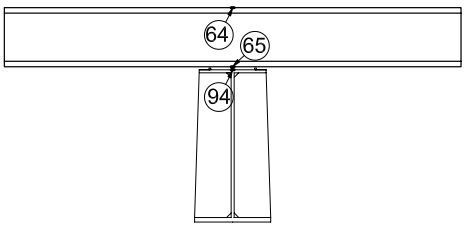

Figure F.33: Strain gages section N - N

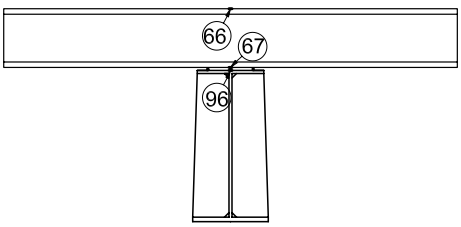

Figure F.34: Strain gages section O - O

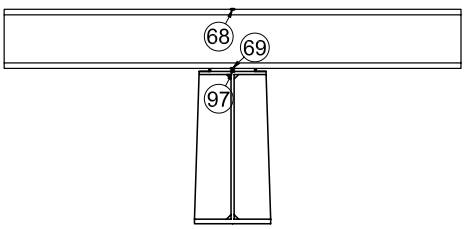

Figure F.35: Strain gages section P - P

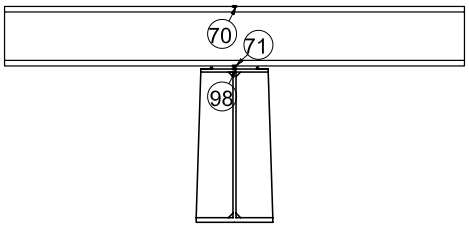

Figure F.36: Strain gages section Q - Q

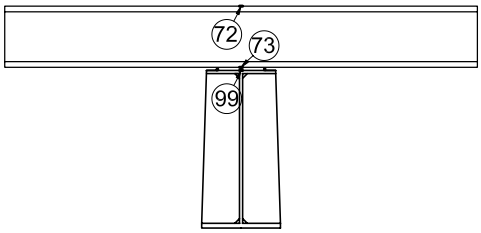

Figure F.37: Strain gages section R - R

List of Figures

List of Tables

Bibliography

[1] Alampalli, S. ; Kunin, J. : Load Testing of An FRP Bridge Deck On a Truss Bridge / Transportation Research and Development Bureau. New York State Department of Transportation, State Campus, Albany New York 12232-0869, July 2001 (FHWA/NY/SR-01/137). – Special Report

[2] Alampalli, S. ; Kunin, J. : Rehabilitaion and Field Testing of an FRP Bridge Deck on a Truss Bridge. In: *Composite Structures* 57 (2002), p. 373–375

[3] Alampalli, S. ; O'Connor, J. ; Yannotti, A. : Fiber Reinforced Polymer Composites for the Superstructure of a Short-Span Rural Bridge. In: *Composite Structures* 58 (2002), p. 21–27

[4] Andrä, H.-P. ; König, G. ; Maier, M. : Einsatz vorgespannter Kohlefaser-Lamellen als Oberflächenspannglieder. In: *Beton- und Stahlbetonbau* 96 (2001), No. 12, p. 737–747

[5] Anonymous: Unidirectionally oriented fiber-reinforced rods for bridges. In: *Plastics engineer* (1987), April, p. 14

[6] Anonymous. *The First All Composite road Bridge Installed in the United States*. www.ksci.com/nncb1.html. November 1996

[7] Anonymous. *Data Sheet NM BPE Lim 465*. Nils Malmgren AB,Box 2039, S-442 02 Ytterby, Sweden. May 1997

[8] Anonymous. *Data Sheet Pliogrip 6660*. P.O. Box 2219, Columbus, OH 43216, USA. 1999

[9] Anonymous. *Bridge Brochure,* H*ardcore* C*omposites*. 618 Lambsons Lane, New Castle, DE 19720, USA. March 2000

[10] Anonymous. *Composite Bridge, Schwerin Germany*. www.creative-pultrusions.com. November 2003

[11] Anonymous: *Global FRP Use for Bridge Applications: Pedestrian*. 600 Mamaronek Avenue, Harrison, NY 10528 : Market and Development and Alliance for the FRP Composites Industry, April 2003. – www.mdacomposites.org

[12] Anonymous: *Global FRP Use for Bridge Applications: Vehicular*. 600 Mamaronek Avenue, Harrison, NY 10528 : Market and Development and Alliance for the FRP Composites Industry, April 2003. – www.mdacomposites.org

[13] Aref, A. ; Parsons, I. : Design and Analysis Procedures for a Novel Fiber Reinforced Plastic Bridge Deck. In: El-Badry, M. (editor): *Advanced Composite Materials in Bridges and Sructures*. Montreal, Quebec, Canada, 1996, p. 743–750

[14] Aref, A. ; Parsons, I. : Design and Performance of a Modular Fiber Reinforced Plastic Bridge. In: *Composites: Part B* 31 (2000), p. 619–628

[15] Bakis, C. ; Bank, L. ; Brown, V. ; Cosenza, E. ; Davalos, J. ; Lesko, J. ; Machida, A. ; Rizkalla, S. ; Triantafillou, T. : Fiber-Reinforced Polymer Composites for Construction - State-of-the-Art Review. In: *Journal of Composites for Construction* (2002), May, p. 73–87. – American Society of Civil Engineers - 150th Anniversary Paper

[16] Ballinger, C. A.: Development of Composites for Civil Engineering. In: *ASCE Specialty Conference on Advanced Composite Materials in Civil Engineering Structures*. New York, 1991, p. 288–301

[17] Bassetti, A. : *Lamelles précontraintes en fibres carbone pour le renforcement de ponts rivetés endommagés par fatigue*. Lausanne, École Polytechnique Fédérale de Lausanne, PhD Thesis, 2001. – Thèse N° 2440

[18] Braestrup, M. B.: Footbridge Constructed From Glass-Fiber-Reinforced Profiles. In: *Structural Engineering International* 4 (1999), p. 256–258

[19] Bridge, R. ; Scott, I. : Connections for Fibre Reinforced Polymer (FRP) Composite Bridges - Issues Related to Design / Centre for Construction Technology and Research. University of Western Sydeny, Locked Bag 1797, South Penrith NSW 1797, Australia, October 2003. – Technical Report

[20] Brüninghoff, H. : *Holzbauwerke: eine ausführliche Erläuterung zu DIN 1052, Teil 1 bis Teil 3*. Beuth-Verlag, 1997. – ISBN 3–410–13739–4

[21] Burgoyne, C. J.: Advanced Composites in Civil Engineering in Europe. In: *Structural Engineering International* Vol. 4 (1999)

[22] Burgoyne, C. ; Head, P. : Aberfeldy Bridge - An Advanced Textile Reinforced Footbridge. In: *TechTextil Symposium Frankfurt* (1993), No. 418

[23] Burgueño, R. ; Karbhari, V. M. ; Seible, F. ; Kolozs, R. T.: Experimental Dynamic Chracterization of an FRP Composite Bridge Superstructure Assembly. In: *Composite Structures* 54 (2001), p. 427–444

[24] Burgueño, R. ; Zhao, L. ; Rovere, H. L. ; Seible, F. ; Karbhari, V. M.: Characterization of Hybrid FRP Beam-Slab Bridge Systems. In: Humar, J. (editor) ; Razaqpur, A. (editor): *Advanced Composite Materials in Bridges and Structures*. Ottawa, Ontario, Canada, August 2000, p. 793–800

[25] Canning, L. : Connections for West Mill Bridge. (2003). – Mouchel Parkman, UK

[26] Cassity, P. : Advanced Composites for Bridge Infrastructure Renewal - Phase II DARPA Agreement No. MDA972-94-3-0030 / Advanced Composites Technology Transfer/Bridge, Infrastructure Renewal Consortium. 2000 (Volume IV, Task 16 - Modular Composite Bridge). – Final Technical Report

[27] Cassity, P. ; Richards, D. ; Gillespie, J. : Compositely Acting FRP Deck and Girder System. In: *Structural Engineering International* 2 (2002), p. 71–75

[28] de Castro San Roman, J. : Experiments on Adhesives / Composite Construction Laboratory. EPFL-ENAC-CCLab, Bât. BP, CH-1015 Lausanne, 2004 (CCLab2000.1b/1). – Technical Report

[29] Clarke, J. L.: FRP Materials for Reinforcing and Strengthening Concrete Structures. In: *Composites and Plastics in Construction.* Waterford, UK : BRE, November 1999. – paper 17

[30] Clarke, J. L.: *The Use of Fibre Composites in Concrete Bridges.* The concrete society, Century House, Telford avenue, Crowthorne Berkishire RG45 6YS : Concrete Bridge developemnt Group, 2000 (Technical Guide No. 3). – ISBN 0 946691 77 0

[31] Cousins, T. E. ; Lesko, J. J.: Plate and Tube Bridge Deck Evaluation in The Deck Test Bed of The Troutville, Virginia, Weight Station / Department of Civil and Environmental Engineering, Virginia Polytechnic Institute & State University. 2004. – Final Contract Report

[32] Cripps, A. ; Harris, B. ; Ibell, T. : *Fibre-Reinforced Polymer Composites in Construction.* 6 Storey's Gate, Westminster, London SW1P 3AU : CIRIA, 2002. – ISBN 0 86017 564 2

[33] Crocker, H. ; Shehata, E. ; Haldane-Wilsone, R. ; Mufti, A. : Innovative Fiber Reinforced Bridge Deck Modules. In: *Third International Conference on Composites in Infrastructure* University of Arizona, 2002. – paper 076

[34] Daly, A. F. ; Cuninghame, J. R.: Performance of a Fibre-Reinforced Polymer Bridge Deck under Dynamic Wheel Loading. In: Hollaway, L. (editor): *Advanced Polymer Composites for Structural Applications in Construction.* Proceedings of the Second International Conference, held at the University of Surrey, Guilford, UK : Woodhead Publishing Limited, April 2004, p. 483–492

[35] Davalos, J. F. ; Qiao, P. ; Xu, X. F. ; Robinson, J. ; Barth, K. E.: Modeling and Characterization of Fiber-Reinforced Plastic Honeycomb Sandwich Panels for Highway Bridge Applications. In: *Composite Structures* 52 (2001), p. 441–452

[36] Deuring, M. : Verstärken von Stahlbeton mit gespannten Faserverbundwerkstoffen / EMPA, Swiss Federal Laboratories for Materials Testing and Research. 1993 (224). – Technical Report

[37] Dorton, R. A. ; Reel, R. : *Methods for Increasing Live Load Capacity of Existing Highway Bridges.* 2101 Constitution Avenue, N.W. Washington, D.C. 20418 : Transportation Research Board, 1997. – ISBN 0–309–06105– 9

[38] Eckel, D. A.: *A Theoretical and Experimental Study of the Behavior of Sanwich Bridge Decks Composed of Composite Materials.* 201 Composites Manufacturing Science Laboratory, Newmark Delaware 19716-3144, University of Delaware, Center for Composite Materials, Master Thesis, October 1998

[39] Eckel, D. A.: *An All Fiber- Reinforced-Polymer-Composite Bridge: Design, Analysis, Fabrication, Full-Scale Experimental Structural Validation, Construction an Erection.* 201 Composites Manufacturing Science Laboratory, Newmark Delaware 19716-3144, University of Delaware, Center for Composite Materials, PhD thesis, 2002

[40] Eibl, J. : *Beton-Kalender 1993, Taschenbuch für Stahlbeton- und Spannbetonbau sowie die verwandten Fächer.* Vol. II. Ernst & Sohn, Verlag für Architektur und technische Wissenschaften Berlin, 1993. – ISBN 3–433–01183–4

[41] European Committee for Standardisation (CEN): *Eurocode 5, Design of timber structures.* Final Draft. October 2002

[42] European Committee for Standardization (CEN): *Eurocode 4; Design of composite steel and concrete structures, Part 1.1: General rules and rules for buildings.* Revised Edited Document. June 2003

[43] Faza, S. ; GangaRao, H. : Pre- and Post-Cracking Behavior of Concrete Beams Reinforced with Fibre-Reinforced Plastic Rebars. In: *Advanced Composite Materials in Bridges and Structures* (1992), p. 151–160

[44] Fiedler, E. : Die Entwicklung des Stahlbrückenbaues in der DDR bis zum Zeitpunkt der Wende ein Rückblick (Teil II). In: *Stahlbau* 70 (2001), No. 5, p. 317–328

[45] Finch, W. W. ; Chajes, M. J. ; Shenton, H. : Field Test of Bridge 1-192 on Old Milltown Road Over Mill Creek / Structural Testing Incorporated. P.O. Box 9817, Newmark, Delaware 19714-9817, August 1999. – Technical Report

[46] Fischer, M. ; Pasquier, M. : Shear Behavior of Structural Adhesives in the Bondline. In: *Construction & Building Materials* 3 (1989), March, No. 1, p. 31–34

[47] Gama, B. A. ; Gillespie, J. W.: Static and Fatigue Response of Composite Bridge Decks Subjected to Static and Fatigue Loads / University

of Delaware, Center for Composite Materials. Newmark, DE, 19711, USA, 2000. – Final Report

[48] Gan, L. H. ; Ye, L. ; Mai, Y.-W. : Design and Evaluation of Various Section Profiles for Pultruded Deck Panels. In: *Composite Structures* 47 (1999), p. 719–725

[49] GangaRao, H. ; Craigo, C. A.: Fiber Reinforced Bridge Decks in the USA. In: *Structural Engineering International* 4 (1999), p. 286–288

[50] GangaRao, H. V. ; Thippeswamy, H. K. ; Shekar, V. ; Craigo, C. : Development of Glass Fiber Reinforced Polymer Composite Bridge Deck. In: *SAMPE Journal* 35 (1999), July/August, No. 4, p. 12–23

[51] Gillespie, J. ; Eckel, D. ; Sabol, S. ; Mertz, D. ; Chajes, M. ; Shenton, H. ; Hu, C. ; Chaudhri, M. ; Faqiri, A. ; Soneji, J. : Bridge 1-351 Over Muddy Run: Design Testing and Erection of an All-Composite Bridge. In: *Transportation Research Record* 2 (2000), No. of Paper 5B0092. – 5th International Bridge Engineering Conference

[52] Hag-Elsafi, O. ; Lund, R. ; Alampalli, S. : Strengthening of a Bridge Pier Capbeam Using Bonded FRP Composite Plates. In: *Composite Structures* Vol. 57 (2002), p. 393 – 403

[53] Hart-Smith, L. J.: Analysis and Design of Advanced Composite Bonded Joints / NASA. 1974 (CR-2218). – Technical Report

[54] He, Y. ; Aref, A. J.: An Optimization Design Procedure for Fiber Reinforced Polymer Web-Core Sandwich Bridge Deck Systems. In: *Composite Structures* 60 (2003), p. 183–195

[55] Hertig, P. : Utilisation des résines Epoxy pour le collage acier-béton dans la constructions mixte. In: *Bulletin technique de la Suisse Romande* 99 (1973), No. 18, p. 374–378

[56] Hill, P. ; Smith, S. ; Barnes, F. : Use of High Modulus Carbon fibres for Reinforcement of Cast Iron Compression Strutts within the London Underground - Project details. In: *Composites and Plastics in Construction.* Watford UK, November 1999. – Paper 16

[57] Hänsch, H. : Anwendung der Klebetechnik zur Schnellmontage einer Trägerrost-Verbundbrücke. In: *Die Strasse* (1976), January, No. 1, p. 27–31

[58] Hänsch, H. ; Krämer, W. : Versuche mit geklebten Verbundkonstruktionen. In: *Die Strasse* (1968), March, No. 3, p. 137–141

[59] Hoffmann, K. : *An Introduction to Measurements using Strain Gages.* Hottinger Baldwin Messtechnik GmbH, Darmstadt, Germany, 1989

[60] Hollaway, L. (Editor): *Handbook of polymer composites for engineers.* Cambridge, England : British Plastics Federation, Woodhead publishing limited, 1994

[61] Hollaway, L. : The Evolution of and the Way Forward for Advanced Polymer Composites in the Civil Infrastructure. In: *Construction and Building Materials* 17 (2003), p. 365–378

[62] Hollaway, L. : The Development and the Future of Advanced Polymer Composites In the Civil Infrastructure. In: *International Conference of Advanced Polymer Composites in Construction (ACIC)* School of Engineering, Civil Engineering, University of Surrey, 2002

[63] Kaiser, H. : *Bewehren von Stahlbeton mit kohlenstoffaserverstärkten Epoxidharzen.* Dübendorf, Switzerland, EMPA, Swiss Federal Laboratories for Materials Testing and Research, PhD Thesis, 1989. – Nr. 8918

[64] Karbhari, V. : Fiber Reinforced Composite Decks for Infrastructure Renewal. In: El-Badry, M. (editor): *Advanced Composite Materials in Bridges and Structures.* Montreal, Quebec, Canada, 1996, p. 759–766

[65] Karbhari, V. ; Seible, F. ; Burgueño, R. ; Davol, A. ; Wernli, M. ; Zhao, L. : Structural Characterization of Fiber-Reinforced Composite Short- and Medium-Span Bridge Systems. In: *Applied Composite Materials* 7 (2000), p. 151–182

[66] Keller, T. : Overview of Fibre-Reinforced Polymers in Bridge Construction. In: *Structural Engineering International* 12 (2002), May, No. 2, p. 66–70

[67] Keller, T. ; de Castro, J. : System Ductility and Redundancy of FRP Structures With Ductile Adhesive Joints. In: *Journal of Composites for Construction.* – submitted

[68] Keller, T. ; de Castro, J. ; Dolley, S. ; Dubois., V. : Use of Fiber Reinforced Polymers in Bridge Construction / Swiss Federal Roads Authority. 2001 (Report No. 555). – Technical Report. State-of-the-Art Report with Application and Research Recommendations

[69] Keller, T. ; Gürtler, H. : Design of Hybrid Bridge Girders with Adhesively Bonded and Compositely Acting FRP Deck. In: *Journal of Composites for Construction.* – submitted

[70] Keller, T. ; Gürtler, H. : In-plane Compression and Shear Performance of Cellular GFRP Bridge Decks Acting as Top Chord of Bridge Girders. In: *Composite Structures* (2004). – approved

[71] Keller, T. ; Gürtler, H. : Quasi-static and Fatigue Performance of a Cellular GFRP Bridge Deck Adhesively Bonded to Steel Main Girders. In: *Composite Structures* (2004). – approved

[72] Keller, T. ; Schollmayer, M. : Plate bending behavior of a pultruded GFRP bridge deck system. In: *Composite Structures* (2004), June, No. 64, p. 285–295. – http://dx.doi.org/10.1016/j.compstruct.2003.08.011

[73] Khalifa, M. A. ; Hodhod, O. A. ; Zaki, M. A.: Analysis and Design Methodology for an FRP Cable-Stayed Pedestrian Bridge. In: *Composites: Part B* 27B (1996), p. 307 – 317

[74] Krämer, W. : Straßenbrücke mit Stahlbetonfertigteilen im Klebeverbund. In: *Die Strasse* (1969), March, No. 3, p. 121–125

[75] Kumar, P. ; Chandrashekhara, K. ; Nanni, A. : Structural Performance of a FRP Bridge Deck. In: *Construction and Building Materials* 18 (2004), p. 35–47

[76] Lee, J. ; Hollaway, L. ; Thorne, A. ; Head, P. : The Structural Characteristics of a Polymer Composite Cellular Box Beam in Bending. In: *Construction and Building Materials* 9 (1995), No. 6, p. 333–340

[77] Luke, S. ; Canning, L. ; Collins, S. ; Knudsen, E. ; Brown, P. ; Taljsten, B. ; Olofsson, I. : Advanded Composite Bridge Decking System - Project ASSET. In: *Structural Engineering International* (2002), May, p. 76–79

[78] Meier, H. ; Meier, U. : Zwei CFK-Kabel für die Storchenbrücke. In: *Scheizer Ingenieur und Architekt* (1996), October, No. 44, p. 980–985

[79] Chapter: New construction materials. Performance, characterization and analysis In: Meier, U. : *Advanced Solutions with Composites in Construction*. Swets & Zeitlinger, Lisse, ISBN 90 2651 858 7, (2001), p. 3–9

[80] Meier, U. ; Deuring, M. ; H.Meier ; Schwelger, G. : *CFRP Bonded Sheets, Reinforcement for Concrete Structures: Properties and Applications*. EMPA, Swiss Federal Laboratories for Materials Testing and Research, 1993

[81] Meier, U. : Brückensanierung mit Hochleistungs - Faserverbundwerkstoffen. In: *Material und Technik* Vol.15 (1987), p. p.125 – 128

[82] Meier, U. : Strengthening of Structures Using Carbon Fiber/Epoxy Composites. In: *Construction and Buildings Materials* Vol.9 (1995), No. N°6, p. p.341–351

[83] Meier, U. ; Kaiser, H. : Strengthening of Structures with CFRP Laminates. In: Iyler, S. L. (editor): *Advanced Composites Materials in Civil Engineering Structures*. 345 East 47th Street, New York : American Society of Civil Engineers, January 1991, p. 224 – 232

[84] Möhler, K. : Über das Tragverhalten von Biegeträgern uind Druckstäben mit zusammengesetzten Querschnitten und nachgiebiger Verbindung / Technische Hochschule Fridericiana zu Karlsruhe. 1956. – Technical report to obtain the *venia legendi*

[85] Moon, F. ; Eckel, D. ; Gillespie, J. : Shear Stud Connection for the Development of Composite Action between Steel Girders and Fiber-Reinforced Birdge Decks. In: *Journal of Structural Engineering* (2002), June, p. 762–770

[86] Motley, D. R. ; Castanos, S. A. ; Richards, D. : Effects of Diagonal Webs in FRP Bridge Decks / North Carolina State University, USA. 2001. – Report

[87] Mufti, A. ; Erki, M. ; Jaeger, L. : Advanced Composite Materials with Applications to Bridges - State of the Art / Canadian Society of Civil Engineers. 1991. – Technical Report

[88] Mufti, A. A.: FRPs and FOSs Lead to Innovation in Canadian Civil Engineering Structures. In: Teng, J.-G. (editor): *FRP Composites in Civil Engineering* Vol. 1. Hong Kong, China : Elsevier Science Ltd, December 2001, p. 49–60

[89] Mukhopadhyaya, P. ; Swamy, R. ; Lynsdale, C. : Influence of Aggressive Exposure Conditions on the Behaviour of Adhesive Bonded Concrete-GFRP Joints. In: *Construction and Buildings Materials* 12 (1998), September, p. 427–446

[90] Murphy, J. : *Reinforced Plastics*. 2nd. Elsevier Advanced Technology, 1998. – Handbook. – ISBN 1 85617 348 8

[91] Natterer, J. ; Hoeft, M. : Zum Tragverhalten von Holz-Beton-Verbundkonstruktionen / Swiss Federal Institute of Technology, Institute for timber structures. 1987 (CERS 1345). – Research report

[92] Plecnik, J. ; Azar, W. : Structural Components, Highway Bridge Deck Applications. In: *International Enzyclopedia of Composites* 6 (1991), p. 430–445

[93] Plunkett, J. D. ; Gill, S. R. ; Meggers, D. A. ; Hurst, K. ; Pickett, J. D. ; Borgstadter, J. D. ; Carter, P. A. ; Hoback, R. L. ; Walker, H. S. ; Held, J. : Fiber Reinforced Polymer Honeycomb Composite Short-Span Bridge for Rapid Installation. In: Bank, L. C. (editor): *Materials and Construction: Exploring the Connection*. Cincinati, Ohio, USA, May 1999, p. 300–307

[94] Qiao, P. ; Davalos, J. F. ; Brown, B. : A Systematic Analysis and Design Approach for Single-Span FRP Deck/Stringer Bridges. In: *Composites: Part B* 31 (2000), p. 593–609

[95] Rahman, A. ; Kingsley, C. ; Kobashi, K. : Service and Ultimate Load Behavior of Bridge Deck Reinforced with Carbon FRP Grid. In: *Journal of composites for construction* (2000), February, p. 16–22

[96] Renton, W. J. ; Vinson, J. : Analysis of Adhesively Bonded Joints Between Panels of Composite Materials. In: *Journal of Applied Mechanics* (1977), March, p. 101–106

[97] Rizkalla, S. ; Williams, B. : Development of Modular GFRP Bridge Decks. In: humar, J. (editor) ; Razaqpur, A. (editor): *Advanced Composite Materials in Bridges And Structures*. Ottawa, Ontario, Canada, August 2000, p. 95–102

[98] Rostásy, R. ; Budelmann, H. : FRP Tendons for the Post-tensioning of Concrete Structures. In: Iyler, S. L. (editor): *Advanced Composites Materials in Civil Engineering Structures.* 345 East 47th Street, New York : American Society of Civil Engineers, January 1991, p. 155 – 166

[99] Sadka, B. ; Daly, A. F. ; Cuninghame, J. : Developments and Design Guideines for Fibre Reinforced Polymer Bridge Decks. In: *Lightweight Bridge Decks - European Bridge Engineering Conference.* Rotterdam, March 2003

[100] Salim, H. A. ; Davalos, J. F. ; Qiao, P. ; Kiger, S. A.: Analysis and Desgin of Fiber Reinforced Plastic Composite Deck-and-Stringer Bridges. In: *Composite Structures* 38 (1997), No. 1-4, p. 295–307

[101] Schneider, K.-J. : *Bautabellen für Ingenieure.* Werner Verlag GmbH, 1996. – ISBN 3–8041–3446–7

[102] Schwarz, H. ; Schlegel, H. : *Metallkleben und glasfaserverstärkte Plaste in der Technik.* 7. Berlin : VEB Verlag Technik, 1973

[103] Schwelger, G. : *Verstärken von Mauerwerk mit Faserverbundwerkstoffen*, Swiss Federal Institue of Technology, Zürich, PhD Thesis, 1994. – No. 10672

[104] Sedlacek, G. ; Trumpf, H. : Fiber-Reinforced Polymer Lightweight Bridge. In: *European Bridge Engineering Conference.* Rotterdam, NL, March 2003

[105] Seible, F. ; Karbhari, V. ; Zhao, L. ; Hose, Y. : Development and Implementation of Modular Bridge Systems. In: Figueiras, J. (editor) ; Juvandes, L. (editor) ; Faria, R. (editor): *Composites in Constructions.* Porto, Portugal : A.A. Balkema Publishers, Lisse, October 2001. – Proceedings of the International Conference Composites in Construction - CCC2001, p. 797–802

[106] Seible, F. : Designing with FRP Composites in the Civil Structural Environment. In: Teng, J.-G. (editor): *FRP Composites in Civil Engineering* Vol. 1, Elsevier Science. Ltd, 2001, p. 73–84

[107] Solomon, G. ; Godwin, G. : Expanded use of Composite Deck Projects in USA. In: *Structural Engineering International* 2 (2002), p. 102–104

[108] Souren, W. : Fibre-Reinforced Polymer Composites in Civil Engineering Structures. In: *Lightweight Bridge Decks - European Bridge Engineering Structures.* Rotterdam, March 2003

[109] Strehler, B. ; Künzle, O. : Static and Dynamic Testing of Fiber-Reinforced Bridge Girders. In: *Structural Engineering International* 4 (1999), p. 300–301

[110] Temeles, A. ; Lesko, J. : Composite Plate & Tube Bridge Deck Design: Evaluation in the Troutville, Virginia Weight Station Test Bed.

In: Humar, J. (editor) ; Razaqpur, A. (editor): *Advanced Composite Materials in Bridges and Structures.* Ottawa, Ontario, Canada, August 2000, p. 801–808

[111] Temeles, A. B.: *Field and Laboratory Tests of a Proposed Bridge Deck Panel Fabricated from Pultruded Fiber-reinforced Components.* Blacksburg, Virginia, USA, Virginia Polytechnic Institute and State University, Master Thesis, May 2001

[112] Tong, L. ; Steven, G. P.: *Analysis and Design of Structural Bonded Joints.* Kluwer Academic Publishers, 1999

[113] Trittler, G. ; Körnen, K. : Die vorgespannte Klebeverbindung (VK-Verbindung eine Weiterentwicklung der Verbindungstechnik im Stahlbau. In: *Der Stahlbau* 33 (1964), Semptember, No. 9, p. 257–269

[114] Tromp, L. : Design of a Composite Draw Bridge. In: *Lightweight Bridge Decks, European Bridge Engineering Conference.* Rotterdam, Netherlands, March 2003. – Paper 8

[115] Turvey, G. : Fibre Reinforced Polymer Composite Structural Pultrusions and Their End Connections. In: BRE (editor): *Composites and Plastics in Constructions.* Watford, UK, November 1999

[116] Turvey, G. : Evaluation of the Structural Performance of Box Beams Fabricated From a System of Pultruded Profiles. In: Figueiras, J. (editor) ; Juvandes, L. (editor) ; Faria, R. (editor): *Composites in Construction.* Porto, Portugal : A.A. Balkema Publishers, Lisse, October 2001. – Proceedings of the International Conference Composites in Construction - CCC2001, p. 803–808

[117] White, D. ; Busel, J. : CFRP & GFRP Composite Applications for Infrastructure Rehabilitation and Repair. In: *Annual Conference NASTO Saratoga* Northeast Association of State Transportation Officials, 2003

[118] Wolff, R. ; Miesseler, H.-J. : Glass-Fiber Prestressing Systems. In: Clarke, J. (editor): *Alternative Materials for the Reinforcement and Prestressing of Concrete.* Blackie, Glasgow, 1993. – ch. 6

[119] Yeung, Y. ; Nayler, A. : Composite Cables for Bridges and Other Structures. In: El-Badry, M. (editor): *Advanced Composite Materials in Bridges and Structures.* Montreal, Quebec, Canada, 1996, p. 245–252

[120] Zhou, A. ; Coleman, J. T. ; Lesko, J. J. ; Cousins, T. E.: Structural Analysis of FRP Bridge Deck Systems from Adhesively Bonded Pultrusion. In: Teng, J.-G. (editor): *FRP Composites in Civil Engineering* Vol. II, Elsevier Science Ltd, 2001, p. 1413–1420

[121] Zureick, A.-H. ; Shih, B. ; Munley, E. : Fiber-Reinforced Polymeric Bridge Deck. In: *Structural Engineering Review* 7 (1995), No. 3, p. 257–266

Index